ANOMALOUS TRANSPORT IN HETEROGENEOUS MEDIA

Inaugural-Dissertation

zur Erlangung des Doktorgrades der
Mathematisch-Naturwissenschaftlichen Fakultät der
Heinrich-Heine-Universität Düsseldorf

vorgelegt von

SIMON KASPAR SCHNYDER
aus Dielsdorf, Schweiz

Düsseldorf, Juni 2014

Aus dem Institut für Theoretische Physik II: Weiche Materie
der Heinrich-Heine-Universität Düsseldorf

Gedruckt mit der Genehmigung der
Mathematisch-Naturwissenschaftlichen Fakultät der
Heinrich-Heine-Universität Düsseldorf

Referent: Prof. Dr. Jürgen Horbach
Koreferent: Prof. Dr. Stefan Egelhaaf

Tag der mündlichen Prüfung:

Acknowledgements

Much of the joy in science lies in collaborating with others. I have been lucky in this regard, as I had the pleasure to work with a number of wonderful people over the last years. I thank all of them for the discussions, their advice and insights, and their company.

In particular, I would like to thank Jürgen Horbach for the exceptional and patient supervision of this work (Diamanten enstehen unter Druck, aber diese Dissertation nicht).

Furthermore, I would like to thank the people with whom I got to work on a number of fruitful projects: Roel Dullens, Thomas Franosch, Felix Höfling, Markus Spanner, Alice Thorneywork, Thomas Voigtmann and David Winter. Special thanks go to Nicolas Höft for his valuable work on making the simulation program fit for the 21st century.

Every day was made more pleasant by my colleagues. Especially, I would like to thank Amit Bhattacharjee, Pinaki Chaudhuri, Marc Engelhardt, Nicolas Höft, Philipp Kuhn, Juliane Schmitz, Gaurav Shrivastav and Henning Weis.

Financial support for this work was provided by DFG research unit FOR-1394 "Nonlinear response to probe vitrification" (HO 2231/7-1).

Summary

The movement of tracers in a homogeneous medium is typically associated with diffusion on long time scales. However, if the tracers are restricted to a fractal geometry, their movement will become anomalous, i.e. not diffusive. This scenario is realized in the Lorentz model (LM) where non-interacting point tracers are placed into a geometry formed by fixed hard-sphere obstacles which are randomly overlapping. At a critical obstacle density the system undergoes a localization transition at which transport becomes anomalous. The dynamics in this system is well understood via a dynamic scaling theory. The Lorentz model is an idealization of a class of heterogenous media. Far more complex heterogeneous media show dynamics similar to the Lorentz model, e.g. anomalous diffusion and the localization of particles. It is thus often assumed that the LM localization transition is the underlying phenomenon. Yet, it is still entirely open how relevant the LM scenario is for the understanding of realistic heterogeneous media and how strongly it becomes modified by increasing the complexity of the systems. Especially, soft interaction potentials and interactions between tracers have been suspected to modify the localization scenario considerably, but have not yet been studied in this respect.

This work's aims are thus two-fold. First, it tries to determine which conditions are necessary for the LM scenario to be realized and whether they are fulfilled in realistic systems. Second, it attempts to understand the rich behavior of realistic heterogeneous media near the localization transition by systematically increasing the complexity of the model, starting from the Lorentz model. One of the main results of this work is that systems with soft interactions behave *fundamentally differently* from their hard-sphere counterparts and that the localization transition in realistic systems is *rounded*, i.e. that a sharp critical point where all particles become localized does not exist anymore.

In this work, it is shown that the LM scenario *can* be reproduced with a fixed matrix made of purely repulsive, soft spheres and a non-interacting gas of tracers *only* if the tracers all have exactly the same energy. If the requirement of all particles having the same energy is lifted — resulting in an ideal gas confined in a soft matrix — the localization transition becomes rounded and the critical scaling breaks down. A similar rounding does not occur for hard-spheres. The rounding was quantified via a hard-sphere mapping as an average over all tracers, with each tracer having a different critical density according to its energy. The wide energy distribution of the tracers responsible for the rounding is a *generic feature* of realistic systems, implying that the LM scenario can apply to realistic heterogeneous media *only approximately*.

Increasing the complexity of the system, the ideal gas was then replaced with an interacting fluid. While the interacting fluid exhibited a rounded localization transition similar to the confined ideal gas, the *critical time-space scaling* of the Lorentz model was *restored* in certain cases — a stark contrast to the confined ideal gas.

Increasing the fluid density was shown to enhance long-time transport in cases. Since the energy barriers in the matrix are finite, particles are able to push each other out of void pockets. This cannot occur in hard-sphere systems. As a result and contradicting previous speculation, it was demonstrated that a soft heterogeneous medium can show an effective *reentrance transition* — where a localized fluid becomes delocalized simply by increasing the fluid density — without requiring a modification of the matrix structure.

Finally, *a rounded localization transition was identified in an experiment*, in which a colloidal fluid was confined in a quasi-two-dimensional random matrix, and successfully interpreted with the help of the simulation data.

Zusammenfassung

Die Bewegung von Teilchen in einem homogenen Medium wird auf langen Zeitskalen diffusiv. Wenn allerdings der für die Teilchen zugängliche Raum eine fraktale Struktur aufweist, wird die Bewegung anomal, d.h. nichtdiffusiv. Diese Situation tritt im Lorentz-Modell auf, in dem ein Gas aus nichtwechselwirkenden, punktförmigen Teilchen in den Hohlraum einer Matrix eingesetzt wird, die aus sich zufällig überlappenden Hartkugelhindernissen besteht. Bei einer kritischen Dichte der Hindernisse perkoliert das Hohlraumvolumen nicht mehr, d.h. es durchdringt nicht mehr das ganze System, sondern zerfällt in endliche Teile. Die Dynamik der Teilchen weist bei der kritischen Dichte einen Lokalisierungsübergang auf, der mit anomaler Diffusion auf langen Zeitskalen verknüpft ist. Die Dynamik der Teilchen in der Nähe des Übergangs kann mit Hilfe einer dynamischen Skalentheorie verstanden werden.

Das Lorentz-Modell stellt eine starke Idealisierung einer Klasse von heterogenen Medien dar. Auch deutlich komplexere heterogene Medien weisen ein Verhalten auf, das stark an das Lorentz-Modell erinnert, inklusive anomaler Diffusion und der Lokalisierung von Teilchen. Es wird daher häufig davon ausgegangen, dass der Lokalisierungsübergang des Lorentz-Modells auch in diesen Systemen auftritt, obwohl es bislang ungeklärt ist, wie wichtig er für das Verständnis dieser Systeme ist. Insbesondere wird erwartet, dass weiche Wechselwirkungspotentiale zwischen Teilchen und Matrix, und Wechselwirkung zwischen den beweglichen Teilchen den Lokalisierungsübergang stark beeinflussen. Dies ist allerdings noch nicht eingehend untersucht worden.

Die Ziele dieser Arbeit sind daher wie folgt: Einerseits soll untersucht werden, unter welchen Bedingungen der Lokalisierungsübergang des Lorentz-Modells auftreten kann und ob diese Bedingungen in realistischen Systemen gegeben sind. Andererseits soll versucht werden, das Verhalten von realistischen heterogenen Medien in der Nähe des Lokalisierungsübergangs zu verstehen. Dazu wird das Verhalten von einer Reihe von Systemen untersucht, die, ausgehend vom Lorentz-Modell, schrittweise komplexer werden. Als eines der Hauptresultate dieser Arbeit konnte gezeigt werden, dass Systeme mit weichen Wechselwirkungen sich fundamental von den entsprechenden Hartkugelsystemen unterscheiden und dass damit in realistischen heterogenen Medien der Lokalisierungsübergang abgerundet ist. Das bedeutet, dass es keinen scharfen kritischen Punkt mehr gibt, an dem alle Teilchen lokalisiert werden.

Zunächst wird gezeigt, dass ein nicht-wechselwirkendes Gas aus Teilchen in einer fixierten Matrix aus abstoßenden, weichen Kugeln, nur dann einen

Lokalisierungsübergang mit dem kritischen Verhalten der Lorentz-Modells aufweist, wenn alle Teilchen genau die gleiche Energie besitzen. Wenn diese Voraussetzung nicht erfüllt ist, entspricht das System stattdessen einem in der Matrix eingeschlossenen idealen Gas und der Lokalisierungsübergang wird abgerundet: Das Skalenverhalten, das im Lorentz-Modell in der Nähe des kritischen Punkts auftritt, ist nicht vorhanden und es gibt keinen scharfen Punkt mehr, an dem alle Teilchen lokalisiert werden. In Hartkugelsystemen hingegen, zeigen diese beiden Fälle das gleiche kritische Verhalten — das des Lorentz-Modells. Obwohl der Lokalisierungsübergang abgerundet ist, lässt sich die Dynamik mittels einer Abbildung auf harte Kugeln als eine Mittelung über die Dynamik des Lorentz-Modells beschreiben. Hierbei kann jedem Teilchen ein anderer kritischer Punkt zugeordnet werden, der sich aus dessen Energie berechnen lässt. Die breite Energieverteilung, die für die Abrundung des Lokalisierungsübergangs verantwortlich ist, ist eine *typische Eigenschaft* von realistischen Systemen. Deshalb kann der Lokalisierungsübergang in realistischen heterogenen Medien *nur näherungsweise* dem des Lorentz-Modells entsprechen.

Durch Einführen einer Wechselwirkung zwischen den beweglichen Teilchen erhöht sich die Komplexität des Systems weiter. Während auch das wechselwirkende System einen abgerundeten Übergang wie das ideale Gas aufweist, tritt in der Nähe des Übergangs wieder das *kritische Skalenverhalten* des Lorentz-Modells auf. In dieser Hinsicht unterscheidet sich das wechselwirkende System stark von dem idealen Gas.

Durch Erhöhen der Dichte der beweglichen Teilchen beschleunigt sich die Dynamik auf langen Zeitskalen. Dies wird dadurch ermöglicht, dass sich die Teilchen gegenseitig aus den Poren der Matrix schieben. Dies ist wiederum nur möglich, da die Energiebarrieren zwischen den Poren endlich sind. Da in Systemen aus harten Kugeln keine endlichen Barrieren vorkommen, ist solch ein Verhalten dort nicht möglich. Außerdem konnte hier gezeigt werden, dass ein vormals lokalisiertes System in der Nähe des Lokalisierungsübergangs durch Erhöhen der Dichte der beweglichen Teilchen delokalisiert werden kann. Vormalig war spekuliert worden, dass solch ein Übergang nur in Systemen möglich sei, in dem die beweglichen Teilchen einen Einfluss auf die Matrix haben, was hier ausgeschlossen ist.

Zu guter Letzt wurde es durch die Simulationen ermöglicht, einen abgerundeten Lokalisierungsübergang in einem Experiment zu identifizieren und diskutieren, in dem eine kolloidale Flüssigkeit in einer quasi-zweidimensionalen Matrix eingeschlossen war.

Contents

Introduction

Heterogeneous media are ubiquitous in every-day life, be it fluids inside sponges, or water percolating through ground coffee. Heterogeneous media are a class of systems which consist of a mobile component confined to a porous and network-like host geometry. How the mobile component explores the geometry is a fundamental and unanswered question as its properties of transport are found to be highly dependent on the structure of the host.

In one of his celebrated works of 1905, Einstein (1905) showed that the dynamics of a tracer particle in a homogeneous medium *always* becomes diffusive at long times: Uncorrelated collisions of the tracer with the medium necessarily lead to a Gaussian probability distribution of displacements as a result of the central limit theorem, with the width of the distribution increasing linearly with time. Thus, the mean-squared displacement of the tracer grows linearly in time.

In contrast, a tracer in a heterogeneous host structure exhibits much richer behavior. For instance, in a fractal host structure its motion at long times becomes anomalous, i.e. the mean-squared displacement grows non-linearly in time.

Anomalous diffusion occurs in many heterogeneous media, which has implications for their transport properties, and naturally one would like to understand how it arises. For one of the most idealized heterogeneous media, the Lorentz model, the origin of anomalous diffusion is fully understood, but it is unclear whether this scenario applies to more complex systems as well.

In the Lorentz model (Lorentz, 1905; Beijeren, 1982), randomly overlapping obstacles are fixed in space to form a matrix and a single point-like tracer particle is inserted into its void space. The number density of obstacles is the only control parameter of the system and the dynamics of the tracer are entirely determined by the structure of the obstacle matrix.

At low obstacle densities the tracer is free to explore most of the network, which leads to diffusive motion of the particle at long times. Upon increasing the density, the matrix becomes denser until at a critical point the void space disconnects and forms finite pockets, localizing the tracer. This critical point has been identified with the percolation point of the void space (Stauffer and Aharony, 2003; Ben-Avraham and Havlin, 2000). The tracer thus undergoes a dynamic critical transition entirely determined by the static structure of the matrix. Upon approaching the percolation point, a correlation length, which describes the size of the largest finite clusters, is found to diverge and the entire void space becomes fractal. This property allows the application of renormalization group theory to determine the critical behavior of the system.

Directly at the percolation point, the tracer exhibits anomalous diffusion, $\delta r^2(t) \sim t^{2/z}$, with the dimension-dependent dynamic exponent $z > 2$.

The transport in the Lorentz model is thus well understood, but it also contains strong idealizations not typically found in realistic systems. Hence, its usefulness in describing the dynamics in more complex systems might be limited. But as the dynamics of more complex heterogeneous media have shown similarities to the Lorentz model, there is hope that its dynamic critical phenomenon might be realized even if its idealizations do not apply. This would be powerful, since it would demonstrate the universality of the localization transition and allow semi-quantitative predictions to be made.

To establish the relevance of the dynamic critical phenomenon of the Lorentz model for the dynamics in heterogeneous media (or lack thereof), its idealizations are systematically tested, here. The thesis focuses in particular on two main aspects of realistic systems:

1. A soft interaction potential between tracer and obstacles which introduces finite energy barriers into the void structure and is expected to have a strong effect on the underlying percolation transition.

2. Introducing an interacting fluid of mobile particles, a main differentiator between the one-particle Lorentz model and realistic systems.

Structure of the thesis The work is organized as follows. First, an introduction into the theory of the Lorentz model and an overview over the literature on heterogeneous media relevant for this work is given.

Then, as a well-controlled starting point, the Lorentz model is reproduced with weakly correlated, soft obstacles and single-energy non-interacting tracer particles in chapter 2. In that system, the presence of a localization transition is confirmed and a range of Lorentz model scaling predictions are successfully tested. A mapping of the soft sphere system onto hard-spheres is discussed, which clarifies the role of energy as an implicit control parameter.

Then, in chapter 3, the tracers are replaced by an ideal gas with a wide energy distribution, a natural step towards an interacting fluid component. The energy distribution leads to a rounding of the critical dynamics of the system close to the critical point. The rounding can be understood easily as an averaging over the single-particle dynamics: A fast tracer can overcome certain energy barriers which a slower particle cannot. Thus each particle obtains a different effective interaction diameter as a function of its energy. This notion is formalized using the discussed hard-sphere mapping. Importantly, the rounding of the transition leads to a break-down of scaling. With the help of the presented simulation results, a rounded localization transition is identified and interpreted in an experiment.

Introducing interactions between the fluid particles turns the system into a quenched-annealed mixture, which is studied in chapter 4. The interactions between the fluid particles slow down the dynamics on intermediate time scales, as the particles become trapped in cages formed by their neighbors. On long times, however, a speeding up of the dynamics is found, as particles push each other over energy barriers. This even leads to a reentrance transition, where systems with a constant fluid diameter transition from a localized to a

delocalized state upon increasing the fluid number density. This effect occurs without the modification of the matrix structure and is not possible in hard-sphere QA mixtures. A comprehensive discussion of the results in comparison to the literature is made.

A precursory study of the corrections to the fluid-particle dynamics introduced by correlations in the matrix is shown in chapter 5. The more strongly correlated the matrix structure is, the more pronounced a caging-like slowing down of the dynamics on intermediate times is found. The long-time dynamics are shown to be independent of matrix correlations.

1

Theory of the Lorentz model and heterogeneous media

This chapter gives an overview on the theory of the Lorentz model. On the example of the random walk, regular diffusion will be discussed shortly and scaling concepts will be introduced. After a short introduction on fractals, the predictions of scaling theory for the Lorentz model will be summarized. The predictions of MCT for the Lorentz model on the percolating cluster are then studied. In the end, the literature is discussed with a focus on works which provide a connection between the Lorentz model and more complex heterogeneous media.

1.1 The random walk and scaling concepts

1.1.1 Random walk

The simplest model for stochastic dynamics is the random walk. It considers the dynamics of a walker, a point-like object that moves on a discrete lattice, one step at a time. The dynamics of the random walk contain a time-space scaling invariance and thus provide an opportunity to introduce the reader to the scaling concepts necessary for the understanding of the Lorentz model.

The simplest realization of the random walk is that of a orthonormal lattice of spacial dimension d and unit spacing between lattice sites, where the walker starts at the origin and has equal probability to move to one of the neighboring sites.

At each time step j, the walker performs a jump $\vec{e}_j$, which is a stochastic variable. Its value is either one of the base vectors of the lattice or its negatives. After n time steps, the walker has moved away from the origin by

$$\vec{r}(n) = \sum_{j=1}^{n} \vec{e}_j.$$

Two exemplary trajectories of the random walk in two dimensions are given in fig. 1.1.

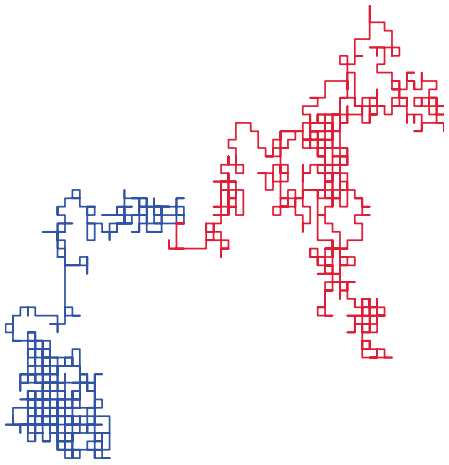

Figure 1.1: Two random walk trajectories on a orthonormal lattice in two dimensions after $n = 1000$ steps.

Each realization of a trajectory for the walker will be different. Important for the understanding of the walker's behaviour are thus averages over all possible trajectories. These averages are denoted by $\langle \ldots \rangle$. Since all directions are equally probable, the average over all possible steps at any one point vanishes, $\langle \vec{e}_j \rangle = 0$. Therefore, the average displacement also vanishes

$$\langle \vec{r}(n) \rangle = 0.$$

So, on average, the walker will explore all directions with equal probability. But the average distance to the origin does not vanish, and can be calculated with the mean-squared displacement (MSD). Because individual steps of the walker are independent, it follows that $\langle \vec{e}_j \cdot \vec{e}_k \rangle = \delta_{jk}$ (Kronecker-δ), and that the MSD grows linearly with the number of steps,

$$\langle r^2(n) \rangle = \left\langle \left(\sum_{j=1}^{n} \vec{e}_j \right)^2 \right\rangle = \left\langle \sum_{j=1}^{n} \vec{e}_j \cdot \vec{e}_j \right\rangle + \left\langle \sum_{j=1}^{n} \sum_{k=1,\neq j}^{n} \vec{e}_j \cdot \vec{e}_k \right\rangle = n.$$

The linear growth with time of the mean-squared displacement is called regular diffusion. The generalization to arbitrary lattice spacing a and the introduction of a time step unit τ with the time t then being defined by $t = n\tau$ leads to

$$\langle r^2(t) \rangle = 2dDt,$$

with diffusion coefficient $D := a^2/(2d\tau)$. The diffusion coefficient incorporates the constants of the random walk and thus contains the full information about the dynamics of the random walk. The equation clearly exposes both the linear time-dependence of the MSD and that the MSD is invariant under the appropriate rescaling of the time step and the length scale where D and t are kept constant. This allows performing the continuum limit, where one gets rid of the discrete steps in space and time,

$$a \to 0 \text{ and } \tau \to 0, \text{ while } \frac{a^2}{\tau} = const.$$

A full probabilistic description of the walker is given by its probability distribution $P(\vec{r}, t)$, which gives the probability of the walker being displaced at time t by the distance vector $\Delta\vec{r}(t) := \vec{r}(t) - \vec{r}(0)$ from its original position at time $t = 0$,

$$P(\vec{r}, t) := \langle \delta(\Delta\vec{r}(t) - \vec{r}) \rangle. \tag{1.1}$$

This quantity is also called the self-part of the van-Hove autocorrelation function, or short, the van-Hove function, (van Hove, 1954; Hansen and McDonald, 2006). The trajectory average for any statistical variable $a(r, t)$ can then be formally expressed as a volume integral over this probability distribution

$$\langle a(r, t) \rangle = \int a(r, t) P(\vec{r}, t) \mathrm{d}^d\vec{r}.$$

For instance, the mean-squared displacement can be written as

$$\langle r^2(t) \rangle := \langle (r(t))^2 \rangle = \int r^2 P(\vec{r}, t) \mathrm{d}^d\vec{r}.$$

Since the lattice is translationally invariant, it does not matter, where the walker started from, and the mean-squared displacement can be written more generally $\delta r^2(t) := \langle (r(t) - r(0))^2 \rangle = \langle r^2(t) \rangle$.

The van-Hove function allows for the definition of moments. The k-th moment is defined by

$$\langle r^k \rangle = \int r^k P(\vec{r}, t) \mathrm{d}^d\vec{r}.$$

Thus the mean-squared displacement is the second moment of the van-Hove function. A probability distribution can be decomposed into its moments and the knowledge of all moments completely determines the original probability distribution.

For the random walk, the calculation of the van-Hove function is simple. As each step of the random walk is described by the same random variable of finite variance, its probability distribution tends to a Gaussian distribution in the long-time limit, as governed by the central limit theorem (Rice, 1988),

$$P(\vec{r}, t) = \frac{1}{(4\pi D t)^{d/2}} \exp\left(-\frac{r^2}{4Dt}\right).$$

As the system is isotropic, the probability distribution only depends on $r := |\vec{r}|$.

The van-Hove function can be brought into a scaling form, which reflects that the function at two different times has the same shape and one can be scaled on top of the other by rescaling space appropriately. This property allowed performing the continuum limit in the first place. The scaling form is achieved by introducing the dimensionless variable $\hat{r} := r/\sqrt{2Dt}$, with which one readily obtains

$$P(r, t) = r^{-d} \mathcal{P}(\hat{r}), \tag{1.2}$$

with scaling function

$$\mathcal{P}(\hat{r}) = \frac{1}{(2\pi)^{d/2}} \hat{r}^d \exp\left(-\frac{\hat{r}^2}{2}\right). \tag{1.3}$$

The prefactor r^{-d} in the scaling form of the van-Hove function reflects that the van-Hove function is a probability *density* and can be seen as a trivial dimensional contribution which ensures that the integral of the van-Hove function can be normalized. Apart from this prefactor, the shape of the van-Hove function is given by the scaling function $\mathcal{P}(\hat{r})$.

This scaling form implies that the trajectory of a random walk itself is scale-free, i.e. that it is a self-similar structure that can be characterized by a fractal dimension.

1.1.2 Fractals

Fractals are geometric objects which look similar or in some cases exactly the same regardless of the distance they are viewed from. This property is called self-similarity or scale-invariance. A typical way of obtaining such structures is by iteratively constructing them with a set of geometric rules. For instance, the Sierpinski triangle, a fractal, is generated by taking a triangle and iteratively removing the center triangle of the first and all resulting triangles. The procedure is illustrated in fig. 1.2. After infinitely many iterations the Sierpinski triangle looks the same on all length scales (provided they are far smaller than the size of the original triangle).

A generic property of fractals is that a non-integer spatial dimension can be assigned to them, the fractal dimension d_f. For instance for the Sierpinski triangle, the more iteration steps are performed, the lower the area of the triangle becomes and the longer the length of its boundary. In fact, after

Figure 1.2: The original triangle and the first 4 iterations of the Sierpinski triangle. *(Source: Wikipedia)*

infinitely many iterations, its area vanishes, while its boundary length diverges.[1] Because it has no measurable area or length, the Sierpinski triangle is neither a two-dimensional nor a one-dimensional object.

The fractal dimension describes how fractal objects scale when the space in which they are embedded is rescaled: If a d_f-dimensional object with length L (i.e. any linear measure of its size) is rescaled by a factor b in each direction, its mass then scales with

$$M(bL) = b^{d_f} M(L), \tag{1.4}$$

just like a two-dimensional object quadruples its area if one doubles its linear extent or three-dimensional object increases its volume eight-fold if one doubles its linear extent. From eq. (1.4), it immediately follows, that the (d_f-dimensional) mass of a fractal is a homogeneous function with some proportionality factor A,

$$M(L) = AL^{d_f}. \tag{1.5}$$

This equation then allows the following interpretation: The mass inside a volume parametrized with length L scales as $M \sim L^{d_f}$. This can, for instance, be a cube with side length L. Note, that therefore the mass density of a fractal calculated in its embedding integer-dimensional space vanishes, $M(L)/L^d \sim L^{d_f - d} \to 0$, for $L \to \infty$.

1.1.3 *Random walk as a stochastic fractal*

It is not necessary to use a deterministic iterative rule to construct a fractal. The rule can be probabilistic instead, leading to a stochastic fractal. In the case of the Sierpinski triangle, the generator could be to divide the original triangle into four identical triangles and instead of removing the middle one, remove one of the four randomly. Even though the structure then cannot be exactly mapped onto itself be rescaling it, it is still called self-similar. This is because the probability distribution of its holes stays scale-invariant.

Random walks are a stochastic fractal. The trajectory of the random walk is generated by the steps of the walker and after infinitely many steps the trajectory becomes self-similar, as evidenced by the scaling-invariance of the resulting gaussian probability distribution, see eq. (1.2). The self-similarity of the random walk is apparent to the eye in the three trajectories shown in fig. 1.3, which show very similar structures and shapes although being of vastly different lengths.

In the case of the random walk, its fractal dimension is called walk dimension, denoted by d_w. The walk dimension can be determined with the following argument. Pick any point on the trajectory. Then all sites on the trajectory that are less than some maximum elapsed walking time t away from that point form a connected structure (this is the same as letting a walker start

[1] Area A_n after n iterations with area A_0 of the original triangle:

$$A_n = A_0 \cdot (3/4)^n \to 0.$$

Boundary length L_n after n iterations with the boundary length L_0 of the original triangle:

$$L_n = L_0(1 + (1/3)\sum_{i=0}^{n}(3/2)^i) \to \infty.$$

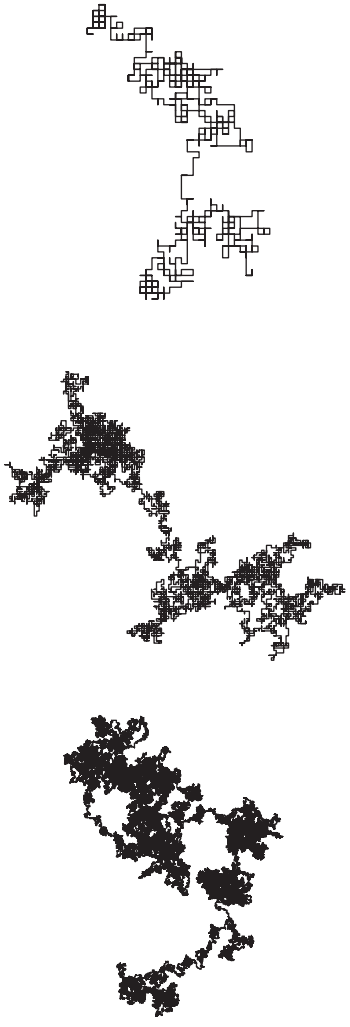

Figure 1.3: Random walk trajectories of length $n = 10^3, 10^4$, and 10^5 *(top to bottom)*.

at that point and then using the whole trajectory after time t). The average linear extent of that structure can then be measured with the root of the MSD, $R(t) := \sqrt{\delta r^2(t)}$. The length of the trajectory then may serve as the mass $M(R)$ of the trajectory. Since the length is proportional to the elapsed time t, one finds

$$M(R) \sim t \sim \delta r^2(t) = R^2.$$

The fractal dimension of the random walk is therefore $d_w = 2$. Therefore, for $d \leq 2$ the random walk trajectory eventually fills space. Some definitions of fractals require that the fractal dimension be strictly smaller than the spatial dimension, $d_f < d$. Then, the random walk cannot be considered a fractal. Of course the time-space scaling property of the random walk is unchanged by this, as is its self-similarity.

A peculiarity of the random walk is that its fractal dimension is the same regardless of the dimension of the embedding space in which the walk is performed.

Diffusion on fractals The mean-squared displacement depends on the walk dimension in the following way

$$\delta r^2(t) \sim t^{2/d_w}.$$

Instead of performing a regular random walk on a orthonormal lattice, the walker can be constrained to a fractal. Then, the directions available to the tracer at each step are correlated, making the dynamics non-Markovian. Compared to the value $d_w = 2$ for the regular random walk, the walk dimension then generically increases. As a consequence, the MSD does not grow linearly with time but instead exhibits anomalous diffusion, i.e. it grows subdiffusively with a power-law in time with an exponent $2/d_w < 1$.

This is the basis for the anomalous dynamics in the Lorentz model, which essentially comprises of a walker on a fractal network.

1.2 *Lorentz model*

What follows is mainly a summary of the relevant results. For a complete introduction to percolation and the Lorentz model, see (Ben-Avraham and Havlin, 2000; Stauffer and Aharony, 2003; Höfling and Franosch, 2013).

The Lorentz model comprises a single, point-like tracer in a fixed matrix of overlapping obstacles of diameter σ. For a schematic, see fig. 1.4. The diameter σ sets the microscopic length scale of the system. N obstacles are randomly placed in a volume V of dimension d. The volume and number of obstacles must be large enough, so that the system can be considered in the limit of infinite system size,

$$N \to \infty, V \to \infty \text{ while } n = const.$$

Tracer and obstacles interact as hard-spheres. Instead of using a point-like tracer it is also possible to assign a diameter to it. Then, the void space available to the tracer center remains the same as long as the sum of the tracer diameter

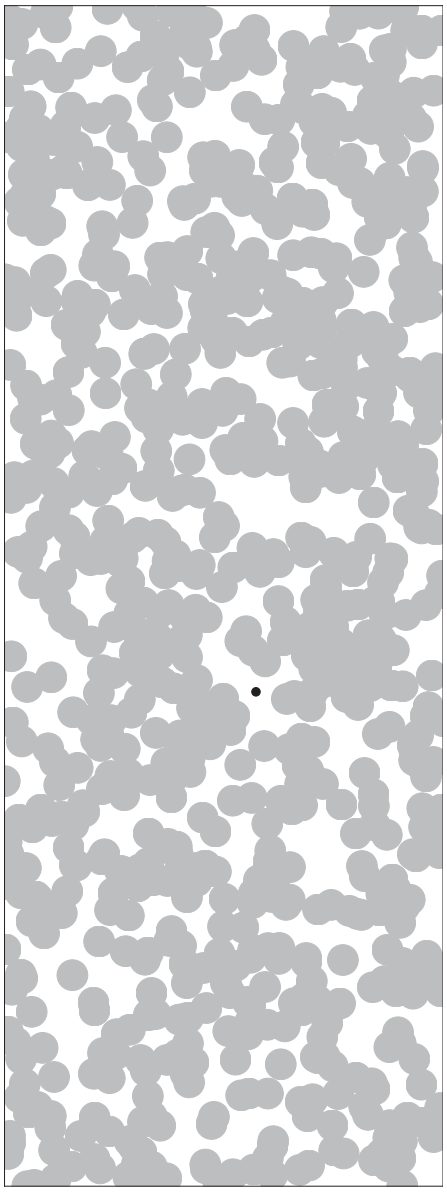

Figure 1.4: Schematic of the Lorentz model. Randomly placed obstacles in grey, point-like tracer as black dot.

and obstacle diameter remains the same. Thus, σ sets the minimum distance between tracer center and obstacle centers. Because the matrix structure is completely random, it can be fully described via a single control parameter: the reduced number density of obstacles,

$$n^* = n(\sigma/2)^d. \tag{1.6}$$

The void space available to the tracer forms distinct clusters which are separated from each other by obstacles. With increasing n^*, clusters become smaller and are separated into smaller clusters. At low obstacle densities, one cluster will be found to percolate the whole system, while at high enough densities this is not possible. In-between there is a critical point, the percolation point n_c^*, where the percolating cluster ceases to exist. Apart from this percolating cluster, the system contains finite void clusters at all densities.

At obstacle densities below the percolation point the tracer is typically free to explore most of the network, which leads to diffusive motion of the particle at long times. At densities above the percolation point, the tracer is trapped in a finite pockets. Directly at the percolation point, the void space is fractal in structure, and the tracer exhibits anomalous diffusion. Close to the critical point, a correlation length ξ — a measure of the linear extent of the largest finite cluster — is found to diverge. This allows the application of renormalization group techniques to determine the critical behavior of all static and dynamics quantities.

The tracer undergoes a dynamic critical transition entirely determined by the static structure of the matrix. It is thus necessary to fully characterize the structure of the void space at and close to the percolation point, before the dynamics of the Lorentz model can be discussed.

Because the system becomes scale-free at the transition, and the scale-invariance is cut-off by a correlation length which diverges in the approach to the transition, it is possible to determine the power-law behavior of all critical quantities. One identifies three independent exponents: An exponent describing the structure of the system *at* the critical point, another exponent describing the modifications to the structure *in the approach to* the transition, and lastly, an exponent for the conductivity of the void structure.

1.2.1 *Percolation*

Directly at the percolation transition the percolating cluster has a fractal structure with fractal dimension $d_f < d$, e.g. its size inside a volume with linear extent L scales as $s_\infty(L) \sim L^{d_f}$ (the fractal scaling holds as long as the size of individual obstacles is negligibly small, $L \gg \sigma$). In fact, at the percolation point not only the percolating cluster but the whole system is self-similar with the same fractal dimension. As a consequence, the probability distribution of cluster sizes s is given by a power-law, $p(s) \propto s^{-1-d/d_f}$ and the linear extent R_s of the clusters scales with their weight as expected for fractals, $s \propto R_s^{d_f}$.

Away from the transition, the full self-similarity is lost. The system only appears self-similar when it is viewed from not too far a distance. A correlation length ξ arises, which represents the typical linear extent of the largest occurring finite clusters. Essentially, the probability distribution of cluster sizes $p(s)$

is cut off at ξ: it decays exponentially on the length scale ξ. For $n^* < n_c^*$, the infinite percolating cluster then only appears fractal on length scales $L \ll \xi$. The whole system is self-similar on such length scales $L \ll \xi$, too. On length scales larger than the correlation length the whole systems appears homogeneous instead. The correlation length ξ thus marks the crossover between a fractal, self-similar regime and a translationally invariant, homogeneous regime.

It is convenient to define a dimensionless separation parameter ε which helps expressing the power-law behavior of quantities near the localization transition,

$$\varepsilon := \frac{n^* - n_c^*}{n_c^*}. \tag{1.7}$$

The correlation length diverges as $\xi \sim |\varepsilon|^{-\nu}$, with critical and universal exponent ν. For $n^* > n_c^*$, there is no percolating, infinite cluster. The same correlation length ξ can be identified and is found to diverge in the same way as in the percolating system. The system is again self-similar on length scales L with $\sigma \ll L \ll \xi$ and becomes homogeneous on length scales $L \gg \xi$.

In approaching the percolation point, many other structural quantities obey power-laws as well; they either vanish or diverge with critical exponents of their own. This is what is known as the scaling hypothesis. The critical behavior of all these quantities can be related to the fractal structure of the system at the critical point and to the way in which ξ diverges. All critical exponents of structural quantities may therefore be expressed as a function of only two exponents, d_f and ν.

For instance, the percolation point can be expressed formally as the obstacle density where the size of the percolating cluster s_∞ in relation to the size of the whole system V undergoes a continuous phase transition. Then, for $n^* > n_c^*$, one has strictly $s_\infty/V = 0$, while below the critical density one finds that the infinite cluster's size decreases with the critical exponent β in the approach to the percolation point,

$$s_\infty/V \propto |\varepsilon|^\beta.$$

From a simple scaling argument[2] β can be deduced,

$$\beta = \nu(d - d_f). \tag{1.8}$$

If one prefers, one can also see ν and β as the fundamental exponents, and express d_f through them. In two dimensions, it is possible to calculate the critical exponents analytically (Stauffer and Aharony, 2003), for three dimensions they can only be determined numerically. The values are reported in table 1.1.

Universality As is common for critical phenomena, the reported critical exponents hold for a wide range of systems, which are then said to belong to the same universality class. It does not matter, for instance, whether the obstacles are defined as overlapping spheres, or as blocked sites on a grid. This is an insight gained by renormalisation group theory, in which the critical exponents are derived in a systematic coarse-graining of the system, where the

[2] The size of the percolating cluster $s_\infty(L)$ inside a given volume V of extent L scales as $s_\infty(L) \sim L^{d_f}$, as long as $L \ll \xi$. Then the probability of any given test volume inside V belonging to the infinite cluster in that region is $s_\infty(L)/V \sim L^{d_f - d}$. For the whole infinite cluster that same probability s_∞/V is given by setting $L = \xi$, because that is the largest scale on which the cluster is self-similar, while the value of $s_\infty(L)$ stays constant for $L > \xi$ (because of the homogeneity of the structure). Therefore

$$s_\infty/V \sim \xi^{d_f - d}.$$

Plugging in the critical expressions for both sides of the equation and comparing the exponents leads to a hyperscaling law (it obtains the name hyperscaling, because it involves the spatial dimension d)

$$|\varepsilon|^\beta \sim |\varepsilon|^{-\nu(d_f - d)},$$
$$\Rightarrow \beta = \nu(d - d_f).$$

self-similarity of the system is used to relate the system on different length scales to each other. The coarse graining is then expressed as a flow in parameter space, in which the universal values of the exponents are determined by a fixed-point. The microscopic differences between different systems become irrelevant in the coarse graining.

Connection to random resistor networks In order to understand transport in a percolating system, it has to be mapped to a random-resistor network. The void space can be thought of as consisting of void pockets connected via channels. The void pockets are then represented as nodes and the channels as edges between the nodes, forming a network of randomly connected nodes. The electric resistance of each edge is then defined as a function of the channel width.

Closed-off clusters in the void space are then represented by parts of the network being cut-off from the rest, or of the connecting edges having infinite resistance. Increasing the density of obstacles decreases the width of channels and increases their resistance. At the percolation threshold the random resistor network is divided into separate parts with no part of the network reaching through the whole system.

The random resistor network for a obstacle configuration can be constructed from the Voronoi tesselation of the obstacle centers, see (Sung and Yethiraj, 2008a) and references therein. The tesselation divides the whole system into volumes such that for each obstacle center there is exactly one volume containing all points which are closer to that center than to any other. The edges of these volumes then present the channels of the random resistor network and the vertices where the edges meet are its nodes. A channel is open to transport if the two neighboring obstacles do not overlap it and closed otherwise. In this fashion, each void cluster can be identified with a set of connected nodes.

A third independent critical exponent μ is needed to describe the dynamics in a percolation network. It describes how the macroscopic conductivity Σ vanishes at the percolation point,

$$\Sigma \sim (-\varepsilon)^{\mu}.$$

Different from the two geometric critical exponents d_f and ν, μ is not generally the same in lattice and continuum percolation. In continuum percolation it is possible that the distribution of channel widths exhibits a divergence in the limit of vanishing channel width. If that divergence is strong enough to dominate the renormalization flow, then the exponent μ becomes larger than the lattice value. This does not occur in 2d, but it does in 3d (Machta and Moore, 1985; Höfling et al., 2008). The values of μ for the different cases are reported in table 1.1.

1.2.2 *Scaling theory of the dynamics*

Now that the geometric scaling of the void space is described, a tracer can be inserted into it. This situation is in the same universality class as the random walker on the lattice percolation network, known as the "ant in the labyrinth", a term first coined by de Gennes (1976).

	d	2	3	
geometric:	d_f	$91/48^{s}$	$2.530(4)^{h2}$	
	ν	$4/3^{s}$	$0.875(1)^{h2}$	
	β	$5/36^{s}$	0.41^{s}	
dynamic:			*lattice*	*continuum*
	μ (all clusters)	1.31^{g}	2.06	2.88^{h1}
	d_w	$2.878(1)^{g}$	$3.88(3)^{h2}$	$4.81(2)^{h2}$
	z (all clusters)	$3.036(1)^{h2}$	$5.07(6)^{h2}$	$6.30(3)^{h2}$

Table 1.1: Geometric and dynamic critical exponents of percolation. The digit in parentheses gives the uncertainty interval in the last digit. Key to the sources: g: (Grassberger, 1999); h1: (Höfling et al., 2008); h2: (Höfling and Franosch, 2013), p. 15; s: (Stauffer and Aharony, 2003), p. 52. The lattice value for μ in 3D was calculated from d_w using eq. (1.10)

Here, the tracer obeys Newtonian dynamics, but other dynamics, like Brownian dynamics, are also possible. Its velocity $\vec{v}$ then determines a microscopic timescale $\tau = \sigma/|\vec{v}|$. Scattering of the tracer by obstacles changes the direction of the velocity but leaves the energy of the tracer conserved. The microcanonic average $\langle \ldots \rangle$ is defined as the average over all possible trajectories of the tracer.

Dynamics on the percolating cluster The simplest case is when the tracer is placed onto the percolating cluster directly at the critical point. Then the percolating cluster is fractal on length scales L larger than the diameter of the obstacles, $L \gg \sigma$. The tracer will then perform anomalous diffusion for indefinite times (as soon as individual scattering events do not play a role anymore, $t \gg \tau$),

$$\delta r^2(t) \sim t^{2/d_w}.$$

The walk dimension d_w was already introduced for the regular walk. It can be used instead of μ as the fundamental dynamic critical exponent. A relation connecting the two exponents will be given in a moment.

Away from the critical point, for densities below the percolation point, the cluster is only self-similar up to the correlation length ξ, and appears homogeneous above that. The dynamics of the tracer thus shows two distinct regimes. On distances shorter than the correlation length, the percolating cluster appears fully fractal, and thus the tracer will still show anomalous diffusion. But after having exceeded the correlation length, the matrix appears homogeneous and due to the central limit theorem the dynamics will necessarily become diffusive, $\delta r^2(t) \sim D_\infty t$ (the index ∞ is to denote quantities defined on the percolating cluster).

The crossover between these two regimes is given by the correlation length ξ and a crossover time t_x can be defined by

$$\delta r^2(t_x) \sim t_x^{2/d_w} \stackrel{!}{=} \xi^2.$$

Therefore, the crossover time diverges along with the correlation length as

$$t_x \sim \xi^{d_w}.$$

The diffusion coefficient D_∞ vanishes at the critical point with a critical exponent μ_∞, which can be related to either μ or d_w,

$$D_\infty \sim (-\varepsilon)^{\mu_\infty}.$$

At t_x, the two asymptotes of anomalous and regular diffusion can both be expected to approximately hold. The comparison then allows determining the

relationship of μ_∞ to the fundamental critical exponents. Thus,

$$t_x^{2/d_w} \sim D_\infty t_x,$$

leads to,

$$\mu_\infty = \nu(d_w - 2).$$

All-cluster average of the dynamics The more general scenario is to allow the tracer onto all clusters. This case will be especially important in the soft-sphere systems considered later, where it is often not possible to identify the percolating cluster and thus the whole network has to be sampled.

Including all finite clusters decreases the exponent of the anomalous diffusion. When a tracer is trapped on a finite cluster, the tracer performs anomalous diffusion just as on the infinite cluster if it has not yet explored the whole cluster. If the walker had time to explore the full cluster, then its MSD has converged to a finite limit which then is a measure of the cluster size. By averaging over the power-law distributed cluster size distribution, one obtains

$$\delta r^2(t) \sim t^{2/z}, \text{ while } \tau \ll t \ll t_x.$$

with the exponent z given by

$$z = \frac{d_w}{1 - (d - d_f)/2}. \tag{1.9}$$

On the percolating side of the transition, $n^* < n_c^*$, the MSD again becomes diffusive once the crossover time t_x is exceeded,

$$\delta r^2(t) \sim 2dDt.$$

Through an Einstein relation, D can be connected to the macroscopic conductivity Σ introduced above, $\Sigma \sim D$. Thus D vanishes at the transition as

$$D \sim (-\varepsilon)^\mu.$$

Finally, as D is closely related to D_∞, μ can be connected to μ_∞ and d_w: Only the percolating cluster contributes to the long-time diffusion but in the all-cluster average most trajectories are not on it. Thus the diffusion coefficient is suppressed by a factor given by the relative weight of the percolating cluster which vanishes with exponent $\beta = \nu(d - d_f)$. Thus the exponent of the all-cluster diffusion coefficient is given by,

$$\begin{aligned}\mu &= \mu_\infty + \beta \\ &= \nu(d_w - 2 + d - d_f).\end{aligned} \tag{1.10}$$

With this, either μ or d_w are conventionally chosen as the fundamental dynamical exponent. The values of the critical exponents are compiled in table 1.1.

On the localized side of the transition, $n^* > n_c^*$, the MSD converges to the mean-cluster size,

$$\delta r^2(t) \sim l^2,$$

which also diverges at the critical point[3],

[3] The MSD is dominated by the largest clusters' contributions, which have size $\xi \sim |\varepsilon|^{-\nu}$. The long time limit of the cluster-resolved MSD is $\delta r_s^2(t) \sim \xi^2$ and the probability of a particle being inside any of the large clusters is $\sim |\varepsilon|^\beta$. The averaging over all cluster sizes therefore reduces to the contribution by the large clusters

$$\delta r^2(t \to \infty) \sim |\varepsilon|^{-2\nu+\beta},$$

and

$$-2\nu + \beta = \nu(-2 + d - d_f).$$

$$l \sim |\varepsilon|^{-\nu(2-d+d_\mathrm{f})/2}. \tag{1.11}$$

The mean-cluster size l is also called the localization length, and it diverges with the correlation length as $l \sim \xi^{1-(d-d_\mathrm{f})/2}$ and with the crossover time $l \sim t_x^{1/z}$. The exponent of the localization length can be written more tightly as

$$-\nu(2-d+d_\mathrm{f})/2 = -\nu d_\mathrm{w}/z. \tag{1.12}$$

Dynamic scaling hypothesis The only relevant length scale for the dynamics near the percolation point is the correlation length ξ, which serves as a cutoff to the self-similar structure of the percolation network. This was used to determine the divergences of geometric and dynamic quantities in the approach to the critical point. The dynamic scaling hypothesis (Hohenberg and Halperin, 1977) goes further than that. It assumes that all dynamic quantities only depend on time and space in relation to ξ: it states that the full time and space dependence of dynamic quantities have a homogeneous scaling form near the critical point. This hypothesis is an extension of the static scaling laws found for static critical phenomena (Goldenfeld, 1992). Thus the scaling form for the MSD can be given as,

$$\delta r^2(t) = t^{2/z}\delta\mathcal{R}^2_\pm(\hat{t}), \tag{1.13}$$

with $\hat{t} := t/t_x$ and $t_x \sim \xi^{-d_\mathrm{w}} \sim l^{-z}$. The scaling functions $R^2_-(\hat{t})$ and $R^2_+(\hat{t})$ then describe the behavior of the MSD on the delocalized and the localized sides of the percolation point, respectively. At short times, $\tau \ll t \ll t_x$, the scaling functions are both constant with the same value, and the scaling reduces to anomalous diffusion. At long times, $\hat{t} \gg 1$, long-time diffusion is reproduced by $R^2_-(\hat{t}) \sim t^{1-2/z}$ on the delocalized side, while on the localized side $R^2_-(\hat{t}) \sim t^{2/z}$ holds. This scaling form contains the information provided by all three critical exponents: the fractal dimension of the percolating cluster, the divergence of the correlation length setting the cross-over, and the scaling of the conductivity.

Time-space scaling on the percolating cluster A similar scaling form can be written down for the van-Hove function. In the Lorentz model, the tracer moves on fractal structures, where the available paths are correlated (simply because the allowed directions are not orthonormal and not the same at each point), so its dynamics are not Markovian anymore. Therefore, all connected probability functions are needed in principle to fully describe the dynamics. Still, the van-Hove function remains a very important quantity.

In the case of regular diffusion, the van-Hove function was a Gaussian, and a scaling function which combined the time and space dependence into a single variable was easily found, see eq. (1.3). The typical assumption for the scaling form of the van-Hove function in fractal systems can be applied to the Lorentz model (Kertesz and Metzger, 1983; Ben-Avraham and Havlin, 2000), and can be seen as a generalization of the form for regular diffusion. Directly at the critical point, it incorporates the scaling of the dynamics with the fractal dimensions d_w and d_f,

$$P_\infty(r,t;n_c^*) = r^{-d}\tilde{\mathcal{P}}_\infty(rt^{-1/d_\mathrm{w}}). \tag{1.14}$$

for large distances, $\sigma \ll r$, and long times, $\tau \ll t$. The reasoning for that form is that the van-Hove function has to satisfy both the scaling properties of the underlying fractal structure and of the dynamics. The prefactor r^{-d} again reflects that the van-Hove function is a probability density and ensures that it is normalizable. Furthermore, the van-Hove function has to follow the time-space scaling of anomalous diffusion, $t^{1/d_w} \sim r$. This is enforced in the argument of the scaling function $\tilde{\mathcal{P}}_\infty$, which makes sure that the shape of the van-Hove function at a time t is always the same on the length scale r^{d_w}. This is analogous to the time-space scaling $\hat{r} \sim r/\sqrt{t}$ in the case of regular diffusion. Furthermore, the scaling function $\tilde{\mathcal{P}}_\infty$ is expected to decay rapidly for $r \gg t^{1/d_w}$. The scaling of the underlying fractal structure of void space is contained in the scaling function $\tilde{\mathcal{P}}_\infty(x)$ at very small arguments $x := rt^{-1/d_w}$. This can be motivated with the following, heuristic argument laid out by Höfling et al. (2011). The return probability $\Pi(w,t)$ is defined as the probability that the tracer has stayed or returned to a sphere of radius w around its origin after the time t,

$$\Pi(w,t) := \int_{r\le w} rP_\infty(r,t)\mathrm{d}^d.$$

If the tracer has explored its surroundings for long enough, $w \ll t^{1/d_w}$, then it can be assumed that close to its origin the void structure has been fully and equally explored, and the return probability becomes proportional to the enclosed fractal volume, $\Pi(w,t) \sim w^{d_f}$. Via eq. (1.14), this implies in turn that $\tilde{\mathcal{P}}_\infty(x \ll 1) \sim x^{d_f}$.

Away from the critical point, the correlation length enters into the scaling of the van-Hove function in the following way (Ben-Avraham and Havlin, 2000; Kertesz and Metzger, 1983; Kammerer et al., 2008),

$$P_\infty(r,t;n^*) = \xi^{-d}\mathcal{P}_\infty(r/\xi, t\xi^{-d_w}).$$

provided that $r, \xi \gg \sigma$ and $t \gg \tau$. The new scaling function reduces to the previous function at the critical point[4], i.e.

$$\lim_{\xi\to\infty} \mathcal{P}_\infty(r/\xi, t\xi^{-d_w}) = (\xi/r)^d\tilde{\mathcal{P}}_\infty\left[(r/\xi)(t\xi^{-d_w})^{-1/d_w}\right].$$

The intermediate scattering function (ISF) is the Fourier transform of the van-Hove function,

$$F_\infty(q,t) := \int \exp(\mathrm{i}\vec{q}\cdot\vec{r})P_\infty(r,t)\mathrm{d}^d r. \tag{1.15}$$

The relevance of the ISF lies partly in the fact that it can be measured in experiments (Hansen and McDonald, 2006). The scaling form of the ISF at the critical point is then directly inherited from the van-Hove function by performing the Fourier transform of eq. (1.14),

$$F_\infty(q,t) = \mathcal{F}_\infty(qt^{1/d_w}) \tag{1.16}$$

for small wavenumbers $q \ll \sigma^{-1}$ and long times $\tau \ll t$. The scaling function of the ISF can be directly obtained by substituting $\vec{r} \mapsto \vec{x}t^{1/d_w}$ and $\vec{q} \mapsto \vec{\kappa}t^{-1/d_w}$,

$$\mathcal{F}_\infty(\kappa) = \int \exp(\mathrm{i}\vec{\kappa}\cdot\vec{x})\, x^{-d}\mathcal{P}_\infty(x)\,\mathrm{d}^d x.$$

With the return probability argument from before one is able to obtain the large-wavenumber behavior $\mathcal{F}_\infty(\kappa \gg 1) \sim \kappa^{-d_f}$. At long times and large wavenumbers, the ISF therefore fully decays to 0, with $F_\infty(q,t) \sim t^{-d_f/d_w}$.

[4] The dependence of the scaling function on ξ gets lost in the limit in a well-defined way, leaving behind a less complicated scaling function.

The scaling function $\mathcal{P}_\infty$ has to *asymptotically* reduce to another scaling function such that the diverging powers of ξ cancel each other out at. This can only be accomplished if r and t show up as a product where the ξ terms cancel each other out. The prefactor ξ^{-d} must be cancelled by the scaling function, as well. Thus, $\mathcal{P}_\infty(r/\xi, t\xi^{-d_w}) \to (\xi/r)^d\tilde{\mathcal{P}}_\infty[(r/\xi)(t\xi^{-d_w})^{-1/d_w}]$.

Time-space scaling in the all-cluster average In contrast to the situation on the percolating cluster, the scaling form of the van-Hove function is less well studied when the full void space is taken into consideration. Still, the scaling form has been conjectured as (Höfling et al., 2006; Kertesz and Metzger, 1983)

$$P(r,t;n^*) = \xi^{d_f-2d}\mathcal{P}_\pm(r/\xi, t\xi^{-d_w}), \tag{1.17}$$

for situations, where the correlation length is already large compared to the obstacles, $\xi \gg \sigma$, for large distances $\sigma \ll r$ and long times $\tau \ll t$. The scaling is expected to hold on both sides of the critical point, with the two scaling functions $\mathcal{P}_\pm$ for either side of the percolation transition. The power of the prefactor ξ^{d_f-2d} was determined by integration over the pocket size distribution in (Kammerer et al., 2008). The conjectured scaling form of the van-Hove function reduces to the scaling form of the MSD, eq. (1.13), by integration, as the latter quantity is the second moment of the former. Although a lot about the scaling functions $\mathcal{P}_\pm$ themselves is not yet known, as for instance their exact behavior at distances $\sigma \ll r \ll \xi$, the scaling properties arising from eq. (1.17) for the MSD and the non-Gaussian parameter (Höfling et al., 2008) have been confirmed in computer simulations (Höfling et al., 2006; Bauer et al., 2010; Pandey, 1984; Höfling et al., 2008).

Directly at the critical point, the limit $\xi \to \infty$ can be performed in the same way as on the percolating cluster, and the scaling simplifies to

$$P(r,t;n_c^*) = r^{d_f-2d}\tilde{\mathcal{P}}(rt^{-1/d_w}),$$

for large distances $\sigma \ll r, \xi$ and long times $\tau \ll t$.

Even less is known about the scaling of the intermediate scattering function in the all-cluster average. The cluster-averaged dynamics are not ergodic: Including all finite clusters leads to a fraction of the tracers being trapped in finite clusters at all densities. This is captured in the long-time limit of the ISF, the non-ergodicity parameter, which becomes finite (Kertesz and Metzger, 1983; Franosch et al., 2011),

$$f(q;n^*) := \lim_{t\to\infty} F(q,t) > 0.$$

The non-ergodicity parameter $f(q;n^*)$ gives the fraction of particles trapped on a length scale $2\pi/q$, at obstacle density n^*. The total fraction of trapped particles is given by the long-wavelength limit of the non-ergodicity parameter, $f(q=0;n^*)$. Directly at the transition, the non-ergodicity parameter shows a singularity (Kertesz and Metzger, 1983). For obstacle densities above the percolation transition, it assumes the value $f(q=0;n^* > n_c^*) = 1$, and it approaches this value from below the transition as

$$1 - f(q=0;n^*) \sim (-\varepsilon)^\beta. \tag{1.18}$$

At the transition, the wavenumber dependence is given as

$$1 - f(q;n_c^*) \sim q^{d-d_f} \tag{1.19}$$

for $q \to 0$. A scaling form proposed by Franosch et al. (2011) for the full non-ergodicity parameter contains these asymptotic results,

$$1 - f(q;n^*) = \xi^{d_f-d}\mathcal{F}_\pm(q\xi) \tag{1.20}$$

for small wavenumbers $q \ll 2\pi/\sigma$ and close to the transition, $\sigma \ll \xi$. The asymptotic behavior of the scaling functions $\mathcal{F}_\pm$ is then given by $\mathcal{F}_-(x \to 0) = const$, $F_+(x \to 0) = 0$, and $\mathcal{F}_\pm(x) \sim x^{d-d_f}$ for $x \gg 1$.

A scaling form containing the time dependence of the ISF in the all-cluster average is not known, as the presence of a non-vanishing long-time limit seems to destroy the scaling form.

1.2.3 *The Lorentz model in mode-coupling theory*

The results of this chapter have been published in (Spanner et al., 2013). The author of this thesis performed the MCT numerics and calculated the asymptotics of the MCT equation with the techniques of (Schnyder, 2010), while the analogous calculation of the asymptotics presented here is Franosch's.

Although the scaling theory outlined in the previous section has been widely successful in describing the behavior of the Lorentz model, it still is a phenomenological theory. It only provides results which hold asymptotically close to the transition, although this can be remedied somewhat by considering corrections to scaling (Kammerer et al., 2008). In contrast, the mode-coupling theory of the glass transition (MCT) is a self-consistent theory developed from first principles (Götze, 2009) and holds for the whole density range. It found great success in describing the glass transition, but it has been applied to the Lorentz model, as well (Götze et al., 1981a,b, 1982).

Even though MCT can be applied to the whole density range, it is crucial that the theory correctly describes the critical dynamics of the Lorentz model. Here, the predictions of MCT in a simplified form — which still contains the universal aspects of the theory — will be compared to simulations on the percolating cluster of the Lorentz model at the critical point. The comparison is performed exemplarily for the intermediate scattering function, which provides the full information about the dynamics, and constrains itself to $d = 3$. For more details on the Lorentz model in MCT, see (Schnyder, 2010), where the $d = 2$ case is considered as well.

The description of the Lorentz model in the framework of MCT follows from a simplification of the MCT theory of a binary mixture (Franosch and Voigtmann, 2002) and keeps the same mathematical structure. In this theory, one component is kept strictly fixed while the other one is considered as a single tracer (Schnyder et al., 2011). The obstacles have the radius R and a number density $n := N/V$ and the single point-like tracer has velocity v.

The starting point of MCT is an exact equation for the intermediate scattering function $F(q,t)$ as obtained from the Mori-Zwanzig projection-operator formalism (Götze, 2009). The formalism leverages that that there are slowly evolving variables and fastly evolving variables, and that when describing the dynamics of the former, the dynamics of the latter is mostly irrelevant. By projection of the full equations of motion onto the slow variables, an exact equation is obtained where the fast variables only occur inside an integration kernel. For the intermediate scattering function, the resulting equation is given by

$$\ddot{F}(q,t) + v_s\dot{F}(q,t) + \Omega(q)^2 F(q,t) + \int_0^t M(q,t-t')\dot{F}(q,t')\mathrm{d}t' = 0. \tag{1.21}$$

The frequency term $\Omega(q)^2 = q^2v^2/3$ arises through assuming ballistic dynamics. The equation is thus similar in form to the equation of the damped harmonic oscillator: the integral term acts as a generalized friction term. The

interaction of the tracer with the obstacles is contained in two terms. 1) The friction coefficient $\nu_s = n\pi R^2 v$ is assumed to be q-independent and encodes a Markovian damping of the dynamics: it describes the friction induced by uncorrelated scattering of the tracer with the obstacles. 2) The memory kernel M contains all non-trivial correlations between tracer and obstacles. It itself consists of a regular background term and a critical term which is the object of the mode-coupling approximation. The regular term of the memory kernel is typically assumed as Markovian, can be expressed as a modification of ν_s, and is ignored in the following.

Closure of the equation is finally obtained by approximating the critical part of the memory kernel self-consistently as a linear function of the intermediate scattering function. The coupling of the tracer dynamics to the obstacles is expressed via coupling coefficients — called vertices — which are entirely determined by the matrix structure and are calculated with the direct correlation function $c_s(q)$ between matrix and tracer (Hansen and McDonald, 2006).

A further simplification is obtained by making use of a generalized hydrodynamics approximation in which the full memory kernel is made independent of the wavenumber q by only considering its long-wavelength limit (Götze et al., 1981b,a),

$$M(q,t) \mapsto M(0,t) =: m(t).$$

The memory kernel is then given by

$$m(t) = \frac{n}{3} \int \frac{\mathrm{d}^3 k}{(2\pi)^3}\, \Omega(k)^2 c_s(k)^2 F(k,t).$$

Its integral can be made one-dimensional in the wavenumber k by switching to spherical coordinates,

$$m(t) = \frac{n}{3} \int_0^\infty \frac{4\pi k^2 \mathrm{d}k}{(2\pi)^3}\, \Omega(k)^2 c_s(k)^2 F(k,t). \tag{1.22}$$

In the case of the Lorentz model, where the obstacles are randomly distributed and hard-spheres, the direct correlation function $c_s(q)$ is essentially given by the spherical Bessel function j_1 (Hansen and McDonald, 2006),

$$c_s(q) = 4\pi R^2 \frac{j_1(qR)}{q}.$$

The asymptotic solution for eqs. (1.21) and (1.22) is typically obtained by first performing a Fourier-Laplace transform, translating the time-dependence into a dependence on frequency z. Conventionally, the Laplace-Fourier transform $\hat{f}(q,z)$ of a function $f(q,t)$ is defined as

$$\hat{f}(q,z) = \mathrm{i} \int_0^\infty f(q,t) \mathrm{e}^{\mathrm{i}zt} \mathrm{d}t.$$

The Fourier-Laplace transform has the convenient property that the long-time limit of the original function $f(q,t)$ can be expressed simply by (Widder, 1972)

$$\lim_{t\to\infty} f(q,t) = \lim_{z\to+0} (-z\hat{f}(q,z)).$$

After transforming, eq. (1.21) reads,

$$\hat{F}(q,z) = \frac{-1}{z - \dfrac{\Omega(q)^2}{z + \mathrm{i}v_s + \hat{m}(z)}}, \tag{1.23}$$

while the Fourier-Laplace transform of the memory kernel $\hat{m}(z)$ is obtained directly from eq. (1.22) — because of the linearity of the equation — by replacing the ISF with its Fourier-Laplace transform. Now, both equations can be combined by inserting eq. (1.23) into the Fourier-Laplace transform of eq. (1.22), which leads to a single equation for the memory kernel

$$z\hat{m}(z) = \frac{n}{3}\int_0^\infty \frac{4\pi k^2 \mathrm{d}k}{(2\pi)^3}\Omega(k)^2 c_s(k)^2 \frac{z(z+\mathrm{i}v_s+\hat{m}(z))}{\Omega(k)^2 - z(z+\mathrm{i}v_s+\hat{m}(z))}.$$

Note that solving for $\hat{m}(z)$ instead of $\hat{F}(q,z)$ is simpler, since the latter quantity contains a divergence at $q \to 0$ which makes expansion of the equation in leading orders impossible. After solving for the memory kernel, the ISF can be determined by re-insertion of $\hat{m}(z)$ into eq. (1.23).

After introducing the abbreviation $\hat{\mu}(z) = z + iv_s + \hat{m}(z)$ and rewriting of the fraction, the equation reads

$$z\hat{\mu}(z) - z^2 - \mathrm{i}v_s z = \frac{n}{3}\int_0^\infty \frac{4\pi k^2 \mathrm{d}k}{(2\pi)^3} c_s(k)^2 \left(z\hat{\mu}(z) + \frac{z^2\hat{\mu}(z)^2}{\Omega(k)^2 - z\hat{\mu}(z)} \right).$$

At the critical density $n_c^{\mathrm{MCT}} = 9/(4\pi R^3)$ a bifurcation in the solution arises, marking the localization transition. There $1 = (n_c^{\mathrm{MCT}}/3)\int 4\pi k^2 \mathrm{d}k (2\pi)^{-3} c_s(k)^2$ holds and thus the first term of the integral can be evaluated

$$z\hat{\mu}(z) - z^2 - \mathrm{i}v_s z = z\hat{\mu}(z) + \frac{n_c^{\mathrm{MCT}}}{3}\int_0^\infty \frac{4\pi k^2 \mathrm{d}k}{(2\pi)^3} c_s(k)^2 \frac{z^2\hat{\mu}(z)^2}{\Omega(k)^2 - z\hat{\mu}(z)}.$$

Thus, at the critical density, $z\mu(z)$ has to become small in the limit of small frequencies, $z \to 0$, in order to satisfy the equation.

Near the critical density, the equation can therefore be expanded in powers of $z\hat{\mu}(z)$. In the expansion, a correction term with non-integer power arises because of the singularity of the integrand at $k \to 0$,

$$-z^2 - \mathrm{i}v_s z = \frac{n_c^{\mathrm{MCT}}}{3}\int_0^\infty \frac{4\pi k^2 \mathrm{d}k}{(2\pi)^3} c_s(k)^2 \frac{z^2\hat{\mu}(z)^2}{\Omega(k)^2} + \mathcal{O}\left((z\hat{\mu}(z))^{5/2}\right).$$

The remaining integral can be carried out, and one obtains up to leading order

$$-\mathrm{i}v_s z = \frac{6R^2}{5\nu^2}(-z\hat{m}(z))^2,$$

which, finally, can be solved for $\hat{m}(z)$. Thus, the critical behavior of the memory kernel is given by

$$-z\hat{m}(z) = \frac{\sqrt{-\mathrm{i}zt_s}\nu^2}{3R^2} + \mathcal{O}(z),$$

with time scale $t_s = 135R/8\nu$. This result had already been obtained by Götze et al. (1981a,b). The critical behavior of the memory kernel can now be re-inserted into eq. (1.23). In the limit of low but finite frequencies z this reduces to

$$-z\hat{F}(q,z) \to \frac{1}{1 + q^2R^2(-\mathrm{i}zt_s)^{-1/2}}.$$

From this result, the time-and-space scaling of the dynamics can be read off directly. The expression depends on the wavenumber q and the frequency z only in the combination z/q^4, which implies a walk dimension of $d_\mathrm{w}^\mathrm{MCT} = 4$. The scaling with the fractal dimension of the obstacle structure can be read off at small distances (small compared to the longest excursion of the tracer, but large against the obstacle diameter), i.e. at large wavenumbers (compare to the the discussion of the scaling form of the van-Hove function on the percolating cluster following eq. (1.14)). The ISF decays for $Rq \gg (|z|t_s)^{-1/4}$ as $\sim q^{-2}$, which implies the fractal dimension $d_\mathrm{f}^\mathrm{MCT} = 2$. Finally, the ISF is obtained by Laplace back-transform and satisfies the same scaling form as eq. (1.16),

$$F(q,t) \sim \mathcal{F}(qt^{1/d_\mathrm{w}}), \tag{1.24}$$

with $\mathcal{F}(\kappa \gg 1) \sim \kappa^{-d_\mathrm{f}}$. The only difference lies in the values for d_f and d_w. Importantly, the critical ISF decays to 0 for finite wavenumbers as $F(q,t) \sim q^{-d_\mathrm{f}} t^{-d_\mathrm{f}/d_\mathrm{w}}$.

The scaling behavior of the ISF as predicted for the Lorentz model in MCT is thus the same as given by dynamic scaling theory when the tracer is restricted to the percolating cluster, with the predicted values for the fractal and walk dimensions being close to the scaling theory results, $d_\mathrm{f} = 2.53$ and $d_\mathrm{w} = 4.81$, see table 1.1. Thus, MCT in the present form does not contain the non-ergodic contributions to the dynamics from tracers trapped in finite clusters, which are present in the full system at all finite densities. As a consequence, the non-ergodicity parameter is predicted by MCT to vanish for finite wavenumbers at densities below the critical density and to grow continuously from 0 at and above the transition. This is in contrast to the actual situation in the Lorentz model, where the non-ergodicity parameter is finite at all finite densities. The situation becomes worse e.g. when the MSD is considered. In scaling theory the exponent of anomalous diffusion z in the full system is different from the one on the percolating cluster d_w. This aspect is not contained in MCT.

Furthermore, the critical behavior found above is partly a result of the generalized hydrodynamics approximation. By keeping the full wavenumber dependence of the memory kernel, a short-wavelength singularity is introduced into the MCT equation which modifies the critical dynamics (Schnyder et al., 2011). The critical behavior in the generalized hydrodynamics approximation is then found only in an intermediate regime. This pecularity is common to all current MCT approaches to the localization transition. It is thus still an open question how to correctly capture the Lorentz model with its fractal structure and divergent length scale in MCT.

Regardless of these fundamental problems, in the following a comparison of the MCT predictions in the generalized hydrodynamics approximation to simulation results on the percolating cluster will be made, showing that for this special case there is qualitative and even semi-quantitative agreement.

In three dimensions, the percolation transition is predicted by MCT in the generalized hydrodynamics approximation to occur at the reduced obstacle density $(n_\mathrm{c}^*)^\mathrm{MCT} = 9/(4\pi) \approx 0.716$, which is close to the real percolation transition at $n_\mathrm{c}^* \approx 0.838$ (Elam et al., 1984; Rintoul, 2000).

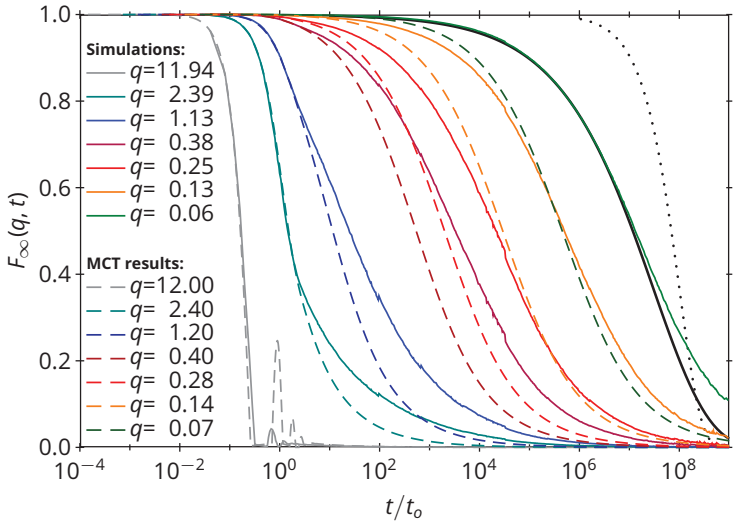

Figure 1.5: Intermediate scattering function $F_\infty(q,t)$ for tracers on the percolating cluster both in simulation (solid lines) and MCT (dashed lines). The unit of time is given by $t_o = R/v$. The simulation is performed directly at the critical density $n_c^* = 0.838$ and compared to mode coupling theory. For comparison, a curve corresponding to exponential relaxation (dotted line) and a stretched exponential $\exp(-(t/\tau_q)^\beta)$, $\beta = 0.39$ (solid black line) are given. *(Redrawn from (Spanner et al., 2013))*

Implementation details For comparison to MCT an event-driven, molecular-dynamics simulation of the Lorentz model on the percolating cluster was implemented by Markus Spanner. The cubic simulation box had a length of length $L = 200R$. Voronoi tesselation of the obstacles was performed to confirm the percolation density $n_c^* = 0.838$ and to identify the percolating cluster. For further details on the implementation of the simulation, see (Spanner et al., 2013). The MCT equations eqs. (1.21) and (1.22) were solved numerically, in addition to the asymptotic solution, to allow a full quantitative comparison to the simulation results. The unit of time for both the simulation and MCT is given by $t_o = R/v$.

The MCT equations were solved on an equidistant time grid in the standard way, documented for instance in (Bayer, 2007). The time grid was incrementally coarsened to be able to solve the equation over many orders of magnitude in time. The integration contained in the memory kernel was performed with the trapezoidal rule on a partly logarithmically-spaced wavenumber grid to correctly capture the long-wavelength behavior. From the smallest wavenumber $q_{\min} = 10^{-8}/R$ to a wavenumber $\Delta q = 0.4/R$, 50 logarithmically spaced wavenumbers were used. From Δq up to the maximum wavenumber $q_{\max} = 24/R$, an equidistant grid of spacing Δq was used. It was confirmed that these numerical parameters are sufficient for correctly solving the equations: The percolation density was found to be shifted slightly to $(n_c^*)^{\mathrm{MCT}} \approx 0.748$ and it converged to the exact value for finer discretizations. Furthermore, the critical behavior of the memory kernel as obtained from the numerical solution matched the asymptotic results to typically within 1% of its amplitude at long times.

Comparison of simulation to MCT and scaling theory The ISF is shown in fig. 1.5 for both the simulation (solid lines) and MCT (dashed lines) over a wide range of wavenumbers q. For all wavenumbers, the unit $1/R$ is always implied from now on. For very large wavenumbers, e.g. $q = 12$, the ISF for both simulation and MCT decays very fast and shows oscillations at $t \approx t_0$ when the tracers perform their first collisions with the obstacles (Hansen and McDonald, 2006; Götze, 2009). For small wavenumbers, e.g. for $q = 0.06$

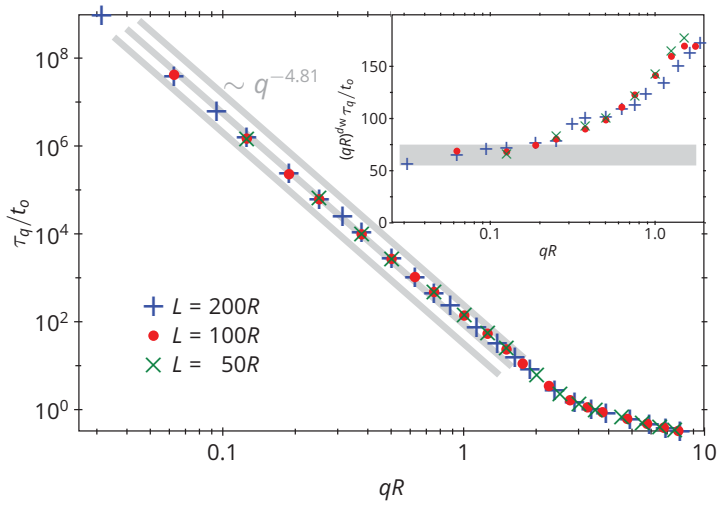

Figure 1.6: Relaxation time τ_q of the intermediate scattering function in the simulation at the critical point as a function of the wavenumber q and of the system size L as indicated in the legend. The power-law behavior with the exponent $-d_w = -4.81$ expected from the dynamic scaling hypothesis is marked by parallel grey lines. *Inset:* Rectification plot of the same data to expose asymptotic behavior. *(Redrawn from (Spanner et al., 2013))*

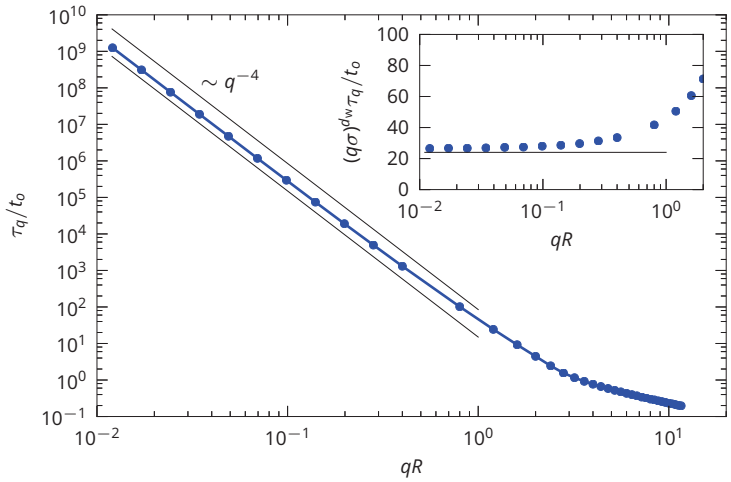

Figure 1.7: Relaxation time τ_q of the intermediate scattering function in mode-coupling theory at the critical point as a function of the wavenumber q. The data points are connected as guide to the eye. The power-law behavior with the exponent $-d_w = -4$ expected from the asymptotic solution of the MCT-equations is marked by parallel black lines. *Inset:* Rectification plot of the same data to expose asymptotic behavior.

the form of the ISF in the simulation becomes strongly stretched and can be adequately described on short and intermediate times via a Kohlrausch-Williams-Watts function $\exp(-(t/\tau_q)^\beta)$, with a stretching exponent $\beta = 0.39$ and a wavenumber dependent timescale τ_q (solid black line). This fit is not able to capture the long-time tail of the ISF, however. The MCT results are similar to the simulation: The shape of the ISF is comparable even though the stretching is less pronounced, especially at small q and long times. It is also apparent that the relaxation times of simulation and MCT move apart at very small q.

A relaxation time τ_q can be defined by $F^s(q, \tau_q) := 1/e$. From the dynamic scaling hypothesis, see section 1.2.2, it is expected that $\tau_q \sim q^{-d_w}$ at the critical point and for small q. This scaling is tested in fig. 1.6 for the simulation, where the relaxation time is shown as a function of the wavenumber and the expected asymptote is marked by parallel grey lines. The relaxation time approaches the asymptotic behavior only very slowly. A stricter test for the approach is a rectification plot which has been performed in the inset. Since for the limit $q \to 0$ one expects $\tau_q \sim q^{-d_w}$ to hold, one should also find that $q^{d_w}\tau_q \to A_\tau$ with a scaling constant A_τ. The inset demonstrates the slow approach to a constant limit value, which can be read off from the plot as $A_\tau = 65 \pm 10$ (grey region). Even though the approach to the critical asymptote is slow, the data is

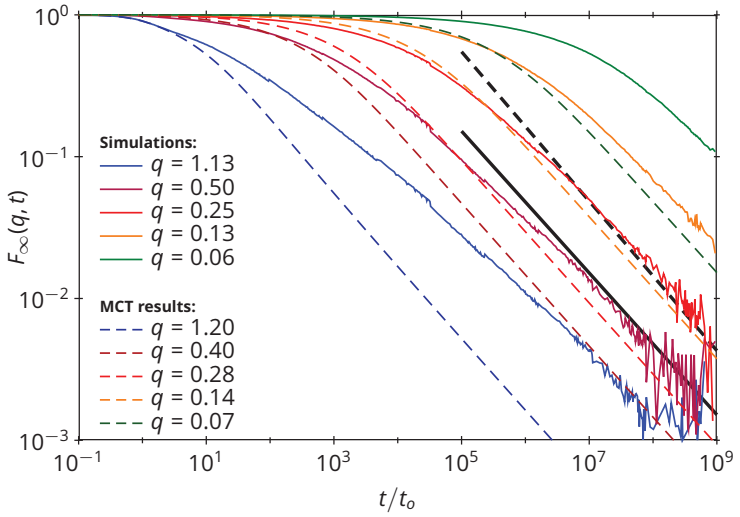

Figure 1.8: Double-logarithmic plot of the intermediate scattering function at the critical point as a function of time for small wavenumbers. The expected asymptotic power-laws for the long-time decay from scaling theory, t^{-d_f/d_w} (black solid line), and MCT, $t^{-1/2}$ (black dashed line), have indistinguishable slopes on the scale of the plot. *(Redrawn from (Spanner et al., 2013))*

compatible with the scaling hypothesis. The same plot but for the MCT data is shown in fig. 1.7. There, the expected asymptote is again $\tau_q \sim q^{-d_w}$, but with $d_w = 4$. In contrast to the simulation, the asymptotic regime is approached earlier. Apart from the difference in the exponent, the simulation and the MCT solution are qualitatively very similar.

The long-time decay of the ISF at the critical point follows a scaling law as well. This is exposed in the double-logarithmic plot in fig. 1.8 of the ISF of both simulation and MCT as a function of time for small wavenumbers, where both MCT and scaling theory predict power-law behavior. From both eq. (1.16) for the scaling hypothesis and eq. (1.24) for MCT, it follows that $F^s(q,t) \sim t^{-d_f/d_w}$, albeit with slightly different exponents. For the scaling hypothesis one finds $d_f/d_w = 0.527$, while for MCT $d_f/d_w = 0.5$ holds. These exponents are so similar, that the slopes of the corresponding power-laws in fig. 1.8 are indistinguishable. Furthermore, both asymptotes are fully compatible with the data.

In extension of the discussed scaling of the ISF with the exponents d_f and d_w, the scaling form for the ISF implies that the full space and time dependence at the critical point can be expressed in the limit of long times and small wavenumbers via a single scaling function $\mathcal{F}(\kappa)$ with $\kappa := qt^{1/d_w}$. Stated differently, the critical ISF will collapse onto $\mathcal{F}$ if rescaled properly. This collapse is tested for the simulation data in introducing a rescaled time $\hat{t} := \kappa^{d_w} \sim q^{d_w} t$ in fig. 1.9. By fixing the rescaled time to $\hat{t} := A_\tau^{-1}(qR)^{d_w} t/t_o$, one makes sure that the ISF decays asymptotically on the timescale $\hat{t} = 1$. Here, the scaling hypothesis value $d_w = 4.81$ was used. The slow convergence of the relaxation time discussed above appears in this plot in the failure of the curves to collapse onto the value $F(\hat{t}^{1/d_w}) = 1/e$ at $\hat{t} = 1$, and for times $\hat{t} \geq 1$. Apart from this, the collapse onto the scaling function is convincing in the limit of vanishing wavenumbers.

As the scaling of the dynamics is due to the divergence of the correlation length, the dynamics is subject to finite-size scaling. This is illustrated in the *left* and *center* insets of fig. 1.9, which show the region around the relaxation timescale for two simulations for smaller system sizes, $L = 50R$ and $100R$, respectively. The scaling becomes the less successful the smaller L is. In addition, the right inset shows that away from the critical density, at density

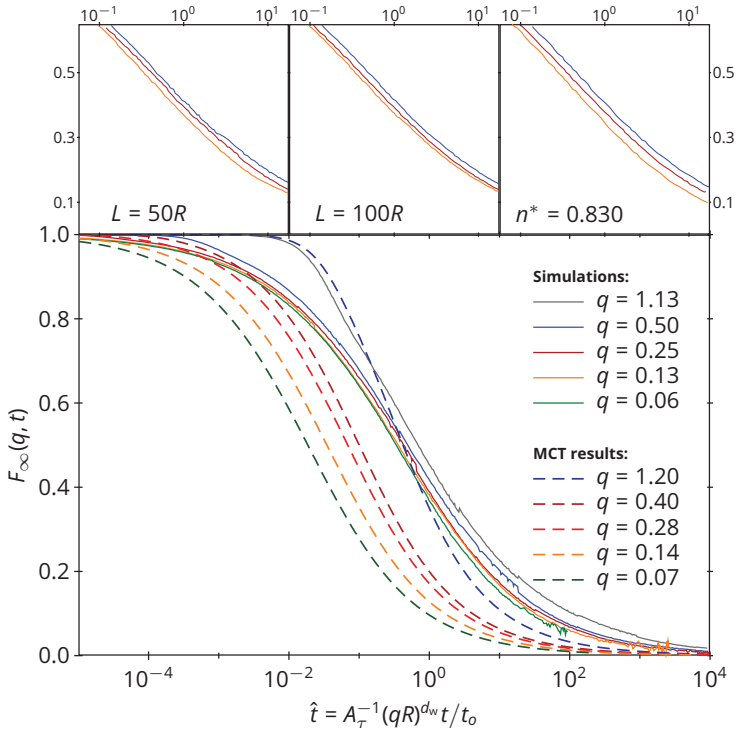

Figure 1.9: The intermediate scattering function of the simulation and mode-coupling theory as a function of rescaled time $\hat{t} = A_\tau^{-1}(qR)^{d_w} t/t_o$ for small wavenumbers q. *Bottom:* The simulation was performed in a system of size $L = 200R$ at the critical point. *Top*: Detail view of the ISF for smaller systems sizes $L = 50R$ *(left)* and $100R$ *(middle)*, exposing finite-size corrections to the scaling, and away from the critical density *(right)*. *(Redrawn from (Spanner et al., 2013))*

$n^* = 0.830$, the scaling does not succeed as well. This underlines how difficult it is to observe the critical scaling in simulations. It is important to use large enough systems and take care in identifying the critical point.

When the same scaling is applied to the MCT data the collapse is slightly less successful but still impressive considering that the unrescaled data shows a spread in the relaxation time of more than 6 orders of magnitude. This is a result of the similarity in the values of the walk dimension d_w.

Alternatively, the scaling collapse of the simulation data and the MCT solution can be tested with the value of $d_w = 4$ predicted by MCT, see fig. 1.10. Then, the collapse of the MCT data is very successful for small wavenumbers while the scaling of the simulation data is still acceptable, especially when considering the wide spread of relaxation times in the unrescaled data.

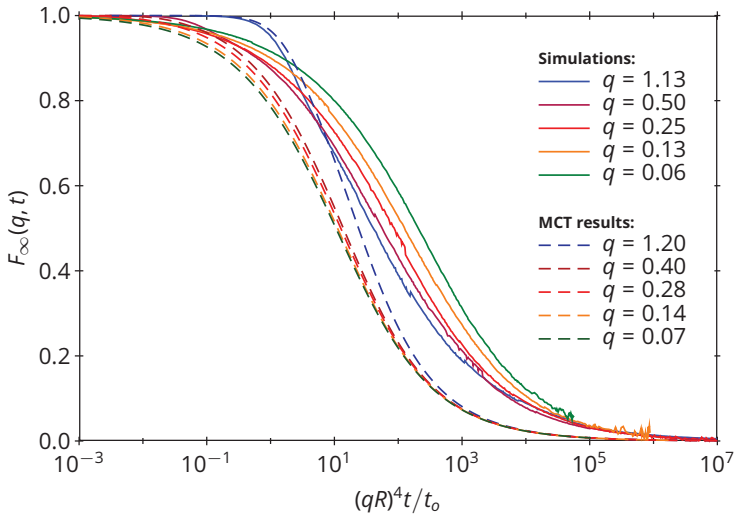

Figure 1.10: The intermediate scattering function of the simulation and mode-coupling theory as a function of rescaled time $\hat{t} = (qR)^4 t/t_o$ for small wavenumbers q, testing the scaling as predicted by MCT. *(Redrawn from (Spanner et al., 2013))*

Summary Even though MCT still has problems in the description of the critical dynamics of the Lorentz model, the presented comparison indicates that at least in the special case of the dynamics on the percolating cluster qualitative agreement is found. It is reassuring that in this special case, the exponents predicted by MCT are nearly correct.

At this point, a modification to MCT has yet to be found which would be able to correctly express the localization transition of the full Lorentz model. This is especially unfortunate as this would allow the study of the interplay of the localization transition and glassy dynamics found in heterogeneous media.

1.3 *Anomalous transport in heterogeneous media*

In this chapter, the localization transition of the Lorentz model has been discussed in detail. The following chapters will focus on generalizing these results to more complex systems. Generally, it can be expected that introducing modifications to the Lorentz model will lead to modifications in the dynamics near the localization transition.

As a first modification of the Lorentz model, the matrix may be made to include structural correlations, by for instance equilibrating the obstacles as a hard-sphere liquid with a given diameter, fixing the particles and then varying the diameter while leaving the matrix unchanged as control parameter (Spanner, 2010). In this way it has been shown that while structural correlations within the matrix shift the localization point they have no effect on the critical dynamics.

Quenched-annealed (QA) systems are the next generalization following from that. Typically they consist of equilibrated particles which are fixed in place to serve as the matrix and of interacting mobile particles inserted into the resulting void space. As a result, the system then has at least two control parameters, the packing fractions of the matrix and the fluid. The main differences to the Lorentz model are then the structural correlations frozen into the matrix and the interactions between the mobile particles.

In a three-dimensional (3D), hard-sphere realization of such a system, anomalous diffusion and the slowing down of the single-particle dynamics have been interpreted as evidence for the presence of a localization transition (Kurzidim et al., 2009, 2010, 2011). The system shows a wealth of localization phenomena, with an ideal glass transition (type-B transition of MCT) occurring at small matrix packing fractions and a localization-delocalization transition at vanishing fluid packing fractions – similar to the Lorentz model scenario. The Lorentz dynamics should be exactly recovered in the limit of fluid packing fraction $\Phi_F \to 0$, but the authors do not test this limit. Conversely, Kurzidim et al. find an anomalous diffusion exponent 0.5 at small but finite fluid packing fraction $\Phi_F = 0.1$, different from the exponent $2/z \approx 0.32$ in the Lorentz model (3D; see section 1.2.3). Kurzidim et al. observe the same exponent 0.5 when only the particles on the percolating cluster are considered. This is also in conflict with the Lorentz model, where the exponent of the anomalous diffusion on the percolating cluster is different from the one found for the whole system. On the percolating cluster, the expected value for the

Lorentz model is $2/d_w \approx 0.41$ (3D; see section 1.2.3). Upon increasing the number of mobile particles, the critical matrix packing fraction of the localization transition is found to decrease. This can be understood intuitively: the percolation point of the matrix is independent of the fluid particles but with increasing fluid packing fraction, the particles may start to block pathways in the matrix and can thus decrease the critical matrix packing fraction at which the fluid particles localize.

These findings are in agreement with the predictions of a variant of the mode-coupling theory of the glass transition (VK-MCT) developed by V. Krakoviack specifically for QA systems (Krakoviack, 2005, 2007, 2009, 2011). The results are obtained for hard-sphere systems, but the predictions of MCT generalize qualitatively to soft-spheres, as well. The only input parameters are structure factors which are calculated in the Percus-Yevick approximation, see (Meroni et al., 1996) and references therein.

The system shows a Lorentz-model-like (Type-A) transition at large matrix packing fractions, where the nonergodicity parameter changes from 0 to a finite value continuously. At the transition, the MSD shows anomalous diffusion, $\delta r^2(t) \sim t^{1/2}$. This is equivalent to the MCT result for the Lorentz model presented in section 1.2.3.

However, the prediction of the theory changes, when the procedure of equilibrating the matrix particles is modified. If the matrix particles are equilibrated in the presence of the fluid particles and only then fixed, an equilibrated mixture (EM) is created. This provides a mechanism by which the matrix structure changes as a function of the packing fraction of the fluid. While VK-MCT predicts roughly the same state diagram for the EM system as for the QA system, there is one crucial difference. At low fluid and high matrix packing fractions, it predicts a shift of the critical matrix packing fraction towards *higher values* when the fluid packing fraction is increased — the opposite from what was observed in the QA system by Kurzidim et al. Thus the EM system contains a reentrance transition, where the system makes a transition from a localized state to a delocalized state and back to a localized state upon simply increasing the fluid packing fraction.

The theory also predicts a a reentrance transition in the case of the QA system, but with a very small amplitude. This is slightly problematic as it conflicts with the fact that a QA system with hard-spheres cannot show a reentrance localization transition, since the percolation of void space is completely independent from the fluid component. But since the predicted shift in the critical packing fraction is so small in the QA case, it can be neglected.

In agreement with the theory, the reentrance scenario has been observed in 3D simulations of an EM system of hard spheres by Kim et al. (2009, 2010, 2011). The system is shown to transition from a localized state to a delocalized state solely by increasing the fluid packing fraction. Away from the transition, both a speeding up of the dynamics on the delocalized side as well as an increase of the localization length on the localized side upon increasing the density of the fluid component are observed. Beside the EM system, a QA system was also studied with the same control parameters, which, in agreement with the systems of Kurzidim et al. and VK-MCT, did not show the reentrance transition.

In general, the state diagrams of both the QA and the EM systems are found to be qualitatively in agreement with VK-MCT.

In both systems, subdiffusion in the MSD was observed at low fluid and high matrix packing fractions, with anomalous exponents depending on the packing fractions but in cases compatible with the Lorentz-model anomalous exponent $2/z \approx 0.32$.

Monodisperse hard spheres are used for both matrix and fluid particles. The packing fractions of the matrix and the fluid component are used as control parameters. The size and mass of the two components are fixed. To determine the full state diagram, a criterion for determining whether a system is localized or not is used: A system is considered to be delocalized if the MSD exceeds an ad hoc barrier, 10^2, before the simulation time 10^4 is elapsed. On the basis of this criterion, it is determined that the EM system *shows* a reentrance and the QA system *does not*. The essential difference of the EM system to the QA system is that the presence of the fluid component influences the matrix structure during equilibration. Increasing the fluid packing fraction then increasingly makes the matrix structure more correlated, opens up pathways in the matrix and shifts the critical matrix packing fraction towards higher values. Such a shifting of the percolation point due to correlations in the matrix has previously been reported (Chang et al., 2004; Mittal et al., 2006; Sung and Yethiraj, 2008b). This picture is further corroborated by a broadening of the pore-size distribution upon increasing the fluid packing fraction. The authors conclude that the reentrance must therefore be the result of the modification of the matrix structure, which is in line with the results of VK-MCT, which only accepts structural information as input.

The data is discussed along a few paths through the parameter space. Most notable are those paths where at constant matrix packing fraction the packing fraction of the fluid component is increased and subsequently a speeding up of the dynamics is observed. By itself, an ad hoc criterion for determining localization is problematic, as a speeding up of the long-time dynamics is not necessarily an indication of a shifting of the localization transition. But Kim et al. find a matrix density for the EM system close to the effective localization transition on the delocalized side where the diffusion first increases upon increasing the fluid density and then decreases again (Kim et al., 2011). The same behavior is not found in the QA system, where increasing the fluid density is found to always decrease the diffusion coefficient (Kim et al., 2011). Additionally, they discuss a matrix density for which the EM system is localized at very small fluid packing fractions (Kim et al., 2011). Upon slightly increasing the fluid density the MSD increases but still appears localized. Further increase of the fluid density then makes the MSD clearly diffusive at long times. Similar behavior is not found in the QA variant of their system, where increasing the fluid density is always found to decrease the amplitude of the MSD(Kim et al., 2011). The delocalization of the dynamics together with the speeding up of the dynamics upon increasing the fluid density constitutes a clear signature of a reentrance transition.

A similar reentrance is observed by Kim et al. in an EM system of bi-disperse purely repulsive soft spheres, while dynamics for a soft QA system are not reported.

Another increase in model complexity represent the glassy binary mixtures studied in simulations by Voigtmann and Horbach (2009). The system serves as an idealization of an ion-conductor. A simulation of a binary mixture of Weeks-Chandler-Anderson (Weeks et al., 1971) spheres with a disparate size ratio was performed. The larger spheres exhibited glassy dynamics upon increasing the density of the system, while the smaller spheres were still diffusive. The glassy component then formed the equivalent of a matrix for the small particles. The MSD of the fluid component showed extensive subdiffusion on intermediate time scales and diffusion on long-time scales. Switching off the interaction between the fluid particles, i.e. reducing the number density of the fluid to 0, lead to a decrease of the long-time diffusion coefficient at high densities. Stated differently, the non-interacting, zero-density system, had slower dynamics than the highly interacting, dense system, exactly as was the case in the EM systems of Krakoviack and Kim et al.

The speeding up of the dynamics was found to be compatible with a standard MCT calculation. In MCT, turning off the mobile particle interactions enters the theory only via the modification of the system's partial structure factors. In the theory, the speeding up of the dynamics of the interacting system is the result of a shift of the localization transition towards a higher fluid particle density when the interaction is turned on. This again represents a reentrance transition as a result of the modified structural correlations in the system, very similar to the situation in the EM system. However, little to no change was observed in the matrix structure factor upon switching off the interaction. This indicates that not the restructuring of the matrix but the modification of the fluid structure was the reason for the shift of the localization transition in that system.

Other simulations of heterogeneous media such as size-disparate binary mixtures (Moreno and Colmenero, 2006) or polymer blends with a large dynamics asymmetry (Moreno and Colmenero, 2008) show anomalous transport as well.

Although the above mentioned systems show some aspects of the Lorentz model scenario, they have not established *systematically* how the Lorentz model dynamics are modified by the introduction of particle interactions and soft potentials. The following chapters aim at providing a direct link from the original hard-sphere Lorentz model to soft-potential quenched-annealed systems.

In particular, this work will focus on the influence of the soft interaction potential on the localization transition. In the standard hard-sphere Lorentz model, barriers formed by the obstacles are insurmountable. The tracer is only able to move from one pocket to the next one if there is a connection between the two. When soft obstacles are introduced, barriers between void space pockets become finite, and thus surmountable. In general, this leads to a rounding of the critical dynamics. It will also be shown, that the reentrance transition can be a result of the soft potential and will arise even in situations where the matrix structure is completely independent of the fluid component.

2

A Lorentz model of soft spheres

As a well-defined starting point, the Lorentz model scenario is first reproduced in two dimensions with a soft potential in a molecular dynamics simulation of a binary mixture of purely repulsive spheres without a hard core. The component called M is fixed and used as matrix. The other component which is called F (for fluid) is made non-interacting to simulate independent realizations of the tracer particle.

2.1 Description of the system

2.1.1 Potential

For the interaction between obstacle matrix and tracers, the Weeks-Chandler-Andersen (WCA) potential (Weeks et al., 1971) was chosen. It is given by the repulsive part of the Lennard-Jones Potential which is cut-off at its minimum $r_{\mathrm{cut}} := 2^{1/6}\sigma_{\alpha\beta}$ and shifted to make it continuous,

$$V_{\alpha\beta}(r) = \begin{cases} \left(4\varepsilon_{\alpha\beta}\left(\left(\frac{\sigma_{\alpha\beta}}{r}\right)^{12} - \left(\frac{\sigma_{\alpha\beta}}{r}\right)^{6}\right) + \varepsilon_{\alpha\beta}\right)\Psi(r) & \text{for } r < r_{\mathrm{cut}}, \\ 0 & \text{for } r \geq r_{\mathrm{cut}}, \end{cases} \tag{2.1}$$

with $\alpha, \beta \in$ (M,F). The particle diameters are given by $\sigma_{\alpha\beta}$. The diameters are chosen to be additive so that the use of two parameters suffices, $\sigma_{\alpha\beta} = (\sigma_\alpha + \sigma_\beta)/2$. Matrix particles are sampled from a uniform distribution $\sigma_{\mathrm{M}} \in [0.85, 1.15]$, to avoid crystallization. Instead of varying the packing fraction of the matrix, the tracer diameter σ_{F} was used as the control parameter. For the matrix-fluid-interaction the polydispersity of the obstacle matrix was ignored: the simplification $\sigma_{\mathrm{MF}} = (1 + \sigma_{\mathrm{F}})/2$ was used. The energy scales are set to $\varepsilon_{\mathrm{MM}} = 1$, $\varepsilon_{\mathrm{MF}} = 0.1$, and $\varepsilon_{\mathrm{FF}} = 0$, while the masses were set to $m_{\mathrm{M}} = m_{\mathrm{F}} = 1$.

A smoothing function $\Psi(r)$ is used to make the potential C^2, which ensures the continuity of forces, the conservation of energy, and thus numerical stability of the algorithm,

$$\Psi(r) := \frac{(r - r_{\mathrm{cut}})^4}{h^4 + (r - r_{\mathrm{cut}})^4}.$$

The width of the smoothing function is chosen to be $h = 0.005$. The WCA potential is shown in fig. 2.1, both with (dotted line) and without (solid line) the smoothing function applied. The inset magnifies the region around r_{cut} and shows that the change caused by the smoothing function to the potential is small.

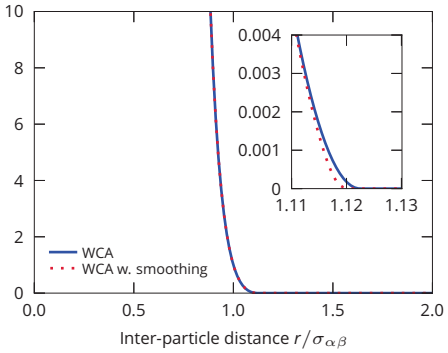

Figure 2.1: Weeks-Chandler-Andersen interaction potential without (solid line) and with smoothing function $\Psi(r)$ applied (dotted line). The latter is used in the simulations. The inset shows the same functions magnified around r_{cut}.

2.1.2 *Numerical integration of the equations of motion*

The system was simulated with Newtonian dynamics. The systems consists of N particles, with each particle i being assigned a mass m_i, position $\vec{r}_i(t)$, and velocity $\vec{v}_i(t)$. The positions of the particles then satisfy,

$$m_i \frac{\mathrm{d}^2\vec{r}_i}{\mathrm{d}t^2} = \frac{\partial V}{\partial \vec{r}_i} = \vec{f}_i. \tag{2.2}$$

The force on each particle, $\vec{f}_i(t)$, is calculated as the negative gradient of the total potential energy V, which itself is the sum over all pair potential energies $V_{\alpha\beta}$ as given by eq. (2.1),

$$V = \sum_{i=0}^{N}\sum_{j>i}^{N} V_{\alpha\beta}(r_{ij}), \text{ with } \vec{r}_{ij} = \vec{r}_i - \vec{r}_j,$$

with the particle types α and β being given by the types of the particles i and j. The force on each particle i is then explicitly given by

$$\vec{f}_i = -\sum_{j\neq i} \frac{\partial V_{\alpha\beta}(r_{ij})}{\partial \vec{r}_i}. \tag{2.3}$$

The system is conservative and thus, its total energy E_{tot} is a conserved quantity,

$$E_{\mathrm{tot}} = \sum_{i=0}^{N} \frac{1}{2} m_i \vec{v}_i^2(t) + V = const.$$

The equations of motion, eqs. (2.2) and (2.3), are numerically integrated with the velocity-Verlet algorithm (Verlet, 1967; Hairer et al., 2002). Provided, all positions and velocities of the particles are known at the starting time, e.g. $t = 0$, the positions and velocities after a timestep δt are then given by

$$\vec{r}_i(t+\delta t) = \vec{r}_i(t) + \delta t \vec{v}_i(t) + \frac{(\delta t)^2}{2m_i}\vec{f}_i(t) + \mathcal{O}\left(\delta t^4\right),$$

$$\vec{v}_i(t+\delta t) = \vec{v}_i(t) + \frac{\delta t}{2m_i}\left(\vec{f}_i(t) + \vec{f}_i(t+\delta t)\right) + \mathcal{O}\left(\delta t^2\right).$$

In this way, the trajectories of the particles can be obtained step-wise.

The velocity-Verlet algorithm is time-reversible and symplectic. As such it nearly conserves phase space and the total energy in conservative systems. More precisely, for sufficiently small timesteps δt, the total energy $E_{\mathrm{tot}}(t)$ of the numerically obtained positions and velocities is time-dependent but stays in an interval of $\mathcal{O}\left((\delta t)^2\right)$ around the original energy E^0_{tot} (Hairer et al., 2002, Theorem 8.1),

$$E_{\mathrm{tot}}(t) = E^0_{\mathrm{tot}} + \mathcal{O}\left((\delta t)^2\right).$$

To ensure stable integration of the equations of motion, the time step $\delta t = 7.2 \times 10^{-4} t_0$ with $t_0 = \left[m_{\mathrm{M}}\sigma_{\mathrm{M}}^2/(\varepsilon_{\mathrm{MM}})\right]^{1/2} = 1$ was chosen (Binder et al., 2004). From here on, units will be typically omitted. The unit for lengths is σ_{M}, for times it is t_0, for energies it is $\varepsilon_{\mathrm{MM}}$.

As this system is a many-particle system, the average $\langle \ldots \rangle$ is defined as the microcanonical average over all particle trajectories. Since the systems are finite, the average must additionally contain an average over matrix configurations. The order in which the averages are performed is important, with the average over trajectories performed first.

2.1.3 *Preparation of the matrix*

N_M obstacle particles were equilibrated in a two-dimensional, quadratic box of side length L at a number density of $n_M = 0.278$ (e.g. $N_M = 1000$ and $L = 60$) at the temperature $k_B T = 1$. Equilibration was achieved with a simplified version of the Andersen thermostat (Andersen, 1980) by randomly selecting the particle velocities from a Maxwell distribution every 100 steps, for at least 10^5 time steps. Then, the obstacles were fixed in space and their positions uniformly rescaled to number density $n_M = 0.625$ (e.g. rescaling the box length from $L = 60$ to $L = 40$). This procedure generates a dense matrix with weak structural correlations, which can be confirmed by the partial structure factor of the matrix particles $S_{MM}(q)$.

Structure factors For binary mixtures, there are three partial structure factors. Let the set of particle indices of the component α be denoted by I_α, then the microscopic partial densities of the components are given by

$$\rho_\alpha(\vec{r}) := \sum_{j \in I_\alpha} \delta(\vec{r} - \vec{r}_j).$$

So the Fourier-transformed partial densities are given by

$$\rho_\alpha(\vec{q}) := \sum_{j \in I_\alpha} \exp(-i\vec{q} \cdot \vec{r}_j).$$

Then, the partial structure factor, which is typically normalized with the total number of particles $N = N_M + N_F$, is defined as (Hansen and McDonald, 2006)

$$S_{\alpha\beta}(q) = \frac{1}{N} \langle \rho_\alpha(\vec{q}) \rho_\beta(-\vec{q}) \rangle. \tag{2.4}$$

Matrix structure The matrix structure factor $S_{MM}(q)$ is shown in fig. 2.2. Here, it is not normalized with the total number of particles but with the number of obstacles N_M and thus tends to a large-wavenumber limit of 1. $S_{MM}(q)$ shows only weak modulations, therefore, the matrix is structurally relatively similar to the completely uncorrelated matrix of the standard Lorentz model.

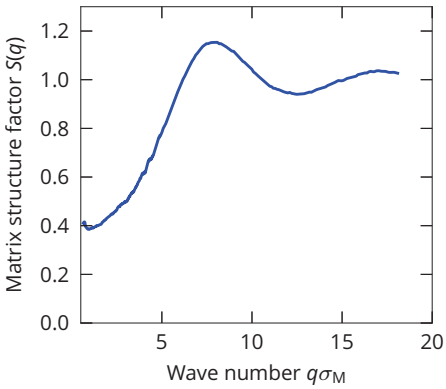

Figure 2.2: Matrix structure factor $S_{MM}(q)$ in a system of length $L = 40\sigma_M$, averaged over 100 independent configurations. *Centered moving average applied.*

As an example, one matrix configuration is shown in fig. 2.3 in grey. The diameter with which the obstacles are presented in the figure is the effective hard-sphere diameter of the obstacles assuming a point-sized tracer. This effective diameter can be obtained as the minimum distance between two obstacles between which the tracer can pass through with its given diameter σ_F and its total energy. For a calculation see section 2.3, where the diameter is calculated in eq. (2.11).

To control finite-size effects, final box lengths were $L = 28.28$, 40, 56.57, 80 and 160. The number of obstacles in these systems was 500, 1000, 2000, 4000 and 16000, respectively. Computed quantities were averaged over 100 independent matrix configurations at each system size.

2.1.4 *Preparation of the tracers*

Instead of varying the number density of obstacles n_M to drive the system over the localization transition, the diameter of the tracers σ_F was used as control

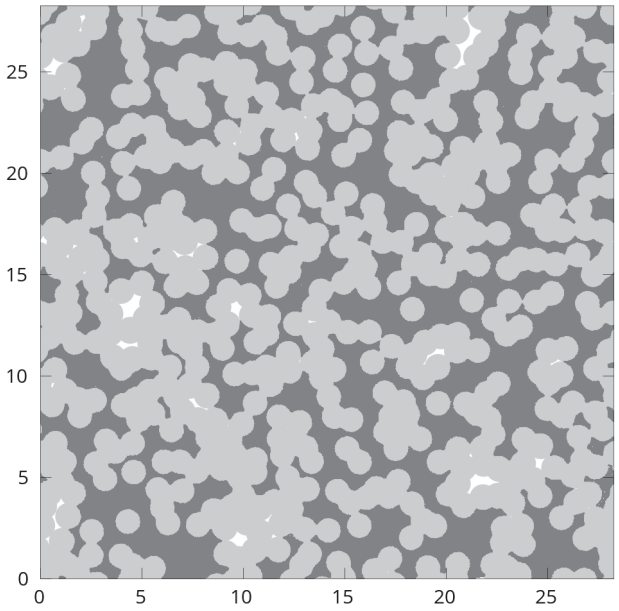

Figure 2.3: All the positional data of a single simulation run over time. A single-energy run with 500 tracers at $\sigma_F = 0.45$. All the tracer positions which were collected over a whole simulation run are represented as dark grey points. The obstacles are represented as hard-spheres in light grey with the effective hard-sphere diameter calculated from 2.11 using the particle energy as input. This system is on the localized side of the transition, but with a correlation length exceeding the system size, thus a percolating path can be found starting from the x-axis at $x \approx 22$ upwards.

parameter. Varying the tracer diameter is more convenient as it allows the re-use of the obstacle matrices. For an illustration of the localization transition through which a tracer goes when its diameter is varied, see fig. 2.4. With a small diameter (black circle), the tracer is free to leave the pocket formed by the obstacles (light grey circles), while it would be trapped if it had a larger diameter (dark grey circle).

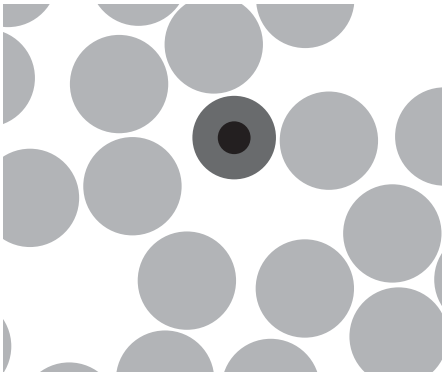

Figure 2.4: Obstacles (light grey) form a matrix for the tracers. A small tracer can escape its pore (black), while a large one is localized (dark grey). *(Schematic representation)*

To further illustrate, the void structure is shown in fig. 2.5 for three systems — a subcritical, the critical and a localized system — which only differ in the value of σ_F. Via the hard-sphere mapping discussed later on in section 2.3, the variation of the tracer diameter σ_F was mapped onto the equivalent variation of the obstacle diameter and via a Voronoi tesselation of the void space, the void clusters were then determined. The percolating cluster, which is highlighted in blue, vanishes as the system crosses the transition.

For each configuration of the system, between 50 and 20000 independent, non-interacting tracers are inserted into the void space. For this, the energies of the tracers demand special attention. In the standard hard-sphere Lorentz model, barriers formed by the obstacles are insurmountable. The tracer is only able to move from one pocket to the next one if there is a connection between the two. With a soft interaction potential like the WCA potential employed here, barriers between void space pockets become finite and surmountable. Thus the energy of the tracer influences the space that is available for exploration, as a tracer with a high energy will be able to overcome more barriers than a tracer with low energy. As a consequence, energy becomes another control parameter and tracers with different energies have different critical points.

Because of this it is important to set all the tracers to the same energy when inserting them into the system, turning the simulation into a microcanonical one-particle system. The particle energy was chosen such that the particles have an average kinetic energy corresponding to $k_B T = 1$ (with the average velocity $\langle v_F \rangle = \sqrt{2k_B T/m_F} = \sqrt{2}$). This energy was numerically obtained from equilibration runs, where non-interacting tracers were inserted into the matrix and then equilibrated at temperature $k_B T = 1$ for at least 10^5 time steps.

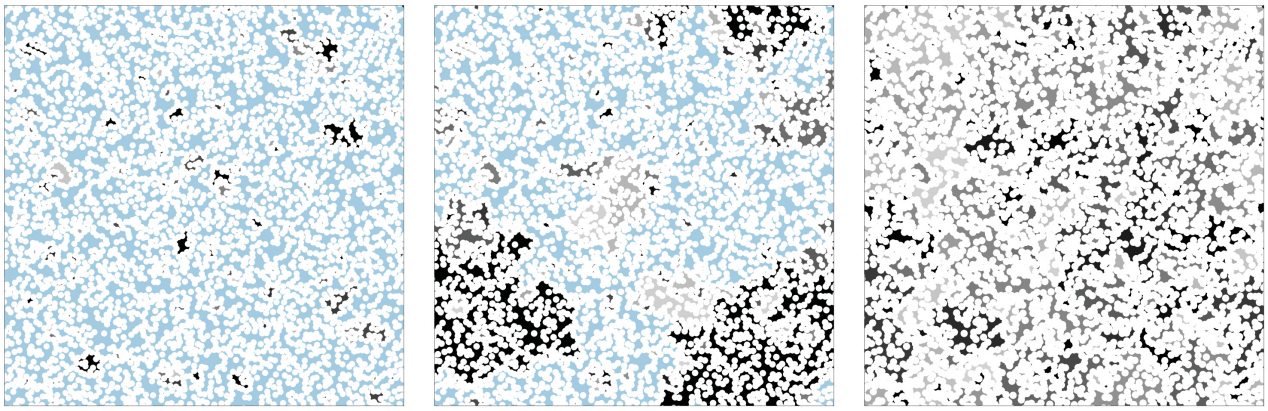

Figure 2.5: Void structure of the simulation for a delocalized state at $\sigma_F = 0.35$ (left), critical state at $\sigma_F = 0.43$ (middle) and localized state at $\sigma_F = 0.6$ (right). Matrix particles are shown as white circles with the effective hard-sphere diameter calculated from 2.11 using the particle energy as input. The percolating cluster in blue, the rest of the clusters in grey and black with a different shade of grey for each distinct cluster. The void clusters were determined via Voronoi tesselation of the void space.

The average energy per particle in these runs was then taken as the energy to be used in production runs. The average energy increased with increasing particle diameter, ranging from $E = 1.08$ at $\sigma_F = 0.1$ to $E = 1.79$ at $\sigma_F = 0.9$.

In production runs, particles were inserted at random positions into the void space, if and only if the potential energy at that position was less than or equal to the previously determined average energy. The particles were then given the rest of the energy in kinetic energy, with the velocity pointing in a random direction. This procedure fulfills the requirement to microcanonical systems that each micro state must be equally probable. Because of this, after insertion of the tracers, it is permissible to immediately start the production run.

2.2 *Dynamics*

The mean-squared displacement $\delta r^2(t)$ of the tracers shown in fig. 2.6 is typical for the Lorentz model. At small tracer diameters, e.g. $\sigma_F = 0.1$, the short-time ballistic regime with $\delta r^2(t) \sim t^2$ is followed by diffusion with $\delta r^2(t) \sim t$ at long times, as most tracers are delocalized and free to explore the infinite cluster of the system. Upon increasing σ_F, the dynamics shows a slowing down and a subdiffusive regime develops on intermediate timescales. Still, for $\sigma_F < 0.43$, diffusion is always recovered at long times. At the diameter $\sigma_F = 0.43$, the MSD stays subdiffusive over the whole simulated time range and asymptotically approaches the expected critical power-law dependence of the Lorentz model, $\delta r^2(t) \sim t^{2/z}$ with $z \approx 3.036$, see section 1.2.2. Thus the localization transition in this system occurs at $\sigma_F^c \approx 0.43$. Characteristically for the localized side of the system, for diameters $\sigma_F > 0.43$, the MCT plateaus off at long times, with the plateau height decreasing in height with increasing σ_F. The MSDs presented here are free of finite-size effects as long as $\delta r^2(t) < (L/2)^2$. For a more detailed discussion of the finite-size effects, see section 2.5.

Suppression of long-time diffusion Additional confirmation that the present system exhibits the Lorentz model localization transition comes from the study

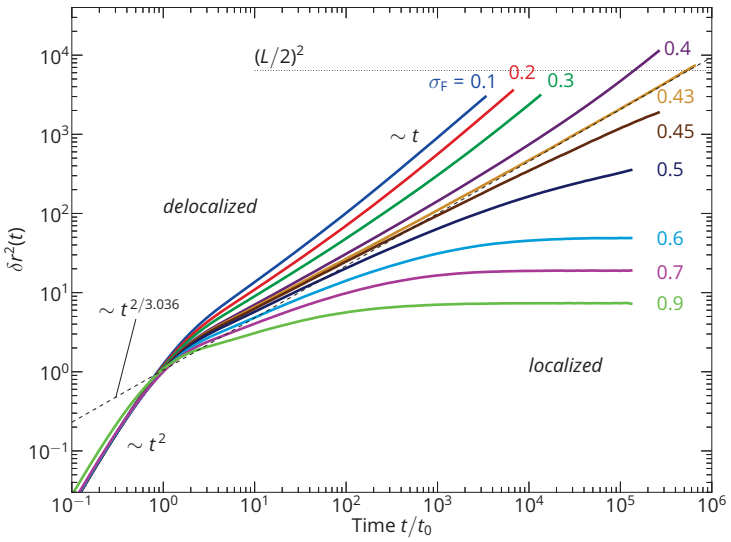

Figure 2.6: Mean-squared displacement for the single-energy two-dimensional Lorentz model for various tracer diameters σ_F as indicated in the figure. The dashed line gives the expected critical asymptote of the two-dimensional Lorentz model. The MSDs are free of finite size effects.

of the long-time diffusion coefficient D. For the distance from the transition

$$\varepsilon = \frac{\sigma_F - \sigma_F^c}{\sigma_F^c}, \tag{2.5}$$

the D is expected to asymptotically vanish as (Ben-Avraham and Havlin, 2000),

$$D \sim |\varepsilon|^\mu.$$

In two dimensions, the critical exponent μ is connected to the other critical exponents by the scaling law given in eq. (1.10), and has the value $\mu = 1.31$, see table 1.1. The diffusion coefficients extracted from the MSD are shown in fig. 2.7. At $\sigma_F = 0.42$ it becomes difficult to obtain the correct value of D free from finite size effects. The vertical bar marks the range between upper and lower bounds for D obtained from finite size analysis, as discussed in section 2.5. The numerically obtained D are fully compatible with the expected asymptotic power-law shown as dashed line. The critical point was assumed to be at $\sigma_F^c = 0.435$, which is very close to the value obtained from the MSD itself. The amplitude of the asymptote was obtained by matching to the data.

A more sensitive approach to confirm the presence of an asymptotic regime is to make a rectification plot. If $D \sim |\varepsilon|^\mu$, then $D^{1/\mu}$ will become proportional to ε close to the critical point. It will become a straight line when plotted as a function of the control parameter σ_F, and deviations from this will clearly visible. Additionally, this approach allows for extrapolation towards the critical diameter. In fig. 2.8 such a rectification plot is performed. The same asymptotic corrections as for the MSD make it that the expected critical behavior only applies close to the critical point, where obtaining the diffusion coefficient becomes difficult. Nevertheless, the critical asymptote matched to the data in fig. 2.7 provides a good description of the lowest diffusities close to the localization transition. Thus $\sigma_F^c = 0.435$ is a valid estimate of the critical point. The behavior of the diffusion coefficient is very similar to what is found in the two-dimensional, ballistic hard-sphere Lorentz model, which is shown in fig. 2.9. The suppression of the long-time diffusion coefficient in this soft-sphere system is thus fully compatible with the Lorentz model scenario. Further confirmation that the present system displays the Lorentz

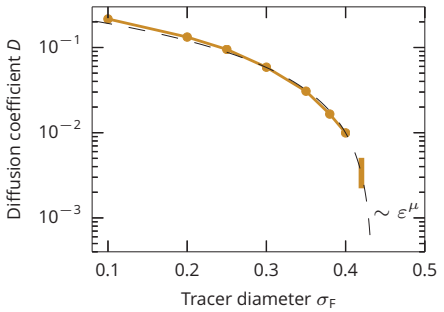

Figure 2.7: The diffusion coefficient D as a function of the tracer diameter. Connected points for data free of finite size effects. The vertical bar at $\sigma_F = 0.42$ marks upper and lower bounds for D obtained from finite size analysis (see section 2.5). Critical asymptote ε^μ of the 2D model with $\varepsilon := (\sigma_F - \sigma_F^c)/\sigma_F^c$, with $\sigma_F^c = 0.435$ and the expected exponent $\mu = 1.31$ as dashed line.

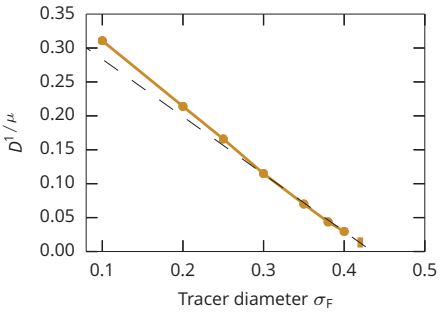

Figure 2.8: Rectification plot of the diffusion coefficient D as a function of the tracer diameter. The dashed line is the same critical asymptote as in fig. 2.7.

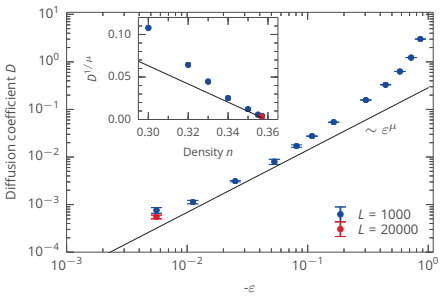

Figure 2.9: The diffusion coefficient D of the 2D hard-sphere Lorentz model with ballistic dynamics as a function of the relative distance to the critical point $\varepsilon := (n^* - n_c^*)/n_c^*$ with critical reduced obstacle density $n_c^* = 0.359$. Critical asymptote with the diffusion exponent $\mu = 1.31$ of the 2D Lorentz model as solid line. *Inset:* Rectification plot of the same data as a function of reduced obstacle density. *Data by Felix Höfling. Printed with permission.*

model transition comes from a scaling analysis of the dynamics which is described in the following.

Scaling of the mean-squared displacement From dynamic scaling theory, see section 1.2.2, it is expected that the MCT asymptotically obeys a scaling form, given in eq. (1.13),

$$\delta r^2(t) = t^{2/z}\delta\mathcal{R}^2_\pm(\hat{t}),$$

with the rescaled time $\hat{t} := t/t_x \sim tl^{-z}$, the localization length l, and two scaling functions $\delta\mathcal{R}^2_\pm(\hat{t})$, one for each side of the transition. The localization length plays the role of a crossover length scale. On the delocalized side, the system becomes diffusive when $\delta r^2(t) \sim l^2$ and the scaling function reduces to $\delta\mathcal{R}^2_-(\hat{t} \gg 1) \sim \hat{t}^{1-2/z}$. On the localized side, the MSD converges to $\delta r^2(t) \sim l^2$. Therefore, the scaling function is required to obey $\delta\mathcal{R}^2_+(\hat{t}) \sim \hat{t}^{2/z}$. At the critical point, l diverges along with the correlation length ξ with $l^z \sim \xi^{d_w} \sim |\varepsilon|^{-\nu d_w}$. The critical behavior of the MSD is thus encoded in the limit $\hat{t} \to 0$. The scaling functions reduce there to $\delta\mathcal{R}^2_\pm(\hat{t} \to 0) \to const$, which corresponds to anomalous diffusion.

There are thus two properties that can be tested for the numerical data. Firstly, if the MSD approaches exactly the $\sim t^{2/z}$ asymptote *at* the critical point. Secondly, if the MSD obeys the asymptotic scaling with l and collapses onto the two master curves *in the approach* to the critical point. Since the scaling function on the delocalized side reduces to diffusion for $\hat{t} \gg 1$, the full scaling analysis can only be successful if the scaling of D with μ already is successful.

Asymptote at the critical point The approach to the critical asymptote $\sim t^{2/z}$ can be exposed sensitively by dividing the MSD by $t^{2/z}$. For the delocalized system, $\delta r^2(t)/t^{2/z}$ diverges at long times, while for localized systems it decays rapidly as $t^{-2/z} \to 0$. The closer to the transition the longer this quantity stays finite and at the critical point it has a constant long time limit. In fig. 2.10 this quantity is shown for the same data as in fig. 2.6. At $\sigma_F = 0.43$, the quantity slowly approaches a constant value close to 1, confirming the approach to the critical asymptote.

That this approach is so slow seems to be a property of the two-dimensional Lorentz model in the case of Newtonian dynamics. There, corrections to the critical asymptote are known to be strong in comparison to the Brownian and the lattice model cases, though a clear reason for this is unknown (F. Höfling, private communications). This makes it difficult to observe the critical behavior of the Lorentz model clearly. Demonstrating this, a comparison of $\delta r^2(t)/t^{2/z}$ for ballistic (i.e. Newtonian) and Brownian hard spheres, and for a lattice system is shown in fig. 2.11 in which the MSD for the ballistic case is shown to converge far slower than the other two cases. This shows however, that the approach towards the critical asymptote for the soft-sphere Lorentz model is clearly qualitatively similar to the scenario in the ballistic hard-sphere system.

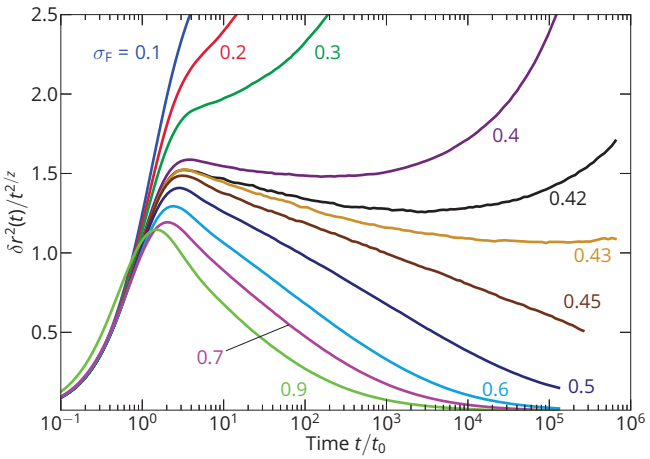

Figure 2.10: Mean-squared displacements divided by the critical asymptote $t^{2/z}$ with $z = 3.036$.

To go one step further, the approach to the critical asymptote can also be tested for compatibility with a scaling prediction which indicates that the approach is eventually dominated by a geometric correction. For Brownian hard-spheres and lattice systems, the scaling form

$$\delta r^2(t) = t^{2/z}\delta\mathcal{R}_\pm^2(\hat{t})(1 + t^{-y}\Delta_\pm(\hat{t})). \tag{2.6}$$

has been derived from a scaling ansatz (Kammerer et al., 2008) and been confirmed in simulations (Kammerer et al., 2008; Bauer et al., 2010). The exponent y is universal and is connected to the exponent Ω — which describes corrections to scaling in the cluster-size distribution — via the hyperscaling law,

$$y = \frac{\Omega(\nu d - \beta)}{z(\nu - \beta/2)}, \tag{2.7}$$

The correction given in eq. (2.6) is therefore of a purely structural origin. In two dimensions the exponent has the value $y \approx 0.49$. Although y is universal, the amplitude of the correction is not, and thus can be very different here from the results found in Brownian and lattice systems. Moreover, strong preasymptotic corrections may mask the correction on the timescales available to simulations. In ballistic dynamics, the correction seems to vanish not with exponent y but with another exponent ≈ 0.16, the origin of which has not been determined yet (F. Höfling, private communications). In principle a non-universal correction could become so large as to hide the universal $-y$-correction over long times, making observation of the correction in a simulation unfeasible[1].

If present, the first order correction can be directly read off from the MSD: At the critical point, $\delta\mathcal{R}_\pm^2(\hat{t})$ reduces to a constant A, so that from the above scaling form in eq. (2.6) it follows that

$$\frac{\delta r^2(t)}{At^{2/z}} - 1 \sim t^{-y}. \tag{2.8}$$

To exploit this here, it is first necessary to determine A by extrapolating it as the long-time limit of $\delta r^2(t)/t^{2/z}$ at the critical point, i.e. from the MSD at $\sigma_F = 0.43$ from fig. 2.10. Unfortunately the simulated time is not sufficiently long to determine A satisfactorily. Instead, the quantity $|\delta r^2(t)/(At^{2/z}) - 1|$ is displayed in fig. 2.12 for a range of possible A. As guides to the eye, the

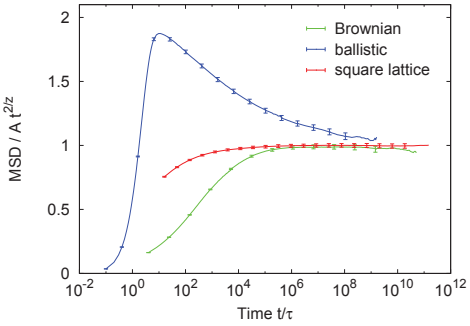

Figure 2.11: Mean-squared displacements at the critical point divided by the critical asymptotes in the two-dimensional Lorentz model for ballistic and Brownian dynamics and the two-dimensional square lattice Lorentz model. *Brownian data extracted from (Bauer et al., 2010), lattice data from (Kammerer et al., 2008), ballistic data by Felix Höfling. Printed with permission.*

[1] Something similar happens for instance in binary Lennard-Jones mixtures, where the critical divergence of the Onsager coefficient is superposed with and strongly modified by a non-critical constant contribution (Das et al., 2006).

expected asymptote t^{-y} (dotted line) and the one determined in simulations of the ballistic hard-sphere Lorentz model, $t^{-0.16}$ are included. It is apparent from the plot that $|\delta r^2(t)/(At^{2/z}) - 1|$ does not decay monotonously at $\sigma_F = 0.43$ which is either an indication for the presence of finite size effects or of the localization transition occurring at a slightly larger σ_F. With the present data it is impossible to determine which scenario applies here. On the simulated timescale, the data can be made compatible with both asymptotes, leaving the question open of whether the universal correction is masked here by preasymptotic corrections or not. To determine the first order correction to scaling correctly, larger systems and longer simulation runs would be needed.

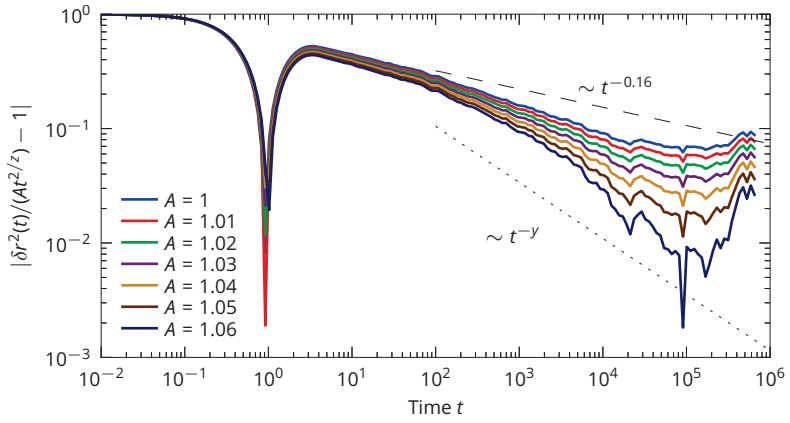

Figure 2.12: Critical mean-squared displacement at $\sigma_F = 0.43$ with the critical long-time asymptote $At^{2/z}$ subtracted and normalized for a range of amplitudes A. The dotted line is compatible with the leading critical correction with exponent y and the dashed line is compatible with the asymptote from Felix Höfling's 2D simulation of the ballistic hard-sphere system.

Collapse of the dynamics onto master curves near the critical point To test the scaling predictions *in the approach to* the localization transition, the collapse of the MSD away from the critical point onto the scaling functions $\delta\mathcal{R}^2_\pm(\hat{t})$ must be attempted. This test is only worthwhile because the vanishing of D in the approach to the localization transition was confirmed to be compatible with the Lorentz model scaling already. If this had not been the case, the attempt to collapse the MSD onto the scaling functions would have been futile, since the scaling function on the delocalized side contains the scaling of D at long times.

In fig. 2.13, the MSD is divided by $t^{2/z}$ and plotted as a function of $t|\varepsilon|^{\nu d_w}$ to expose the two scaling functions. The critical point $\sigma_F^c = 0.43$ sets ε via eq. (2.5).

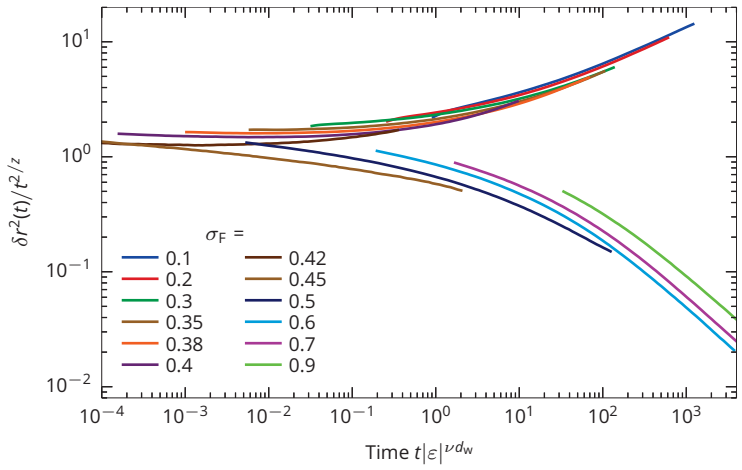

Figure 2.13: Rescaled mean-squared displacement as a function of rescaled times $t|\varepsilon|^{\nu d_w}$ for a range of diameters as indicated in the legend. For the calculation of ε, it was assumed that $\sigma_F^c = 0.43$, here.

Only data satisfying $t \gg t_0 (= 1)$ and $\sqrt{\delta r^2(t)} \gg \sigma_M (= 1)$ is shown. The two scaling functions are discernible but full data collapse is not achieved. The collapse at long times on the delocalized side reflects the power-law dependence of the diffusion coefficient, $D \sim (-\varepsilon)^{\mu}$.

The collapse works as well as can be expected for the Lorentz model without taking the first order correction to scaling into account, e.g. as demonstrated by Höfling et al. (2006) in the case of the three-dimensional Lorentz model. Using the first order correction $\sim t^{-y}$, however, would introduce at least one more fitting parameter to estimate the amplitude of the correction term or would require identifying the amplitude at the critical point which was not achieved in the previous paragraph. Simulating closer to the transition would also improve the scaling but would require considerably larger systems and longer simulation times, which was outside the scope for this work.

The collapse of the MSD onto the two scaling functions is not fully convincing on its own, but it gives further indication that the present system is a realization of the Lorentz model dynamics.

Van-Hove function Most of the necessary information about the localization of the system could already be deducted from the MSD, but to obtain the full information of the tracer dynamics it is useful to study the self part of the van-Hove function $P(r,t) := \langle \delta(\vec{r} - \Delta\vec{r}(t)) \rangle$, with the displacement of the tracer $\Delta\vec{r}(t) := \vec{r}(t) - \vec{r}(0)$ at time t. This function gives the probability that the tracer has been displaced by a distance $\vec{r}$ at a given time t, see eq. (1.1) and discussion. The van-Hove function is shown in fig. 2.14 for a range of tracer diameters σ_F, spanning the whole simulated diameter range. This allows for extensive study of the modification of $P(r,t)$ as the system crosses the localization transition. The plots of the van-Hove function shows how the tracers explore the network over time.

The upward spike at $t = 1.5$, which can be seen in nearly all the plots in fig. 2.14 is a result of the requirement that all particles have the same energy. Most of the space available to the tracers leaves the particles without potential energy. When the particles are inserted into the matrix, most particles therefore have no potential energy and gain the required energy as kinetic energy fully. A majority of particles therefore has the maximum possible velocity at the beginning of the simulation. Before the first collision with an obstacle, these particles then all cover the same distance in any given time, leading to the pronounced spike in the data. After the first collision, this feature vanishes immediately. For the densest system, $\sigma_F = 0.9$ the spike is not present due to the strong increase in the average potential energy.

The van-Hove function displays two bumps on the delocalized side. One at short distances, signifying the portion of tracers which are localized in finite pockets, and whose peak position does not move over time. The other peak moves to large distances over time, as the tracers explore the void space. This second bump weakens as the tracer diameter is increased and is not present for the localized systems, $\sigma_F > 0.43$.

At $\sigma_F = 0.5$, the van-Hove function does not fully converge to its long-time limit over the course of the simulation, but a slowing down of the dynamics is discernible at the largest observed time. At $\sigma_F = 0.6$, the van-Hove function fully converges to its long-time limit over the duration of the simulation, which

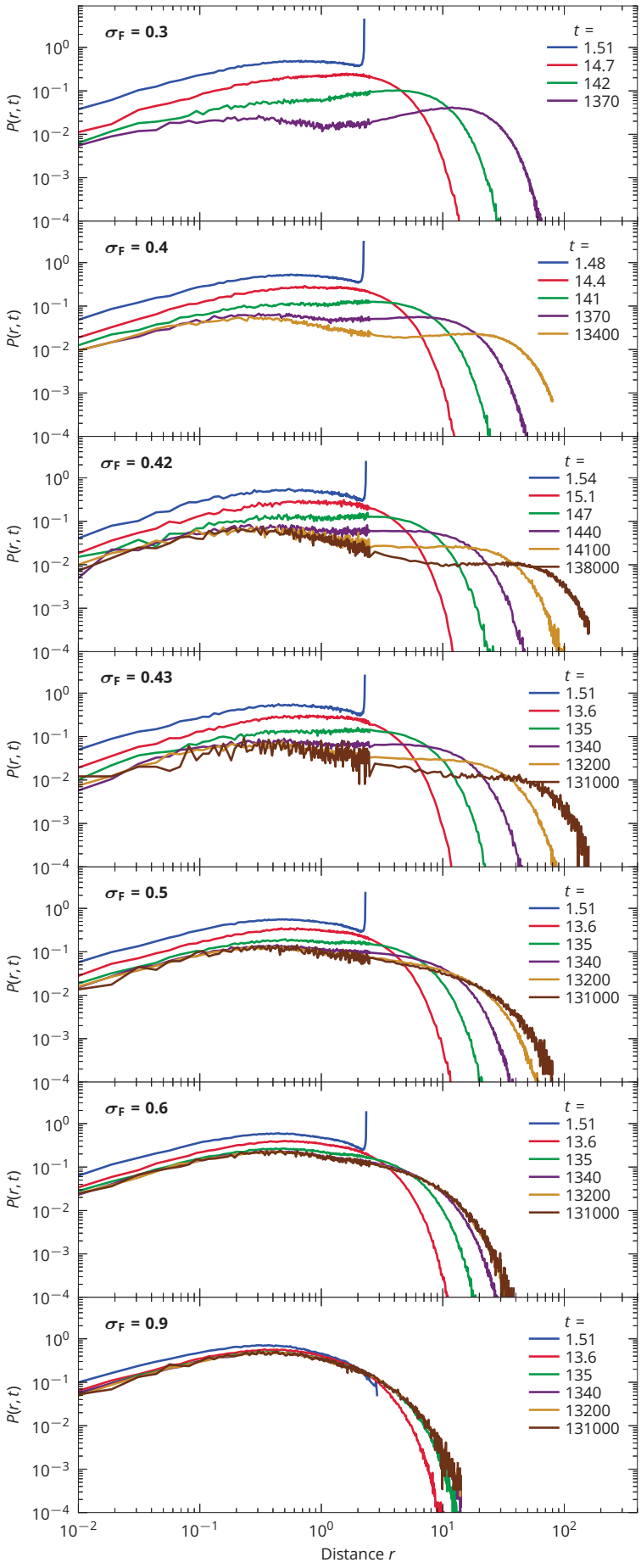

Figure 2.14: Plot of van-Hove function $P(r,t)$ for a range of tracer diameters $\sigma_F = 0.3, 0.4, 0.42, 0.43, 0.5, 0.6$, and 0.9. $P(r,t)$ is shown as a function of distance r for a range of times t as indicated in the legends. The apparent divergence of the van-Hove function at time $t = 1.51$ is an artifact of the single-energy system and is explained in the text. It has no consequences on the long-time dynamics and vanishes once the tracers have performed the first collision with an obstacle.

can be seen in the complete overlap of the curves for $t = 13200$ and $t = 131000$. For $\sigma_F = 0.9$ this happens even earlier, $P(r,t)$ is nearly unmodified for $t > 135$.

Scaling of the van-Hove function As already discussed in the previous chapter, the van-Hove function in the Lorentz model fulfills a scaling form of time and space. For the all-cluster scaling, a scaling form has been conjectured but not yet tested in detail in simulations. The conjectured form, as presented in eq. (1.17), reads

$$P(r,t) = \xi^{d_f-2d}\mathcal{P}_{\pm}(r/\xi, t\xi^{-d_w}).$$

From this form the scaling of the MSD presented above has been derived. Because the scaling of the MSD near the critical point was not entirely successful there is no reason to expect that the scaling should work better for the van-Hove function. It is however worthwhile to test the scaling of the van-Hove function directly at the critical point. As was pointed out in section 1.2.2, the scaling form then reduces to

$$P(r,t) = r^{d_f-2d}\tilde{\mathcal{P}}(rt^{-1/d_w}),$$

This scaling form assumes that the van-Hove function is defined and normalized according to the volume/area integral $\int_{\mathbb{R}^d} P(r,t)\mathrm{d}^d r \stackrel{!}{=} 1$. Here, the van-Hove function is defined and normalized in respect to the one-dimensional integral $\int_0^\infty P(r,t)\mathrm{d}r \stackrel{!}{=} 1$ and thus incorporates an additional r^{d-1}-factor into $P(r,t)$. To account for this, the scaling relation must then read

$$P(r,t) = r^{d_f-d-1}\tilde{\mathcal{P}}(rt^{-1/d_w}). \tag{2.9}$$

In fig. 2.15 this critical all-cluster scaling is applied to all the data. Collapse is found for the diameter range $\sigma_F \in [0.4, 0.43]$, where the critical point is located. For these σ_F, data spanning 4 decades in time — during which the peak of the distribution is shifted by 2 decades in space — nearly completely collapse onto one master curve. One of the unsolved issues in the study of the all-cluster scaling of the van-Hove function is the behavior of the scaling function $\tilde{\mathcal{P}}(x)$ for $x \ll 1$. The data at $\sigma_F = 0.42$ and 0.43 seem to indicate that the master curve tends to a constant for small rt^{-1/d_w}, i.e. $\tilde{\mathcal{P}}(x \to 0) \to const$, but without a theoretical argument behind this the quality of the data is too poor to make a conclusion.

Even though the intermediate scattering function encodes the same information as the van-Hove function it is worthwhile to discuss a few aspects of it, since it is especially sensitive to the presence of localized particles.

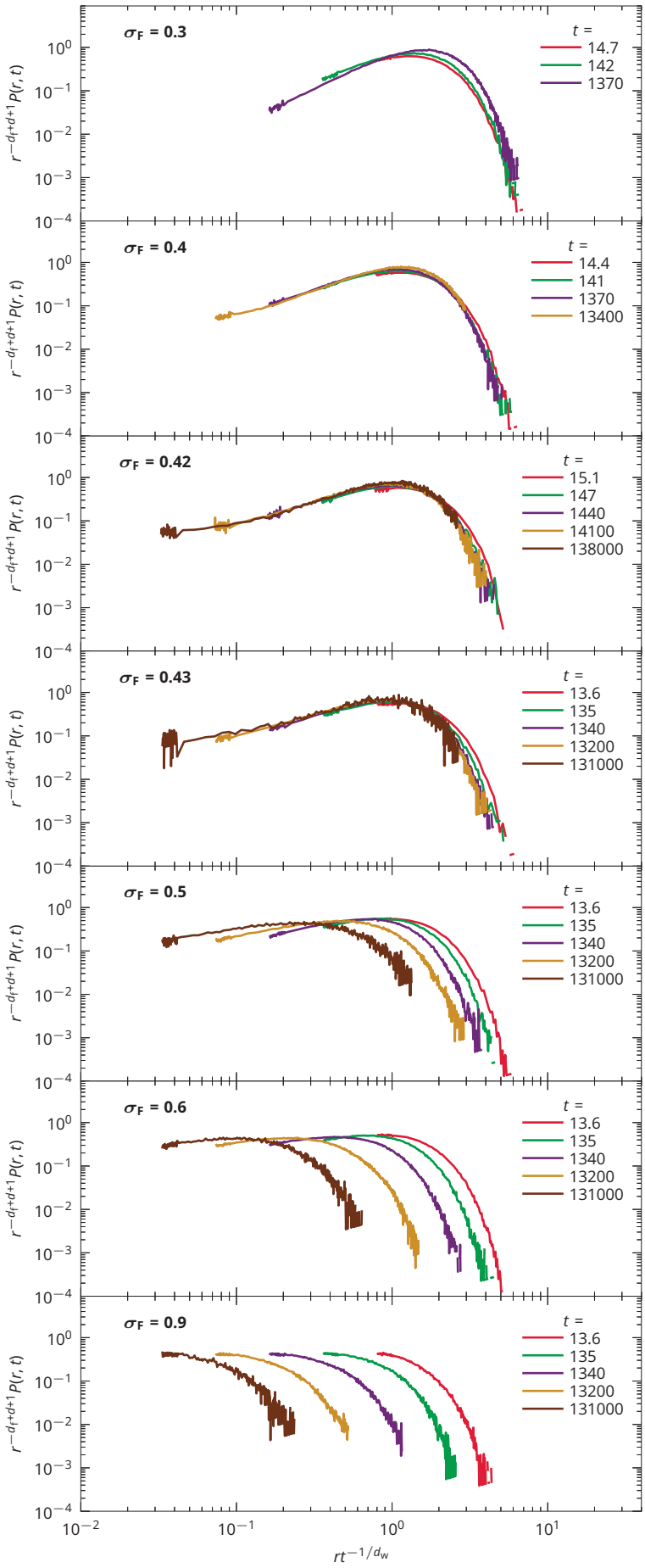

Figure 2.15: Plot of the rescaled van-Hove function, assuming the scaling of the all-cluster average at the critical point, as outlined in the text and eq. (2.9).

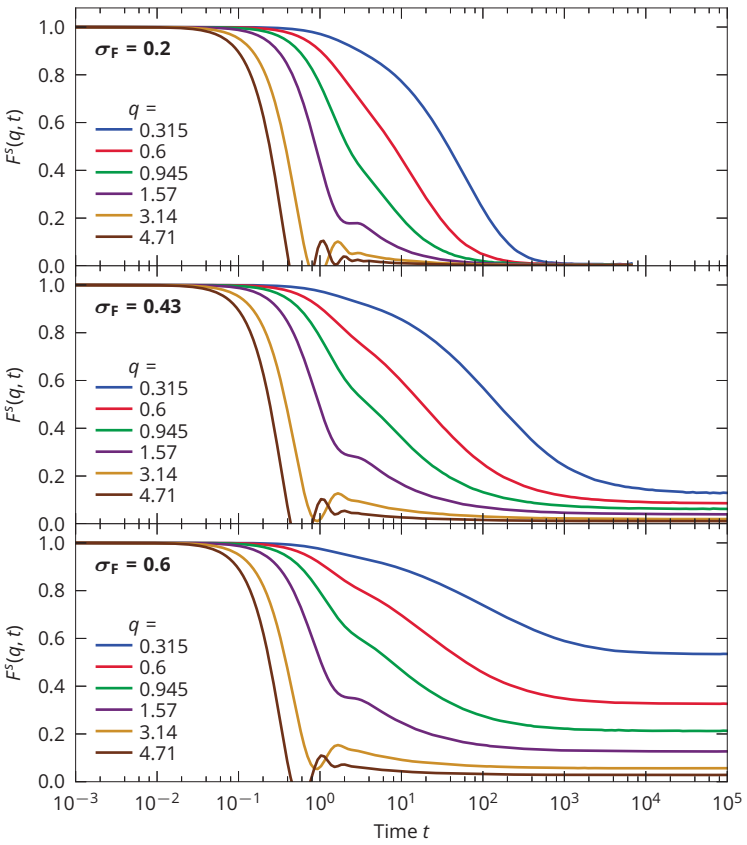

Figure 2.16: Semilogarithmic plot of the self-part of the intermediate scattering function as function of time for a range of q of a delocalized state at $\sigma_F = 0.2$ *(top)*, the critical state at 0.43 *(middle)* and a localized state at 0.6 *(bottom)*.

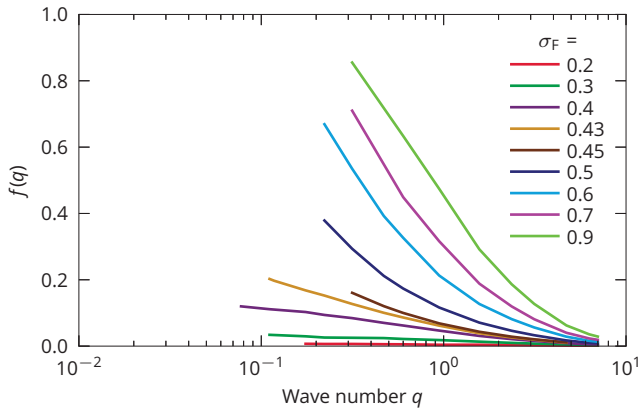

Figure 2.17: Semilogarithmic plot of the non-ergodicity parameter $f(q)$ as a function of the wavenumber q for the whole studied range of particle diameters σ_F.

Intermediate scattering function As the Fourier transform of the self-part of the van-Hove function, the self-part of the intermediate scattering function does not contain additional information. But it strongly exposes localized particles in its long-time limit, the non-ergodicity paremater $f(q)$, which measures the fraction of particles trapped on the length scale $2\pi/q$. Since the ISF is calculated in the all-cluster average, there will always be contributions from particles trapped in small void pockets, and $f(q) > 0$ for all finite σ_F. In fig. 2.16, the ISF is presented for three exemplary systems, for a delocalized state at $\sigma_F = 0.2$ *(top)*, the critical state at 0.43 *(middle)* and a localized state at 0.6 *(bottom)*. All states have — apart from an increase in the long-time limit —

qualitatively the same ISF. The shape of the curves is also very similar to data obtained on the percolating cluster, see fig. 1.5. The general increase of $f(q)$ with σ_F can be seen in fig. 2.17.

The generic presence of a finite long-time limit makes it more involved to determine the localization transition from the intermediate scattering function alone and no predictions for the scaling of the ISF in the full system exist. However, a scaling has been suggested for $f(q)$ in the approach to the critical point, see eq. (1.20) and corresponding discussion, which can be tested. The system size was not large enough to extrapolate $f(q)$ in the limit $q \to 0$ and therefore the expected divergence $f(q = 0) \sim |\varepsilon|^\beta$ in the approach to the transition, see eq. (1.18), could not be tested. But the behavior of $f(q)$ at the critical point with $1 - f(q) \sim q^{d-d_f}$, as described by eq. (1.19), could be tested. In a double-logarithmic plot in fig. 2.18, $1 - f(q)$ is plotted as a function of q at the critical point, $\sigma_F = 0.43$. For comparison, the critical scaling prediction is shown as a black line with the amplitude roughly matched to the data. The prediction is expected to hold for $q \to 0$ so it is not surprising that the data does not match the asymptote for large q. At low q, the non-ergodicity parameter seems to approach the asymptote, but unfortunately the data do not extend to low enough wavenumbers to be entirely sure. Still, the data does not contradict the prediction.

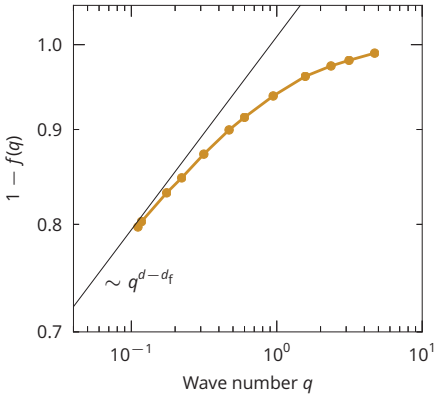

Figure 2.18: Double-logarithmic plot of the non-ergodicity parameter $f(q)$ at $\sigma_F = 0.43$ (at the critical point) as a function of the wavenumber q. It is plotted as $1 - f(q)$ for comparison to the critical asymptote $1 - f(q) \sim q^{d-df}$ (black line).

Velocity autocorrelation function Another opportunity to test scaling predictions is the velocity autocorrelation function (VACF). In simulations of the lattice Lorentz model, the velocity autocorrelation function $Z(t)$,

$$Z(t) := \frac{1}{d}\langle \vec{v}(0)\vec{v}(t)\rangle = \frac{1}{2d}\frac{\mathrm{d}^2\delta r^2(t)}{\mathrm{d}t^2}, \tag{2.10}$$

shows a long-time tail $Z(t) \sim t^{-(d+2)/2}$ for small densities away from the critical point (Lowe et al., 1997). This tail has also been derived for Newtonian dynamics (Ernst and Weyland, 1971). In two dimensions this amounts to $Z(t) \sim -t^{-2}$, which would correspond to a logarithmic contribution to the MSD. Additionally, from the critical behavior of the MSD a different power-law dependence is inherited close to the critical point, $Z(t) \sim t^{2/z-2}$.

The long-time tails of the VACF have been studied in detail also in the 2d Lorentz model for Brownian dynamics, and a crossover from the hydrodynamic t^{-2} to the critical $t^{2/z-2}$-law is found as density is varied (Bauer et al., 2010). For all close-to-critical systems, the VACF first follows the critical asymptote but eventually goes to $Z(t) \sim t^{-2}$. The timescale associated with that cross over diverges at the critical point. This confirms the universality of the t^{-2} power law.

In fig. 2.19 *(left)*, the VACF calculated from the MSD is displayed for tracer diameters σ_F on the delocalized side of the transition. The VACF becomes negative after time $t \approx 1$ and then tends to 0. The final decay to 0 is displayed magnified in the inset. This exposes the strong noise present in the data, which even leads to positive values at some times $t \gtrsim 10$. Still, it might be fruitful to check the final decay for the presence of the two described power laws. For this, $-Z(t)$ is plotted in double-logarithmic presentation in fig. 2.19 *(right)*. The noise becomes even more visible in this plot and wherever the VACF becomes positive, it leads to an interruption of the plotted lines. Even with

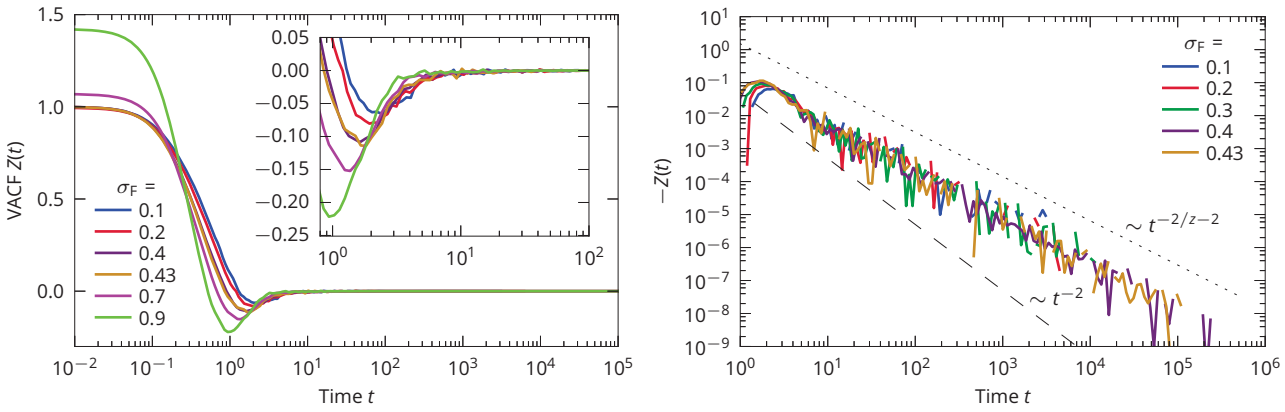

Figure 2.19: *Left:* Velocity autocorrelation function for a range of tracer diameters σ_F as indicated in the legend in a linear-log plot. *Inset:* Enlarged view of the same data, emphasizing the final decay to 0. *Right:* Double-logarithmic plot of $-Z(t)$ as a function of time t. Hydrodynamic asymptote $\sim t^{-2}$ (dashed line) and critical asymptote $\sim t^{2/3.036-2}$ (dotted line) are drawn into the figure to guide the eye.

the poor quality of the data the VACF clearly follows the critical asymptote $Z(t) \sim -t^{2/z-2}$ for all the shown σ_F, again in agreement with the Lorentz model behavior. The $Z(t) \sim -t^{-2}$ is never observed. This is due to the fact, that none of the systems were simulated in the dilute limit, as the matrix always has the same, relatively high density. It is interesting that systems far from the critical point show the critical power-law in the VACF but not in the MSD. The former has simply lost the diffusive part of the latter due to the application of the derivative and thus exposes the critical power-law at earlier times and smaller σ_F. To observe the crossover to the $-t^{-2}$ power law and to get rid of the noise, longer simulations runs with better statistics would be required. Still, the obtained results are once more in line with what to expect from the Lorentz model.

This concludes the discussion of the dynamics in the soft-sphere Lorentz model. A range of scaling properties of the Lorentz model were confirmed to apply to the soft-sphere system discussed here. In the next section, a mapping of the soft-sphere onto a hard-sphere system will be discussed. With this it is possible to calculate the effective hard-sphere critical density and compare it to the known value of the hard-sphere Lorentz model.

2.3 *Mapping a soft-sphere onto a hard-sphere system*

With a simple argument, the soft-sphere Lorentz model may be mapped onto the hard-sphere Lorentz model, provided the tracer always has the same energy. The following argument expands on a calculation by Felix Höfling (private communications).

The localization transition of the tracers coincides with the percolation transition of the available void space. To correctly map a soft-sphere Lorentz model onto a hard-sphere Lorentz model it is therefore most important to map the topology of the void space correctly: open channels in the void space must stay open under the mapping and closed ones stay closed.

A conventional mapping from soft onto hard spheres would be the Barker-Henderson mapping (Barker and Henderson, 1967; Hansen and McDonald, 2006), which averages over the whole potential distribution to obtain an effective diameter. In general, such a mapping doesn't guarantee that the topology of the void space remain unchanged under the mapping.

Here, the conservation of the topology is accomplished with a mapping onto hard-sphere obstacles with point-like tracers. In this mapping, the effective hard-sphere diameter of the obstacles $\sigma_{\mathrm{hs}}(\sigma_{\mathrm{F}}, E)$ is calculated as the distance between two obstacles forming a channel through which a tracer with a diameter σ_{F} and energy E is barely able to pass.

In two dimensions, a channel which connects two pockets is almost always defined by two obstacles, see fig. 2.20 for an illustration of the situation. A tracer which is placed directly in the middle between two obstacles which are placed at a distance $\sigma_{\mathrm{hs}} := 2r$ has at least the total potential energy U (see eq. (2.1))

$$U = 2V_{\mathrm{MF}}(r) = 2\left(4\varepsilon_{\mathrm{MF}}\left(\left(\frac{2\sigma_{\mathrm{MF}}}{\sigma_{\mathrm{hs}}}\right)^{12} - \left(\frac{2\sigma_{\mathrm{MF}}}{\sigma_{\mathrm{hs}}}\right)^{6}\right) + \varepsilon_{\mathrm{MF}}\right)\Psi\left(\frac{\sigma_{\mathrm{hs}}}{2}\right),$$

with $\sigma_{\mathrm{MF}} = (\sigma_{\mathrm{M}} + \sigma_{\mathrm{F}})/2$. In the following $\Psi(r)$ will be neglected. The tracer is then just about unable to pass the gap if that potential energy equals its total energy, [2]

$$\begin{aligned} E &\stackrel{!}{=} 8\varepsilon_{\mathrm{MF}}\left(\left(\frac{2\sigma_{\mathrm{MF}}}{\sigma_{\mathrm{hs}}}\right)^{12} - \left(\frac{2\sigma_{\mathrm{MF}}}{\sigma_{\mathrm{hs}}}\right)^{6}\right) + 2\varepsilon_{\mathrm{MF}} \\ \Rightarrow \sigma_{\mathrm{hs}} &= 2\left(\frac{1}{2} + \sqrt{\frac{E}{8\varepsilon_{\mathrm{MF}}}}\right)^{-1/6}\sigma_{\mathrm{MF}}. \end{aligned} \tag{2.11}$$

This is the same situation as for a point-like tracer encountering hard-sphere obstacles with diameters of the same size as the distance between the obstacles. The described situations is therefore equivalent to a system of a point-sized tracer and hard-sphere obstacles with diameter σ_{hs}. Equation (2.11) thus provides a mapping from the soft-potential system with tracer energy E and tracer diameter σ_{F} onto a hard-sphere matrix with diameter σ_{hs} and point-like tracers.

In fig. 2.20, the area available to the soft-sphere tracers lies outside the black equipotential line where the tracers energy equals its potential energy, $U = E$. After the mapping, the point-like tracer is assumed to be able to access the area outside the two red circles marking the hard-sphere obstacles. The resulting difference in available area will be shown to be negligible for the dynamics. The same holds for modifications to the mapping from channels formed by three or more obstacles.

The eq. (2.11) implies the hard-sphere diameter can be used as the only control parameter, i.e. that two systems with the same σ_{hs} would have the same dynamics. That this is true will be confirmed in the discussion of the confined ideal gas, in section 3.4. Even before showing that dynamics are correctly mapped it is important to repeat that, since the mapping respects the topology of the matrix, the percolation point $\sigma_{\mathrm{F}}^{\mathrm{c}}$ is necessarily mapped onto the percolation point $\sigma_{\mathrm{hs}}^{\mathrm{c}}$ correctly. Therefore, a percolating system will stay percolating under the mapping and a localized system will stay localized.

The mapping furthermore shows why it is relevant to set all tracer particles to exactly the same energy to preserve a sharply-defined localization transition in the system. Eq. (2.11) has been used to calculate the hard-sphere diameter of the obstacles for displaying the matrix in figs. 2.3 and 2.5.

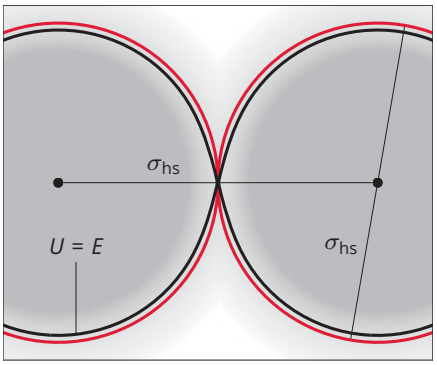

Figure 2.20: Sketch of two obstacles at the distance where the channel between them vanishes for a tracer with diameter σ_{F} and energy E. The obstacle centers are shown as points. The height of the total potential energy U — which is a function of σ_{F} — at each point of the sketch is given in gray scale. The equipotential line where the potential energy U exactly matches the particle energy E is shown in black and encloses the area unavailable to the tracer. The effective hard-sphere diameter then corresponds to the obstacles marked in red.

[2] This result is obtained by substituting with $\rho := (2\sigma_{\mathrm{MF}}/\sigma_{\mathrm{hs}})^6$, solving the resulting quadratic equation, $E = 8\varepsilon(\rho^2 - \rho) + 2\varepsilon$, and picking the solution which obeys $\rho \leq 1/2$ (the cutoff condition of the WCA potential), $\rho = 1/2 + \sqrt{E/(8\varepsilon)}$.

With the hard-sphere mapping, the critical hard-sphere density of the present system can be readily calculated. The reduced obstacle density in the hard-sphere mapping, n^*_{hs} can then be expressed in the following way

$$n^*_{\mathrm{hs}} := n_{\mathrm{M}} \frac{\sigma^2_{\mathrm{hs}}}{4} = n_{\mathrm{M}} \left(\frac{1}{2} + \sqrt{\frac{E}{8\varepsilon_{\mathrm{MF}}}} \right)^{-1/3} \sigma^2_{\mathrm{MF}},$$

with $n_{\mathrm{M}} := N_{\mathrm{M}}/L^2$ denoting the number density of obstacles. For the soft-sphere, single-energy Lorentz model covered here, critical behavior was observed at $\sigma^{\mathrm{c}}_{\mathrm{F}} = 0.435$, i.e. at $\sigma^{\mathrm{c}}_{\mathrm{MF}} = (\sigma_{\mathrm{M}} + \sigma^{\mathrm{c}}_{\mathrm{F}})/2 \approx 0.718$, at obstacle density $0.625\sigma_{\mathrm{M}}^{-2}$, at energy $E \approx 1.143$ and with energy scale $\varepsilon_{\mathrm{MF}} = 0.1$. This then gives the critical hard-sphere diameter $\sigma^{\mathrm{c}}_{\mathrm{hs}} \approx 1.31$ and the critical reduced obstacle density $(n^*_{\mathrm{hs}})^{\mathrm{c}} \approx 0.270$. This result is confirmed by the independent calculation of the percolation threshold for the used matrix configurations for hard-spheres by Markus Spanner via Voronoi tesselation of the void space (private communications with Spanner, 2014). He obtained the critical diameter $\sigma^{\mathrm{c}}_{\mathrm{hs}} = 1.31 \pm 0.01$ and thus a critical reduced obstacle density $(n^*_{\mathrm{hs}})^{\mathrm{c}} = 0.270 \pm 0.005$, in complete agreement with the hard-sphere mapped result.[3] This is proof of the validity of the hard-sphere mapping.

The critical density found here is lower than in the two-dimensional hard-sphere Lorentz model, which has critical density $(n^*_{\mathrm{hs}})^{\mathrm{c}} = 0.359$ (Bauer et al., 2010). This relation is expected, since in the former case the obstacles are correlated and fill space more effectively. The same tendency is found in other Lorentz models with correlated obstacles, e.g. for obstacles with hard-cores which are not allowed to overlap (Spanner, 2010).

[3] The Voronoi tesselation of the obstacle positions allows construction of the percolation network, as was shortly outlined in section 1.2.1. For each of the 100 matrix configurations, the density upon which the network stops percolating the system was determined. Due to their finite size, each system has a different percolation density. Here, the average of these percolation densities is reported, while the error margin is given by their standard deviation.

2.4 *Summary*

In this chapter it has been shown that the presented system — weakly correlated obstacles, interacting with single-energy, non-interacting tracers via the WCA interaction potential — is a realization of the Lorentz model. Upon variation of the tracer particle diameter σ_{F} the system undergoes a transition from delocalization to localization with the expected power-law-like anomalous diffusion occuring in the MSD at a critical point in-between. The long-time diffusion found on the delocalized side becomes suppressed in approaching the transition, vanishing with the expected power-law. Further scaling properties like the collapse of the MSD and the van-Hove function onto master curves close to and at the transition were found to be compatible with the data.

A mapping of the system onto an equivalent hard-sphere system was achieved which conserves the topology of the matrix structure. In this way, it was revealed that the energy of the tracers is an implicit control parameter and that the energy of the tracers must necessarily be the same for the system to be mappable onto a single hard-sphere density. The effective hard-sphere critical density — calculated from the tracer energy and the tracer diameter — agreed with the percolation threshold determined from a Voronoi tesselation.

Before discussing the implications of introducing an ideal gas into the matrix, the treatment of finite size effects will be briefly discussed.

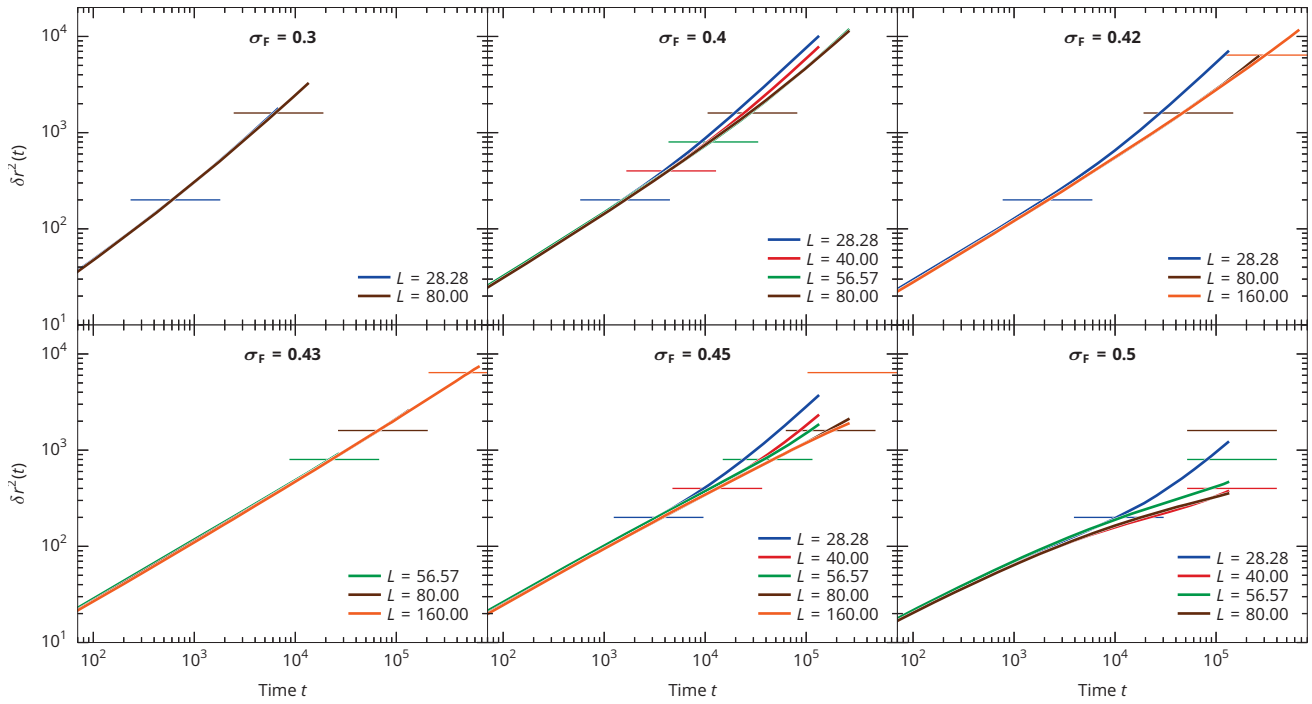

Figure 2.21: Mean-squared displacements for a range of tracer diameters σ_F as indicated in the titles. For each diameter, the simulation box length L was varied as indicated in the legends. The barrier $(L/2)^2$ up to which the MSD typically is without finite size effects has been drawn in as horizontal lines for all L, colors as indicated in the legends.

2.5 *Finite-size scaling*

Because the localization transition of the Lorentz model is a critical dynamical phenomenon with a divergent correlation length ξ, the observed dynamics will be greatly modified in cases where ξ is of the order of the box size L of the simulation. It is therefore very important to make sure that the obtained results are independent of the employed system size. The simplest way of making sure of that is to calculate the same quantities for a range of increasing simulation sizes. When the results are the same for two different box sizes, then they are without finite size effects.

The MSD is one of the quantities which are the most sensitive to finite size effects and therefore very suitable for an analysis of finite-size scaling. Near the localization transition, the MSD will be subdiffusive as long as the tracers have not explored distances comparable to the localization length l, i.e. as long as $\delta r^2(t) \ll l^2$ holds. If the system size is smaller than the localization length, the MSD will become diffusive too soon, namely as soon as particles have traversed distances comparable to the system size. As a rule of thumb, the MSD will become diffusive once it crosses the barrier $\delta r^2(t) \approx (L/2)^2$. This rule of thumb will be tested and confirmed in the following.

The MSD was calculated for a wide range of diameters σ_F and a range of box sizes L and is shown in fig. 2.21, grouped according to σ_F. The barrier $(L/2)^2$ is drawn into the plots as horizontal lines crossing the MSD. Both the MSD and the barriers are colored corresponding to L as indicated in the legends.

For low $\sigma_F = 0.3$ — far away from the critical point — the MSD very early on exceeds $(L/2)^2$ in the case of $L = 28.28$. If the correlation length exceeded the system size, $\xi \geq L$, here, then the dynamics would be drastically different when simulating at $L = 80$. This is not the case, which indicates that the correlation length must be far smaller than the linear size of the simulation box, $\xi \ll 28.28$

and that the observed dynamics at $\sigma_F = 0.3$ are free of finite size effects.

Closer to the critical point, ξ and with it l increases, and the MSD becomes more strongly dependent on the box size. Indeed, for $\sigma_F = 0.4$, the MSD only becomes independent of the box size for $L > 56.57$. But the MSD for different L agree always with each other, as long as none of the MSD have crossed their corresponding barrier $(L/2)^2$. It also becomes clear here, that that the MSD is often free of finite-size effects even if it has already crossed $(L/2)^2$.

At $\sigma_F = 0.42$, there is a slight modification of the dynamics even between $L = 80$ and 160. But the variation is so small that the results obtained in the $L = 160$ system can be assumed to be correct in these cases. Note also that $(L/2)^2$ for $L = 160$ is crossed by the MSD only at the very end of the simulation.

The simulation at $\sigma_F = 0.43$ does not show finite size effects at all because the simulations at $L = 56.57$ and $L = 80$ were not run long enough for the finite size effects to occur. This would be potentially problematic were it not clear that the rule of thumb holds here and that the system at $L = 160$ only very slightly exceeds $(L/2)^2$.

At $\sigma_F = 0.45$, finite size effects are again very pronounced and simulation at $L = 160$ is necessary.

At $\sigma_F = 0.5$, the system is again far from the localization transition and smaller system sizes suffice. While at $L = 40$, a small upturn in the MSD might be taken as the onset of diffusion, the MSD definitely converges to the size-independent result at $L = 56.57$. The variation between the results at $L = 56.57$ and $L = 80$ can be attributed to poorer sampling of the void space, which becomes considerably more difficult to do on the localized side. The MSD does not approach the barrier $(L/2)^2$ for $L \geq 56.57$.

For systems with even higher σ_F, the correlation length can be expected to have even more decreased and it is therefore sufficient to simulate them at $L = 40$. In conclusion, the barrier $(L/2)^2$ below which the MSD stays without finite-size effects is found to hold generally. Therefore, if one wants to simulate up to times $t = 10^6$ in this system, it is safe to use $L = 160$. Far from the critical point, much smaller system sizes are also unproblematic.

Extrapolating diffusion coefficients close to the critical point As the above analysis of the finite size effects in the MSDs shows, finite size effects lead to an overestimation of the diffusion coefficient. But for systems close to the localization transition, where it is difficult to simulate for long enough times and in large enough systems to calculate the correct diffusion coefficient, the scaling of the diffusion coefficient with the system size can be used to extrapolate to a lower bound for D.

At the critical point, where the localization length ξ diverges, D vanishes with $D \sim L^{-\mu/\nu}$ with $\mu = 1.31$ and $\nu = 4/3$. Slightly away from the critical point, at a distance ε, the same relationship holds for small system sizes but D converges to its true finite value as soon as $L \gg \xi$ (Höfling et al., 2008),

$$D(\varepsilon, L) \sim \begin{cases} L^{-\mu/\nu}, & \text{for } L \ll \xi, \\ (-\varepsilon)^{\mu}, & \text{for } L \gg \xi \text{ and } \varepsilon \to 0. \end{cases} \tag{2.12}$$

Regardless of the exact scaling function, the following ad-hoc fit function should approximately apply in the scaling regime but represent a true lower

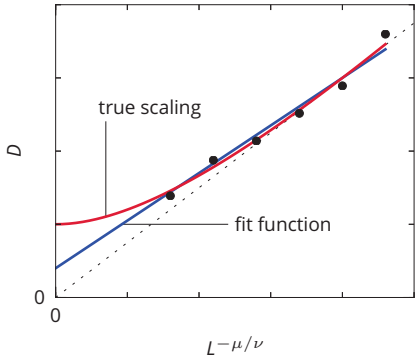

Figure 2.22: Schematic of the behavior of D as a function of the system size. Dots represent data points obtained from simulations (not actually simulated for this figure) plotted as a function of $L^{-\mu/\nu}$. The true scaling (red line) is some unknown function fulfilling eq. (2.12). The ad-hoc fit from eq. (2.13) (blue line) provides a lower bound for D at $L^{-\mu/\nu} = 0$. The dotted line gives the finite size scaling at $L \ll \xi$.

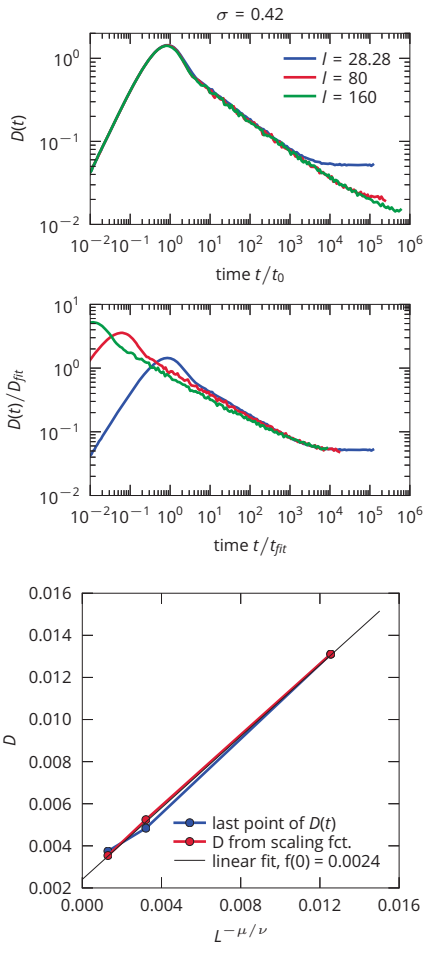

Figure 2.23: *Top:* Time-dependent diffusion coefficient $D(t)$ for a range of simulation box sizes L as indicated in the legend. *Middle:* Same data rescaled to scaling function describing the final decay on to the long-time limit. *Bottom:* Last simulated values of $D(t)$ and corrected values from the scaling approach as a function of rescaled box length L.

bound D_{lower} in the $L \to \infty$ limit,

$$D = aL^{-\mu/\nu} + D_{\text{lower}}, \tag{2.13}$$

with some constant a. Fitting this function to the diffusion coefficient D as a function of $L^{-\mu/\nu}$ for a range of simulations with different L, one then obtains D_{lower} as a true lower bound for D. For a schematic of this, see fig. 2.22.

The extrapolation procedure is demonstrated here at $\sigma_{\text{F}} = 0.42$. The system was simulated at three system sizes $L = 28.28$, 80, and 160, for which the time-dependent diffusion coefficient $D(t) = \mathrm{d}\delta r^2(t)/\mathrm{d}t$ is shown in fig. 2.23 *(top)*. For $L = 28.28$, the long-time diffusion coefficient can be directly read off. For the two larger system sizes, $D(t)$ has not quite converged to its respective long-time limit. But, the decay towards the long-time limit follows a scaling function and so the long-time limits can be extrapolated from scaling $D(t)$ for the three system sizes on top of each other, see fig. 2.23 *(middle)*. In a last step, the D that were obtained from that extrapolation are plotted as a function of the expected scaling $L^{-\mu/\nu}$ and fitted with eq. (2.13), see fig. 2.23 *(bottom)*. In this way, one obtains $D_{\text{lower}} = 0.0024$. An upper bound to the diffusion coefficient can be obtained from the last obtained value of $D(t)$ at the largest simulated system size, thus $D < 0.0047$.

These two bounds are used to display the diffusion coefficient at $\sigma_{\text{F}} = 0.42$ in fig. 2.7 as a vertical bar. Additionally, the same procedure is used in the following sections in figs. 3.5 and 4.16 whenever a direct measurement of a D free of finite size effects was not possible.

3
An ideal gas in a porous medium

The simplest generalization of the Lorentz model discussed in the previous section is achieved by assigning a Maxwell-Boltzmann distribution the the velocities of the tracers, turning them into an ideal gas confined in a porous medium. This is the logical next step towards a realistic heterogeneous medium containing a fully interacting fluid component. The introduction of an energy distribution has implications for the dynamics of the system close to the localization transition which will be discussed in the following.

As previously described, the barriers between void pockets in the system are finite if the interaction potential is soft. Tracer particles with different energies then explore the matrix with the obstacles having different effective hard-sphere diameters, as calculated in section 2.3. Particles with a high enough energy are delocalized, while particles with low energies are localized. Thus, the wide distribution of particle energies found in a typical system leads to an averaging of the dynamics over a wide distribution of particle states, from delocalized to localized. It will be demonstrated that this averaging of the dynamics rounds the localization transition, in the sense that a sharp point where all particles become localized does not exist. The MSD will be diffusive, as long as a few particles have a high-enough energy to be delocalized, even when most of the particles are localized. The rounding of the transition destroys the scaling properties of the system, for instance the critical anomalous exponent of the MSD cannot be observed anymore. Instead a wide range of effective exponents are found which are a result of the underlying energy averaging.

The mapping of soft-sphere diameters onto hard-sphere diameters as discussed in the previous section is used to analytically express the energy averaging present in the confined-ideal-gas. For instance, when the MSD is calculated as a function of tracer energy as well as the tracer diameter, then the hard-sphere mapping leads to complete agreement with the single-energy data and scaling predictions are again fulfilled.

In contrast to the MSD — which is dominated by the mobile particles — the behavior of the ISF is dominated by the localized particles. Because of this, the ISF generically obtains a larger long-time limit compared to the single-energy case, as the energy distribution causes more particles to be localized at a given σ_F. In a way, the dynamics of the confined-ideal gas is therefore more heterogeneous than that in the single-energy case.

3.1 *Preparation of the confined ideal gas*

The confined ideal gas differs from the system discussed in chapter 2 in only one aspect: instead of a single energy, the mobile component possesses a wide energy distribution. Three different insertion methods were tried out and found to lead to the same distribution of energies and the same dynamics:

1. *Naïve insertion:* For each particle an insertion position was randomly picked and was inserted at that position if it was far enough from neighboring particles according to an ad hoc minimum distance: It was required that the distance to the nearest obstacle may not be smaller than $0.65\sigma_{\mathrm{M}}$ and to the nearest tracer may not be smaller than $0.2\sigma_{\mathrm{M}}$. Especially the latter condition is unphysical, which is why this criterion was eventually discarded.

2. *Boltzmann-weighted insertion:* an insertion position for a tracer particle was randomly picked. Then the potential energy U of the particle at that position was calculated and the particle insertion was accepted with probability $\min[1, \exp(-\beta U)]$.

3. *Grand-canonical Monte Carlo insertion:* the particle configurations were generated in a grand-canonical Monte Carlo simulation by taking snapshots of the system when the system had been simulated for long enough and the number of particles was as needed. For details, see appendix A.

Detailed comparison between the insertion methods is made in appendix A, where the three methods are found to lead to the same dynamics. The bulk of the discussed data was calculated for systems created with criterion 1, which was replaced by criterion 2 and 3 for the most recent data. Typically between 100 and 1000 particles were inserted into each of 100 matrix configurations. To allow for comparison to the single-energy case the average particle energy in the systems was kept the same, with the same temperature $k_{\mathrm{B}}T = 1$. The particles were equilibrated at that temperature for at least 10^5 steps with a simplified version of the Andersen thermostat (Andersen, 1980) by randomly selecting their velocities from the Maxwell distribution every 100 steps. Since the equilibration is performed in the canonical ensemble the total energy of the individual systems fluctuate around an average energy. For the microcanonic production runs, the systems were brought to the same total energy by rescaling all tracer velocities in a given system with the same constant, leaving the relative distribution of energies unchanged.

It should be noted that at very large diameters the energies of the individual systems often deviate strongly from the average energy and bringing the systems to the same energy changes their kinetic energy strongly. This occurred at $\sigma_{\mathrm{F}} = 0.9$, where the temperature became shifted to $\mathrm{k_B}T \approx 1.42$ as a result. This has no qualitative effect but has to be considered quantitatively in a few places in the analysis.

Energy distribution of the gas of tracers The energy of a single fluid particle with position $\vec{r}$ and velocity $\vec{v}$ interacting only with the matrix particles is given by

$$E_1(r, v) := \frac{1}{2}m\vec{v}^2 + \sum_{j \in I_{\mathrm{M}}} V_{\mathrm{MF}}(|\vec{r} - \vec{r}_j|).$$

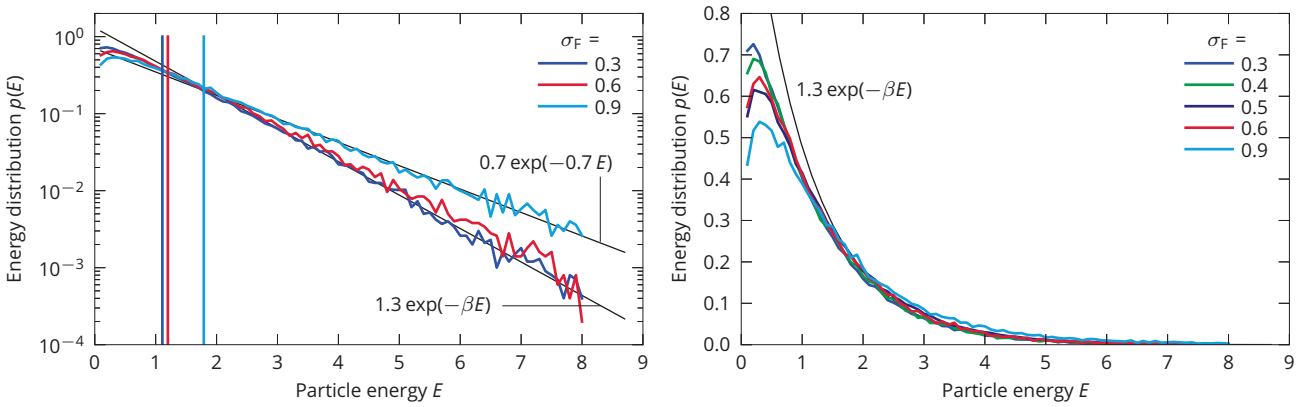

Figure 3.1: *Left:* Energy distribution $p(E)$ of the confined ideal gas for the particle diameters $\sigma_F = 0.3, 0.6, 0.9$. Average energies of these systems are shown as vertical lines in corresponding colors. Exponential asymptotes for large E shown as black line. *Right:* The same distribution for a greater number of σ_F in a linear plot with the same exponential asymptote as black line.

The probability density of a single particle having the energy E is then defined as the integral over phase space available to it at the given energy,

$$p(E) := \langle \delta(E_1(r, v) - E) \rangle. \tag{3.1}$$

To calculate the particle energy distribution $p(E)$ numerically, the tracer energies were evaluated at the beginning of the simulation run and were grouped into either 80 or 120 bins with a width of $\Delta E = 0.1$ each. Each bin is denoted by its upper bounding energy. Tracers with energies larger than the largest represented bin were ignored. This typically amounted to ignoring less than 0.1% of the particles. The histogram was then averaged over all realizations and normalized by dividing by the total number of tracer particles N_F per realization and by the bin width ΔE, resulting in $p(E)$. The smallest representable value of $p(E)$ for the simulations was thus $\Delta p = 1/(\text{number of systems} \cdot n_F \cdot \Delta E)$. This typically resulted in $\Delta p = 1/(100 \cdot 1000 \cdot 0.1) = 10^{-4}$.

The resulting particle energy distribution $p(E)$ is shown in fig. 3.1 for a range of diameters σ_F with the average energies of the systems marked as vertical lines in the corresponding colors. In fig. 3.1 *(left)*, the distribution is shown semilogarithmically to expose its exponential behavior at large E. The average energy of the systems, marked by the vertical lines, changes only weakly between $\sigma_F = 0.3$ and 0.6 but is strongly increased at $\sigma_F = 0.9$, partly because of the increase in temperature discussed previously. An exponential function with $\beta = 1/k_B T$ using the temperature $k_B T = 1$ of the system (lower black line) matches the large-E behavior at $\sigma_F = 0.3$ and 0.6. The deviation from the exponential distribution at small energies is caused by the external potential of the obstacles which cuts off the probability distribution. The increased temperature at $\sigma_F = 0.9$ becomes apparent here in the changed slope of the exponential tail which correctly reflects the increased temperature $1/k_B T \approx 0.70$. For a better view of the deviations from the exponential at small energies, $p(E)$ is plotted regularly in fig. 3.1 *(right)* for a greater number of σ_F.

Production runs were obtained in the microcanonical regime, so the energy of each particle was conserved over a single run of the simulation.

Structure of the accessible volume That the confined ideal gas is different from the single-energy case, is immediately apparent from the positional data of a simulation run. In fig. 3.2 *(right)*, all the recorded tracer positions of a single

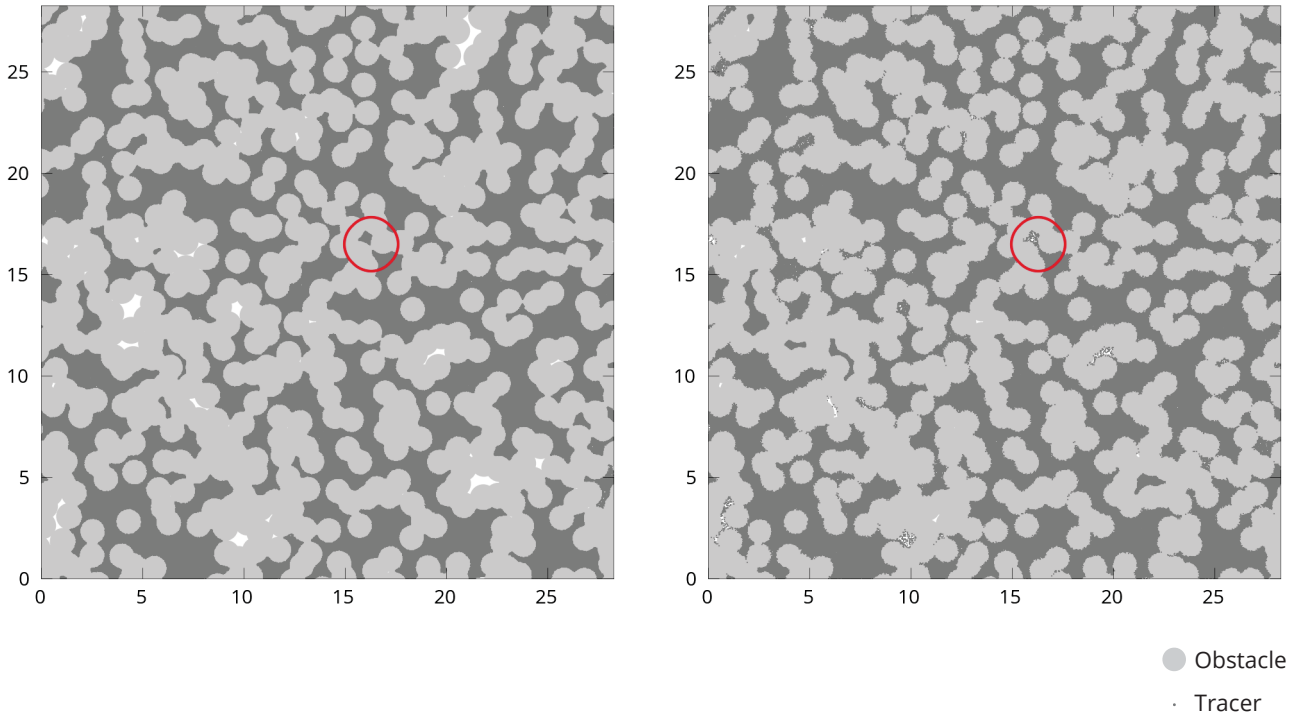

Figure 3.2: *Left:* All the positional data of 500 tracers with $\sigma_F = 0.45$ of a single simulation run in the single-energy case. All the tracer positions which were collected over a whole simulation run are represented as dark grey points. The obstacles are represented as hard-spheres in light grey with the effective hard-sphere radius calculated from eq. (2.11) using the average particle energy. (Replotted from fig. 2.3). *Right:* A confined ideal gas in the same matrix at the same parameters. A red circle marks a channel which is closed in the single-energy case but open in the confined ideal gas.

simulation run are shown as dark grey points. They are superposed over the obstacles, shown as light grey disks with their effective hard-sphere diameter as calculated from the average particle energy, see eq. (2.11). The position data for the single-energy case for the same obstacle matrix was already shown in fig. 2.3 and is replotted here in fig. 3.2 *(left)* for comparison. In the single-energy case the same effective hard-sphere diameter provides a good description of the region unavailable to the tracers. Compared to the single-energy case, the void space in the confined-ideal gas is less clearly defined: Some particles get closer to the obstacles than in the single-energy case and are found to be overlaying the matrix. Compared to the single-energy case, the boundaries of the matrix have become less clearly defined and appear rougher. Pockets of void space that were previously separate have become connected (one example marked by a red circle).

As the fluid particles are not interacting, their structure factor $S_{FF}(q)$ becomes a pure measure of the structural correlations of the void space itself. It is therefore a useful quantity to determine the average changes to the accessible volume brought about by the introduction of an energy spectrum. In fig. 3.3, $S_{FF}(q)$ is shown for the single-energy case (dashed lines) and the confined-ideal gas (solid lines) for a range of σ_F, simulated at the same number density $n_F = 0.625$. In comparison, the structure factors of the confined ideal gas are generally larger than the corresponding ones for the single-energy case.

More useful than $S_{FF}(q)$ would be both the distribution of pore sizes and the connected structure factor which is like the structure factor, only that it correlates only particles which are on the same cluster. This however would require a way of identifying clusters. This is difficult for the single-energy soft-potential Lorentz model, but impossible when each particle has a different energy.

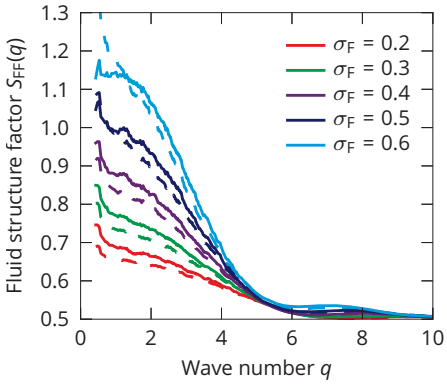

Figure 3.3: Fluid particle structure factor $S_{FF}(q)$ as a function of the wavenumber q for a range of fluid particle diameters σ_F as indicated in the legend. Dashed lines for single-energy system, solid lines for confined ideal gas. *Centered moving average applied.*

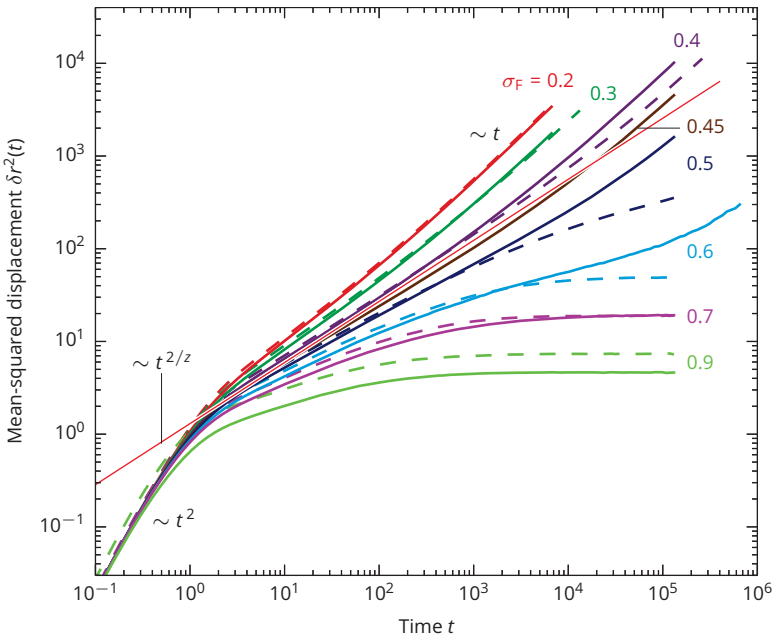

Figure 3.4: Mean-squared displacements for the confined ideal gas for various fluid particle diameters σ_F as indicated in the figure (solid lines). For comparison, mean-squared displacements at the same diameters in the case of a single tracer energy (dashed lines, same colors indicate same diameters, same data as in fig. 2.6). The critical asymptote of the Lorentz model, $\sim t^{2/z}$ with exponent $z = 3.036$, is superposed as a thin red line over the data.

3.2 *Dynamics of the full system*

The change in the dynamics introduced by the energy distribution is directly apparent in the MSD, which is shown in fig. 3.4. The MSD of the confined ideal gas is shown as solid lines for a range of diameters, superposed over the single-energy data obtained for the same diameters as dashed lines. Generally speaking, the confined ideal gas MSD follow the single-energy MSD on short and intermediate times and then deviate. The difference between the two cases is the least pronounced farthest from the critical point, at $\sigma_F = 0.2$ and 0.3 on the delocalized side, and at $\sigma_F = 0.7$ and 0.8 on the localized side. The most striking difference occurs, when the single-energy system is already localized, while the ideal gas system clearly is not, e.g. between $\sigma_F = 0.45$ and 0.6. The localization transition occurs between $\sigma_F = 0.6$ and 0.7. The MSD at $\sigma_F = 0.6$ on intermediate times seems to tend to a constant long-time limit before becoming diffusive.

As a remainder of the Lorentz model transition, between $\sigma_F = 0.4$ and 0.45, the MSD follows the expected critical anomalous diffusion for a short time before becoming diffusive. At higher σ_F, effective exponents arise in an interplay of localized and delocalized dynamics: Subdiffusion is sustained for the longest time at $\sigma_F = 0.5$, where the MSD is compatible with an exponent $2/z = 0.56$. At $\sigma_F = 0.6$, the MSD is compatible with an effective anomalous exponent $2/z \approx 0.25$.

The long-time diffusion coefficient D of the confined ideal gas is also strongly modified compared to the single-energy case. Most importantly, the behavior of D cannot be made to match the critical behavior of the Lorentz model anymore. In fig. 3.5 *(top)* the diffusion coefficient D of the confined ideal gas is shown as a function of the tracer diameter in comparison to the already presented data for the single-energy case. As could be already seen in the MSD, the diffusion coefficient of the confined ideal gas is similar to the one of

the single-energy case at small tracer diameters σ_F, but starts to exceed it at $\sigma_F \approx 0.35$. Additionally the diffusive regime extends to far larger σ_F.

That the dependence of D is not compatible with the critical asymptote $D \sim \varepsilon^\mu$ is demonstrated by the rectification plot in fig. 3.5 *(bottom)*. There, $D^{1/\mu}$ is plotted as a function of σ_F, which would turn the critical asymptote into a straight line with the root of the line marking the localization point. Clearly, $D^{1/\mu}$ for the confined ideal gas is strongly curved in the approach $D^{1/\mu} \to 0$. This demonstrates the rounding of the transition.

However, it is possible to identify an effective power-law for the diffusion coefficient which is not connected to the Lorentz model. Assuming that the effective transition occurs at $\sigma_F^c = 0.6$, the diffusion coefficient of the confined ideal gas becomes compatible with a power-law. This can be seen in fig. 3.6, where D is shown for both the confined ideal gas and the single-energy system as a function of the separation parameter. While the single-energy D follows the expected power-law, $D \sim |\varepsilon|^\mu$, the confined ideal gas D follows a power-law with a very different exponent, $D \sim |\varepsilon|^{2.8}$. Clearly, the confined ideal gas does not become fully localized at $\sigma_F = 0.6$, so the effective power-law will break down necessarily at some $\varepsilon \leq 0.1$. The effective scaling is not necessarily a sign of scale invariance in the approach to a localization transition — as is the case of the scaling in the Lorentz model — and is most likely accidental.

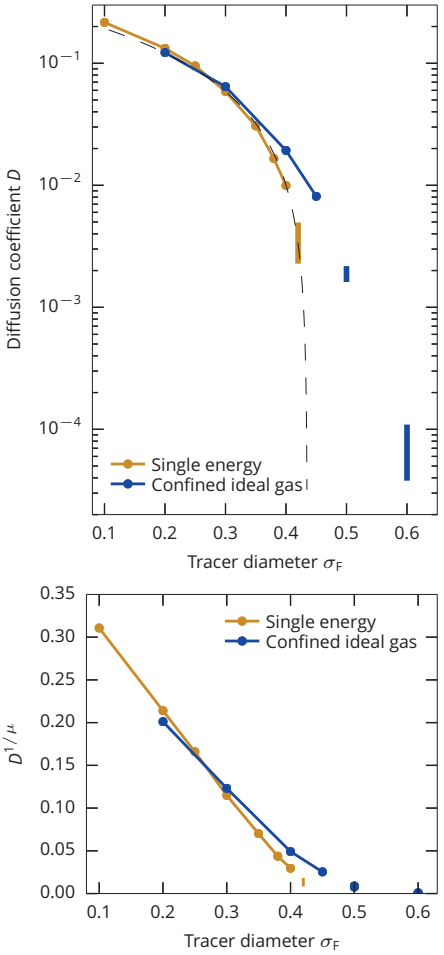

Figure 3.5: *Top:* Diffusion coefficient of the confined ideal gas and the single-energy case as a function of the tracer diameter σ_F. Connected dots for data free of finite size effects; vertical bars give upper and lower bounds obtained from finite size scaling, see section 2.5. *Bottom:* Rectification plot of the same data. Where finite-size-scaling bounds become too close for displaying, the bounds are marked by unconnected dots instead.

From inspection of the MSD directly it is already clear that the critical asymptote of the Lorentz model, $\delta r^2(t) \sim t^{2/z}$ is never approached. It is therefore not fruitful to discuss the approach to the critical asymptote in a similar manner as in section 2.2 for figs. 2.10 and 2.13. Only for completeness is the collapse of the MSD near the localization point onto two scaling functions tested here. In the Lorentz model, one would expect, see eq. (1.13),

$$\delta r^2(t) = t^{2/z} \delta \mathcal{R}_\pm^2(\hat{t}),$$

with $\hat{t} := t/t_x \sim t l^{-z}$ and localization length l, with $l^{-z} \sim |\varepsilon|^{\nu d_w}$ on both sides of the transition. This scaling is applied in fig. 3.7, where the MSD is divided by the critical asymptote and then shown as a function of time rescaled by the localization length, in analogy to fig. 2.13. For the calculation of the separation parameter ε, the localization transition has been assumed to take place at $\sigma_F^c = 0.6$. In contrast to fig. 2.13, the collapse onto the two scaling functions, for the delocalized and the localized states, respectively, is not achieved, here. Most clearly, this is apparent for the state at $\sigma_F = 0.55$ which presents an intermediary case between the two scaling functions. Its rescaled MSD appears to be on the localized side but then turns strongly upwards, i.e. becomes diffusive. This does not present a finite size effect.

In the same way with which an effective scaling was found for the diffusion coefficient, an effective scaling can be found for the MSD which improves the collapse onto scaling functions considerably. This is achieved by treating the localization length l, which enters the scaling function by rescaling time, as a free parameter. The results are shown in fig. 3.8. On the left, the rescaled MSD is found to mostly collapse onto the localized and delocalized scaling functions. Only for the MSD at $\sigma_F = 0.5$ and 0.55 the scaling does not work well. The localization lengths l with which the collapse was achieved are shown on the right as a function of the separation parameter ε with open circles for

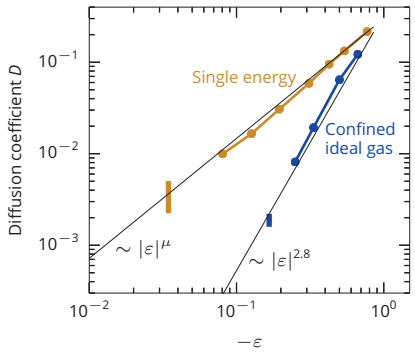

Figure 3.6: Diffusion coefficient D of confined ideal gas and the single-energy case as a function of the separation parameter $\varepsilon := (\sigma_F - \sigma_F^c)/\sigma_F^c$. For the calculation of ε, the parameters $\sigma_F^c = 0.435$ (single energy) and $\sigma_F^c = 0.6$ (confined ideal gas) was used. Black lines mark asymptotes with the exponent of the Lorentz model, $\sim |\varepsilon|^\mu$ with $\mu = 1.31$, and an effective exponent, $\sim |\varepsilon|^{2.8}$.

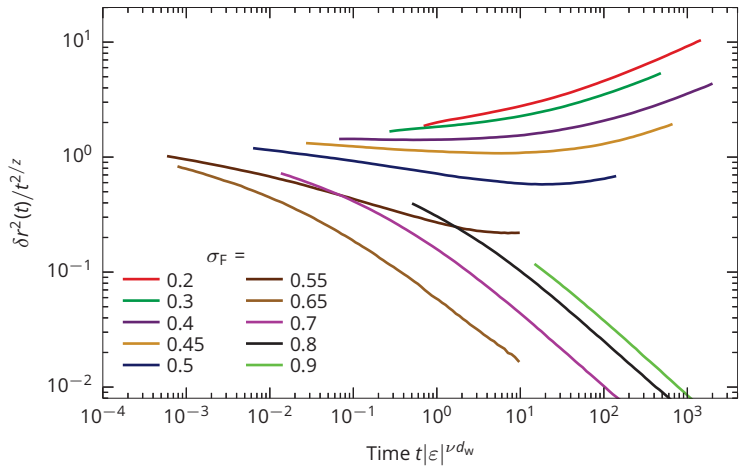

Figure 3.7: Rescaled mean-squared displacement of the confined ideal gas as a function of rescaled time $t\varepsilon^{\nu d_w}$ for a range of diameters σ_F as indicated in the legend. For the calculation of the separation parameter, the localization transition was assumed to take place at $\sigma_F^c = 0.6$.

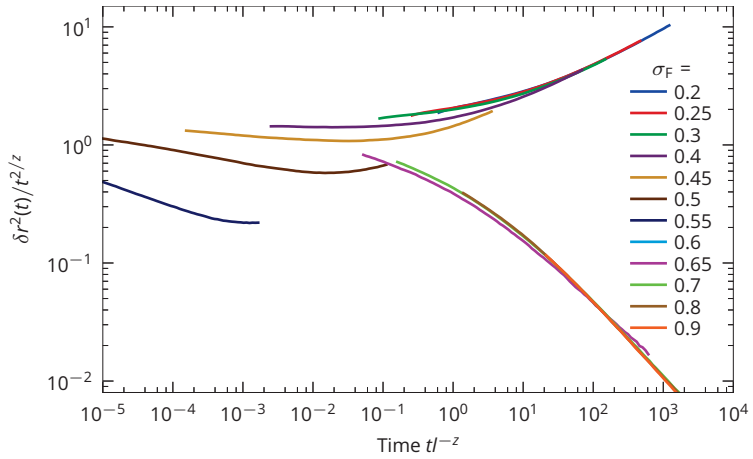

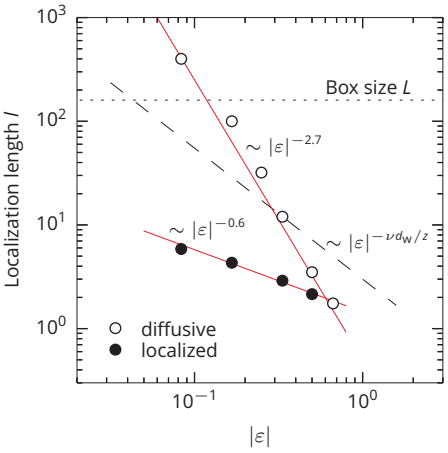

Figure 3.8: *Left:* Rescaled mean-squared displacement of the confined ideal gas as a function of rescaled times tl^{-z} for a range of diameters as indicated in the legend. *Right:* Mean-void-cluster sizes l used for the scaling of the MSD as a function of the separation parameter ε.

the delocalized, diffusive side and closed circles on the localized side. Since l was treated as a fit parameter, it was possible for it to exceed the simulation size L. For the calculation of ε, the critical point was again assumed to be at $\sigma_F^c = 0.6$. In the Lorentz model, l is expected to diverge as $l \sim |\varepsilon|^{-\nu d_w/z}$ (dashed line), see eq. (1.12). The Lorentz model scaling is not obeyed on both sides of the transition. Instead, the localization length l is found to follow effective power-laws on both sides of the transition, but with different exponents. The divergence of the l with an effective exponent of −2.7 on the delocalized side is directly inherited from the effective exponent of the diffusion.

The modification of the dynamics in the confined ideal gas in comparison to the single energy case can be understood in terms of an energy average. In the former, the particle energies are sampled from a broad energy distribution. Particles with an energy higher than the energy used in the single-energy case will tend to be more mobile. Even if most of the system's particles are localized, some high-energy particles will still be delocalized. Then, the MSD— because it is very sensitive to contributions from delocalized particles — will become diffusive as long as there are some delocalized particles contained in the system. The critical subdiffusion for the systems between $\sigma_F = 0.4$ and 0.45 is therefore strongly masked by diffusive contributions from high-energy particles, and even the MSD at $\sigma_F = 0.6$, becomes diffusive, even though most particles at that

diameter are localized. As the fluid diameter is increased, less and less particles are diffusive, the system's diffusion coefficient becomes smaller, and the MSD appears localized for longer times. This rounding of the transition also makes it impossible to associate the localization transition with a critical anomalous exponent and only effective exponents can be inferred. In the following, the rounding of the transition is explored quantitatively.

3.3 *Effective hard-sphere distribution*

The rounding of the transition reported above can be understood, if the hard-sphere mapping of section 2.3 is used to map the energy distribution $p(E)$ of the tracer particles onto a distribution of effective hard-sphere diameters $p(\sigma_{\mathrm{hs}})$. A variable substitution of the corresponding integral leads to the mapping,

$$\begin{aligned}\int_0^\infty p(E)\mathrm{d}E &= \int_{\sigma_{\mathrm{hs}}(E=0)}^{\sigma_{\mathrm{hs}}(E=\infty)} p(E(\sigma_{\mathrm{hs}}))\frac{\mathrm{d}E}{\mathrm{d}\sigma_{\mathrm{hs}}}\mathrm{d}\sigma_{\mathrm{hs}} \\ &=: \int_{\sigma_{\mathrm{hs}}(E=\infty)}^{\sigma_{\mathrm{hs}}(E=0)} p(\sigma_{\mathrm{hs}})\mathrm{d}\sigma_{\mathrm{hs}} \\ \Rightarrow p(\sigma_{\mathrm{hs}}) &= -p(E(\sigma_{\mathrm{hs}}))\frac{\mathrm{d}E}{\mathrm{d}\sigma_{\mathrm{hs}}}. \end{aligned} \tag{3.2}$$

The negative sign enters through reversing the integration limits and reflects that the effective hard-sphere diameter becomes smaller with increasing particle energy and vice-versa. The new probability distribution $p(\sigma_{\mathrm{hs}})$ is automatically normalized if $p(E)$ is normalized. From eq. (2.11) it immediately follows that,

$$E(\sigma_{\mathrm{hs}}) = 8\varepsilon_{\mathrm{MF}}\left(\left(\frac{2\sigma_{\mathrm{MF}}}{\sigma_{\mathrm{hs}}}\right)^{12} - \left(\frac{2\sigma_{\mathrm{MF}}}{\sigma_{\mathrm{hs}}}\right)^{6}\right) + 2\varepsilon_{\mathrm{MF}}, \tag{3.3}$$

$$\frac{\mathrm{d}E}{\mathrm{d}\sigma_{\mathrm{hs}}} = -48\varepsilon_{\mathrm{MF}}\left(2\frac{(2\sigma_{\mathrm{MF}})^{12}}{(\sigma_{\mathrm{hs}})^{13}} - \frac{(2\sigma_{\mathrm{MF}})^{6}}{(\sigma_{\mathrm{hs}})^{7}}\right). \tag{3.4}$$

For each particle an effective hard-sphere diameter can be determined. Particles with $\sigma_{\mathrm{hs}} = \sigma_{\mathrm{hs}}^{\mathrm{c}}$ are at the localization transition, those with $\sigma_{\mathrm{hs}} < \sigma_{\mathrm{hs}}^{\mathrm{c}}$ effectively explore a matrix containing a percolating cluster, and those with $\sigma_{\mathrm{hs}} > \sigma_{\mathrm{hs}}^{\mathrm{c}}$ are localized. Therefore, as long as there is a part of the distribution on the percolating side, i.e. $p(\sigma_{\mathrm{hs}}) > 0$ for some $\sigma_{\mathrm{hs}} < \sigma_{\mathrm{hs}}^{\mathrm{c}}$, then the system will contain delocalized particles and will exhibit diffusion at long times.

Increasing σ_{F} shifts the whole distribution. This can be easily demonstrated with the numerically obtained energy distribution, converted into $p(\sigma_{\mathrm{hs}})$. To display $p(\sigma_{\mathrm{hs}})$ it is practical to plot $p(E)\,\mathrm{d}E/\mathrm{d}\sigma_{\mathrm{hs}}$ versus $\sigma_{\mathrm{hs}}(E)$ (from eq. (2.11)) parametrically with parameter E. The hard-sphere diameter distributions obtained that way are shown in fig. 3.9. They are plotted semi-logarithmically to in particular expose the behavior of the distribution at small σ_{hs}. The distributions are limited at small σ_{hs} by the largest energy for which $p(E)$ was calculated and at large σ_{hs} by the energy being $E = 0$. The distribution has similar shape for all σ_{F} and it gets shifted towards larger σ_{hs} when σ_{F} is increased. From the plot it can be immediately read off that at least the systems with $\sigma_{\mathrm{F}} \leq 0.6$ contain delocalized particles. This finding is fully compatible with the MSD of these states becoming diffusive.

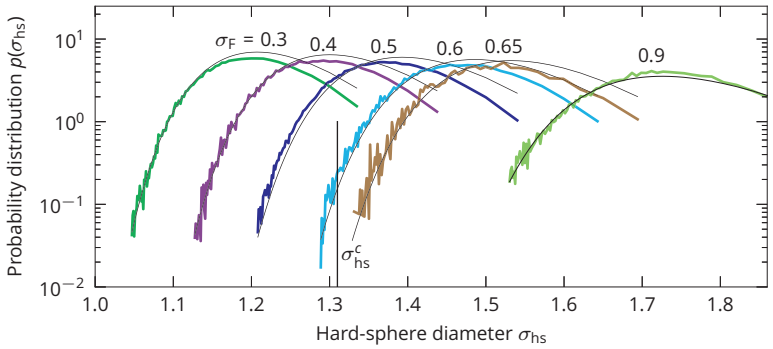

Figure 3.9: Plot of the distribution of effective hard-sphere diameters $p(\sigma_{hs})$ for a range of σ_F as indicated in the figure. The distributions were calculated as indicated in the text with the numerically obtained particle energies, shown in part in fig. 3.1. The critical hard-sphere diameter $\sigma^c_{hs} = 1.31$ as determined in section 2.3 is marked with a vertical line. The analytic approximation given in eq. (3.5) is shown for all σ_F as solid black curves.

A few properties of the distribution $p(\sigma_{hs})$ can be determined analytically using an approximation of the energy distribution. Relevant for the transport in the confined ideal gas are the particles with high energy. It is was observed in fig. 3.1, that the energy distribution decays as $p(E) \sim \exp(-\beta E)$ for large E. With this, the distribution $p(\sigma_{hs})$ can be immediately estimated at small σ_{hs}. After fitting $p = A\exp(-\beta E)$ to the energy distribution, eqs. (3.2) to (3.4) then evaluate to

$$p(\sigma_{hs}) \approx A\exp\left(-\beta\, 8\varepsilon_{MF}\left(\left(\frac{2\sigma_{MF}}{\sigma_{hs}}\right)^{12} - \left(\frac{2\sigma_{MF}}{\sigma_{hs}}\right)^{6}\right) + 2\varepsilon_{MF}\right) \times 48\varepsilon_{MF}\left(2\frac{(2\sigma_{MF})^{12}}{(\sigma_{hs})^{13}} - \frac{(2\sigma_{MF})^{6}}{(\sigma_{hs})^{7}}\right). \tag{3.5}$$

The approximation is superposed over the numerical data as black lines in fig. 3.9. For $\sigma_F \leq 0.65$, the amplitude $A = 1.3$ was used for the energy distribution fit and the temperature corresponded to $\beta = 1$. For $\sigma_F = 0.9$, the amplitude was $A = 0.7$ and the temperature corresponded to $\beta = 0.7$ as a result of the equilibration procedure described in section 3.1. The exponential fits with these parameters are shown in fig. 3.1. The approximation matches the actual hard-sphere distributions well, especially at small σ_{hs}.

The latter term of the approximation diverges in the limit $\sigma_{hs} \to 0$, but the exponential function tends to 0 more strongly, so that in total

$$\lim_{\sigma_{hs}\to 0} p(\sigma_{hs}) = 0.$$

Still, for all finite σ_{hs}, the probability distribution stays positive

$$p(\sigma_{hs}) > 0, \text{ for } \sigma_{hs} > 0. \tag{3.6}$$

The approximation of $p(E)$ as an exponential function can be expected to become strictly correct in the limit $E \to \infty$, which is the relevant limit for determining the behavior of $p(\sigma_{hs})$ at small σ_{hs}. It can therefore be concluded that the real distribution $p(\sigma_{hs})$ also stays positive for all finite σ_{hs}. Therefore, a part of the distribution is always on the delocalized side. Strictly speaking, this means that there is *no true localization transition in the confined ideal gas*, as there is always a finite probability of some tracers being delocalized.

Specifically, the fraction of particles whose energy corresponds to a percolating system p_{perc} can be calculated approximately as a function of σ_F,

$$p_{perc} := \int_0^{\sigma^c_{hs}} p(\sigma_{hs})\mathrm{d}\sigma_{hs} = \int_{E(\sigma^c_{hs})}^{E(\sigma_{hs}=0)} p(E)\mathrm{d}E$$
$$= P(E(\sigma_{hs} = 0)) - P(E(\sigma^c_{hs})),$$

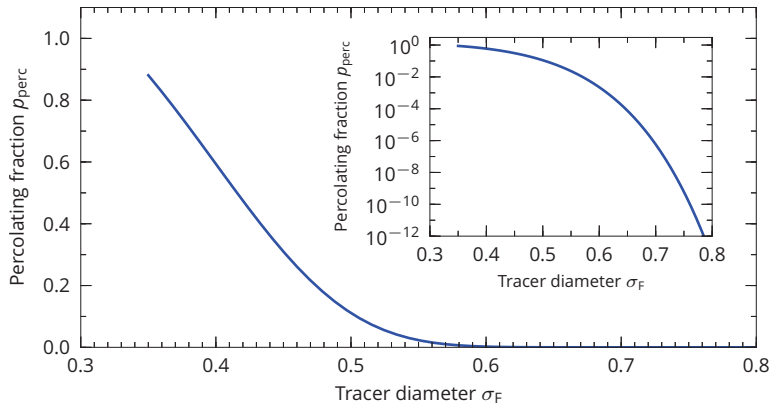

Figure 3.10: Estimate of the percolating fraction p_{perc}, the probability that any given tracer particle has an energy corresponding to a percolating system as a function of σ_F, as given by eq. (3.7). Parameters were $A = 1.3$, $\beta = 1$, $\varepsilon_{MF} = 0.1$, and $\sigma^c_{hs} = 1.31$. *Inset:* The same function in a semilogarithmic plot.

with $P(E)$ being the antiderivative to $p(E)$. If $p(E) \approx A\exp(-\beta E)$ with some constant A, then $P(E) \approx -(A/\beta)\exp(-\beta E)$ and

$$p_{\mathrm{perc}} \approx \frac{A}{\beta}\exp(-\beta E(\sigma^c_{hs})) - \frac{A}{\beta}\exp(-\beta E(\sigma_{hs} = 0)).$$

Since $\lim_{\sigma_{hs}\to 0} E(\sigma_{hs}) = +\infty$ holds, p_{perc} immediately simplifies to

$$p_{\mathrm{perc}} \approx \frac{A}{\beta}\exp(-\beta E(\sigma^c_{hs})).$$

This can then be evaluated with eq. (3.3) to

$$p_{\mathrm{perc}} \approx \frac{A}{\beta}\exp\left(-8\beta\varepsilon_{MF}\left(\left(\frac{2\sigma_{MF}}{\sigma^c_{hs}}\right)^{12} - \left(\frac{2\sigma_{MF}}{\sigma^c_{hs}}\right)^{6}\right) - 2\beta\varepsilon_{MF}\right). \tag{3.7}$$

Obviously, setting A to a constant for all σ_F is an approximation, but a reasonable one for at least $\sigma_F \leq 0.65$ (this can be seen in fig. 3.1). It should also be noted, that the exponential approximation overestimates the value of p_{perc} for small σ_F, since the energy distribution at small E is overestimated. However, both points are not particularly relevant for the discussion of the rounding of the localization transition, which occurs mostly in the range $0.4 < \sigma_F < 0.65$, where the approximation of p_{perc} works well.

For $A = 1.3$, $\beta = 1$, $\varepsilon_{MF} = 0.1$, and $\sigma^c = 1.31$ the cumulative probability in exponential approximation is shown in fig. 3.10. For $\sigma_F < 0.5$ one finds that the percolating fraction is large, $p_{\mathrm{perc}} > 0.1$, indicating that a large fraction of the particles are delocalized. At $\sigma_F = 0.6$, p_{perc} has fallen below 10^{-2}, which can be seen more clearly in the inset where p_{perc} is plotted logarithmically as a function of σ_F. At higher σ_F, p_{perc} decays rapidly but stays positive. At $\sigma_F = 0.6$ the MSD was still found to become diffusive. This essentially presents the limit where the number of delocalized particles is still large enough so that diffusion can be observed easily.

While the percolating fraction p_{perc} illustrates that all systems become diffusive eventually, finite size effects can suppress this in simulations. At large σ_F, for finite systems, p_{perc} eventually becomes so small that all particles are found in a localized state.

By calculating the fraction of particles experiencing a percolating system, p_{perc}, the rounding of the localization transition was quantified. But for the hard-sphere mapping to be fully useful, it is necessary to demonstrate that indeed the hard-sphere diameter σ_{hs} is the relevant control parameter and that

the influence of the particle energy E on the dynamics can be fully understood by its effect on σ_{hs}. For this purpose the dynamics will now be studied in more detail.

3.4 *Energy-resolved dynamics*

This section will conclusively show that particles with the same σ_{hs} have equivalent dynamics, except for a trivial rescaling of time and length scales. This will then be used to show that the dynamics of the confined ideal gas presents an average weighted with $p(\sigma_{\mathrm{hs}})$ over the single-energy dynamics presented previously. The analysis will focus on the MSD and the diffusion coefficient, but it can be easily generalized to arbitrary dynamical quantities.

For this analysis, it is necessary to calculate the MSD as a function of the tracer energy E. The tracers were grouped according to their energies, exactly as for the calculation of the energy distribution $p(E)$, and the MSD was then averaged over tracers with roughly the same energy. As an example, the energy-resolved MSD is shown for $\sigma_{\mathrm{F}} = 0.3$ in fig. 3.11 *(top)* for a range of energies. This clearly shows that in a single system the whole Lorentz model scenario is represented: delocalized particles at large energies coexist with localized particles at low energies. Via the hard-sphere mapping, the energy-distributed MSD, $\delta r^2(t;E)$ directly corresponds to the hard-sphere distributed $\delta r^2(t;\sigma_{\mathrm{hs}})$.

The dynamics in the hard-sphere Lorentz model can be fully described in dimensionless quantities: For a tracer in a hard-sphere system, its velocity v_{F} only determines how fast it moves along its trajectory, but it does not have an influence on the trajectory itself. Similarly, the size of the obstacles σ_{hs} (assuming a point tracer) only sets a trivial length scale and two systems with the same reduced obstacle density $n_{\mathrm{hs}}^{\mathrm{c}}$ are equivalent. Thus, the velocity v_{F} and the size of the obstacles σ_{hs} can be used to express trivial time and length scales, and a dimensionless time t^* and position r^* can be introduced,

$$\begin{aligned} t^* &:= t\,\frac{v_{\mathrm{F}}}{\sigma_{\mathrm{hs}}}, \\ r^*(t^*) &:= r(t)\frac{1}{\sigma_{\mathrm{hs}}}. \end{aligned}$$

This fixes the dimensionless velocity $\mathrm{d}r^*/\mathrm{d}t^*$ to unity and the number density n_{hs} of the matrix to the reduced number density n^*. Formulated in a dimensionless way, the dynamics in the hard-sphere Lorentz model thus depends only on the reduced obstacle density n^*. The dimensionless MSD, for example, then reads

$$(\delta r^2(t^*))^* = \langle (r^*(t^*) - r^*(0))\rangle = \frac{1}{\sigma_{\mathrm{hs}}^2}\langle (r(t) - r(0))\rangle = \frac{1}{\sigma_{\mathrm{hs}}^2}\delta r^2(t).$$

The energy-distributed MSD is shown in the dimensionless rescaling for exemplary $\sigma_{\mathrm{F}} = 0.3$ in fig. 3.11 *(bottom)*. The rescaling of the particle velocity to unity is immediately apparent in the microscopic regime $t^* = \mathcal{O}(1)$. The dimensionless diffusion coefficient D^* then relates to the non-rescaled D in

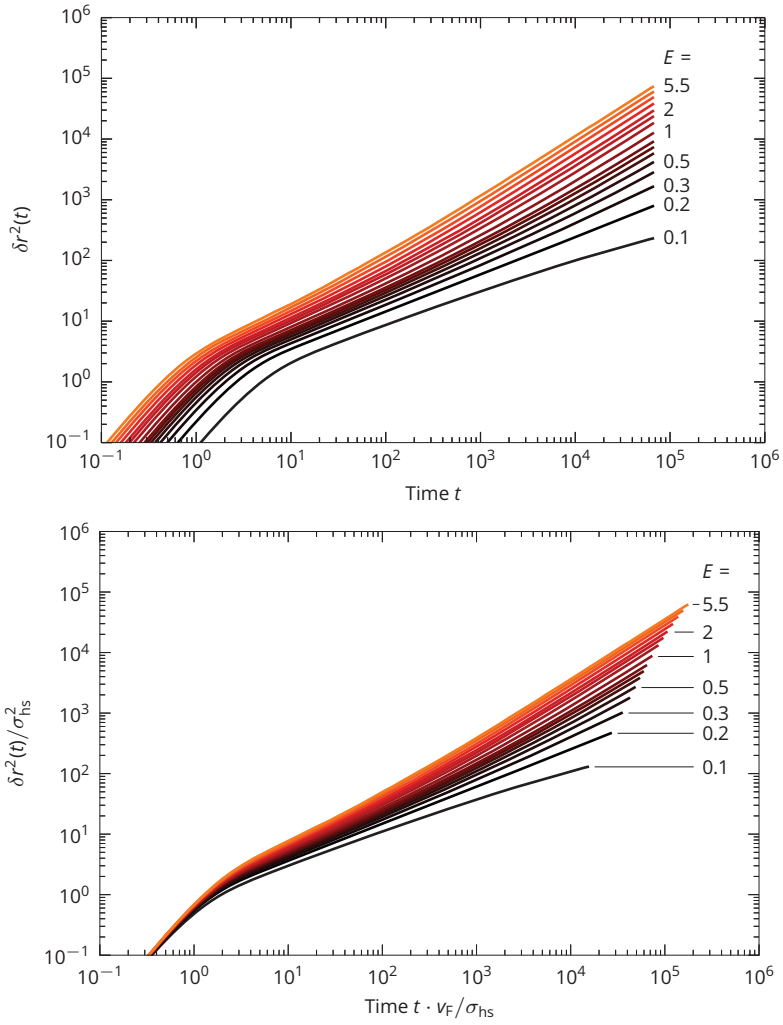

Figure 3.11: *Top:* Plot of the energy-resolved mean-squared displacement as a function of time t in the confined ideal gas at $\sigma_F = 0.3$. The MSD were averaged over particle trajectories grouped according to their energy. Width of the energy bins $\Delta E = 0.1$. Energies of the bins are shown as labels adjacent to the corresponding MSD in the figure. *Bottom:* Rescaling of the same data to dimensionless variables as described in the text.

the following way

$$\begin{aligned}
&\left\langle (r(t) - r(0))^2 \right\rangle \to 2dDt \\
&\Rightarrow \sigma_{hs}^2 \left\langle (r^*(t^*) - r^*(0))^2 \right\rangle \to 2dDt^* \frac{\sigma_{hs}}{v_F} \\
&\Rightarrow \left\langle (r^*(t^*) - r^*(0))^2 \right\rangle \to 2dDt^* \frac{1}{\sigma_{hs} v_F} = 2dD^* t^* \\
&\Rightarrow D^* = \frac{1}{\sigma_{hs} v_F} D.
\end{aligned}$$

Thus, all systems can be rescaled with σ_{hs} and v_F such that the diffusion coefficient becomes a dimensionless quantity and independent of these quantities, $D^*_{hs}(n^*)$. To demonstrate the agreement between the single-energy diffusion coefficients and the energy-distributed diffusion coefficient, both have to first be rescaled into the dimensionless form. From the energy, σ_{hs} can be easily calculated, while v_F can be measured in the microscopic regime of the MSD, where $\delta r^2(t) = v_F^2 t^2$ holds. Instead of expressing the diffusion coefficient as a function of the reduced number density, it is presented as a function of the control parameter σ_{hs}. Both parameters are interchangeable here, because the number density of obstacles in the system is held constant.

In fig. 3.12 *(top)*, the single-energy diffusion coefficient is shown in the hard-

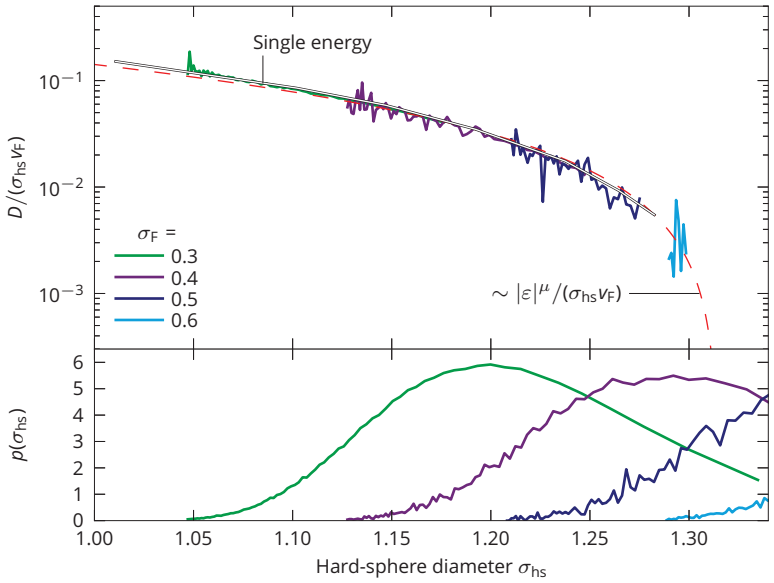

Figure 3.12: *Top:* Diffusion coefficient D as a function of the effective hard-sphere diameter $\sigma_{hs}(\sigma_F, E)$ in the confined ideal gas for a range of diameters σ_F as indicated in the legend. Hard-sphere diameters calculated from the particle energy distribution $p(E)$ with eq. (2.11). Single energy data as superposed solid white line. Critical asymptote of the Lorentz model $\sim |\varepsilon|^\mu$ as determined for the single-energy case in fig. 2.7 was mapped onto effective hard-sphere diameters, rescaled, and plotted as red dashed line. *Bottom:* Corresponding distributions of hard-sphere diameters $p(\sigma_{hs})$, calculated with eq. (3.2) with the numerically obtained $p(E)$.

sphere mapping and in dimensionless representation as a solid white line. The critical asymptote of the Lorentz model as determined for the single-energy case is superposed as a dashed red line. The energy-distributed diffusion coefficient of the confined ideal gas in dimensionless representation is shown for a range of σ_F. The distribution of effective hard-sphere diameters for the presented systems, which is shown in fig. 3.12 *(bottom)*, emphasizes the wide range of effective hard-sphere diameters present in the systems. The diffusion coefficients are shown for all the energies where the simulation time was sufficient for the MSD to cross over into long-time diffusion. Finite-size effects can be ruled out by the same criteria as in the single-energy case.

Although the data of the confined ideal gas contains considerable amounts of noise, the full agreement with the single-energy case is convincing. This gives confirmation that the hard-sphere mapping of both the tracer energy E and the interaction diameter σ_F onto a single hard-sphere diameter σ_{hs} is fully successful, in that it not only correctly maps the topology of the void space but also the dynamics of the system.

Now it has been confirmed that for each energy E and diameter σ_F the energy-resolved diffusion coefficient can be expressed by the hard-sphere diffusion coefficient $D(\sigma_F, E) = D^*(\sigma_{hs}(\sigma_F, E))\sigma_{hs}(\sigma_F, E)\nu_F(\sigma_F, E)$. Then it also becomes immediately clear that the system average of the diffusion coefficient is an integral over the hard-sphere diffusion coefficient weighted with the effective hard-sphere distribution of the system,

$$\begin{aligned} D(\sigma_F) &= \int D(\sigma_F, E) p(\sigma_F, E) \mathrm{d}E \\ &= \int D^*(\sigma_{hs}) \sigma_{hs} \nu_F(\sigma_F, \sigma_{hs}) p(\sigma_F, \sigma_{hs}) \mathrm{d}\sigma_{hs}. \end{aligned}$$

For the second equation, the notation is made to reflect that — in general — both ν_F and $p(\sigma_{hs})$ will depend strongly on σ_F, while D^* does not at all.

The integral expresses the rounding of the localization transition in the confined ideal gas analytically and makes it directly clear why the scaling properties of the Lorentz model do not hold here: Even though $D^*(\sigma_{hs})$

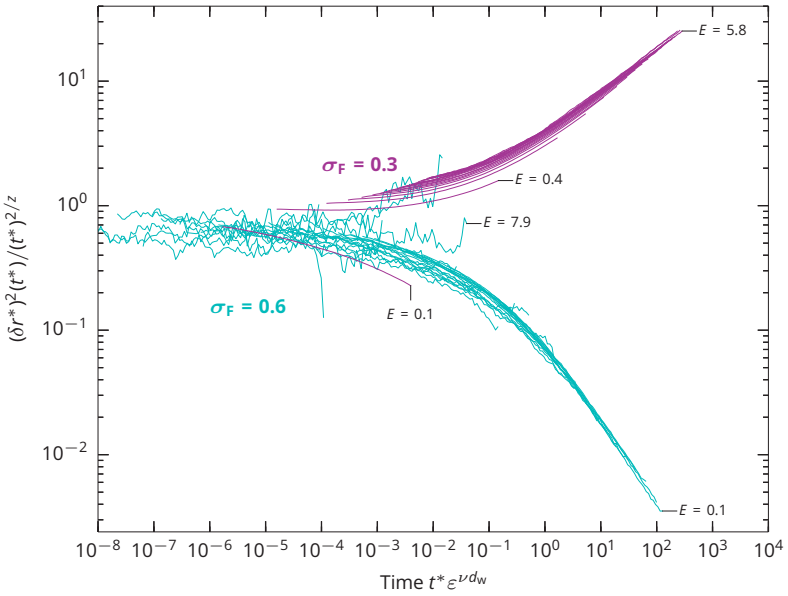

Figure 3.13: Mean-squared displacement divided by the critical asymptote as a function of time rescaled with the distance ε to the critical point, all in unit-less rescaling. For the calculation of ε, the critical point was assumed to be at $\sigma_{hs}^c = 1.31$ (corresponding to $\sigma_F^c = 0.43$). The system at $\sigma_F = 0.3$ is shown in purple, the system at $\sigma_F = 0.6$ in cyan. Some exemplary MSDs are annotated with their energies E.

follows a critical power-law, the lack of corresponding power-laws for $\nu_F(\sigma_{hs})$ and $p(\sigma_{hs})$ in general mean that $D(\sigma_F)$ will also not follow a power-law. This can be directly inferred from fig. 3.5.

Since both the velocity distribution and the probability distribution are strictly positive functions, i.e. $\nu_F(\sigma_{hs}) > 0$ and $p(\sigma_{hs}) > 0$ for $\sigma_{hs} > 0$, the integral will always give $D(\sigma_F) > 0$ in the confined ideal gas: For all finite σ_F the MSD will eventually become diffusive. Therefore, the MSD for $\sigma_F > 0.6$ observed in fig. 3.4 can only be effectively localized.

Scaling of the mean-squared displacement Since the energy-resolved dynamics of the confined ideal gas corresponds to the single-energy dynamics, it can be expected that the time and space scaling of the MSD is found here as well. To demonstrate this, the MSD is shown in fig. 3.13 divided by the critical asymptote as a function of time rescaled with the expected dependence on the distance from the critical point ε. The MSD is shown for two systems: The mostly delocalized state at $\sigma_F = 0.3$ is shown in purple, and the mostly localized state at $\sigma_F = 0.6$ is shown in cyan.

At $\sigma_F = 0.3$, the system is delocalized for all but the two lowest energy bins, $E \leq 0.1$ and $0.1 < E \leq 0.2$ (not shown). The MSD for the lowest two energy bins nearly falls on the localized scaling function, while the other collapse on the delocalized scaling function. The collapse is as successful as in the single-energy case, which is shown in fig. 2.13.

At $\sigma_F = 0.6$, the simulation had to be performed for a far longer time and thus only 500 tracers per system were simulated, giving a total of 50000 tracers for the 100 matrix realizations. As a result, the statistics are considerably worse. Still, for most energies, the system is clearly localized and the MSD collapses onto the localized scaling function. At high energies the noise in the data increases considerably as the statistics become worse and it becomes impossible to determine whether the MSD correctly falls onto the delocalized scaling function or not. However, the agreement with the localized scaling function at lower energies is as convincing as in the single-energy case.

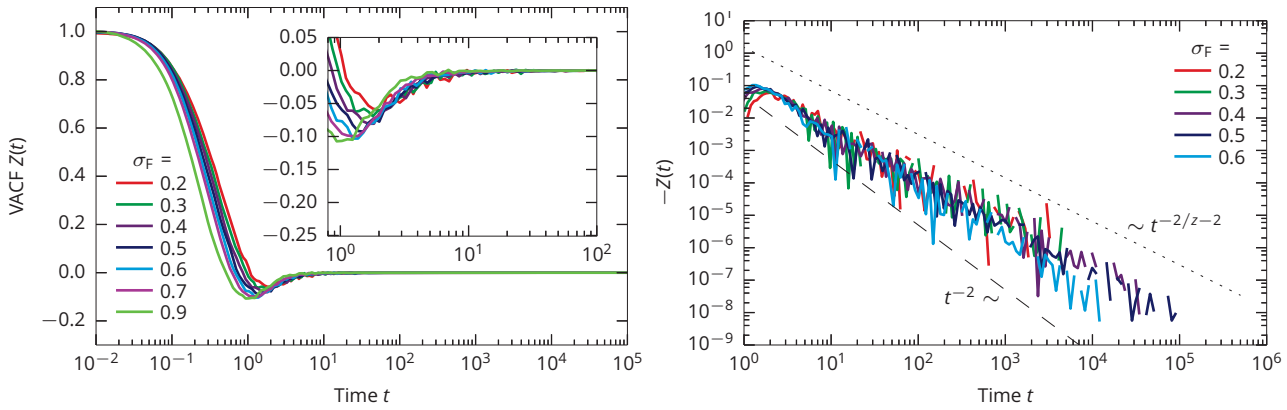

Figure 3.14: *Left:* Velocity autocorrelation function $Z(t)$ of the confined ideal gas for a range of tracer diameters σ_F as indicated in the legend. *Inset:* Enlarged view of the same data, emphasizing the final decay to 0. *Right:* Double-logarithmic plot of $-Z(t)$ as a function of time t. The hydrodynamic asymptote $\sim t^{-2}$ (dashed line) and the critical asymptote $\sim t^{2/z-2}$ with $z = 3.036$ (dotted line) are drawn into the figure to guide the eye.

The collapse is equally successful for other σ_F as well (not shown here). The general agreement with the scaling prediction of the Lorentz model serves as a further illustration that the energy-resolved dynamics of the confined ideal gas corresponds to the Lorentz model scenario.

Now that the averaging of the dynamics in the confined ideal gas is understood, a few remaining results are reported to conclude the discussion of the dynamics.

3.5 *Dynamics of the full system — continued*

Velocity autocorrelation function Returning back to the discussion of the system averages, the velocity autocorrelation function $Z(t)$ of the confined ideal gas behaves very similarly to the single energy case. Decaying from $Z(t) = 1$, it becomes negative at $t \approx 1$ and then tends to 0, as is shown in fig. 3.14 *(left)*. Compared to the single energy case, the undershoot of the VACF does not become as low, see fig. 3.14 *(left, inset)*. The inset also exposes the considerable noise found in the data. As in the single-energy case, the noise is strong enough in the data to make it difficult to study the final decay to 0. Nevertheless, an attempt is made in fig. 3.14 *(right)*, where the long-time tail of the VACF is shown in a double-logarithmic plot. The tail is compatible with the critical asymptote $\sim t^{2/z-2}$ with $z = 3.036$ derived from the MSD, just as in the single-energy case. The hydrodynamic tail is again not observed.

This general agreement to the single-energy case is entirely expected. Contrary to the MSD, the VACF of the single-energy case consistently decayed with the $t^{2/z-2}$-power law over the whole studied range of σ_F and thus the averaged dynamics will inherit this. The critical scaling in the case of the MSD was destroyed by the non-critical contribution of long-time diffusion which was always present in the average but is not contained in the VACF due to the application of the derivative. Thus, there is no discernible qualitative difference between the single-energy and the confined-ideal-gas cases as far as the VACF is concerned.

Van-Hove function The self-part of the van-Hove correlation function, however, is strongly modified by the averaging and as a result does not have the scaling properties of the Lorentz model.

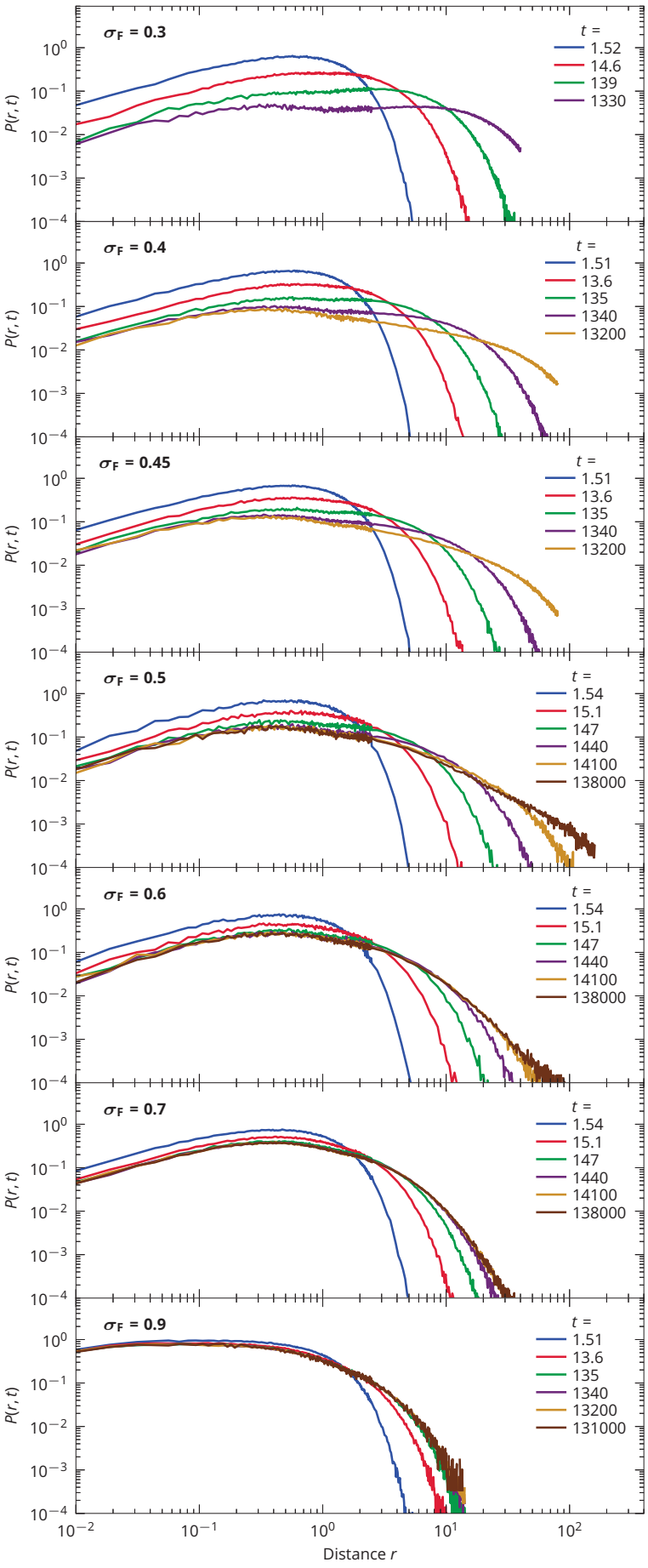

Figure 3.15: Plot of van-Hove function $P(r,t)$ of the confined ideal gas for a range of tracer diameters σ_F = 0.3, 0.4, 0.45, 0.5, 0.6, 0.7 and 0.9. $P(r,t)$ is shown as a function of distance r for a range of times t as indicated in the legends. Compare to fig. 2.14 for the van-Hove function in the single-energy case.

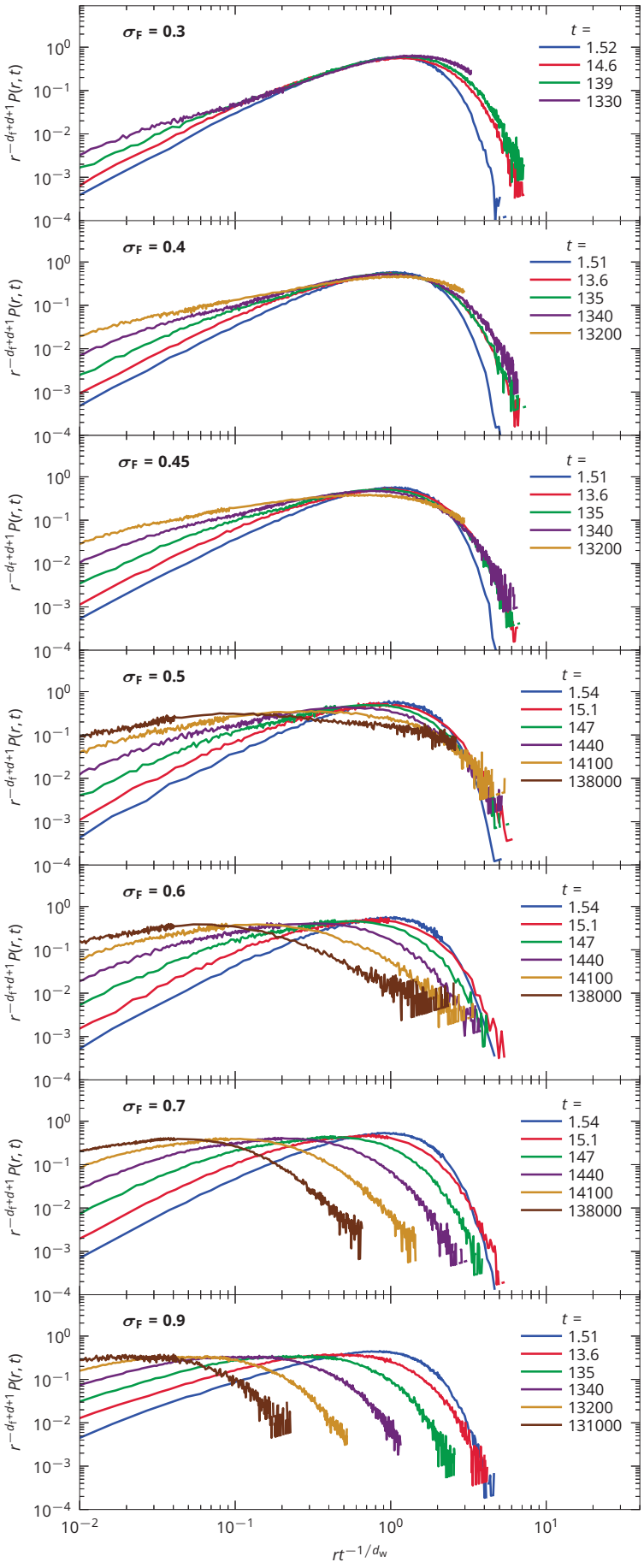

Figure 3.16: Plot of the rescaled van-Hove function assuming the scaling of the all-cluster average at the critical point. The scaling accounts for the different normalization used here than in the preceeding chapter.

In fig. 3.15, the van-Hove function $P(r, t)$ is shown as a function of distance r for a range of times t and for the whole range of simulated systems. As σ_F is increased, the system crosses the *effective* localization transition. At low σ_F, there is a considerable broadening of the distribution over time, which represents the exploration by the particles of their surroundings. The shape of the distribution is changed compared to the single-energy case. In the single-energy case there were two peaks — with one staying at a fixed, small distance and the other moving away over time — while in the confined ideal gas there is only one very broad distribution with one peak. This is clear indication of the strong energy-averaging present in the system.

At the diameters $\sigma_F = 0.5$ and 0.6 the distribution seems to nearly converge to a long-time limit. At ever longer times t, the distribution is only modified on ever larger length scales r. This indicates the localization of most particles, which make up the converged part of the van-Hove function, while only a few particles are still delocalized. The extremely slow spatial decay is an indication of the broad distribution of localization lengths present in the system, which in turn is a representation of the broad energy distribution of tracers. Apart from the weak time evolution present even at long times, the systems at $\sigma_F = 0.5$ and 0.6 have a van-Hove function more characteristic of a localized system. This nicely indicates the increased heterogeneity of the confined ideal gas in comparison to the single-energy case.

At the largest shown diameters, $\sigma_F = 0.7$ and 0.9, the van-Hove function does not show any evolution at large times anymore, i.e. the system is effectively localized. From the discussion of the energy averaging, however, one must conclude that this is due to the limited simulation time and the finite size of the system (which places a limit on the sampling of the energy distribution).

The energy averaging does not only destroy the scaling properties of the MSD but also those of the van-Hove function, from which the former quantity is derived. This is illustrated in fig. 3.16, where the expected scaling for the all-cluster average of the Lorentz model at the critical point is applied to the data. It is enlightening to compare this to to the single-energy case in fig. 2.15 (on p. 53). The scaling might be considered the most convincing for $\sigma_F = 0.3$ but this is where the system is still clearly delocalized. There, at intermediate times an effective collapse of the function occurs. But the energy averaging leads to a broadening of the van-Hove function over time, which then destroys the scaling. At the *effective* localization transition — somewhere between $\sigma_F = 0.6$ and 0.7, the van-Hove function is already so strongly dominated by the localized particles, that the critical scaling is impossible.

The relevance of localized particles is explored further with a short discussion of the intermediate scattering function.

Intermediate scattering function It is relevant to discuss the ISF in addition to the van-Hove function as it exposes the localization of particles in its long-time limit $f(q)$. In fig. 3.17 the ISF is shown as solid lines for the exemplary $\sigma_F = 0.6$ for a range of wavenumbers q. This data is superimposed over the ISF of the single-energy case for the same σ_F. Both systems have qualitatively very similar ISF. At large wavenumbers, the single-energy system's ISF shows oscillations, which are averaged out in the confined ideal gas.

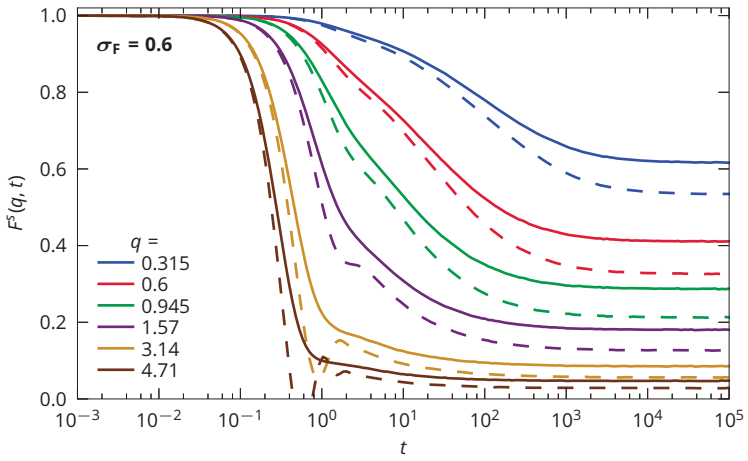

Figure 3.17: Intermediate scattering functions as function of time t for a range of wavenumbers q at σ_F = 0.6 for the confined ideal gas (solid lines) and the single-energy case (dashed lines).

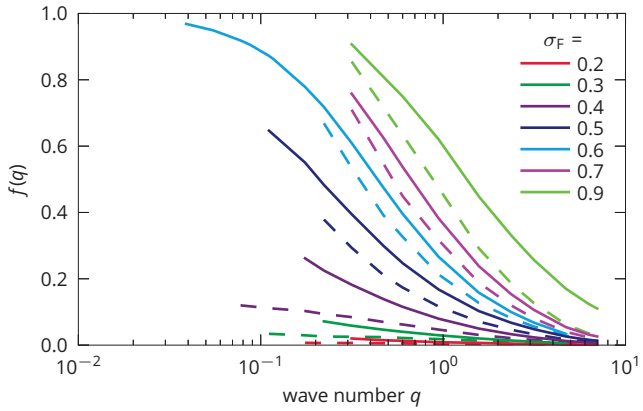

Figure 3.18: Semilogarithmic plot of the long-time limit $f(q)$ of the intermediate scattering function as a function of wavenumber q for a range of diameters σ_F. The data for the confined ideal gas (solid lines) is superposed over the single-energy data (dashed lines) for comparison, with identical colors signifying identical diameters.

Apart from that, the two systems only differ in that the confined ideal gas has a larger long-time limit at all q. This holds true for all σ_F, which is demonstrated in fig. 3.18 where the long-time limit $f(q)$ is given for a range of diameters σ_F spanning from strongly delocalized to strongly localized systems. The $f(q)$ of the ideal gas (solid lines) are larger than those of the single-energy system (dashed lines) which indicates stronger localization of the particles in the former systems. This might be considered surprising as the MSD generally showed enhanced dynamics in the confined ideal gas at long times. The apparent conflict can be immediately resolved: In addition to faster than average particles, the energy distribution of the confined ideal gas also contains many particles with lower than average energy which are in turn on average more localized than the particles in the single-energy system. The dynamics of the confined ideal gas is therefore more heterogeneous than that of the single-energy system.

3.6 *Rounded localization transition in experiment*

It must be noted that the result of this thesis were used for the interpretation of an experiment. The rounding of the localization transition was observed in an experimental realization of a two-dimensional fluid in random confinement (Skinner et al., 2013). A binary mixture of superparamagnetic colloidal particles

of disparate size was confined between glass plates. The larger particles acted as spacers and became fixed between the glass plates, serving as the matrix. The smaller particles stayed mobile and served as the fluid compoment. An external magnetic field allowed modifying the interaction between the particles and thus their effective sizes. In this way, it was possible to vary the fluid and matrix packing fractions over a wide range without changing the matrix structure. The MSD of the fluid particles was diffusive at low matrix packing fractions, localized at large matrix packing fractions, and showed subdiffusion on intermediate timescales. With the help of the data of the single-energy case and the confined ideal gas of this thesis, it was made possible to interpret the rounding of this localization transition.

3.7 Summary

This chapter showed that an ideal gas confined in a soft porous matrix exhibits only a rounded localization transition. The system seems to undergo a transition in the long-time dynamics from diffusive dynamics at small particle diameters to localized dynamics at large particle diameters. But it was demonstrated that the observed transition is only an apparent one and the system is expected to become diffusive at all diameters. In contrast, an ideal gas confined by hard-sphere obstacles is equivalent to the Lorentz model and would show a sharp transition.

The destruction of the transition was shown to be a direct result of the soft interaction potential. Particles with higher energies are able to move closer to the soft obstacles, and the distribution of particle energies leads to a distribution of effective matrix densities. This can be completely understood via the hard-sphere mapping discussed in section 2.3. With the mapping, the dynamics of the confined-ideal-gas system can be expressed as an energy average over the Lorentz model dynamics. As a direct demonstration of this, the self-diffusion coefficient was measured as a function of the particle energy and was shown to match the single-energy data of chapter 2 after mapping both onto equivalent hard-sphere diameters.

Because of the high-energy tail of the particles' energy distribution, there is thus always a finite probability of a particle having a large-enough energy to be delocalized, i.e., to have a hard-sphere diameter corresponding to a delocalized system. This was analytically shown in an integral over the delocalized portion of the hard-sphere distribution. Therefore, the apparent critical diameter — at which the system's MSD is subdiffusive over the whole simulation time — is a function of the simulation time.

The averaging of the dynamics leads to a rounding of the apparent transition and the loss of the scaling properties of the Lorentz model. This was observed directly in the van-Hove function and indirectly in the lack of a critical anomalous diffusion regime in the MSD, as well as in the lack of a power-law in the vanishing of the diffusion coefficient. The rounding of the transition is a generic result of having a mobile component with an energy distribution in a soft matrix. It can therefore be expected that it is impossible to observe the ideal Lorentz model localization transition in realistic systems. In line with this, a rounded localization transition has been identified in a experimental model system for heterogeneous media.

The energy distribution not only enhances the dynamics but also generally increases the non-ergodicity parameter of the system, as some particles become strongly localized by their lack of energy. The dynamics is thus far more heterogenous than in the single-energy system.

The rounding of the localization transition also presents a challenge for MCT which predicts sharp transitions. It remains open how one would would be able to incorporate the rounding into the theory.

In the next chapter, the introduction of fluid-fluid interactions and their influence on the effective localization transition will be discussed. Before that, an estimate of the relevance of finite-size effects for the presented results is given.

3.8 Finite-size scaling

Again it is important to rule out finite size effects in the discussed results. For this purpose, the MSD is studied as a function of the system size L for a range of σ_F, analogously to section 2.5. When the MSD is (nearly) unchanged for two different system sizes, the MSD can be considered free of finite size effects. All other studied quantities are less sensitive to finite size effects and need therefore not be discussed, here. In the following, it will be demonstrated that it is typically sufficient to use system size $L = 56.57$, but to fully avoid finite size effects in all systems, system sizes of $L = 160$ or larger are recommended.

The MSD are shown in fig. 3.19 for the tracer diameters $\sigma_F = 0.4$, 0.45, 0.5, 0.6, and 0.7 and for system sizes up to $L = 160$ as given in the legends. The rule of thumb that the MSD is completely free of finite size effects as long as it does not exceed $(L/2)^2$ cannot be used here, because each MSD presents an average over vastly more heterogenous dynamics than in the single-energy case.

Because of the energy distribution of the tracers, nearly all systems contain particles which are effectively at the localization point and are thus very susceptible to finite size effects. Therefore, finite size scaling comes into play in a far wider range of diameters σ_F compared to the single-energy case. Still, the modification of the dynamics due to finite size effects is in general weaker because most systems mostly contain non-critical particles.

Finite size effects at small diameters, e.g. at $\sigma_F = 0.4$, are comparable to the single-energy case (compare to fig. 2.21) and are still very weak. The MSD is nearly unmodified between the two systems, $L = 40$ and 80, therefore $L = 80$ can be considered large enough to obtain reliable results at $\sigma_F < 0.4$. Finite size effects are also weak at very large diameters, e.g. at $\sigma_F = 0.7$. There, some variation in the MSD is found between the system sizes $L = 40$, 56.57, and 80, but this is because it becomes more difficult to sample the void space correctly in highly localized systems.

That finite size effects are not as pronounced in the confined ideal gas compared to the single energy case is visible at $\sigma_F = 0.45$, where the MSD has converged already at $L = 56.57$ instead of still being size dependent at $L = 160$ like the single-energy case.

At $\sigma_F = 0.5$ and 0.6, the MSD completely agrees for the two system sizes $L = 80$ and 160 in the time span simulated for $L = 80$. For this time span, the MSD therefore is free of finite size effects. Even though the MSD nearly

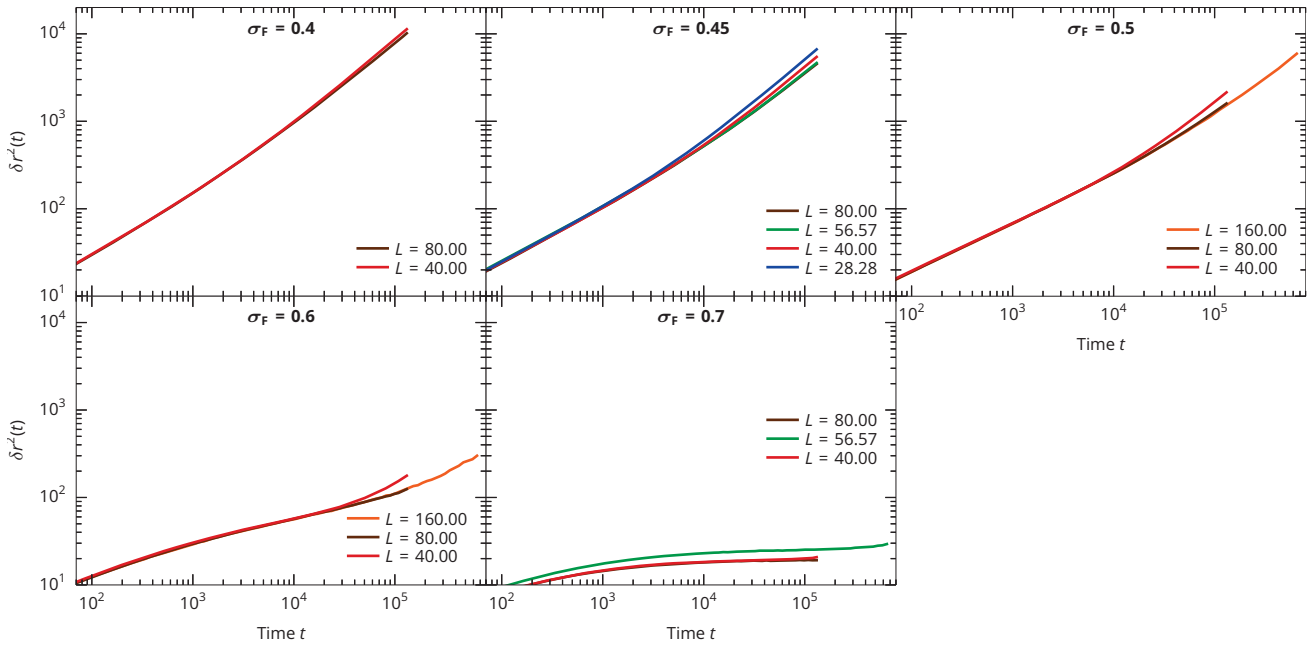

Figure 3.19: Mean-squared displacements of the confined ideal gas for a range of tracer diameters σ_F as indicated in the titles. For each diameter, the simulation box length L was varied as indicated in the legends.

becomes diffusive during that time span, it was not possible to determine the diffusion coefficient and the same extrapolation as in the single-energy case had to be performed. In order to precisely determine the diffusion coefficient, larger system sizes and longer simulation runs would be needed. It must be stressed, however, that even though the magnitude of the diffusion coefficient of these systems could not be exactly determined, it is absolutely clear that some particles in these systems are delocalized. This becomes evident once the energy-resolved MSD is studied for finite size effects, which is done in the following.

For the discussion of the energy-resolved dynamics it was also very important to exclude finite size effects. To determine the energy-resolved diffusion coefficients shown in fig. 3.12, only energies were considered for which the MSD had already become diffusive before crossing $(L/2)^2$, or shortly after. In the energy-resolved dynamics, this criterion is once again applicable. A difficult case is shown in fig. 3.20 for $\sigma_F = 0.5$, where the energy-resolved mean-squared displacement is shown for the two different system sizes, $L = 80$ (dashed lines) and $L = 160$ (solid lines). Both systems are shown to illustrate again the complete agreement between them. The lowest energy for which the diffusion coefficient was calculated was $E = 3.6$, whose MSD becomes diffusive just as it crosses $(L/2)^2$. For larger energies, the MSD becomes diffusive earlier. For these energies, the energy-resolved diffusion coefficient is therefore free of finite-size effects.

This figure also makes it clear that only a very small fraction of the particles can even cause finite size effects at $L = 160$. For all energies $E > 3.6$, the MSD becomes diffusive before the particles travel through the whole system and for energies $E < 2.1$, the larger system indicates localization on a length scale smaller then the simulation size. Therefore only particles with energies $2.1 < E < 3.6$ can even contribute to finite size scaling here.

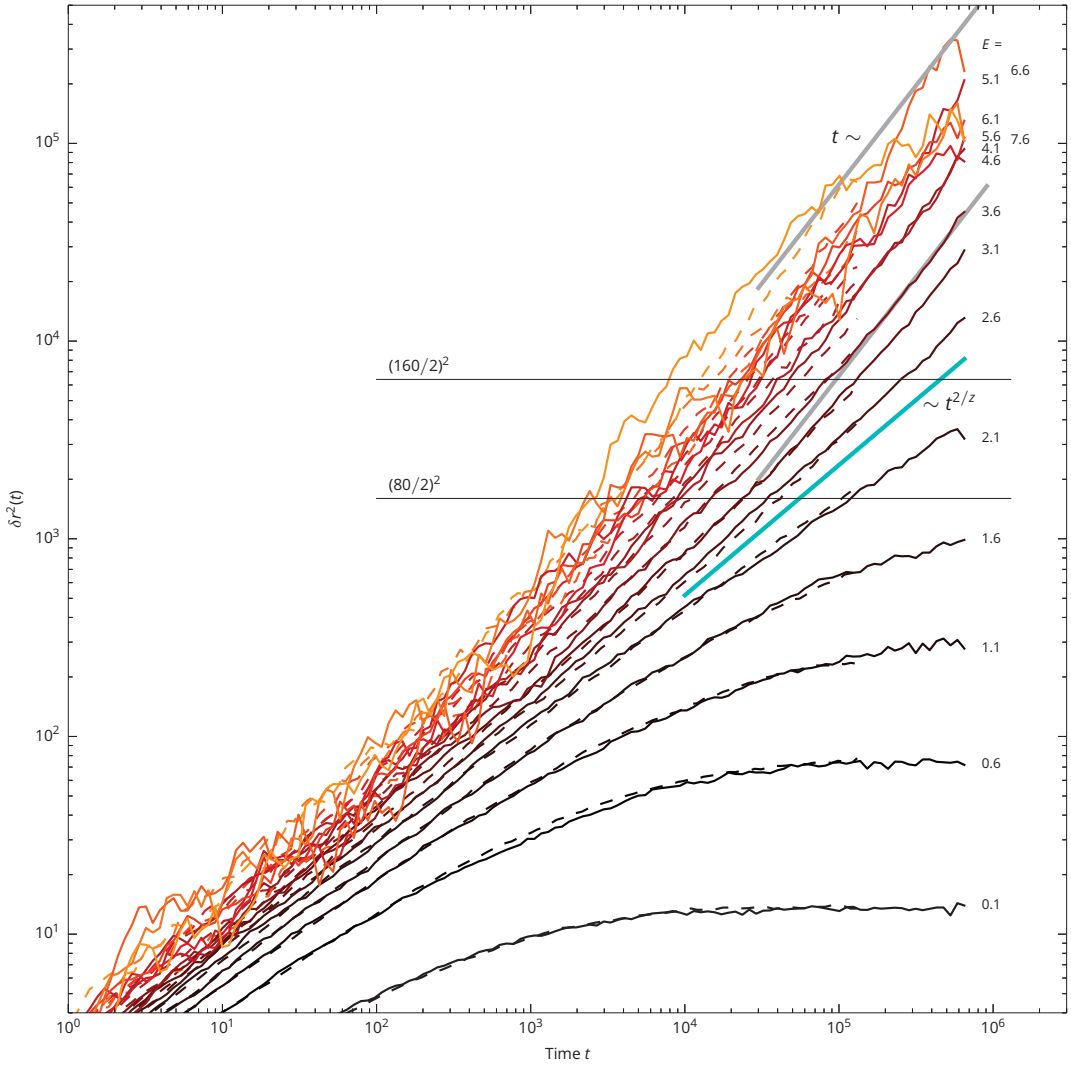

Still, the largest system size used in this work, $L = 160$, is at the lowest acceptable limit for the study of the localization transition. It is strongly recommended for future work that larger systems are studied.

Figure 3.20: Mean-squared displacement of the confined ideal gas for two different system sizes, $L = 80$ (dashed lines) and $L = 160$ (solid lines), resolved for the particle energy E, as labelled in the plot. Horizontal lines mark boundaries above which finite size effects might occur, see section 2.5. A power-law $\sim t^{2/z}$ with the critical exponent $z = 3.036$ is shown as a cyan line. Energy-resolved diffusion coefficients D were determined for energies $E > 3.6$ and the obtained range for D is marked by two broad lines.

4
A soft quenched-annealed mixture

It was shown in the previous chapter, that the introduction of a realistic energy distribution to a soft-sphere Lorentz model rounds the localization transition. Strictly speaking the transition ceases to exist: There is always a finite probability of finding a delocalized tracer particle. Therefore, the system can only ever be localized on the timescale of the simulation. The resulting system retained some of the characteristics of a localization transition but lost all scaling properties of the Lorentz model. In this section it will now be discussed how the dynamics is changed by the final step towards a quenched-annealed system: the introduction of interactions between the mobile particles.

The interaction between the fluid particles has an immediate effect: As particles collide, they exchange energy. Thus, different from the non-interacting case, there is no conservation of the single-particle energy anymore (while the total energy of all fluid particles is still conserved).

As already discussed in section 1.3, a variety of heterogeneous media with an interacting mobile component have shown dynamics partly compatible with a Lorentz-model-like localization transition, including subdiffusion with the correct exponent, slowing down of long-time diffusion and in cases localization upon increasing the density of the matrix. But interesting modifications to the Lorentz-model scenario such as the modification of the anomalous exponent in the hard-sphere QA system of Kurzidim et al. (2009, 2010, 2011) or the reentrance scenario both in the EM systems of Krakoviack (2009, 2010, 2011) and Kim et al. (2009, 2010, 2011), as well as in binary mixtures by Voigtmann and Horbach (2009) have also been observed.

In this chapter, it will be shown that these phenomena can be observed in a soft QA system near an effective localization transition. Increasing the fluid number density while keeping all other parameters constant can lead to a modification of the effective exponent, to a speeding up of the long-time dynamics and to an increase of the localization length, all without modification of the matrix structure. In addition, a reentrance transition is identified. It will be shown that these effects are a superposition of the cooperative dynamics of the particles and the softness of the matrix potential.

Additionally, the effective localization transition at a high fluid density will be studied extensively to determine which aspects of the Lorentz-model transition remain in interacting systems, and which are masked or modified. For this it will be essential to perform an analysis of the scaling properties of the system near the localization transition.

4.1 *Preparation of the fluid component*

The same obstacle matrices are used as in the single energy case and the confined ideal gas. The interaction between mobile particles is introduced by setting the fluid-fluid energy scale of the Weeks-Chandler-Andersen potential to unity, $\varepsilon_{FF} = 1$, see eq. (2.1). Because the mobile particles are now interacting, they are referred to as fluid particles instead of as tracers from now on.

The fluid particle configurations were prepared at temperature $Tk_B = 1$ with one of two different insertion methods, the naïve insertion and the grand-canonical particle insertion, which were already used for the confined ideal gas. The differences in the dynamics for these two insertion methods are negligible and do not affect the following discussion, see appendix A.2.

After inserting all particles, the system is equilibrated at $Tk_B = 1$ by randomly selecting the particle velocities from the Maxwell distribution every 100 time steps for at least 10^6 steps and up to $2 \cdot 10^8$ steps. This presents a simplified version of the Andersen thermostat (Andersen, 1980). Because of the interactions between the fluid particles, the equilibration time becomes considerably longer compared to the confined ideal gas and increases greatly with the density of the fluid particles. After equilibration, production runs are performed in the micro-canonical regime, with simulation times extending up to but not exceeding the equilibration time. For this purpose, all individual systems are brought to the same energy — the average energy of all systems during the equilibration run — by rescaling all fluid velocities uniformly.

State diagram Through the interaction of the fluid particles, the system gains an additional control parameter: the number density of fluid particles n_F,

$$n_F := \frac{N_F}{L^2}.$$

Variation of n_F and σ_F both change the reduced number density $n_F^* := \sigma_F^2 n_F/4$ of fluid particles in the system but in general have a different effect on the dynamics.

The effect of the interactions on the dynamics was studied systematically with a range of simulations, where n_F and σ_F were varied independently. All simulated states are displayed in fig. 4.1. The states where the MSD became diffusive during the simulations, i.e. for $t < 7 \cdot 10^5$, are marked as delocalized (○), whereas all other states are marked as effectively localized (×). The points are connected by lines to indicate paths along which the modification of the dynamics will be discussed in the following. The confined-ideal-gas case of the previous section represents the $n_F \to 0$-limit of the interacting case. Starting from the confined-ideal-gas case, n_F was increased for constant σ_F to study the modification of the dynamics by the gradual increase of the interaction between particles. This was performed in three cases, at $\sigma_F = 0.5$ to study the delocalized side, at $\sigma_F = 0.8$ to study the localized side and at $\sigma_F = 0.65$ to study the reentrance transition. This allows for comparison to the speeding up of dynamics close to the transition reported in the literature. Additionally, a path at constant $n_F = 0.625$ but varying σ_F was used to cross the localization transition and study the modification of said transition by the interaction of the particles. This provided the opportunity of testing scaling predictions of the Lorentz model.

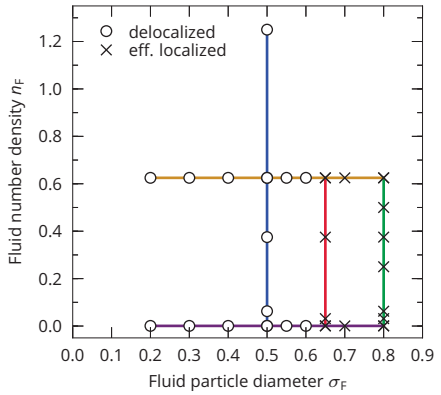

Figure 4.1: Plot of the explored parameter range with all simulated state points marked as points along 4 paths in the interacting fluid case. For $n_F = 0$, the states of the confined ideal gas are shown. The states where the MSD became diffusive during the simulations, i.e. for $t < 7 \cdot 10^5$, are marked as delocalized (○), whereas all other states are marked as effectively localized (×).

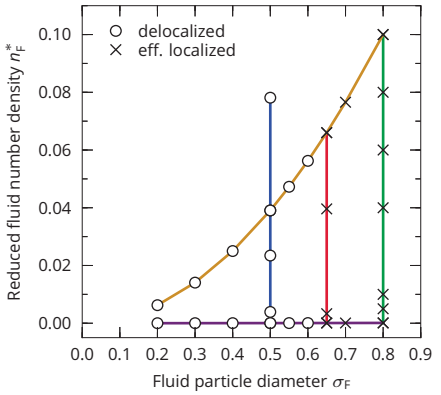

Figure 4.2: Plot of the explored parameter range with all simulated state points marked as points along 4 paths in the interacting fluid case in the space of reduced number density n_F^* and fluid particle diameter σ_F. For $n_F^* = 0$, the states of the confined ideal gas are shown. The states where the MSD became diffusive during the simulations, i.e. for $t < 7 \cdot 10^5$, are marked as delocalized (○), whereas all other states are marked as effectively localized (×).

As the particles change their energy over time, particles cannot be assigned a constant effective hard-sphere diameter. So an exact mapping of the system onto the Lorentz model is not possible anymore. However, the effective hard-sphere distribution of the system will still prove valuable for the analysis.

It is furthermore important to stress that the Lorentz model cannot be exactly recovered in the quenched-annealed system. The $n_F \to 0$ limit recovers only the confined ideal gas with its rounded transition.

Simulation snapshot The positional data obtained over a whole simulation run with an interacting fluid look very similar to the confined ideal gas. In fig. 4.3, all the positions recorded in a single simulation run with interacting fluid particles at $n_F = 0.625$ are shown as dark grey points, overlaying the obstacles shown in light grey with an effective hard-sphere diameter calculated from the average particle energy with eq. (2.11). For the same obstacle matrix with a confined ideal gas with the same number of fluid particles, the positional data is shown in fig. 3.2 on the right.

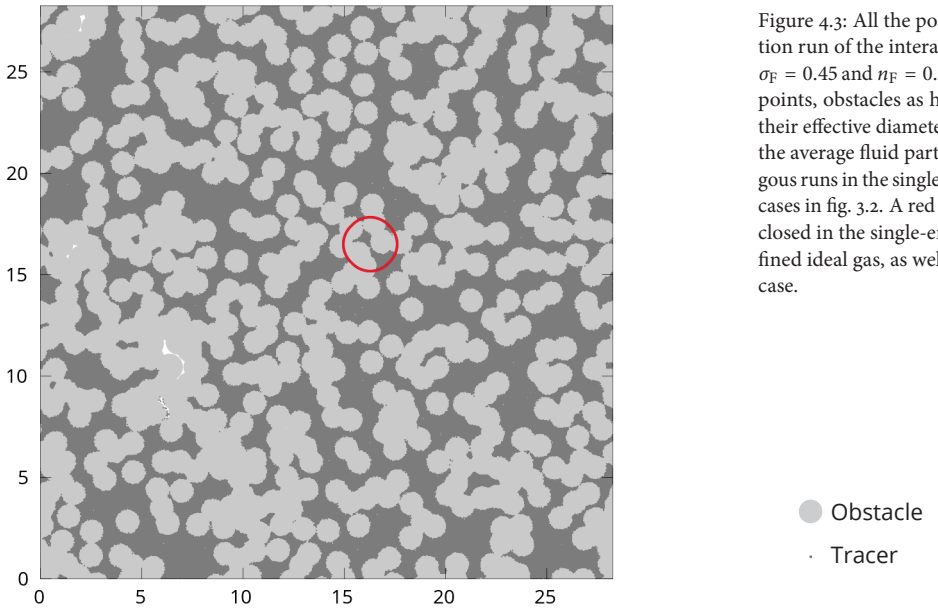

Figure 4.3: All the positional data of a single simulation run of the interacting fluid system over time at $\sigma_F = 0.45$ and $n_F = 0.625$. Fluid particles as dark grey points, obstacles as hard-spheres in light grey with their effective diameter calculated from eq. (2.11) and the average fluid particle energy. Compare to analogous runs in the single-energy and confined-ideal-gas cases in fig. 3.2. A red circle marks a channel which is closed in the single-energy case but open in the confined ideal gas, as well as in the quenched-annealed case.

4.2 *Dynamics I: Increasing the number of fluid particles speeds up the dynamics*

To study the effect of the interaction on the dynamics systematically, it is useful to gradually increase the number density n_F of interacting particles in the system. This scenario will be studied on the delocalized side at constant $\sigma_F = 0.5$, on the localized side at $\sigma_F = 0.8$, and at $\sigma_F = 0.65$ as an edge case showing the reentrance transition. For these paths through the state diagram, the confined ideal gas then serves as the starting point, as it is represents the $n_F \to 0$-limit of the interacting case. This procedure is analogous to the ones used in Krakoviack's, Kim's, and Voigtmann and Horbach's work, where the fluid density was increased while keeping all other parameters constant, and thus provides excellent opportunity for comparison.

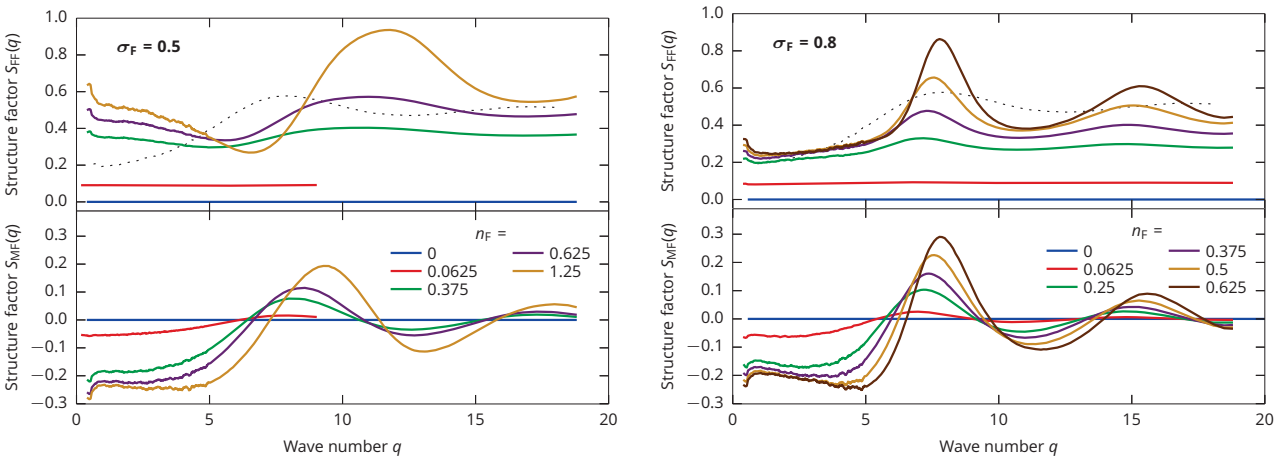

Figure 4.4: The partial structure factors $S_{FF}(q)$ and S_{MF} as a function of the wavenumber q. *Left, top:* Fluid-fluid structure factor $S_{FF}(q)$ at $\sigma_F = 0.5$ for a range of fluid number densities as indicated in the legend below. The dotted line gives the partial structure factor of the matrix $S_{MM}(q)$ (redrawn from fig. 2.2). *Left, bottom:* Fluid-matrix structure factor $S_{MF}(q)$ at $\sigma_F = 0.5$ for the same densities. Centered moving average applied to all partial structural factors to reduce statistical noise. *Right, top and bottom:* Same as on the left, but for $\sigma_F = 0.8$.

The introduction of interaction between fluid particles directly changes the structure of the mobile component. As a measure of the strength of the interactions, which will be relevant for the interpretation of the dynamics, it is therefore relevant to study the structure.

Structure The amplitude of the structure factor grows with increasing n_F. As an example, the partial structure factors S_{FF} and S_{MF} as introduced in section 2.1.3 are shown in fig. 4.4 *(left, top and bottom)* for a range of systems with constant $\sigma_F = 0.5$ where the number density was gradually increased. This system is on the delocalized side of the transition. For reference, the matrix structure factor is given as a black dotted line. The normalization is such that the partial structure factor $S_{FF}(q)$ tends at large wavenumbers to the concentration of fluid particles, $S_{FF}(q \to \infty) \to n_F/(n_F + n_M)$. The large wavenumber limit of S_{MF} is given by $S_{MF}(q \to \infty) \to 0$. The structure factor in the limit $n_F \to 0$ is entirely given by the normalization, $S_{FF}(q) \propto n_F/(n_F + n_M) \to 0$ and $S_{MF}(q) = 0$. It must be stressed that a confined ideal gas with a large number of non-interacting particles has a fluid-fluid structure factor different from that since its number density is not 0, but that the dynamics of the $n_F \to 0$-system and the confined ideal gas are the same.

For the smallest simulated number density $n_F = 0.0625$, the partial structure factors have nearly no structure. The fluid-fluid structure factor $S_{FF}(q)$ is simply at constant $n_F/(n_F + n_M)$, indicating no correlations at all in the system. Structurally, this system is still extremely close to the ideal gas. This is relevant to note, as the dynamics at even this low density will be shown to be different from the ideal gas scenario already. At $n_F = 0.375$ the structure factor's amplitude grows. The structure factor becomes more pronounced for $n_F = 0.625$ and $n_F = 1.25$, and develops a maximum which moves to larger q as the density is increased. At the highest shown density, $n_F = 1.25$, the location of the maximum is at $q \approx 11.8$, close to $2\pi/\sigma_F \approx 12.6$, which points towards dense packing of fluid particles. At that density, the fluid contains more structural correlations than the matrix itself. In accordance with the behavior of $S_{FF}(q)$, the matrix-fluid partial structure factor S_{MF}, which is shown as in fig. 4.4 (left, bottom), also increases in amplitude as n_F increases.

The structure factor behaves similarly at larger diameters where the system is localized, e.g. for $\sigma_F = 0.8$, which is shown in fig. 4.4 *(right)*. The structure

factor for the $n_F \to 0$-limit is given as a constant $S_{FF}(q) = 0$. For very small number densities, e.g. $n_F = 0.0625$, the structure factor does not show any correlations and $S_{FF}(q) = n_F/(n_F + n_M)$ at all finite q. Structurally, the system is thus nearly indistinguishable from the $n_F \to 0$-limit. Only at far larger number densities the fluid-fluid correlations start to play a role. A main peak develops, which moves with increasing number density. At the highest number density $n_F = 0.625$ the peak is at $q \approx 7.9$ which is nearly exactly $2\pi/\sigma_F$ indicating that the fluid particles are densely packed. Again, $S_{FF}(q)$ has a higher amplitude than $S_{MM}(q)$ at the highest densities, indicating that the fluid is more correlated than the matrix. The partial matrix-fluid structure factor $S_{MF}(q)$ increases in amplitude as well as n_F is increased.

The structure factors will become relevant for the discussion of the dynamics. Another important property of the system for that discussion is the energy distribution of particles. In chapter 3 the energy distribution of particles was shown to be of great relevance to the dynamics as it is directly responsible for the rounding of the localization transition. The introduction of interactions between the fluid particles naturally modifies the energy distribution and precisely this modification will be analyzed in the following section.

Energy distribution Because of the added interaction, the average energy per particle generally increases. Unfortunately, the calculation of the energy distribution and the estimation of its effect on the dynamics is not as straightforward as in the ideal-gas case. Because the particles exchange energy regularly the energy per particle is not conserved anymore. This in turn means that it is not possible to calculate a constant effective hard-sphere diameter of the obstacles for each fluid particle. Rather, each particle will at any given time explore the matrix with an effective hard-sphere diameter corresponding to its present energy, and the effective hard-sphere diameter of the surrounding obstacles will fluctuate with the energy. Still, in equilibrium the energy distribution itself can be expected to be time-independent. Importantly, the fraction of particles with energies corresponding to a delocalized state will remain also time-independent. This makes it still worthwhile to determine the energy distribution of the fluid particles.

It is not immediately clear how to assign the potential energy of a pair of fluid particles to the individual particles. One way of doing it is assigning each particle half of the pair's potential energy.[1] If the set of indices of the obstacle particles is called I_M and the set of indices of the fluid particles is called I_F, then the total energy of the system E is given by

$$E = \sum_{j \in I_F} \frac{1}{2} m \vec{v}_j^2 + \sum_{j \in I_F} \sum_{k \in I_M} V(|\vec{r}_j - \vec{r}_k|) + \frac{1}{2} \sum_{j \in I_F} \sum_{k \in I_F, k \neq j} V(|\vec{r}_j - \vec{r}_k|).$$

Therefore, the energy E_j of an individual fluid particle with index j is then comprised of its kinetic energy, its potential energy coming from the interaction with the obstacles, and half of the potential energy coming from the interaction with the other fluid particles

$$E_j = \frac{1}{2} m \vec{v}_j^2 + \sum_{k \in I_M} V(|\vec{r}_j - \vec{r}_k|) + \frac{1}{2} \sum_{k \in I_F, k \neq j} V(|\vec{r}_j - \vec{r}_k|).$$

Mainly the last sum of this equation increases with introducing more interacting particles into the system but also the potential energy of the interaction

[1] Why each particle gets half of the pair potential energy can be motivated simply. Place a pair of identical fluid particles into void space without any obstacles and at a short enough distance, so that they have some potential energy. Then, they will move apart and the potential energy will be transformed into kinetic energy. Because the particles are identical, each will obtain half of the energy.

with obstacles as fluid particles get pushed closer to the obstacles by their neighbors.

The single-particle energy distribution $p(E)$ is then defined as as an integral over the phase space accessible to the particle at the given energy E,

$$p(E) := \left\langle \delta(E_j(r,v) - E) \right\rangle,$$

equivalently to eq. (3.1) in the confined ideal gas. In practice, the distribution is calculated in the simulation with a discrete binning of the particle energies, as already discussed for the confined ideal gas. The largest energy for which the distribution is calculated is typically 8, in some cases 12. With this, it is made sure that the measured distribution reflects the energies of most if not all particles in the system. In the discussed systems, typically far less than 0.2% of the particles are ignored because their energy is too large for the histogram implementation.

In the case of the delocalized system at $\sigma_F = 0.5$, the energy distribution of interacting fluid particles $p(E)$ is shown in fig. 4.5 *(top)* for increasing number density n_F. The confined-ideal-gas case is shown as the $n_F \to 0$ limit. For $n_F = 0.38$, the probability of a particle having $E < 1$ is only very slightly diminished in relation to the confined ideal gas. Apart from this, the distribution is nearly unchanged. One has to go to higher number densities to find strong modification of the energy distribution. For $n_F = 1.2$, the probability of finding a particle with low energy is greatly diminished and the energy distribution broadens noticeably. Similarly to the confined ideal gas at large σ_F, the high-energy tail of the energy distribution is found to increase in amplitude at large number densities. But in contrast to the situation there, this is not associated with an increase in temperature, here.

The same general trend can be observed at $\sigma_F = 0.65$, shown in fig. 4.5 *(middle)*. The distribution is unchanged from the confined ideal gas at $n_F = 0.031$ and begins to broaden at $n_F = 0.625$.

On the effectively localized side of the transition, the energy distribution behaves similarly. Exemplarily, for $\sigma_F = 0.8$, the energy distribution is shown in fig. 4.5 *(bottom)* for increasing number density n_F. Compared to the previous two cases, the energy distribution is more susceptible to an increase of n_F and the broadening of the distribution becomes quite pronounced.

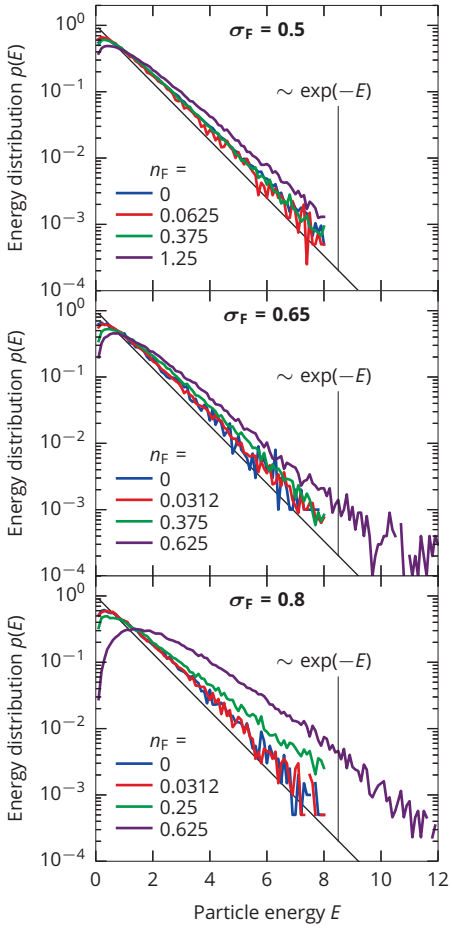

Figure 4.5: Energy distribution $p(E)$ of the interacting fluid system at $\sigma_F = 0.5$, 0.65 and 0.8 *(top to bottom)* where the fluid number density is varied as indicated in the legend.

Distribution of the effective hard-sphere diameter The hard-sphere diameter distribution $p(\sigma_{hs})$ is a powerful tool, since it allows discussing the modification of the effective localization transition quantitatively even though strictly speaking there is no localization transition anymore: a shift of $p(\sigma_{hs})$ relative to the critical hard-sphere diameter σ_{hs}^c constitutes a shift of the localization transition.

From $p(E)$, the distribution of the effective hard-sphere diameter $p(\sigma_{hs})$ was calculated with the help of eqs. (3.2-3.4) and is displayed for $\sigma_F = 0.5$ in fig. 4.6 *(top)*. Large fluid particle energies E are mapped onto small σ_{hs}. The critical hard-sphere diameter $\sigma_{hs}^c \approx 1.31$ as determined in section 2.3 is marked by a vertical black line. Diameters $\sigma_{hs} < \sigma_{hs}^c$ correspond to particles currently experiencing a percolating system (but they may still be localized in a closed-off pocket). Increasing n_F only slightly modifies the whole distribution. Generally, at $\sigma_F = 0.5$ the peak of the distribution — whose position is mostly determined

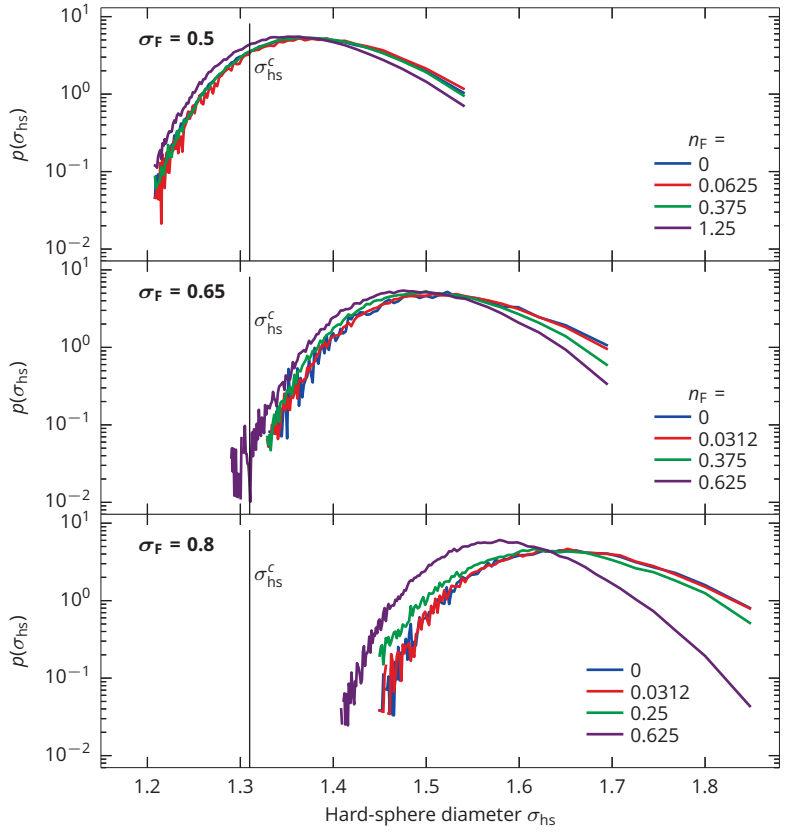

Figure 4.6: *Top:* Effective hard-sphere diameter distribution $p(\sigma_{hs})$ of the interacting fluid system at $\sigma_F = 0.5$ and a range of fluid number densities n_F. The distribution $p(\sigma_{hs})$ was calculated with eq. (3.2) with the numerically obtained $p(E)$. The critical effective hard-sphere diameter $\sigma^c_{hs} = 1.31$, at which the localization transition occurs, is marked with a black vertical line. *Middle:* The same for $\sigma_F = 0.65$. *Bottom:* The same for $\sigma_F = 0.8$.

by the value of σ_F — is on the localized side. Therefore, most particles are localized at any given time. In the cases $n_F = 0$, 0.062, and 0.38, the distribution is nearly unchanged. For $n_F = 1.2$, the maximum of the distribution shifts slightly towards σ^c_{hs}, indicating that more particles ought to be delocalized at any given time. This indicates the shift of the localization transition towards higher σ_F. This statement concerns itself only with the topology of the void space, of course, and completely neglects other localization mechanisms like the glass transition.

For the effectively localized case at $\sigma_F = 0.8$, $p(\sigma_{hs})$ is shown in fig. 4.6 *(bottom)*. The whole measured distribution at all n_F is to the right of σ^c_{hs}, i.e. all particles of the simulation are localized. This is not to say that a larger simulation with more particles would not show $p(\sigma_{hs}) > 0$ for $\sigma_{hs} < \sigma^c_{hs}$, and would thus be delocalized. As was the case for $\sigma_F = 0.5$, the distribution is nearly unchanged for the small number densities $n_F = 0$, 0.031, and 0.25, but becomes shifted towards smaller σ_{hs} at $n_F = 0.62$.

This generic shift of the distribution upon increasing n_F should lead from effective localization to delocalization in a system sitting closer to the localization transition. Exactly such a situation occurs at $\sigma_F = 0.65$, the $p(\sigma_{hs})$ of which is shown in fig. 4.6 *(middle)*. At small diameters $n_F \leq 0.375$, the whole measured distribution $p(\sigma_F)$ is fully on the localized side and thus the system is effectively localized. But the shift of $p(\sigma_{hs})$ in the denser system at $n_F = 0.625$ is large enough to allow particles to become delocalized, i.e. $p(\sigma_{hs} < \sigma^c_{hs}) > 0$ for some σ_{hs}. The system thus becomes delocalized solely by increasing the number of fluid particles. This constitutes a reentrance transition.

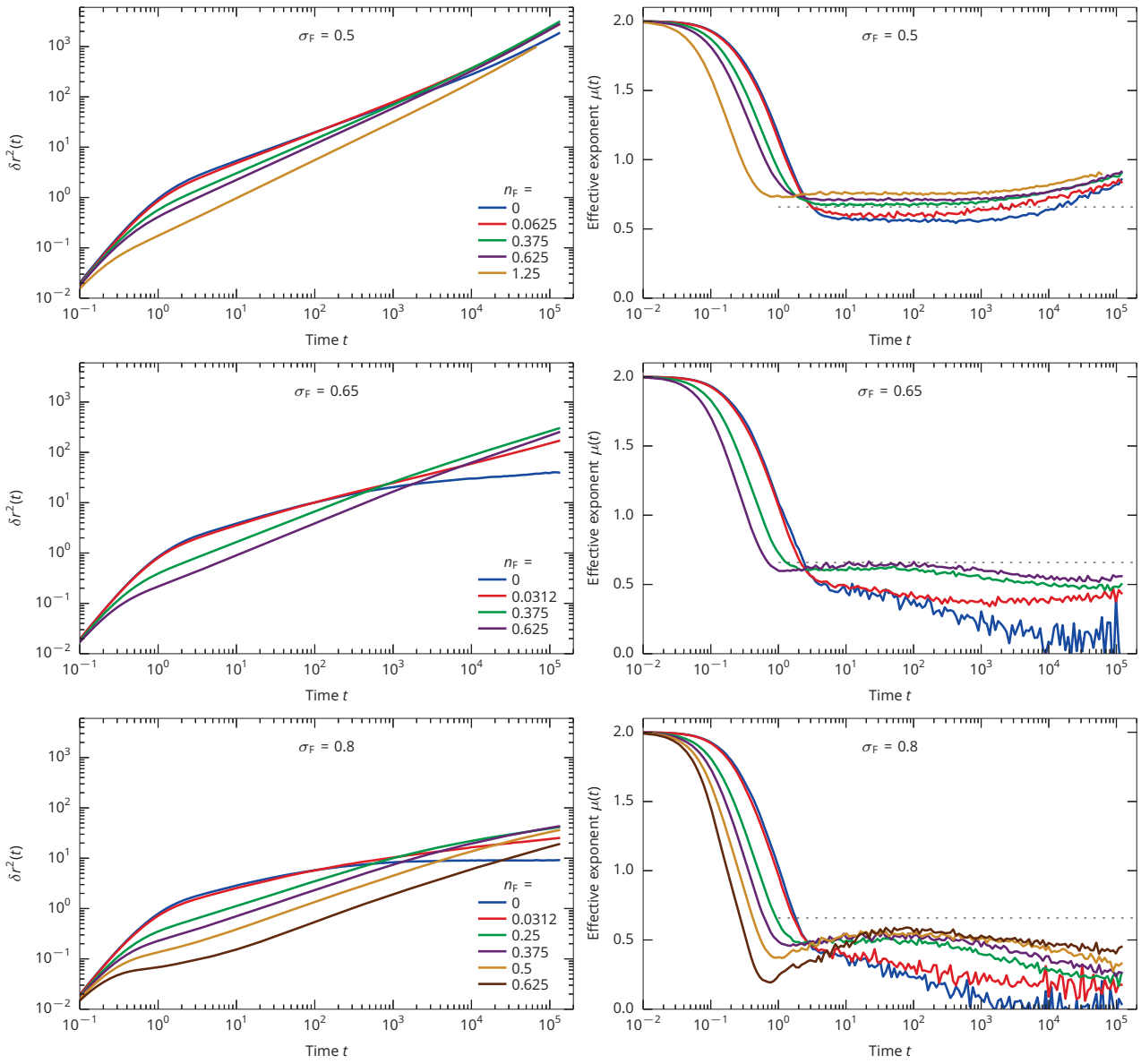

Figure 4.7: *Left:* Mean-squared displacements of the interacting-particle system for $\sigma_F = 0.5$ *(top)*, 0.65 *(middle)* and 0.8 *(bottom)*, and a range of n_F as indicated in the legends. *Right:* Effective exponent $\mu(t)$ for the same data. The exponent of the Lorentz model $2/z = 2/3.036$ is given by the dotted line.

The discussion of the hard-sphere diameter distribution is only merited if the distribution reflects the actual dynamics. This will be confirmed in the following.

Dynamics on the delocalized side The dynamics of the system undergoes strong changes on both sides of the transition as the number of fluid particles is increased. The MSD at $\sigma_F = 0.5$ as the example for a delocalized system is shown in fig. 4.7 *(top, left)* for a range of n_F. The confined ideal gas ($n_F = 0$) shows subdiffusion on intermediate times before becoming diffusive at long times. All studied systems at $\sigma_F = 0.5$ stay delocalized, which could be anticipated from the effective hard-sphere distributions. The MSD at $n_F = 0.062$, while nearly unchanged at small and intermediate times, shows considerably enhanced long-time diffusion. This notably happens even though structurally the system is very much like the confined-ideal gas system (see fig. 4.4) and the energy distribution is nearly unchanged.

It is thus most likely that this speeding up of the dynamics stems from the *exchange* of energies between particles. Thus more particles have a high energy at some point during the simulation and are then able to escape void pockets and explore more of the void space. With this, a speeding up of the dynamics is possible *without modification of the energy distribution* itself and does not represent a shift of the localization transition. That the variation in the fluid particle energy has such an effect on the dynamics is most likely only possible in systems with soft interactions, where the barriers between void pockets are finite and thus surmountable by particles with large energy.

The MSD for the cases $n_F = 0.38$ and 0.62 are decreased on short and intermediate times compared to the confined ideal gas. This happens because collisions of particles with their neighbors slow down the exploration of the void volume. But at long times the MSD catch up with the system at $n_F = 0.062$. Both are still weakly structurally correlated and the energy distribution is nearly unchanged. At the highest simulated number density, $n_F = 1.2$, the dynamics is further slowed down on intermediate timescales, associated with the now strong structural correlations in $S_{FF}(q)$. At long timescales, the diffusion has slowed down compared to the systems at intermediate n_F but is very similar to the confined-ideal-gas case. This happens even though a larger fraction of particles is delocalized at any given time than in the less dense systems. This indicates increasing competition in the long-time dynamics between the speedup via frequent energy exchange between particles and the slowing down via the repulsion of particles by their immediate neighbors. This data shows that a speeding up of the long-time dynamics is not necessarily caused by a shift of the localization transition and vice versa.

Along with the slowing down on intermediate timescales, the effective exponent of the MSD changes, which is defined as

$$\mu(t) := \frac{\mathrm{d}(\log \delta r^2(t))}{\mathrm{d}(\log t)}.$$

This quantity gives the apparent exponent of the MSD at any time. In the ballistic regime at short times it reads $\mu(t \to 0) = 2$, while at long times in the diffusive regime it assumes the value $\mu(t \to \infty) = 1$. In the case of critical subdiffusion, where the MSD follows a power-law $\delta r^2(t) \sim t^{2/z}$ for an extended time, the effective exponent reads $\mu(t) = 2/z$ and thus allows identifying subdiffusive regimes where the MSD follows a power-law for an extended time. The effective exponent of the MSD is plotted in fig. 4.7 *(top, right)*. For comparison, the critical exponent of the two-dimensional Lorentz model is drawn in as $2/z = 2/3.036$ (dotted black line). This plot exposes that for all 5 systems a regime can be identified where the effective exponent is constant over at least two decades in time. It can be easily read off that increasing n_F increases the subdiffusion exponent from below $2/z$ for the ideal gas case to above it for the denser systems. This demonstrates that the exponent of the subdiffusive regime can be readily tuned via the number density. In the case of $n_F = 0.38$, the exponent nearly matches $2/z$ which should be seen as accidental as the system is still clearly diffusive at long times.

Dynamics on the localized side For effectively localized systems a similar modification of the dynamics is found. As an example, the MSD for $\sigma_F = 0.8$

and a range of n_F is shown in fig. 4.7 *(bottom, left)*. Again, the ideal gas case represents the $n_F \to 0$ limit which shows a clearly localized system.

Increasing the number density to $n_F = 0.031$ leaves the dynamics on short and intermediate times unchanged. More relevant is the strong increase of the localization length, which can be observed even though the interaction between the mobile particles slows down the approach of the MSD to the long-time limit, so much so that it does not converge over the course of the simulation. It can be seen from fig. 4.6 *(bottom)* that the energy distributions of the ideal gas case and $n_F = 0.031$ system are practically the same as encounters between fluid particles are still rare. Just as in the delocalized system, the exchange of energy between particles leads to more particles having a large energy at some point during the simulation. At some point most particles will have a higher energy than their original energy and will thus be more likely to escape their original pocket than a non-interacting tracer in the ideal gas. This then leads to the observed increase in the localization length.

At $n_F = 0.25$, the dynamics on intermediate times begins to slow down, just as on the delocalized side. The localization length increases again. This coincides with a change in the energy distribution and thus a slight shift of the effective hard-sphere diameter distribution $p(\sigma_{hs})$ towards σ_{hs}^c.

As the number density is further increased, the short and intermediate times dynamics become slower, as particles are increasingly deflected by their mobile neighbors. The slowing down becomes so strong at the two densest simulated systems ($n_F = 0.5$ and 0.62) that a plateau is starting to form in the MSD, which is associated with the caging localization mechanism of the glass transition. The onset of the plateau is more prominently visible in the effective exponent $\mu(t)$ of the MSD shown in fig. 4.7 *(bottom, right)* where it shows up as a strong dip in $\mu(t)$ at $t \approx 1$. The long-time dynamics is a little more complex. At $n_F = 0.38$ the localization length seems to approach the same value as for $n_F = 0.25$ and then possibly decreases again for higher densities. To confirm this, it would be necessary to far extend the simulation time, which was unfeasible. At these high densities, the effective particle distribution is strongly shifted towards the critical σ_{hs}^c which would indicate that the localization length always increases with increasing n_F, but that this is masked by the general slowing down of the dynamics due to increased caging. At all simulated finite number densities the localization length exceeds its value in the confined ideal gas.

Effective reentrance transition The system at $\sigma_F = 0.65$ presents an intermediate case, the MSD of which is shown in fig. 4.7 *(middle, left)*. At $n_F \to 0$, the system appears localized. The corresponding distribution $p(\sigma_{hs})$ gives indication that even though most if not all particles in the system are localized, a few are very close to the localization transition. This is reflected in the MSD as very slight growth over the whole course of the simulation. Still, on the timescale of the simulation, the system is localized. Upon increasing n_F the localization length increases while the intermediate-time dynamics slow downs. At very high densities, is difficult to tell whether the systems are delocalized or not from the MSD alone. Still, long-time diffusion of the MSD can be anticipated from the upward bend in the effective exponent $\mu(t)$ in fig. 4.7 *(middle, right)* at long times for all finite densities. This would be in agreement with the energy distribution in fig. 4.6 *(middle)*, which indeed indicated the delocalization of

some particles at any given time and which would also imply that MSD will eventually become diffusive. Since, strictly speaking, all soft systems must be considered delocalized, the transition from effectively localized to visibly delocalized upon increasing the number density of the fluid component does not strictly constitute a reentrance transition. But with the knowledge about the shifting of $p(\sigma_{\mathrm{hs}})$ as a function of the number density, a case for the shift of the localization transition towards larger σ_{F} and thus a reentrance transition at constant σ_{F} can be made.

Discussion In conclusion, three distinct mechanisms were identified here, which are all a result of the introduction of interactions between fluid particles:

1. After first introducing fluid interactions at very small fluid densities, particle energies are frequently changed in collisions, which makes the long-time dynamics speed up and the localization length increase. For this neither a modification of the structure of the system nor a change in the energy distribution is needed. In effect, this means that particles help each other over barriers in the matrix, simply be exchanging energy. This mechanism *does not* shift the localization transition, i.e. it does not shift the hard-sphere diameter distribution relative to the critical diameter.

2. Further increasing the number density starts to modify the energy distribution such that the effective hard-sphere distribution is shifted relative to the critical diameter and towards smaller values. Among other things, this can lead to delocalization of a previously localized system, creating a reentrance transition. The reentrance corresponds directly to a shift of the localization transition towards larger diameters σ_{F} at constant number density. This mechanism does not necessarily increase the long-time diffusivity but definitely increases the localization length. That the long-time diffusion would not necessarily be enhanced is due to the competition with the following effect.

3. The increased density also leads to caging of particles by their neighbors, which slows down the dynamics of the system in general. This is most easily identified on intermediate timescales where the caging does not directly compete with the previously described mechanisms. This mechanism will typically lead to a glass transition, the localization of the particles on the length scale of neighbor-to-neighbor distance, at large fluid number densities. This would be in line with MCT predictions for such systems.

The rounding of the localization transition along with the superposition of the latter two mechanisms makes detecting a shift of the transition difficult from the MSD alone. A speeding up of the long-time diffusion or the increase of the localization length cannot necessarily be seen as a signature of such a shift. Here, it was possible to mend this problem by determining the effective hard-sphere distribution of the system. If the whole distribution of the system is on the localized side of $\sigma_{\mathrm{hs}}^{\mathrm{c}}$, the system will be localized. If not, the system will be delocalized. A shift of the localization transition then is represented by a shift of the hard-sphere diameter distribution. The exponential tail of the particle energy distribution implies that all systems are in principle delocalized but systems at large σ_{F} only on timescales inaccessible to simulation.

The presented observations are qualitatively similar to the results in the literature discussed earlier. The same speeding up of the long-time dynamics in a delocalized system as well as the increase of the localization length upon increasing the fluid density were observed in the EM system of Kim et al. (2009, 2010, 2011). There, it was argued that a structural change in the matrix led to a shift of the localization transition which in turn increased the diffusivity of the system, which was further corroborated by Krakoviack (2009, 2010, 2011) in a MCT study for a similar system. Moreover, it was argued that the structural rearrangement was strictly necessary to allow for such a shift. But here a different, simpler situation presents itself: In the presented system the matrix structure is completely independent from the fluid component. Thus the speeding up of the dynamics was achieved *without* the modification of the matrix structure. The only property needed for this to happen was that the fluid particles interact with each other and with the matrix via a soft potential along with an increase in the fluid number density.

Strikingly, in Kim et al. (2011) a reentrance transition was observed for a close to the localization transition, which was localized at small fluid densities and became delocalized at high fluid densities. This was evidenced by the transition of the MSD from slowly converging towards a constant long-time limit at low densities to being clearly diffusive at larger densities. Such a reentrance can indeed be caused by the modification of the matrix structure by the fluid component, as discussed by the authors. Still, very similar dynamics was observed here at $\sigma_F = 0.65$, which was only different in that the simulation time was not long enough to clearly expose the diffusive behavior at the higher densities.

The presented observations also qualitatively match the dynamics of the smaller component in the glassy binary mixture studied by Voigtmann and Horbach (2009). The mobile, fluid component showed slower long-time dynamics when the interactions between the mobile fluid particles were switched off compared to the case when the interaction were switched on. There, notably, little to no change was observed in the matrix-matrix structure factor in the simulation upon switching off the interaction. This indicates that not the restructuring of the matrix was the reason for the speeding up of the dynamics. The speeding up of the dynamics was found to be compatible with a standard MCT calculation taking the simulation's partial structure factors as input. The system with switched off interactions had a localization transition at a smaller matrix density than the system with switched on interactions. This invites the interpretation that in MCT the shift of the transition is entirely due to the modification of the fluid structure. In the terms of the present discussion, the modification of the fluid structure might well be associated with a large enough modification of the energy distribution to account for the observed shift in the localization transition.

To provide a complete characterization of the system's dynamics, the van-Hove function and the intermediate scattering function will be discussed briefly in the following.

Van-Hove function The self-part of the van-Hove function $P(r, t)$ for the delocalized path at $\sigma_F = 0.5$ is shown in fig. 4.8. The most striking changes

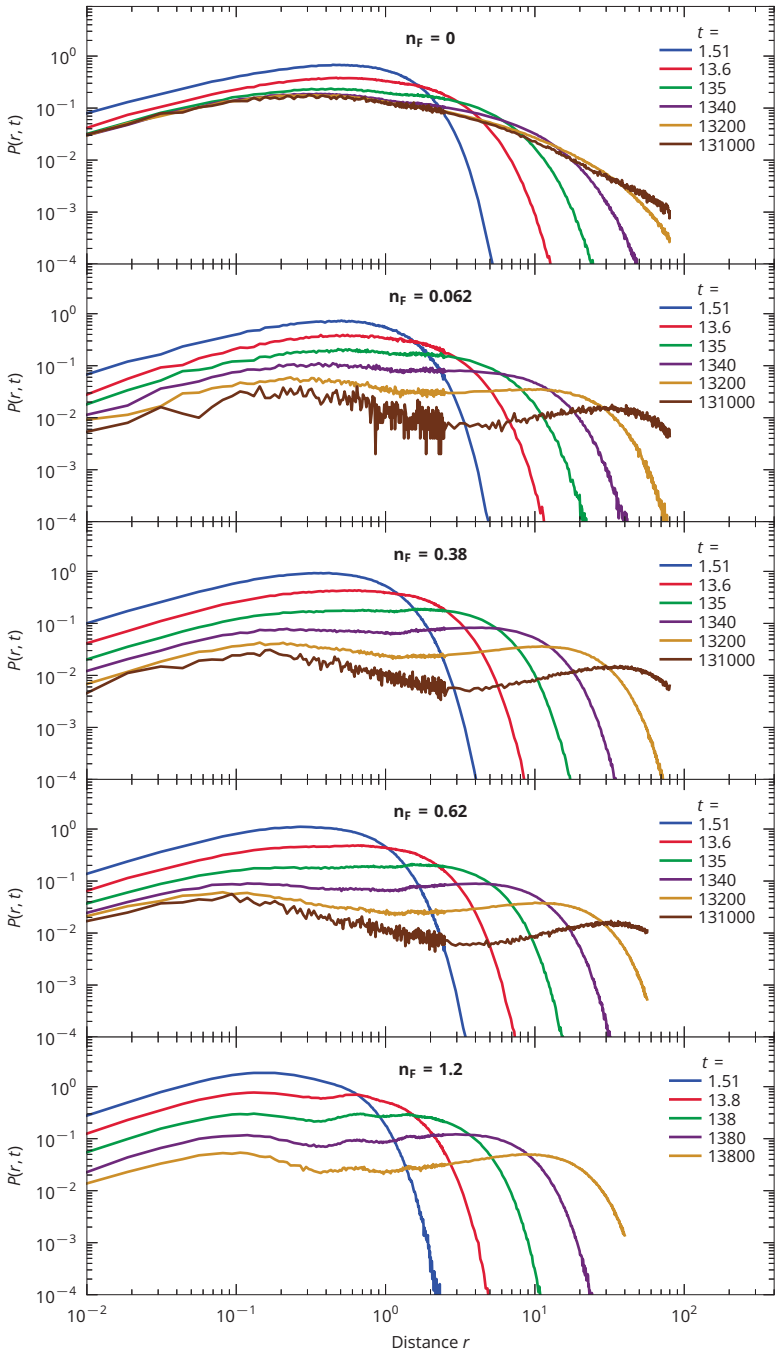

Figure 4.8: Plot of the self-part of the van-Hove function $P(r,t)$ of the interacting fluid component for $\sigma_F = 0.5$ and a range of fluid number densities $n_F = 0$ (ideal gas), 0.062, 0.38, 0.62, and 1.2 as indicated in the titles. $P(r,t)$ is shown as a function of distance r for a range of times t as indicated in the legends.

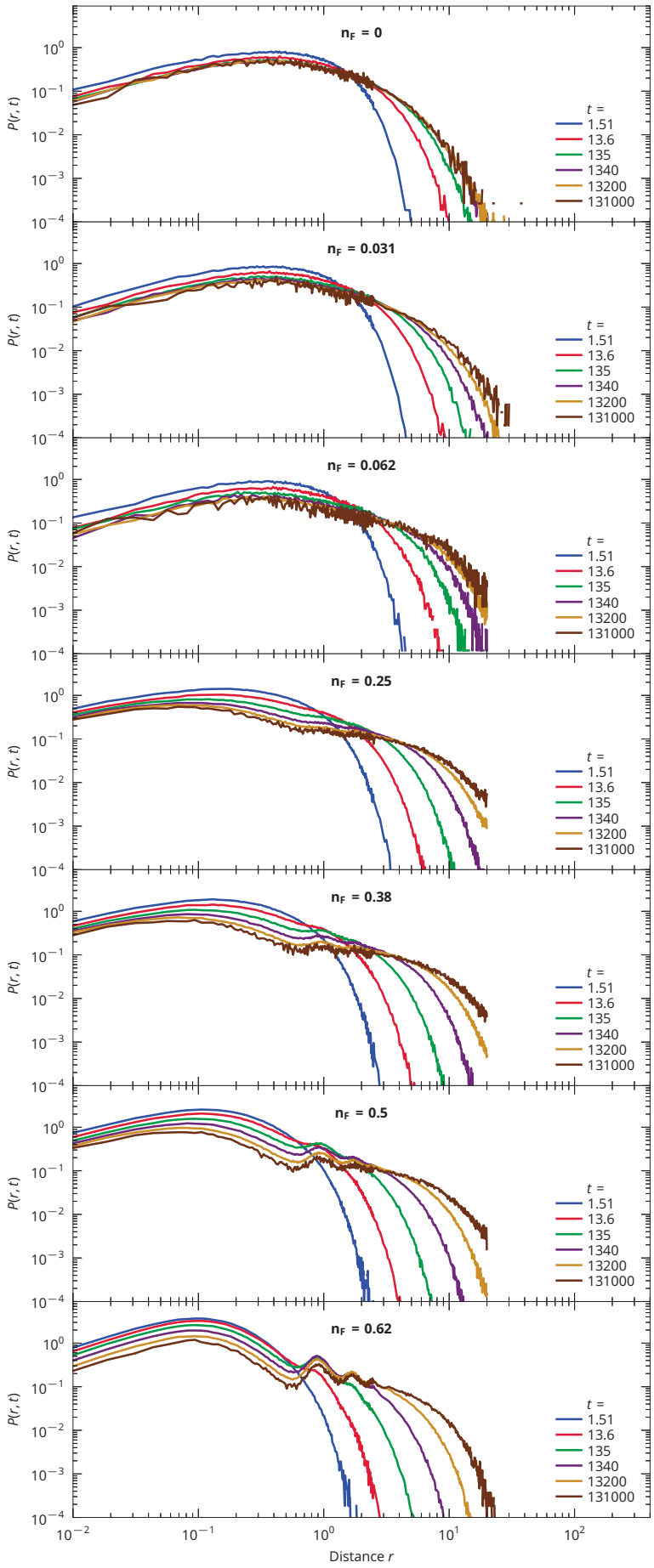

Figure 4.9: Plot of the self-part of the van-Hove function $P(r,t)$ of the interacting fluid component for $\sigma_F = 0.8$ and a range of fluid number densities $n_F = 0$ (ideal gas), 0.031, 0.062, 0.25, 0.38, 0.5, and 0.62 as indicated in the titles. $P(r,t)$ is shown as a function of distance r for a range of times t as indicated in the legends.

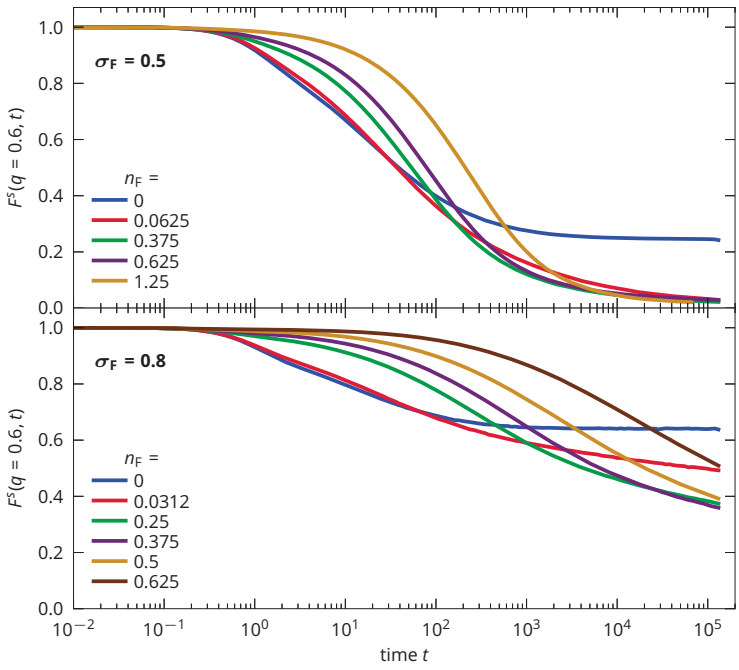

Figure 4.10: Intermediate scattering function of the interacting fluid system for $\sigma_F = 0.5$ *(top)* and $\sigma_F = 0.8$ *(bottom)* at $q = 0.6$ for a range of total number of fluid particles N_F.

upon increasing n_F occur at long times and large distances. The ideal gas case shows a very smooth and broad distribution which slowly decays at large distances. This indicates the localization of most fluid particles. In contrast, the dense systems exhibit a peak which moves to larger distances over time. Accompanied with this is the stronger decrease of the van-Hove function over time at very small distances[2]. All in all, the van-Hove function at finite n_F resembles more closely the single-energy case, see fig. 2.14 for comparison, than the confined ideal gas.

The self-part of the van-Hove function $P(r, t)$ for the localized path at $\sigma_F = 0.8$ is shown in fig. 4.9. While the ideal gas case ($n_F = 0$) is strongly localized and converges to its long-time limit over the course of the simulation, this is not true for the systems where n_F is finite. In the latter case, the fluid particles are still exploring the void space and the van-Hove function is still undergoing changes at the end of the simulation. With increasing n_F, the van-Hove function develops a series of local maxima at distances $r \approx 0.9$, 1.7, and 2.4 which are roughly integer multiples of the particle diameter and indicate the growing structural correlation of the fluid particles induced by increasing the number of fluid particles.

[2] This is not connected to the artifacts introduced by the naïve particle insertion discussed in appendix A, which can cause the van-Hove function to converge too early at small distances. All systems shown in fig. 4.9 except the one with $n_F = 0.62$ were inserted grand-canonically and are thus free of the artifact.

Intermediate scattering function Because the ISF contains the same information as the van-Hove function it will only shortly be discussed. The ISF is very sensitive to the presence of localized particles which strongly influence the long-time limit. Because the relaxation time becomes very large for finite n_F it was not possible to calculate the long-time limit of the ISF, here. Instead, the full ISF is shown for an exemplary, small wavenumber $q = 0.6$ in fig. 4.10.

On the delocalized side at $\sigma_F = 0.5$, the ISF is drastically changed when n_F becomes finite. The ideal gas case ($n_F = 0$) has a large finite long-time limit, indicating the localization of a large portion on the particles (on the length scale $2\pi/q$). At $n_F = 0.0625$, where structure and energy distribution are still

nearly undistinguishable from the ideal gas, the ISF decays to nearly 0 over the course of the simulation. It is entirely possible that it would fully decay to 0 if given sufficient time. This clearly demonstrates that nearly every particle in this system will eventually leave its original pocket when it is allowed to frequently exchange energy with other particles. Upon further increasing n_F, the long-time limit stays at or near 0, while the relaxation time is growing due to the enhanced interaction between fluid particles.

On the localized side, the long-time limit of the ISF is also significantly decreased upon introducing interactions between the fluid particles, as can be seen in fig. 4.10 *(bottom)*. Because the relaxation time far exceeds the simulation time it is not possible to conclusively tell whether the long-time limit decreases monotonically with n_F. At $n_F = 0.375$ the ISF has the lowest value at the end of the simulation. This is in agreement with the MSD having the largest value for that system at the end of the simulation. With increasing n_F, the relaxation time strongly grows.

Now that the gradual introduction of particles gave insight into the general modification of the dynamics, the localization transition will be studied in a scaling analysis in the next section. timescale

4.3 *Dynamics II: Investigation of the critical asymptotics*

To study the scaling near the localization transition for the interacting fluid particles, it is necessary to cross it. For this purpose, a path with constant number density was chosen, where the fluid particle diameter was varied. This path is in analogy to the paths used in the single-energy and ideal-gas cases and allows the testing of scaling properties. It is marked as the yellow path in fig. 4.1 and fig. 4.2, redrawn here to the right.

In the study of the confined ideal gas it was shown that the localization transition is necessarily rounded once soft interactions are present in the system. The same is expected to hold here. For the confined-ideal-gas case, it had been determined that scaling was violated but it will be shown in the following that the interacting case is more compatible with the scaling predictions again. It is the aim of this section to determine which properties of the Lorentz model scenario hold in the interacting system and which do not.

The number density of fluid particles is held at constant $n_F = 0.625$ while the diameter σ_F is varied. This is the second largest value of n_F simulated for the system with $\sigma_F = 0.5$ of the previous section, and the largest value of n_F for the system with $\sigma_F = 0.8$. This relatively high number density was found in the previous section to result in a strong slowing down of the dynamics at intermediate timescales and was found to cause multiple peaks in the self-part of the van-Hove function stemming from the strong interaction of the fluid particles with themselves. Therefore, the modification of the dynamics is considerable and the influence on the localization dynamics can be expected to be strong. To quantify the correlations found at this number density, a short discussion of the structure factor follows.

Structure The partial structure factors $S_{FF}(q)$ and $S_{MF}(q)$ are shown in fig. 4.13 for a range of interaction diameters σ_F along the studied path. At

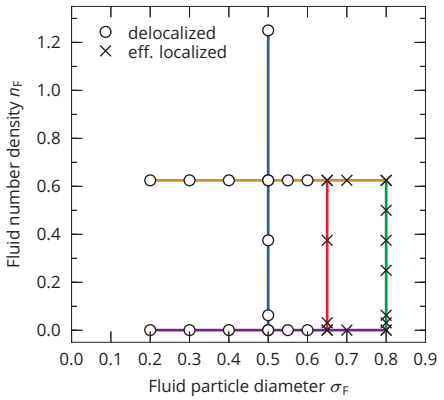

Figure 4.11: Plot of the explored parameter range with all simulated state points marked as points along the 5 discussed paths in the interacting fluid case. *The same plot as fig. 4.1.*

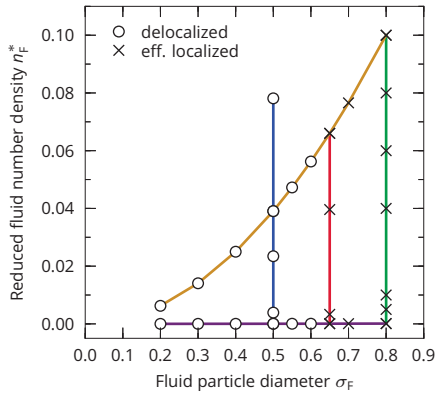

Figure 4.12: Plot of the explored parameter range in the space of reduced number density n_F^* and fluid particle diameter σ_F, with all simulated state points marked as points along the 5 discussed paths in the interacting fluid case. *The same plot as fig. 4.2.*

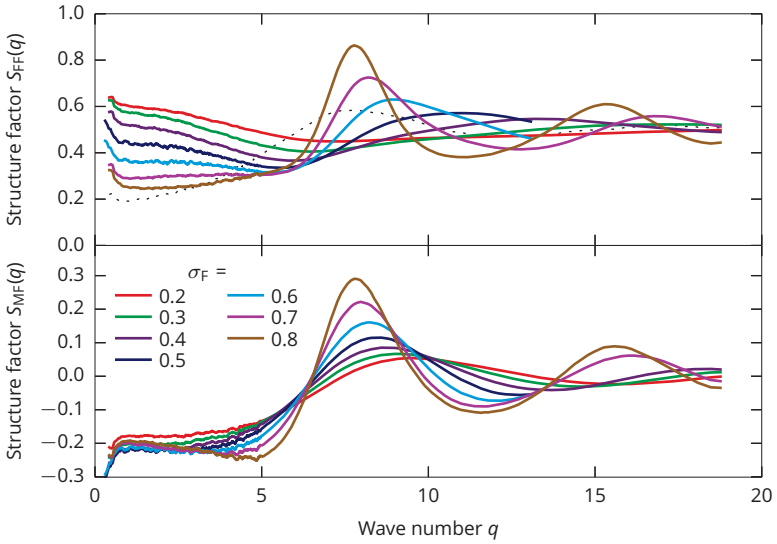

Figure 4.13: The partial structure factors $S_{FF}(q)$ *(top)* and $S_{MF}(q)$ *(bottom)* of the interacting system for a range of interaction diameters σ_F at constant number density $n_F = 0.625$. The structure factor of the matrix is given as black dotted line in the top figure.

the smallest simulated diameter, $\sigma_F = 0.2$, $S_{FF}(q)$ only weakly deviates from the constant large wavenumber limit $n_F/(n_F + n_M)$, i.e. the system is structurally very similar to the confined ideal gas. Upon increasing σ_F, $S_{FF}(q)$ develops peaks which reflect the dense packing of the particles. At the same time, the amplitude at small wavenumbers decreases, indicating that the compressibility decreases with σ_F. Analogously, the amplitude of the matrix-fluid structure factor $S_{MF}(q)$ also grows with σ_F and develops peaks. (note that the structure factors for $\sigma_F = 0.5$ and 0.8 were already displayed in fig. 4.4).

Mean-squared displacement The dynamics is again studied with the MSD, which unsurprisingly shows an effective localization transition as the diameter is increased. But the dynamics is qualitatively much closer to the Lorentz model scenario than the study of the confined ideal gas would have lead one to expect. For the whole simulated path, the MSD is shown in fig. 4.14 as solid lines. For reference, the data is superposed over the confined-ideal-gas MSD at the same diameters, shown as lighter colored, solid lines. The confined-ideal-gas data, again, represents the $n_F \to 0$ limit and thus the dynamics without interactions. The data is nearly free of finite size effects and where they arise they do not change the discussion, see section 4.5.

The system with the smallest diameter, $\sigma_F = 0.2$ shows nearly the same MSD as the corresponding ideal-gas system. On intermediate times the dynamics is slowed down as already discussed in section 4.2. But in contrast to the discussion there, the MSD stays below the confined-ideal-gas MSD, even in the diffusive regime at long times. As most particles are delocalized at this σ_F, the interaction of fluid particles with each other cannot serve as a mechanism for freeing particles and thus only causes the slowing-down of the dynamics on intermediate timescales. The same occurs in (Voigtmann and Horbach, 2009) at small σ_F for the system with switched on fluid interactions.

Increasing the tracer radius leads to a slowing-down of the dynamics but not as strongly as in the confined ideal gas. At $\sigma_F = 0.4$ the interacting fluid system first shows enhanced long-time diffusion in comparison to the confined ideal gas. From there on, the MSD of the interacting system always exceeds

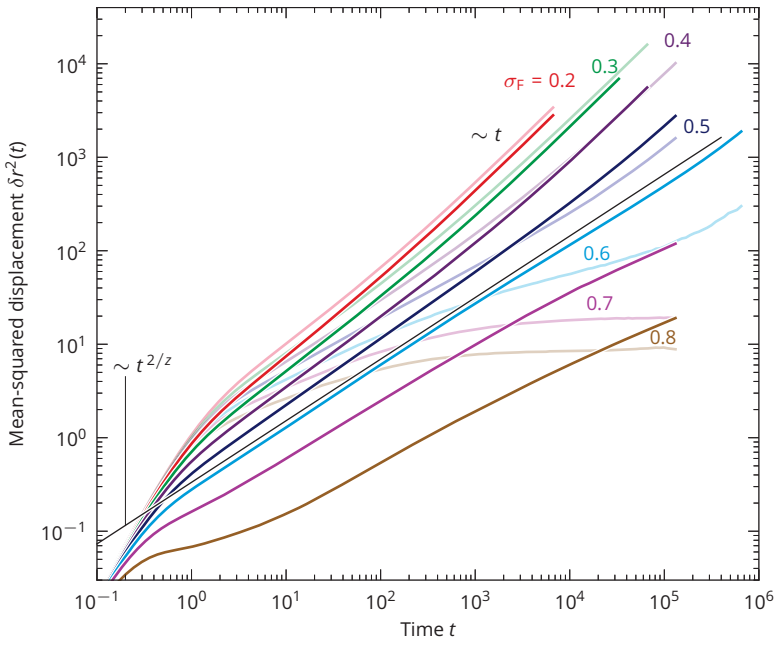

Figure 4.14: Mean-squared displacement for the interacting fluid system over a range of tracer diameters σ_F as solid lines. MSD of the confined ideal gas with the same color scheme as lightly colored, solid lines. Power-law with the expected critical exponent, $\sim t^{2/3.036}$, as black line.

that of the ideal-gas system at long times.

For $\sigma_F \leq 0.5$ the MSD becomes diffusive during the simulation time, but shows a subdiffusive regime which extends in duration as σ_F is increased. The duration of the subdiffusive regime is far longer than in the confined ideal gas and even than in the single-energy case, see fig. 2.6 for comparison.

At $\sigma_F = 0.6$ the MSD stays subdiffusive over nearly the whole duration of the simulation. It is compatible with a power-law with exactly the Lorentz-model exponent, $\delta r^2(t) \sim t^{2/z}$, over at least 4 decades in time (for $1 < t < 10^4$). Only at very large times the MSD deviates from the power-law and becomes diffusive. One should not overstate the importance of the extended subdiffusion found at $\sigma_F = 0.6$. In section 4.2 it was demonstrated that the effective exponent of the MSD is strongly modified by the number density n_F. It is thus entirely possible that the agreement with the Lorentz-model exponent is purely accidental. Towards this interpretation speaks the fact, that the subdiffusion begins already at very short times when the dynamics are expected to be still strongly modified by the interaction of the fluid particles with each other.

Furthermore, the MSD at $\sigma_F = 0.6$ shows clear signs of a rounded transition. Its effective exponent begins to decrease at $t \approx 10^4$ which would indicate a localized system if it were not for the diffusive long-time behavior. This behavior is in agreement with the hard-sphere diameter distribution $p(\sigma_{hs})$, shown in fig. 4.15, which shows that while most particles are localized, a few are not. The situation here is therefore similar to that found in the confined ideal gas, e.g. at $\sigma_F = 0.6$ in fig. 3.4, although it is less pronounced, here.

For the diameters $\sigma_F = 0.7$, and 0.8 the MSD slows down again. The slope of the MSD seems to be indicating that the MSD is approaching a constant limit, but the simulated time is not sufficient to observe this. Again, keeping the discussion of the confined ideal gas in mind, it is still expected that all MSD will eventually become diffusive, at times unavailable to the simulation.

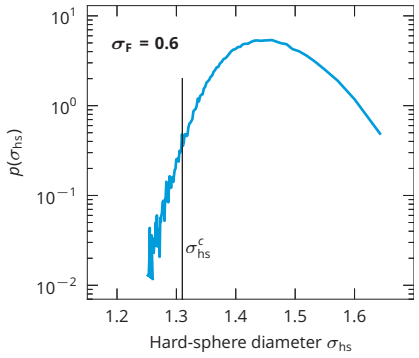

Figure 4.15: Effective hard-sphere distribution $p(\sigma_{hs})$ of the interacting fluid system at $\sigma_F = 0.6$ at fluid number density $n_F = 0.625$. The critical hard-sphere diameter $\sigma_{hs}^c = 0.131$ at which localization occurs is marked by a vertical line.

The MSD at constant n_F but varying σ_F can be compared to the glassy binary mixture in (Voigtmann and Horbach, 2009), where the number density of fluid particles was varied. Even though the procedures of making the system denser varies in these two approaches, qualitatively a very similar localization scenario occurs. In (Voigtmann and Horbach, 2009), the dynamics of the fluid particles is studied for a range of number densities with and without interactions between the fluid particles. The system without the fluid interactions represents the analogue to the confined ideal gas, here, while the system with the fluid interactions represents the analogue to the system at $n_F = 0.625$. At small densities, the MSD of the fluid particles in (Voigtmann and Horbach, 2009) is slowed down by switching on the interactions, just as it is the case here at small diameters. Then, at intermediate densities, the MSD of the interacting fluid overtakes the MSD of the noninteracting fluid, just as was the case at intermediate σ_F, here. Even though the system used here is simpler — the matrix is strictly fixed and not slowly relaxing as is the case in the binary mixture — the dynamics qualitatively agree fully. This indicates that the remaining movement of the glassy matrix particles in the binary mixture is largely irrelevant for the fluid particle dynamics.

The system at $n_F = 0.625$ exhibits an (effective) localization transition between $0.6 < \sigma_F < 0.7$. The behavior of the MSD at $\sigma_F = 0.6$ is most compatible with the Lorentz model as it shows extended subdiffusion with the expected exponent, but with signs of a rounding of the transition.

There is no reason to assume that the rounding is not taking place in the interacting case, especially because its single requirement is fulfilled, namely that the fluid particles have a wide energy distribution. But in contrast to the confined ideal gas, the extended subdiffusion at $\sigma_F = 0.6$ seems to indicate that the properties of the Lorentz model can be more easily observed in the interacting case, after all. Thus, it is natural to check whether more scaling properties of the Lorentz model are fulfilled by the interacting system. For instance, whether the scaling of the dynamics *in the approach to* the localization transition is compatible with the theoretical expectation can be directly studied with the behavior of the long-time diffusion.

Suppression of long-time diffusion In the approach to the effective localization transition, the long-time diffusion coefficient D is strongly suppressed. The diffusion coefficients obtained from the MSD are shown in fig. 4.16 *(top)* as a function of the particle diameter σ_F in comparison to the single-energy data and the confined ideal gas data ($n_F = 0$). Again, connected dots mark the data directly read off from the MSD, while the vertical bars give lower and upper bounds for D obtained from an extrapolation during the finite-size analysis as described in section 2.5. As already discussed for the MSD, diffusion in the interacting system is slower at small σ_F compared to both the single-energy and the confined-ideal-gas case. At $\sigma_F \approx 0.35$ the diffusion coefficient of the interacting system becomes larger than in the other two systems and stays larger.

As already discussed in detail, the long-time diffusion coefficient in the Lorentz model vanishes asymptotically with a power-law $D \sim \varepsilon^\mu$ with $\varepsilon = (\sigma_F - \sigma_F^c)/\sigma_F^c$ and $\mu = 1.31$ at the localization transition. In general, it cannot be

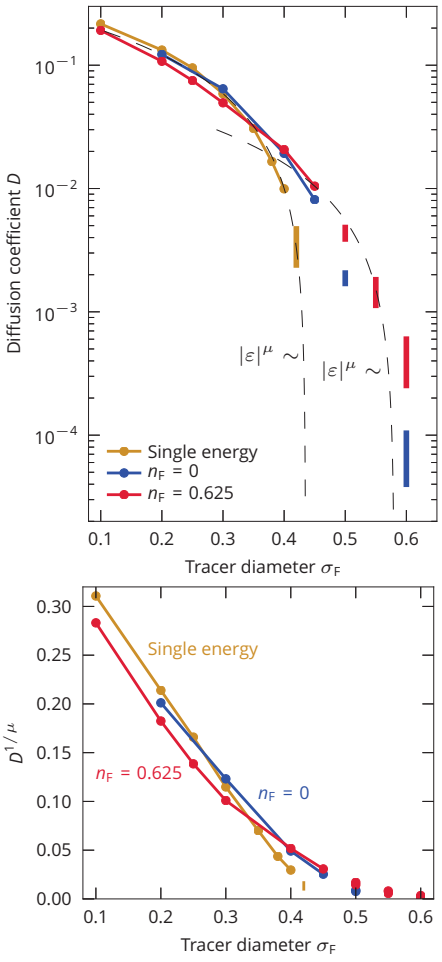

Figure 4.16: *Top:* Diffusion coefficient D as function of the fluid particle diameter σ_F for single-energy (yellow), confined-ideal-gas particles, i.e., $n_F = 0$ (blue), and interacting fluid particles with $n_F = 0.625$ (red). Possible critical asymptotes compatible with the two-dimensional Lorentz model for the single-energy and $n_F = 0.625$ cases shown as black dashed lines. Connected dots for diffusion coefficients directly obtained from MSD. Vertical bars give upper and lower bounds of the diffusion coefficients obtained from extrapolation in finite size analysis, see section 2.5. *Below:* Rectification plot of the diffusion coefficients with the expected Lorentz exponent $\mu = 1.31$.

expected that such asymptotic critical behavior can be observed far from the critical point. Often in critical phenomena, one has to approach the critical point to within $\varepsilon \sim \mathcal{O}(0.01)$ to observe critical behavior, e.g. see in (Das et al., 2006). That the single-energy data agrees so well with the critical power-law asymptote can thus not be expected to hold in general. In the case of the interacting system at $n_F = 0.625$, the data cannot be described by a similar power-law with the correct exponent μ. A rectification plot is shown in fig. 4.16 *(bottom)*, where diffusion coefficients in agreement with the critical asymptote would show up as a straight line. In this representation, D of the interacting system is strongly curved over the whole diameter range. The two plots show how similar the behavior of the diffusion coefficient in the interacting system is to the behavior in the confined ideal gas.

The similarity of the interacting system to the confined ideal gas is demonstrated further in the effective scaling present in the diffusion coefficient. In fig. 4.17, the diffusion coefficient of the interacting system at $\sigma_F = 0.625$ is shown as a function of the separation parameter ε. For the calculation of ε, the effective transition diameter was assumed at $\sigma_F^c = 0.65$. The diffusion coefficients of the single-energy and the confined-ideal-gas cases are shown for comparison, using the transition diameters $\sigma_F^c = 0.435$ and $\sigma_F^c = 0.6$, respectively. While the single-energy case clearly follows the asymptote $|\varepsilon|^\mu$ of the Lorentz model, the interacting case and the confined ideal gas follow the same effective power-law, $|\varepsilon|^{2.8}$. As in the confined ideal gas, this scaling is expected to break down at smaller ε, simply because there is no sharp localization transition in the system. The fact that both the confined ideal gas and the interacting system seem to follow the same effective scaling does not prove anything, but it is an interesting coincidence. It seems to indicate that the long-time dynamics are not too strongly changed by the interaction between fluid particles, except from a general shifting of the effective transition with increasing fluid density (via the shifting of the energy distribution). This is in strong contrast to the general slowing down of the dynamics on intermediate times.

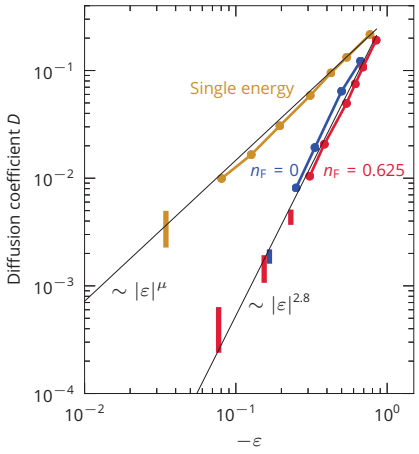

Figure 4.17: Diffusion coefficient D of the interacting system at $n_F = 0.625$, of the confined ideal gas ($n_F = 0$) and the single-energy case as a function of the separation parameter ε. For the calculation of ε, the parameters $\sigma_F^c = 0.435$ (single energy), $\sigma_F^c = 0.6$ (confined ideal gas), and $\sigma_F^c = 0.65$ ($n_F = 0.625$) was used. Black lines mark asymptotes with the exponent of the Lorentz model, $\sim |\varepsilon|^\mu$, and an effective exponent, $\sim |\varepsilon|^{2.8}$.

Scaling of the mean-squared displacement As the long-time diffusion coefficient is not compatible with the critical power-law of the Lorentz model, there is no possibility that the MSD near the transition will collapse onto a master curve with the Lorentz model scaling. However, analogously to the effective scaling found in the confined ideal gas in fig. 3.8, the localization length can be used as a free parameter to determine the effective scaling of the MSD, here. In fig. 4.18 *(left)*, the MSD is divided by the critical asymptote $t^{2/z}$ and plotted as a function of rescaled times tl^{-z}. The MSDs on delocalized and localized sides of the transition collapse onto master curves with moderate success.

The MSD at $\sigma_F = 0.65$ is compatible with the localized scaling function, but shows a slight upwards turn at the end, which is a signal of the presence of delocalized particle states, as discussed in section 4.2.

Assuming an effective transition at $\sigma_F^c = 0.65$, the localization length l is shown as a function of the separation parameter ε in fig. 4.18 *(right)*. Note, that since the scaling is only effective, the localization length l should not be interpreted as a localization length, necessarily. Therefore it is not an indication of finite size effects that l exceeds the simulation box. The localization length l follows an effective power-law $l \sim |\varepsilon|^{2.8}$ with nearly the same exponent as

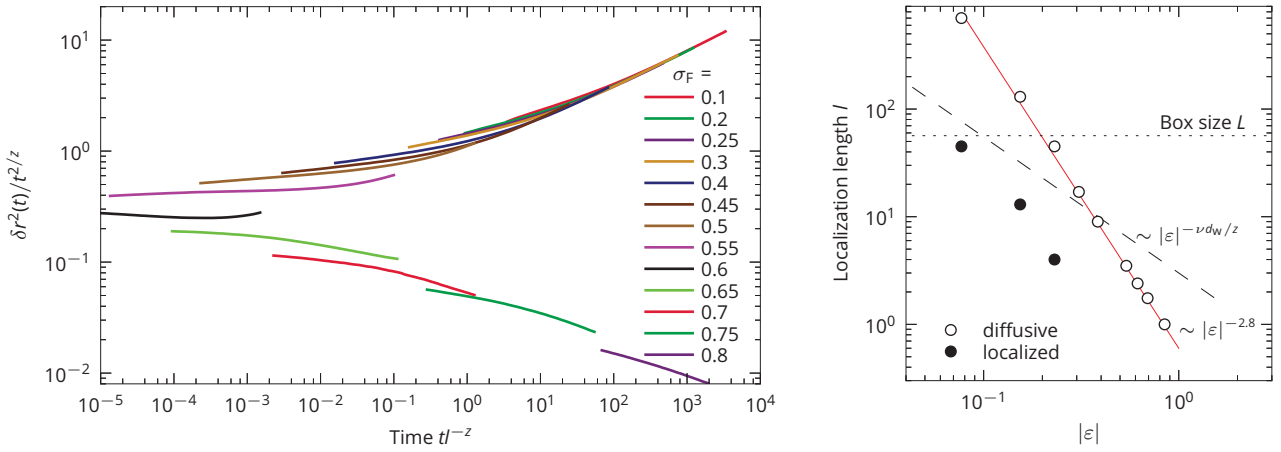

Figure 4.18: *Left:* Mean-squared displacement $\delta r^2(t)$ divided by the critical asymptote of the Lorentz model, $t^{2/z}$ as a function of rescaled time tl^{-z} with localization length l used as fitting parameter. *Right:* The fitted localization length l as a function of the distance ε to the effective localization transition estimated to occur at $\sigma_F^c = 0.65$. The power-law behavior in the Lorentz model, as given in eq. (1.12), is indicated by a black dashed line, while the actual effective power-law is given by a solid red line.

found for the confined ideal gas over the whole range of ε on the diffusive side (compare to fig. 3.8). On the localized side, not enough data points are available to discuss effective scaling. Still, the effective scaling in the approach to the effective localization transition is roughly as successful as in the confined ideal gas.

Further information about the scaling of the system can be obtained with the van-Hove function.

Van-Hove function The full information about the single-particle dynamics of the system is contained in the self-part of the van-Hove correlation function $P(r,t)$, which is displayed in fig. 4.19 for a range of σ_F along the studied path. It is shown as a function of the distance r for a series of times t to expose spatial information not contained in the MSD.

At very small diameters, $\sigma_F = 0.2$ or 0.3, the van-Hove function $P(r,t)$ is very similar to both the single-energy case, see fig. 2.14, and to the confined ideal gas, see fig. 3.15. As time increases, the particles move farther away, as indicated by the maximum of the distribution moving outward, and the distribution broadens. At very large times, a local maximum at a small r develops.

As the diameter is increased, the shape of the van-Hove function changes slowly. The maximum at small r becomes more pronounced, while the second maximum slowly is turned into a shoulder. The evolution of the shape is very similar to the situation in the single-energy case. In contrast, the ideal gas does not develop this two-peak structure at all.

At $\sigma_F = 0.55$ and 0.6, the van-Hove function is very similar to the critical single-energy system at $\sigma_F = 0.43$, in the way that the out-moving part of $P(r,t)$ does not have a maximum, i.e. the van-Hove function is constant over a wide range of r at any given, long time. The critical appearance is consistent with the subdiffusive growth of the MSD reported earlier. A similar behavior is never observed in the confined ideal gas.

In contrast to the single-energy system, the systems with large diameters, $\sigma_F > 0.6$, never fully converge to a long-time limit because of the strongly increased relaxation time of the interacting system. In addition, the fluid particles become densely packed and the van-Hove function develops a series of local maxima and minima on the order of the next-neighbor distance.

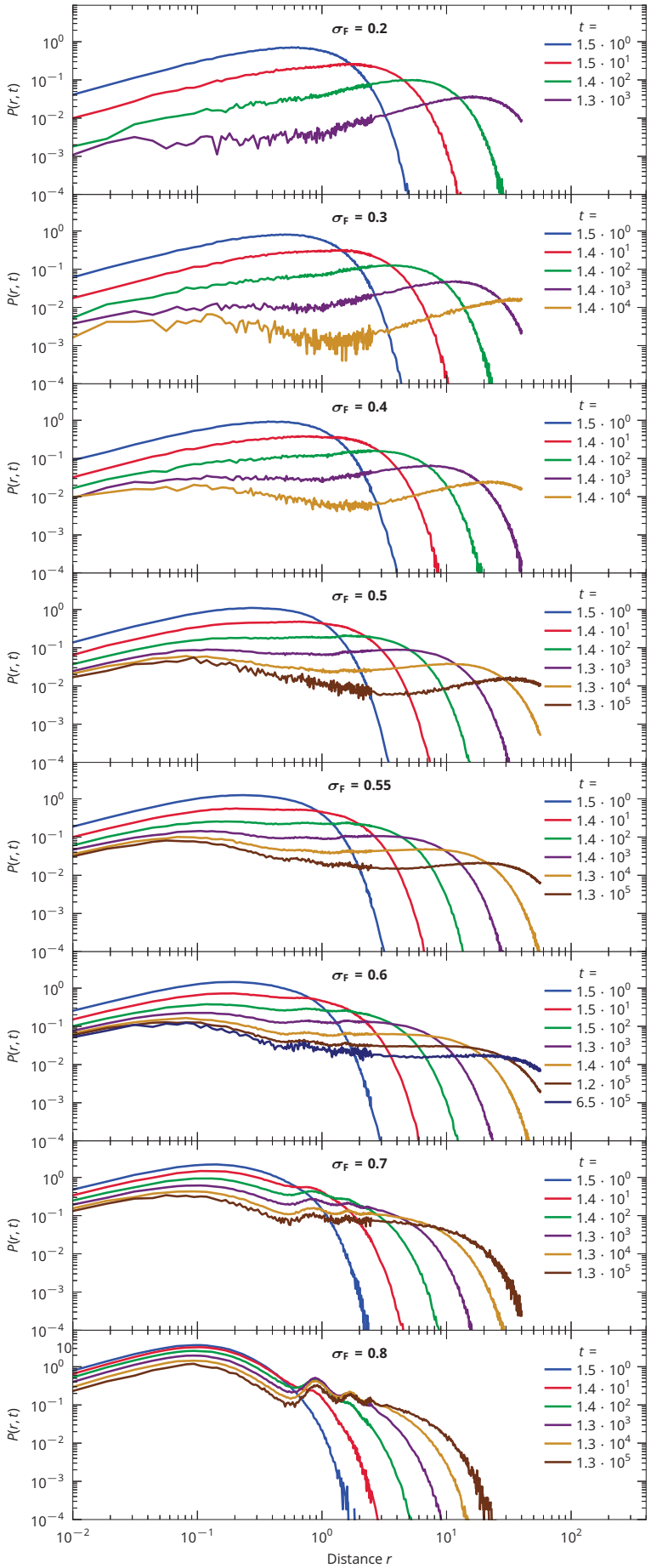

Figure 4.19: Double-logarithmic plot of the self-part of the van-Hove function $P(r,t)$ for a range of fluid particle diameters $\sigma_F = 0.2, 0.3, 0.4, 0.5, 0.6, 0.7$, and 0.8, with constant $n_F = 0.625$. $P(r,t)$ is shown as a function of distance r for a range of times as indicated in the legends.

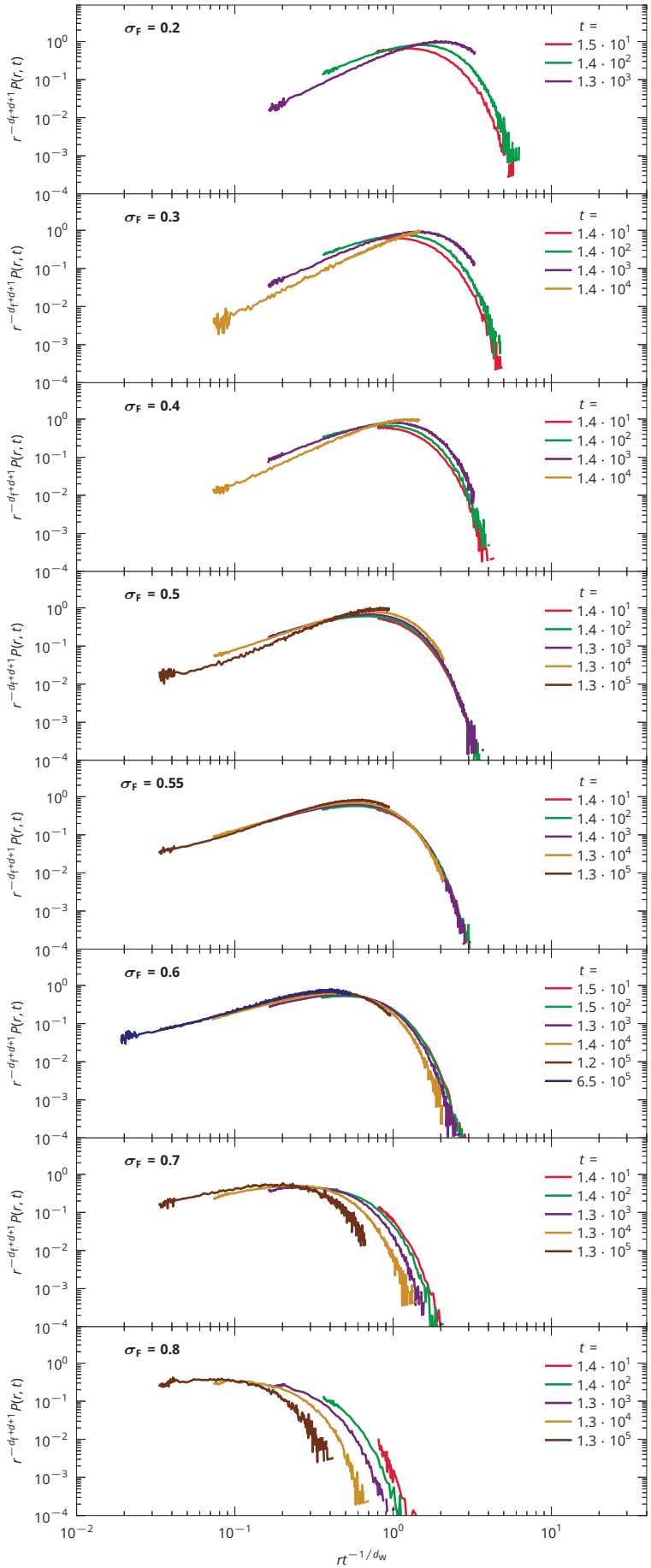

Figure 4.20: Rescaled van-Hove function as a function of rescaled time assuming the scaling of the all-cluster average at the critical point.

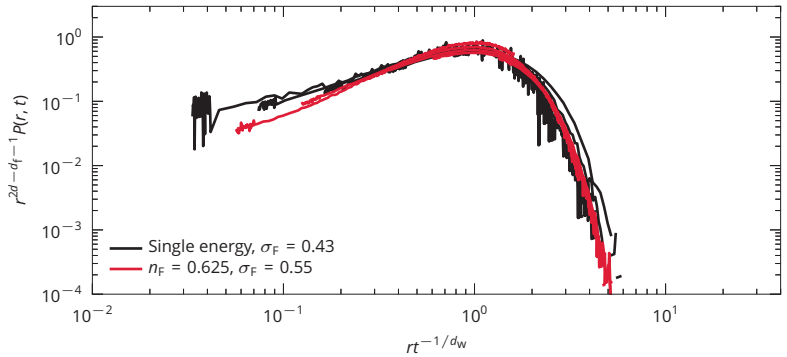

Figure 4.21: Superposition of the rescaled van-Hove function of the single-energy case and the interacting system for $n_F = 0.625$ where the scaling of the Lorentz model works best: at $\sigma_F = 0.43$ for the single-energy case (black lines) and at $\sigma_F = 0.55$ for the interacting case (red lines). The data is replotted in full from figs. 2.15 and 4.20. The time and space argument rt^{-1/d_w} of the interacting case has been multiplied with a constant $c = 1.7$ to achieve overlap with the single-energy system.

Qualitatively, the van-Hove function becomes very similar to the one of the mobile component in ion-conductors (Horbach et al., 2001).

Since the van-Hove function at $\sigma_F = 0.55$ and 0.6 looks like its critical counterpart in the single-energy case, and the MSD at $\sigma_F = 0.6$ shows anomalous diffusion over a large time interval, there is a strong indication that the van-Hove function of the interacting system fulfills the critical time-space scaling of the Lorentz model, at least on intermediate times. This will be tested now.

Scaling of the van-Hove function In fig. 4.20, the time-space scaling of the dynamics in the all-cluster average at the critical point, see eq. (1.17), is applied to the van-Hove function. For comparison, see the same rescaling for the single-energy data in fig. 2.15. For the rescaling only data with $r > 2$ and $t > 2$ has been used, as this is the simplest criterion for excluding the microscopic domain where the scaling cannot be applied. The scaling works very well for $\sigma_F = 0.55$ and $\sigma_F = 0.6$, which showed extensive subdiffusion in the MSD. Data spanning 4 orders of magnitude in time and roughly 2 orders of magnitude in distance have been successfully scaled on top of each other. Note that the scaling works best at $\sigma_F = 0.55$, where the MSD still becomes diffusive. Thus the scaling is expected to break down for larger times than displayed here.

For comparison to the scaling in the single-energy case, the rescaled van-Hove function at $\sigma_F = 0.55$ is shown superposed over the rescaled van-Hove function of the single-energy case at the critical $\sigma_F = 0.43$ in fig. 4.21. In order to achieve overlap, the time and space argument of the interacting case has been multiplied by one constant $c = 1.7$ for all curves. After this simple fitting procedure, which can be interpreted as a matching of an effective microscopic timescale, near complete overlap of the data is found. The same works nearly as well for $\sigma_F = 0.6$ (not shown). The van-Hove function of the interacting case at $n_F = 0.625$ thus agrees extremely well with the single-energy case, i.e. the Lorentz model. So even if the localization transition is rounded, the van-Hove function at $0.55 \leq \sigma_F \leq 0.6$ scales with the critical time-space scaling of the Lorentz model on the times and distances available to the simulation. Nothing similar occurred in the confined ideal gas.

Intermediate scattering function Since the self-part of the intermediate scattering function $F^s(q,t)$ contains the same information as the van-Hove function it is not necessary to discuss it in much detail. As was already found in the discussion of fig. 4.10, the long-time limit $f(q)$ of the intermediate scattering function is strongly decreased in the interacting system compared to the con-

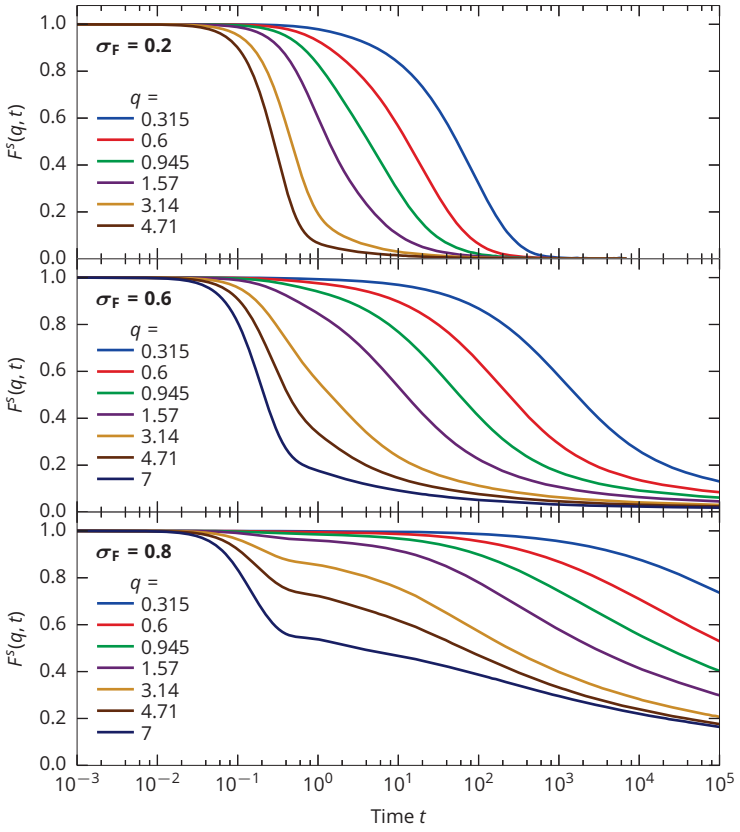

Figure 4.22: Self-part of the intermediate scattering function $F^s(q,t)$ of the interacting fluid system at $n_F = 0.625$ as a function of time t for a range of wavenumbers q. $F^s(q,t)$ is shown for a delocalized state at $\sigma_F = 0.2$ *(top)*, a near-critical state at $\sigma_F = 0.6$ *(middle)*, and a localized state at $\sigma_F = 0.8$ *(bottom)*.

fined ideal gas, which means the fluid particles are considerably less localized in the interacting system. For the systems with $\sigma_F \leq 0.5$, the long-time limit could be determined for $q \geq 0.157$ and was found to vanish there, i.e. $f(q) = 0$, whereas the long-time limit $f(q)$ in the confined ideal became visibly different from 0 already for $\sigma_F = 0.2$, see fig. 3.18. For the larger σ_F, the relaxation time was too large to determine $f(q)$. Instead, it is necessary to plot the full time-dependence of $F^s(q,t)$ to argue about the long-time behavior.

Qualitatively, the ISF of the interacting system has more in common with the single-energy case than with the confined ideal gas, as was the case with the van-Hove function. To explain this, the ISF is shown in fig. 4.22 for a delocalized state at $\sigma_F = 0.2$ *(top)*, a near-critical state at $\sigma_F = 0.6$ *(middle)*, and a localized state at $\sigma_F = 0.8$ *(bottom)*. The clearly delocalized systems with $\sigma_F < 0.6$ all decay to a very small long-time limit. The system at $\sigma_F = 0.6$, which is near the effective localization transition, decays to a small long-time limit and is thus similar to the critical state at $\sigma_F = 0.43$ in the single-energy case, shown in fig. 2.16. Finally, the (effectively) localized systems, here exemplarily represented by the ISF at $\sigma_F = 0.8$, probably have a large long-time limit, but in any case decay only very slowly over the course of a simulation. Therefore, the increase of the long-time limit with σ_F along with σ_F occurs roughly in the same manner as in the single-energy case. In contrast, the confined ideal gas had far more heterogeneous dynamics, where at diameters $\sigma_F \approx 0.6$ the MSD was still diffusive while the $f(q)$ was already very large.

Discussion — Homogenization of the dynamics by fluid interactions In the confined ideal gas it was found that systems with soft interactions cannot exhibit a sharp Lorentz-model transition due to averaging of the dynamics as soon as the mobile particles have an energy distribution. Even more so, the transition is expected to be rounded so strongly that at all finite fluid particle diameters σ_F the system never really becomes localized. The reason for this is the exponential tail of the energy distribution which implies that there is always a finite probability of finding a particle in a fixed matrix of soft particles with a high-enough energy to be delocalized. The energy distribution of the interacting fluid particles of the presently discussed system has that same property, see fig. 4.5, and thus the transition can be expected to be strongly rounded as well. Indeed, there is evidence that this is the case. For instance, the suppression of the diffusion coefficient and the MSD follow the same effective scaling as in the confined ideal gas and cannot be made compatible with the critical scaling of the Lorentz model. Furthermore, even though the MSD at $\sigma_F = 0.6$ has characteristics of a near-critical, *localized* system, it becomes *diffusive* at long times. This is corroborated with the hard-sphere diameter distribution, which contains both delocalized and localized states.

On the other hand, the critical time-and-space scaling of the Lorentz model is found to hold for $\sigma_F = 0.55$ and 0.6 and the scaling function of the van-Hove function was found to be nearly exactly the same as in the single-energy case. Since these systems still have diffusive MSD, one cannot expect the scaling to hold indefinitely, but on the times and distances accessible to the simulation it does. Conversely, a similar scaling did not succeed at all in the confined-ideal-gas, see fig. 3.16. Therefore, either the critical scaling found here is purely accidental and would not occur for other fluid densities, or the interaction of the fluid particles with each other generically removes some of the characteristics of the energy averaging identified in the confined ideal gas.

One crucial way in which the confined ideal gas is different from the interacting fluid case is that in the former system the energy of each particle is conserved individually and it is possible to distinguish particles from each other by their energy. This has strong implications. Particles which are localized in the beginning of the simulation will never become delocalized and vice versa. This makes the dynamics quite heterogeneous as localized and delocalized particles coexist in the same system.

The interaction between fluid particles homogenizes the dynamics. Exchange of energy allows formerly localized particles to become either delocalized or at least to escape their original void pocket. This was evidenced by the increase of both the diffusion coefficient and the localization length upon introducing the fluid interactions in section 4.2. More formally speaking, it can be expected that the exchange of energy leads to practically all particles sampling the whole energy distribution over time. Thus, the fluid particles of the interacting fluid system are indistinguishable.

In-between contacts with other fluid particles, the energy of a fluid particle is conserved and an effective hard-sphere diameter can be assigned to it. Each time the particle energy is changed by a collision with another fluid particle, the effective hard-sphere diameter changes with it. As each particle samples the full energy distribution, it also samples the full hard-sphere diameter distribution. The particle will therefore experience some areas of the matrix as very dense

— when it has a low energy — and some as sparse — whenever it has a high energy. On average, that could either amount to a localized or a delocalized particle, but this property should then hold for all particles. In the interacting system, if one particle is delocalized, all are. This is decidedly not the case in the confined ideal gas.

This homogenization of the dynamics was directly observed: While the confined ideal gas had very large non-ergodicity parameters $f(q)$ in states with clearly diffusive MSDs — indicating very heterogeneous dynamics — the interacting systems had a very small non-ergodicity parameter in the states where the MSD was still clearly diffusive. This held also for states with a very small number of particles, see fig. 4.10.

It is not entirely clear how the homogenization of the dynamics would be responsible for restoring the critical scaling found for $0.55 \leq \sigma_F \leq 0.6$, but one might try the following argument: From the effective hard-sphere diameter distribution at $\sigma_F = 0.6$, it can be inferred that only a small portion of the fluid particles are delocalized at any given time. Of these particles, most are at or very near the critical point. The dynamics of that system is therefore an average over the dynamics of particles which are localized most of the time or — when delocalized — are at the critical point. The periods spent by the particles in a localized state then might merely serve to rescale the microscopic timescale. As a result one would encounter critical dynamics, but slowed down compared to the single-energy case. This argument would also explain why the scaling function of the van-Hove function is nearly exactly the same as in the single-energy case, except for a trivial rescaling of the microscopic timescale.

At smaller fluid particle diameters, $\sigma_F < 0.6$, a greater part of the energy distribution falls on the delocalized side and the dynamics are again more strongly averaged. This then destroys the agreement with the single-energy case and brings the dynamics closer to the one of the confined ideal gas. Precisely this then is the reason why the Lorentz model scaling is not observed *in the approach* to the effective localization transition but only *at* the transition.

To study the homogenization of the dynamics more systematically, it might prove fruitful to study the crossing of the localization transition in an interacting fluid system at very small n_F. Then, the homogenizing effect of the energy exchanges would still take place but any other effects of the interaction of fluid particles on the dynamics, e.g. the modification of the dynamics on short and intermediate times via caging, would become negligible.

4.4 Summary

In this chapter, the dynamics of interacting fluid particles confined in a soft porous matrix was studied. The focus of the analysis was on the modification of the dynamics by the interaction between the fluid particles. For this, the interaction was switched on in a controlled way by increasing the number density of fluid particles from 0, thereby providing the connection between the confined ideal gas and quenched-annealed mixtures. The confined ideal gas is then found in the limit of vanishing fluid density.

Quenched-annealed systems with soft potentials exhibit a rounded localization transition In the confined ideal gas, the mapping of the energy distribution of

the fluid particles onto effective hard-sphere diameters allowed expressing the rounding of the localization transition analytically. Since the energy distribution had an exponential high-energy tail, it could be shown that the probability of a particle being delocalized is finite for all finite obstacle densities, i.e. there is no true localization transition anymore.

Introducing interactions between the fluid particles, the energy of fluid particles is not conserved anymore, but the energy distribution is only weakly changed. Since the high-energy tail of the energy distribution is found unchanged in the interacting systems, it can be concluded that there is no sharp localization transition in soft quenched-annealed systems, as well. However, in some respects the interacting fluid system was found to have dynamics far more compatible with the Lorentz model predictions than with the confined ideal gas.

Speeding-up of the dynamics by fluid interactions By holding the particle diameter constant and increasing the number density it was shown that the cooperation of particles has a complex influence on the dynamics. In comparison to the confined ideal gas, on the delocalized side of the localization transition the dynamics in general slow down on intermediate timescales but speed up in many cases on long timescales. The speed-up was observed even and especially at very small number densities, where the structure and the energy distribution of the particles was nearly unchanged compared to the confined ideal gas. The speeding-up of the dynamics could therefore be traced back solely to the fact that particles exchange energy with each other, i.e. that particle energies change over time. The exchanging of energy also had the effect of delocalizing particles, i.e. particles pushing each other out of finite void pockets, which was observed in the strong decrease of the non-ergodicity parameter, the long-time limit of the self-part of the intermediate scattering function. In contrast to the confined ideal gas, where localized and delocalized particles coexist, the interacting fluid system consists of particles which switch between localized and delocalized *states* but are all undistinguishable. Thus, the frequent exchange of energy led to a homogenization of the dynamics.

On the localized side of the effective transition, increasing the number density lead to an increase of the localization length of the systems, and thus also demonstrated that particles push each other out of void pockets.

At high number densities, the onset of dynamics dominated by fluid-fluid interactions was identified. On the localized side, the MSD began to display a plateau which is typically associated with caging and the glass transition. On both sides of the transition, the van-Hove function started to display a series of maxima indicating the close packing of fluid particles.

Effective reentrance transition At larger number densities, the energy distribution of the particles became shifted towards larger energies. Since the energy distribution can be mapped onto an effective hard-sphere diameter distribution for the obstacles and the critical hard-sphere diameter is a constant independent of energy, the shift of the energy distribution directly implies an increase in the delocalized fraction of particles at any given time. In this way, an effectively localized system was found to become delocalized upon increasing the number density. This represents a reentrance transition.

The reported dynamics is qualitatively identical to behavior reported for equilibrated-mixture systems which differ from quenched-annealed systems in the way the matrix component is produced. In equilibrated-mixture systems, the fluid component is present in the simulation during the equilibration of the matrix and leads to modifications of the matrix structure with increasing fluid density. It was postulated previously that such a mechanism allowing for the modification of the matrix structure by the fluid component was *necessary* for a reentrance transition to occur. Here, it was shown that such a mechanism is *not* necessary, since the matrix was completely independent from the fluid particles.

Lorentz-model-like scaling at the effective localization transition The effective exponent of the anomalous diffusion found in the MSDs was shown to be highly tunable by variation of the number density. This enforces the point that the delocalization scenario of the Lorentz model cannot be identified by solely observing subdiffusion with the expected exponent for a few orders of magnitude, but that a study of the scaling in the approach and at the localization transition is necessary. Such a scaling analysis was performed in the second part of this chapter.

The effective localization transition was crossed by varying the fluid particle diameter while keeping the number density constant. This approach allowed direct comparison to the single-energy case of chapter 2 and the confined ideal gas of chapter 3. In this way, a system was identified where the MSD was found subdiffusive over nearly the whole simulation time. In contrast to the confined ideal gas, the subdiffusive MSD matched a power-law, $\delta r^2(t) \sim t^{2/z}$ with the Lorentz model exponent $z = 3.036$, and for a far longer time than in the single-energy case. The van-Hove function of that system not only obeyed the critical time-space scaling expected for the Lorentz model, the resulting scaling function matched the one of the single-energy case nearly exactly, save for a trivial rescaling of the microscopic timescale. The system thus fulfilled the Lorentz model scaling predictions *at* the transition, breaking only down at the end of the simulation.

However, the dynamics showed signs of a rounded transition, since the MSD seemed to begin converging to a finite long-time limit before becoming diffusive. Also, the scaling predictions *in the approach to* the transition were not fulfilled. The suppression of the diffusion coefficient in the approach to the transition was more compatible with the effective scaling found in the confined ideal gas than the predictions for the Lorentz model, and likewise the scaling of the MSD.

An attempt was made at explaining why the homogenization of the dynamics in the interacting fluid would lead to a better agreement of the dynamics with the Lorentz model than was the case for the confined ideal gas.

This chapter is finished by a short study of the finite-size scaling in the interacting fluid systems.

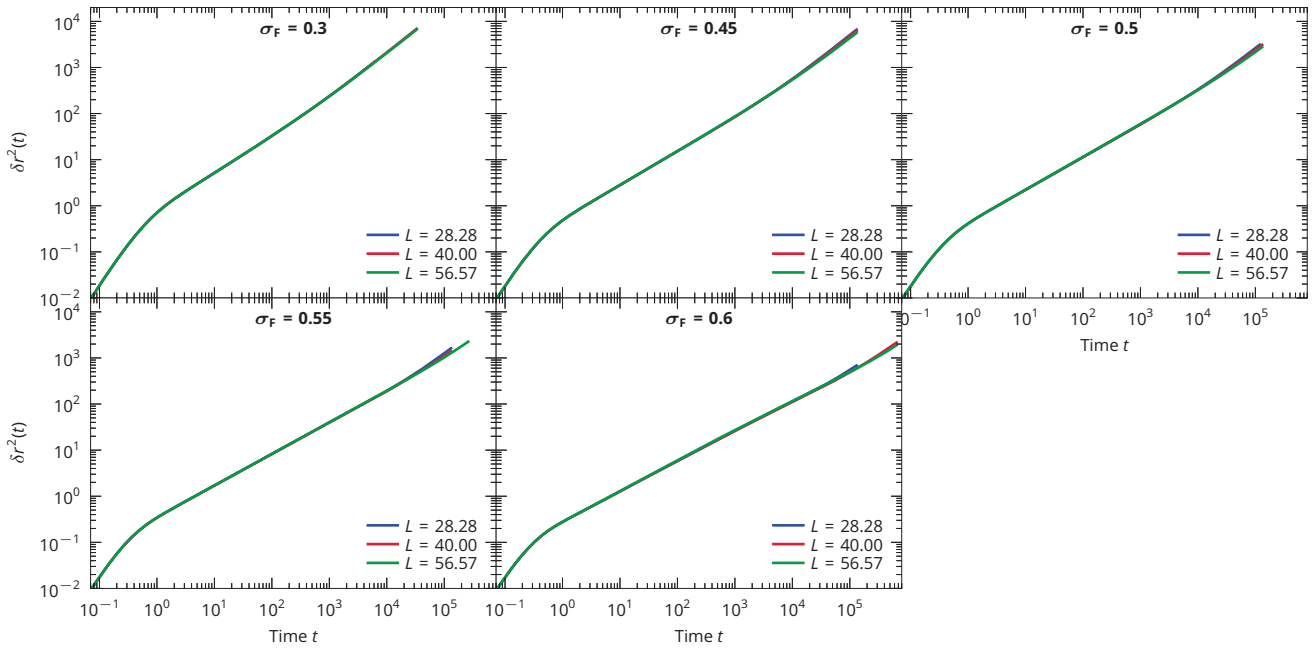

Figure 4.23: Mean-squared displacements of the interacting fluid case for a range of fluid particle diameters σ_F as indicated in the titles. For each diameter, the simulation box length L was varied as indicated in the legends.

4.5 *Finite-size scaling*

It is as important to control finite size effects in the interacting system as in the single-energy system and the confined ideal gas. Unfortunately, it is far more difficult to simulate large interacting systems because the number of interacting particles scales quadratically with the system size if one wants to keep the number density constant. Fortunately, the finite size scaling is found to be as weak or weaker as in the confined ideal gas.

To estimate finite size effects, the systems with constant number density $n_F = 0.625$ — which were discussed in section 4.3 — were simulated at multiple system sizes. The MSD for these systems are shown in fig. 4.23. The system with $\sigma_F = 0.3$ is without finite size effects at $L = 40$, already. Therefore it is sufficient to simulate the systems with $\sigma_F \leq 0.3$ at $L = 40$. The parameter range $0.3 < \sigma_F \leq 0.6$ proved more difficult. The cases $\sigma_F = 0.45$, 0.5, 0.55, and 0.6 still showed a difference in the MSD between the system sizes $L = 40$ and 56.57. Comparison of the MSD at $\sigma_F = 0.45$ to the corresponding MSD in the confined ideal gas, see fig. 3.20, shows that the finite size scaling in the former system appears comparable or weaker than in the latter. In the confined ideal gas at $\sigma_F = 0.45$, the MSD was free of finite size effects at $L = 56.57$ so it is likely that the interacting system is free of finite size effects, as well. The presence of finite size effects cannot be ruled out entirely for $0.45 < \sigma_F \leq 0.6$ at $L = 56.57$, but they are so weak that the entire discussion of the dynamics in fig. 4.23 can be considered correct.

Determining the diffusion coefficient at $\sigma_F = 0.5$, 0.55, and 0.6 was possible by extrapolation as outlined in section 2.5. The same extrapolation was performed at $\sigma_F = 0.45$ but the extrapolated diffusion coefficient was so close to the value at $L = 56.57$ as to be indistinguishable in the plot. This is further confirmation that the simulation at $\sigma_F = 0.45$ and $L = 56.57$ is free of finite size effects.

σ_F	n_F	L
0.5	0.0625	80
0.5	0.375	80
0.5	0.625	56.57
0.5	1.25	40
0.65	0.0312	160
0.65	0.375	56.57
0.65	0.625	40
0.8	0.0312	80
0.8	0.250	40
0.8	0.375	40
0.8	0.500	40
0.8	0.625	40

Table 4.1: The control parameters σ_F and n_F and the used simulation size L for the data presented in section 4.2.

At the lower number densities in section 4.2, it became possible to use larger system sizes. From the study of finite size scaling in the confined ideal gas it was inferred that for simulation times up to $t = 10^5$, box size $L = 80$ should be sufficient for the low densities. Therefore, the system size was chosen as large as possible for low number densities and then was decreased incrementally. The chosen system sizes are reported for reference in table 4.1. The presented results should be free of finite size effects, but a more systematic study was not performed.

5
Matrix correlations in quenched-annealed mixtures

In the preceding chapters the role of soft interaction potentials and interactions between fluid particles in the dynamics of the Lorentz model was analyzed extensively. In that way, the connection between the Lorentz model and the more complicated quenched-annealed systems was established. One remaining aspect in which quenched-annealed systems differ from the Lorentz model is in the structural correlations found in the matrix component of the former.

The universality class of the geometric properties of the percolation transition does not change upon variation of the matrix correlations (Torquato, 2002). However, the transport properties of a percolating network are not necessarily universal: If the distribution of channel widths w in the percolation network has a singularity at $w \to 0$, it can lead to a splitting of the universality class. This happens in the case of the continuum percolation transition in three dimensions, as was shortly discussed in section 1.2.1. It is thus possible that correlations in the matrix modify the channel-width distributions sufficiently to produce a modification of the universality class.

The universality of the critical dynamics has been confirmed in a variant of the Lorentz model with correlated obstacles: the cherry-pit model (Spanner, 2010). There, obstacles are defined by two radii. One radius defines obstacle *cores*, which are not allowed to overlap. The other radius defines the regular hard-sphere which cannot be entered by the tracer. At vanishing core radius, this system reduces to the regular Lorentz model, while at large core radii the obstacles become tightly packed and nearly non-overlapping hard-spheres. For this model, Spanner (2010) demonstrated that while the localization density is strongly shifted by the introduction of matrix correlations, the channel-width distribution is only slightly modified, and the critical dynamics are always those of the regular Lorentz model. The single-energy system discussed in chapter 2 is also an illustration of the universality, as it contained structural correlations in the obstacle matrix while exhibiting the critical dynamics of the Lorentz model.

Still, even though the localization transition is universal, one expects pre-asymptotic corrections to the dynamics when the matrix is correlated. For instance, the presence of cages on the lengthscale of the obstacle diameter in a matrix with a glassy structure may introduce a modification in the microscopic dynamics of the tracers. The following is a first exploration of the effect of structural correlations on the dynamics of a confined ideal gas in an attempt to identify such corrections to the universal behavior.

5.1 *Description of the system*

The system was very similar to the one described in chapter 2 but the simulations were performed in three dimensions. The WCA interaction potential was used for the interaction of both the matrix and fluid particles with the same parameters as in the two-dimensional systems. The systems were prepared in exactly the same manner with the sole exception of the preparation of the matrix.

Preparation of the matrix A systematic way to modify the structural correlations frozen in the matrix is the variation of the temperature T_M at which the matrix particles are equilibrated before fixing their positions. The smaller T_M, the more correlated their structure will be. In this formulation, the completely uncorrelated Lorentz model matrix can be produced for $T_M \to \infty$. To study the dynamics systematically, matrix configurations at the temperatures $T_M k_B = 2/3$, 40, 320, and 10^5 were used. From here on, the unit k_B is always implied in the temperatures.

The matrix configurations consisted of 1000 particles in a cubic simulation box with side length 9.55, resulting in a number density of $n_M = 1.15$. In order to avoid crystallization, the matrix particle diameters were sampled from a uniform distribution $\sigma_M \in [0.85, 1.15]$, just as in the 2D system. For the tracer-matrix interaction, the obstacles were all set to diameter $\sigma_M = 1$.

The matrix structures at the highest temperature were produced first, and were then successively cooled down to reach the lower matrix temperatures, as this makes it easier to obtain properly equilibrated configurations at the lowest temperatures. The particles were equilibrated with a simplified version of the Andersen thermostat (Andersen, 1980) by randomly selecting the particle velocities from a Maxwell distribution at the chosen temperature T_M every 100 steps for either 10^6 steps ($T_M \geq 3$), 10^7 steps ($1.5 \leq T_M < 3$) or 10^8 steps ($T_M < 1.5$). The simulation time step for the equilibration procedure had to be decreased for the higher temperatures, in accordance with the increase of the typical velocities of the particles. The systems at the temperatures $T_M \geq 320$ were simulated with time step $\delta t = 1.4 \cdot 10^{-5} t_0$, while the simulations of the colder systems used $\delta t = 7.2 \cdot 10^{-4} t_0$.

To make sure that the equilibration times are sufficient, microcanonical runs were performed after the equilibration, where the relaxation time of the system could be measured. Here, the relaxation time τ was defined by the point where the self-part of the intermediate scattering function has decayed to $F^s(q, \tau) := 1/e$ at $q = 7$. These relaxation times are shown in fig. 5.1 as a function of the equilibration temperature T_M. The relaxation times are as one would expect for this system.

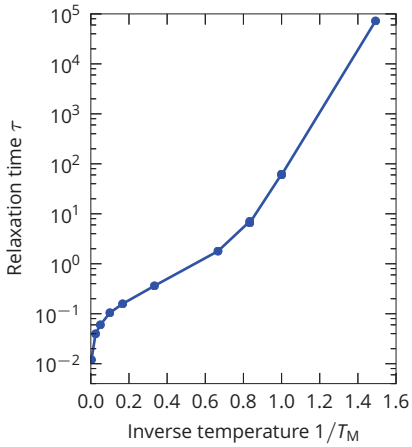

Figure 5.1: Relaxation times τ of the matrix particles in microcanonic runs after equilibration as a function of the inverse of the equilibration temperature $1/T_M$. Relaxation times defined as $F^s(q, \tau) := 1/e$ at $q = 7$. At the temperatures $T_M = 1$ and 1.2, two data points each are shown and found to completely overlap, with the length of the preceding equilibration run differing by a factor of 10.

At each temperature, 48 independent matrix configurations were obtained to allow for averaging over the matrix structure. The structure factor $S_{MM}(q)$ of the matrix configurations is shown in fig. 5.2 for all used matrix temperatures. As expected, systems become more correlated with decreasing temperature: The system at $T_M = 10^5$ shows a nearly constant structure factor and is thus very close to the Lorentz model structure, while the system at $T_M = 2/3$ shows large peaks in its structure factor and thus represents a strongly correlated system. If the matrix particles at $T_M = 2/3$ were allowed to move, they would

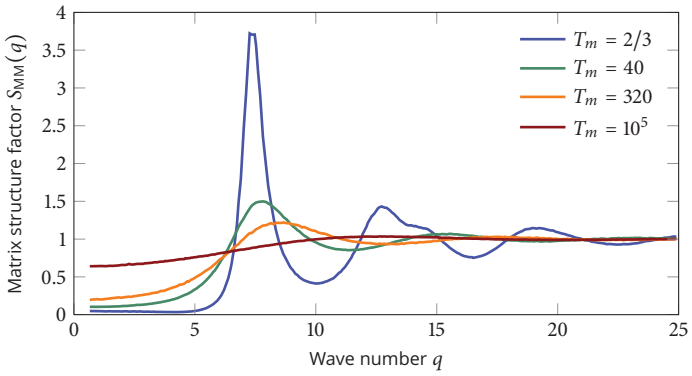

Figure 5.2: Structure factor $S_{MM}(q)$ of the obstacle matrix for various equilibration temperatures T_M as indicated in the legend at number density $n_M = 1.15$. *Moving average applied.*

already exhibit glassy behavior, as can be seen in a simulation of the same system in (Voigtmann and Horbach, 2009). The two systems at $T_M = 40$ and 320 present intermediate steps between the two extremes.

5.2 *Dynamics*

In addition to a study of the effect of the matrix correlations on the tracer dynamics, a few of the observations made for the 2D systems will be demonstrated for the 3D system as well.

Single-energy system exhibits localization transition The MSD of the single-energy system at $T_M = 2/3$ is shown as solid lines for a range of tracer diameters σ_F in fig. 5.3 *(top)*. The system clearly undergoes a Lorentz-model localization transition at $\sigma_F^c \approx 0.45$, in analogy to the 2D case discussed in chapter 2. The effective exponents of the MSD are shown in fig. 5.3 *(bottom)*. The critical anomalous exponent of the continuous Lorentz model in three dimensions is $z \approx 6.25$, with $\delta r^2(t) \sim t^{2/z}$ (see section 1.2.2) and is marked in the plot of the effective exponent as the horizontal black line. The MSD of the single-energy case at $\sigma_F = 0.45$ exhibits subdiffusive growth compatible with that exponent at the end of the simulation run, indicating that this state is close to the localization transition. An asymptotic scaling analysis was not performed.

Averaging of the dynamics of the confined ideal gas As was the case in 2D, the dynamics of the confined ideal gas in 3D present an energy average over the single-energy dynamics and the localization transition becomes rounded as a result. This is demonstrated exemplarily at the matrix temperature $T_M = 2/3$ with the MSD in fig. 5.3 where the confined-ideal-gas data is shown as dashed lines for the limits of the diameter range, $\sigma_F = 0.4$ and 0.52, superposed over the single-energy data. While the single-energy system undergoes a Lorentz-model localization transition at $\sigma_F^c \approx 0.45$, the MSD of the confined ideal gas becomes diffusive even at $\sigma_F = 0.52$, analogously to the observations discussed in chapter 3.

A formalization of the energy averaging as it was performed in section 3.3 for the confined ideal gas in 2D was not achieved, here. The mapping onto a hard-sphere system is more difficult to perform in three dimensions because narrow channels in the void space are generically defined by three obstacles. This makes it problematic to associate the potential energy needed to pass the

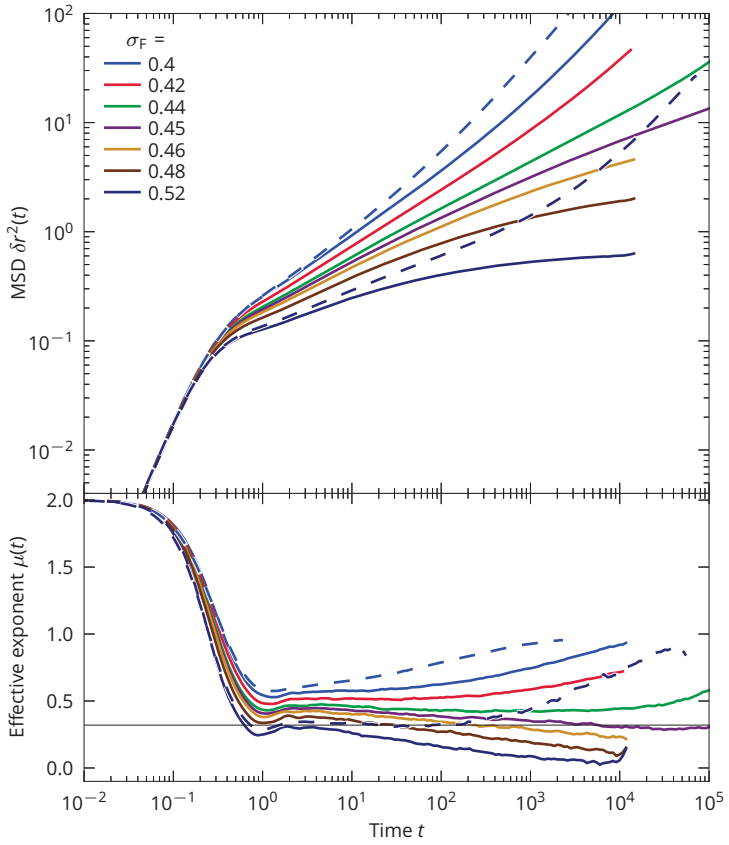

Figure 5.3: *Top:* Mean-squared displacement for the single-energy case at matrix temperature $T_M = 2/3$ for a range of tracer diameters σ_F as indicated in the legend. The MSD of the confined ideal gas at the diameters $\sigma_F = 0.4$ and 0.52 is superposed as dashed lines. *Bottom:* Effective exponent of the MSD shown above. The anomalous exponent of the Lorentz model, $2/z \approx 2/6.25 = 0.32$, is shown as a solid black line.

channel with a single hard-sphere radius. Qualitatively, however, the energy averaging in 3D is very much the same as in 2D.

Interacting fluid particles When an interacting fluid component is considered, the dynamics are modified in a similar way to the 2D case, which was discussed in section 4.3. In fig. 5.4 *(top)*, the MSD of interacting fluid particles at number density $n_F = 1.15$ (i.e. 1000 particles in a cubic box with side length $L = 9.55$) is shown at matrix temperature $T_M = 2/3$ compared to the confined-ideal-gas data at the same diameters σ_F. At short and intermediate times, the interacting-fluid MSD is smaller than the confined-ideal-gas MSD, but it overtakes it at long times.

In contrast to the two-dimensional systems, the interacting fluid at the investigated number density *does not* show dynamics compatible with the Lorentz model, not even on intermediate times. This is especially visible in the effective exponent shown in fig. 5.4 *(bottom)*. The critical exponent of the Lorentz model, $2/z \approx 2/6.25 = 0.32$ is shown as a solid black line. At no value of σ_F does the effective exponent match the critical exponent more than momentarily. This illustrates that the idealized transition of the Lorentz model does not occur in systems with interacting mobile particles with soft potentials.

Variation of the structural correlations in the matrix and its effect on the tracer dynamics Simulations of the confined ideal gas were performed for the four matrix temperatures $T_M = 2/3$, 40, 320, and 10^5. Simulations of the single-energy case would have been preferable since they would expose the critical

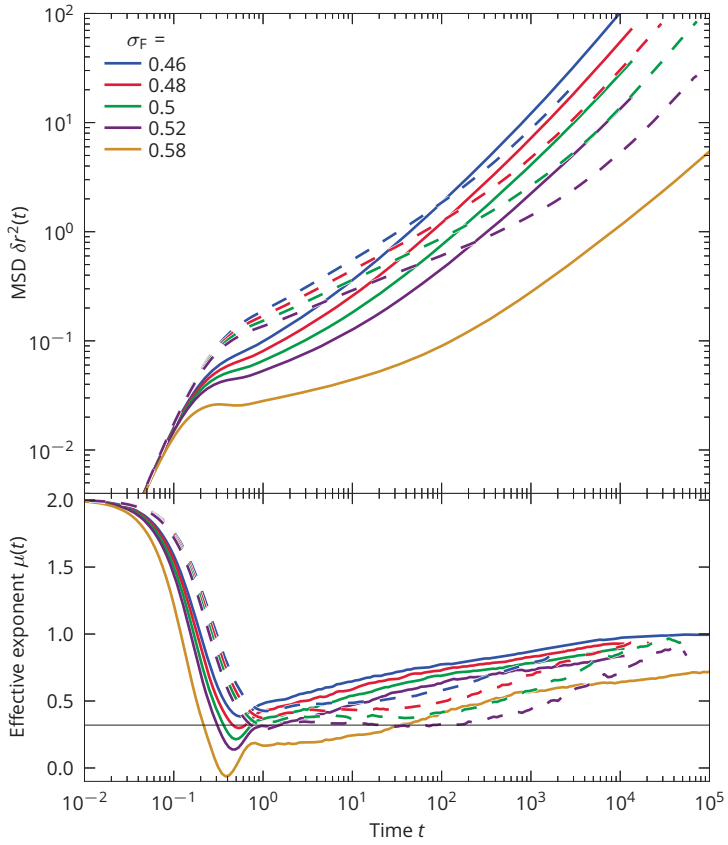

Figure 5.4: Mean-squared displacement *(top)* and effective exponent *(bottom)* of interacting fluid particles at number density $n_F = 1.15$ as solid lines for a range of the diameters σ_F as indicated in the legend. Superposed as dashed lines are the MSD of the confined ideal gas, i.e. the $n_F \to 0$ limit, at the same diameters. For $\sigma_F = 0.58$, no confined-ideal-gas data is available. The anomalous exponent of the Lorentz model, $2/z \approx 2/6.25 = 0.32$, is shown in the bottom plot as a solid black line.

behavior of the Lorentz model. The confined ideal gas was only used since the simulations were performed at a time before the difference between the confined-ideal-gas and the single-energy cases were clear to the author. Nevertheless, a few observations can be made for this data as well.

The MSD of the simulated systems are shown in fig. 5.5 *(left)*. For each temperature, the fluid diameter σ_F was varied over a wide range to observe a slowing down of the dynamics. From the plots it is apparent that the dynamics is qualitatively similar for all matrix temperatures and comparable to the dynamics of the 2D realization of the confined ideal gas discussed in chapter 3.

For a similar slowing down of the dynamics, the tracer diameter σ_F needs to be larger in systems with a larger T_M. This is reflection of the fact that at larger T_M, the obstacles have more overlap and thus fill space less efficiently. This leads to a shift in the localization density, i.e. for a localization to occur the tracers need to have a larger σ_F at larger T_M.

To better expose any differences between the dynamics at different T_M, it is useful to compare states with similar long-time behavior. For this, the MSD — being an integral over the displacements of the particle — is not ideal, because slight differences in the dynamics accumulate over time. A differential quantity like the effective exponent $\mu(t)$ exposes similarities in the long-time behavior better. For the comparison of the dynamics, $\mu(t)$ is shown in fig. 5.6 in three plots, for a range of T_M and σ_F. In each plot, data obtained for the different T_M is grouped such that the long-time behavior of $\mu(t)$ is the same, so as to expose differences on short- and intermediate times. The plots are organized such that the dynamics is the fastest in the *(top)* plot. The selection of the data

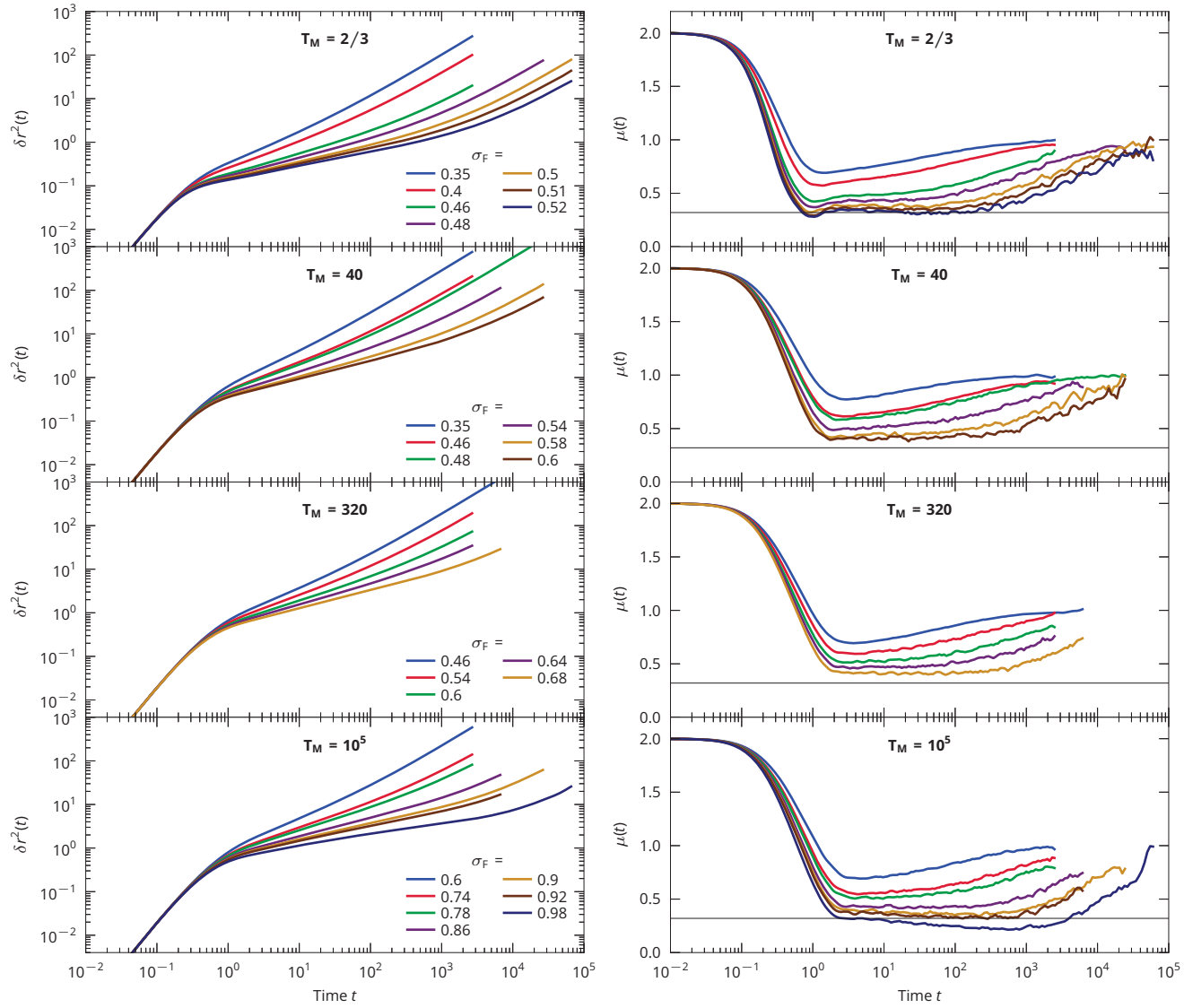

Figure 5.5: Mean-squared displacement $\delta r^2(t)$ *(left)* and corresponding effective exponent $\mu(t)$ *(right)* for the matrix temperatures $T_M = 2/3$, 40, 320, and 10^5 and fluid particle diameters σ_F as given in the legends. The anomalous exponent of the Lorentz model $2/z \approx 0.32$ is marked by a horizontal solid line in the plots of $\mu(t)$.

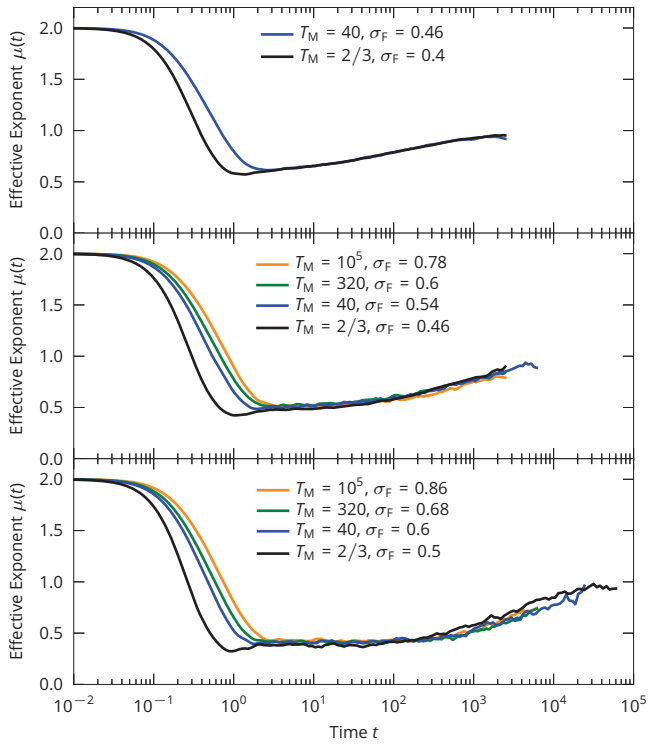

Figure 5.6: Effective exponent $\mu(t)$ of the mean-squared displacement for a range of matrix temperatures T_M and tracer diameters σ_F as indicated in the legends. Data is grouped so that the long-time behavior is matched.

was performed by hand and does not imply that the systems in each plot have the same distance from their respective effective transitions.

In order to achieve a match of the long-time dynamics, the tracer diameter σ_F has to be increased with the matrix temperature, to account for the shift in the localization density. Apart from this, the matching works remarkably well, as the behavior of the effective exponent is the *same* for the presented systems from a time $t \approx 3$ on. The long-time dynamics of the confined ideal gas might therefore be seen as independent from matrix correlations, except for a trivial shift in the localization density.

On short times, however, clear differences arise. The lower the matrix temperature is, the earlier and the faster does the effective exponent decay, indicating that the tracers come into contact with obstacles at an earlier time. Additionally, at $T_M = 2/3$ the effective exponent develops an undershoot at a time $t \approx 1$, reminiscent of the signature of caging in glass-forming systems (Horbach et al., 2010). This implies that the tracers are trapped for a short time in cages formed by the obstacles. That this trapping seems not to influence the long-time dynamics is noteworthy.

5.3 *Summary*

In analogy to the two-dimensional systems in chapters 2 to 4, with which the link between the Lorentz model and quenched-annealed systems was systematically studied, analogous systems were simulated here in three dimensions. The presented results are preliminary but allow to draw a few conclusions.

The main observations of the 2D systems were found to hold for the 3D systems, as well. For tracers at a single energy, when inserted into a matrix of obstacles, the system undergoes a Lorentz-model localization transition

when the tracer diameter is increased. When an ideal gas of mobile particles is inserted into the matrix, the resulting dynamics are an energy average over the single-energy dynamics. When the mobile particles are allowed to interact, the system is a realization of a quenched-annealed system. Then, the single-particle dynamics are found to be enhanced in comparison to the confined ideal gas'. More clearly apparent than in the 2D system, the dynamics of the quenched-annealed system in 3D is not compatible with the Lorentz model dynamics.

In addition, the structural correlations of the matrix obstacles were systematically varied in an effort to investigate pre-asymptotic corrections to the dynamics. The correlations were controlled with the temperature at which the matrix was equilibrated. This allowed a continuous manipulation of the structural correlations, ranging from the uncorrelated matrix at infinite matrix temperature to a strongly correlated structure at low matrix temperature.

Simulations of a confined ideal gas at different matrix temperatures revealed that while the matrix structure has an influence on the short time dynamics of non-interacting tracers, the long time dynamics are unchanged.

6
Conclusions and outlook

The aim of this work was to systematically investigate the connection between the Lorentz model and more complex heterogeneous media, and determine the relevance of the Lorentz model localization scenario for more complex heterogeneous media. In particular, the influence of a soft interaction potential and of the interactions between mobile particles on the localization scenario were investigated in simulations of two-dimensional systems. Thereby, it was shown that the dynamics of soft heterogeneous media is generically different from the dynamics of their hard-sphere counterparts.

Soft-sphere Lorentz model It was shown that the Lorentz model can be reproduced with a matrix of purely repulsive, soft spheres and a non-interacting gas of tracers *only* if the tracers all have exactly the same energy. This requirement is unneeded in hard-sphere systems, where the energy of the particles only modifies the microscopic timescale. A hard-sphere mapping was developed which revealed that both the soft-sphere interaction diameter and the particle energy play the role of control parameters but that both can be contained in an effective hard-sphere density. A similar mapping has not been achieved for three dimensions, yet.

Rounding of the transition in heterogeneous media If the requirement of all particles having the same energy is lifted — turning the system into an ideal gas confined in a soft matrix — the localization transition in the Lorentz model generically becomes rounded, i.e. the critical scaling of the Lorentz model is not found and a sharp transition point where all particles become localized cannot be identified. The wide energy distribution of the tracers which was found to be responsible for the rounding is a *generic feature* of realistic systems. This implies that the Lorentz model scenario can apply to realistic heterogeneous media *only* approximately and the scaling properties of the Lorentz model *generally cannot be observed*. Still, the rounding of the transition can be understood in this case via the hard-sphere mapping as an energy average over all tracers, with each tracer having a different critical density according to its energy.

Enhancement of transport by increasing the fluid density Expressing the system's dynamics via an energy average is not possible anymore once a further step towards realistic systems is taken: When the ideal gas is replaced with an interacting fluid, the particles frequently collide with each other. This makes it

impossible to map the system back onto the one-particle Lorentz model. However, the interacting fluid showed effective scaling of its long-time dynamics comparable to the confined ideal gas which implies that there is an underlying connection which is yet to be explored.

Increasing the fluid density was shown to enhance transport on long times. It was shown that this was due to the frequent energy exchange of particles, which lead to particles pushing each other out of pockets in the matrix structure. The same phenomenon cannot occur in hard-sphere systems, where the void space is independent of the energy of the particles and there are no energy barriers between pockets of void space. Indeed, it has been shown in simulations of QA mixtures e.g. by (Kurzidim et al., 2010), that increasing the fluid density in hard-sphere systems typically *slows down* transport.

Interacting fluid exhibits critical scaling compatible with Lorentz model Near the effective transition of the system, where transport did not become diffusive or localized over the course of the simulation, the interacting system showed the critical time-space scaling of the Lorentz model. This is in stark contrast to the confined ideal gas system. The reason behind this might be the homogenizing effect of the energy exchange between fluid particles: in the interacting fluid, if one particle is delocalized, it can pass this state to a localized particle by exchanging energy with it. Thus, as long as a single particle is delocalized, all are. If the system is dense enough that all delocalized particles are close to the transition, the dynamics might follow the Lorentz model scenario, even fulfilling the critical scaling. The occurrence of time-space scaling at one fluid density should not be overstated, since it is very common for effective scaling to occur and the agreement might be accidental. Therefore, additional study of the localization transition over a wide range of fluid densities is necessary to conclude whether the Lorentz model is still a relevant idealization for confined interacting fluids.

Effective reentrance transition While the hard-sphere mapping cannot be used to express the dynamics of the interacting fluid as an energy average, it can still be used to the categorize the particles into momentarily localized and delocalized particles as a function of their energy. This was applied to investigate the occurrence of a reentrance transition. It had previously been speculated that a reentrance transition in a heterogenous medium with a fixed matrix is only possible when there is an additional mechanism allowing for the modification of the matrix structure by the fluid component. This is true for hard-sphere systems, but was shown here to not hold in soft systems. Instead, an effective reentrance transition was identified in a system where the matrix structure is completely independent from the fluid, but is entirely due to the modification of the energy landscape by the increase of the fluid density. Extending the simulations to higher fluid densities would be valuable. On the one hand, the increase in the average particle energy is be expected to shift the effective localization transition towards even larger matrix packing fractions, making the systems even more mobile. On the other hand, another localization mechanism in the form of caging is expected to become important. How the interplay of these two mechanisms affects the dynamics is not obvious.

Since the fluid interactions clearly have a strong influence on the behavior

of heterogenous media, further insights would also be expected from a study of the collective dynamics.

Rounded localization transition in an experiment The results obtained in this work have shown themselves to be valuable in the interpretation of an experiment of a heterogeneous medium. The experiment consists of a colloidal fluid confined in a quasi-two-dimensional random matrix, and exhibits a rounded localization transition. Because the experiment allows the variation of the fluid and matrix packing fractions over a wide parameter range, this opens up exciting opportunities for the further study of heterogeneous media. For instance, as stated above, the interplay between the localization transition and glassy dynamics at high fluid densities would be a valuable subject, and would allow comparison to corresponding simulations.

A
Insertion of the fluid component into the matrix

A.1 Preparation of the confined ideal gas

For the insertion of the confined ideal gas into the matrix, three different insertion methods were tested and found to lead to the same distribution of energies and the same dynamics:

1. *Naïve insertion:* For each tracer particle an insertion position was randomly picked. It was inserted at that position if it was far enough from neighboring particles according to an ad hoc minimum distance: It was required that the distance to the nearest obstacle may not be smaller than $0.65\sigma_{\mathrm{M}}$ and to the nearest tracer may not be smaller than $0.2\sigma_{\mathrm{M}}$. Especially the latter requirement is unphysical, which is why this criterion was eventually discarded.

2. *Boltzmann-weighted insertion:* an insertion position for a tracer particle was randomly picked. Then the potential energy U of the particle at that position was calculated and the particle insertion was accepted with probability $\min[1, \exp(-\beta U)]$.

3. *Grand-canonical Monte Carlo insertion:* the particle configurations were generated in a grand-canonical Monte Carlo simulation by taking snapshots of the system when the system had been simulated for long enough and the number of particles was as needed. Specifically, successive umbrella sampling (Virnau and Müller, 2004) was used to more easily generate configurations with the appropriate particle number. In the implemented version of the method it is required that the average number of particles in the system be increased in steps of 1 from 0. At each step, 500000 insertions and deletions of particles were performed.

The bulk of the discussed data was calculated for systems created with criterion 1, which was replaced by criterion 2 and 3 for the most recent data.

The three insertion methods and the resulting dynamics will now be studied on the example of the self-part of the van-Hove function as this gives the full information about the tracer dynamics. In fig. A.1, the van-Hove function is shown for the three insertion methods for three simulation runs that are otherwise identical. The van-Hove function is shown for three different times, one at the beginning of the runs (t = 0.1), one at an intermediate time (t = 23.6), and one at the end of the runs (t = 6660). All three insertion methods, the naïve (solid lines), the Boltzmann-weighted particle insertion (dotted

lines) and the the grand-canonical particle insertion (dashed lines) give nearly indistinguishable results. The differences between the insertion methods are not large enough to rise above the noise present in the data.

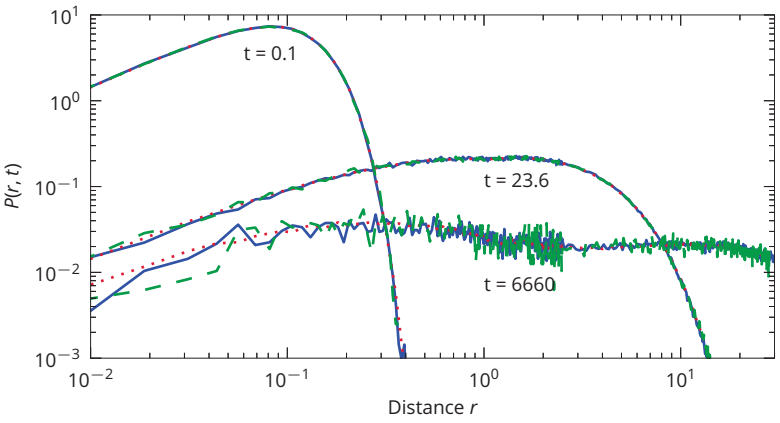

Figure A.1: Double-logarithmic plots of the van-Hove function for the ideal gas with tracer diameter $\sigma_F = 0.3$ as a function of distance r for a range of times as annotated in the plot. Comparison of the naïve insertion method (solid lines), the Boltzmann-weighted insertion method (dotted lines), and the grand-canonical insertion method (dashed lines) for the ideal gas with tracer diameter $\sigma_F = 0.3$.

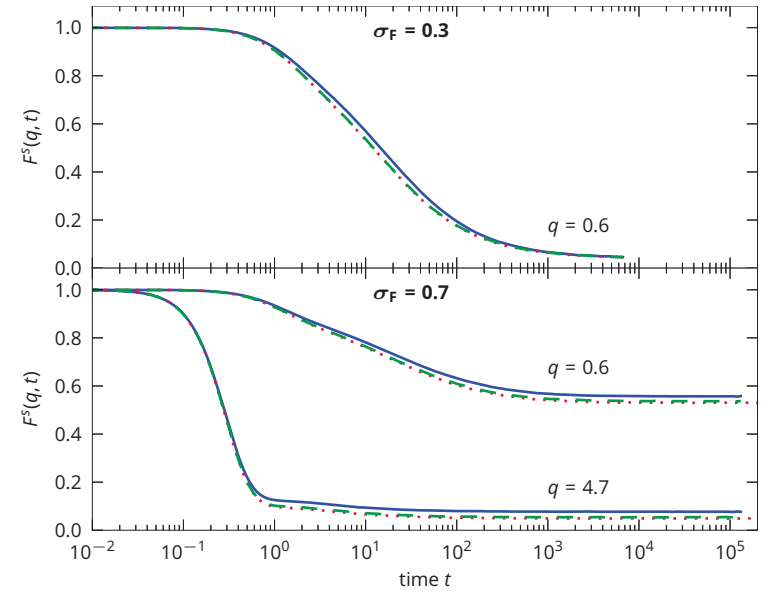

Figure A.2: *Top:* Plot of the intermediate scattering function at $\sigma_F = 0.3$ as a function of time t at wave number $q = 0.6$ for the naïve insertion method (solid line), Boltzmann-weighted insertion method (dotted line), and grand-canonical insertion method (dashed line). *Bottom:* The same plot at $\sigma_F = 0.7$ and at $q = 0.6, 4.7$.

To further study the localization of particles, it is useful to check the self-part of the intermediate scattering function $F^s(q,t)$ for differences between the insertion methods. Even though it is the Fourier transform of the van-Hove function and thus contains the same information, it exposes localized particles better in the form of the non-ergodicity parameter $f(q)$, the long-time limit of $F^s(q,t)$. In fig. A.2, the ISF is shown for $\sigma_F = 0.3$ (top panel) on the delocalized side and $\sigma_F = 0.7$ (bottom panel) on the localized side of the transition. For $\sigma_F = 0.3$ the three insertion methods are compared at the wave number $q = 0.6$, exemplarily. Apart from a slight difference in the relaxation time, all three insertion methods result in a comparable ISF. Most notably, the long-time limit is the same for all three systems. At $\sigma_F = 0.7$, the three insertion methods are compared for two wave numbers, $q = 0.6$ and 4.7, where the naïve insertion method does show a slightly enlarged long-time limit compared to the other two methods which produce nearly exactly the same results.

The full q-dependence of the long-time limit $f(q)$ for both systems is shown in fig. A.3 for the three insertion methods. At $\sigma_F = 0.3$, all three insertion

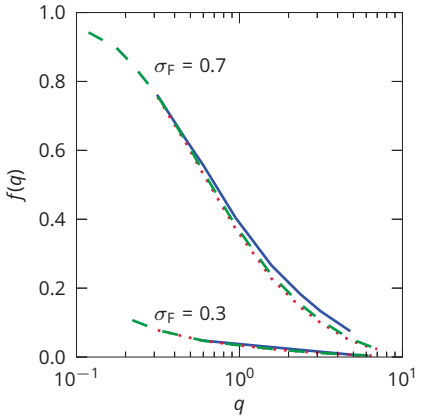

Figure A.3: Semilogarithmic plot of the long-time limit $f(q)$ of the self-part of the intermediate scattering function $f^s(q,t)$ as a function of the wave number q at $\sigma_F = 0.3$ and 0.7 for the the naïve insertion method (solid lines), Boltzmann-weighted insertion method (dotted lines), and grand-canonical insertion method (dashed lines).

methods result in the same values over the whole q-range, while at $\sigma_F = 0.7$ the naïve insertion method results in slightly enlarged values at large q-values but converges towards the other methods at small q.

In conclusion, the naïve insertion method tends to overestimate localization on very small lengthscales slightly but results in the correct dynamics otherwise. In light of this, the data obtained with the naïve insertion method was not discarded in the main discussion.

A.2 Preparation of the interacting fluid in QA systems

The interacting fluid was inserted into the matrix in a similar fashion as the confined ideal gas, but only the naïve and the grand-canonical method were used.

Increase in the average energy in systems at large fluid particle diameters At very large particle diameters σ_F, the naïve insertion mechanism can insert particles into pockets in the void space which are too small. As a result, said particles then have a higher than statistically expected potential energy. After the equilibration, it was standard procedure to rescale the particle energies in each system such that the total energy was the same in all systems. In some cases the collective potential energy of a given system was larger than the total average energy of all systems, making the rescaling impossible. Because of this, at $\sigma_F = 0.8$, one system (of 100) had to be excluded from the simulation. The same did not occur in the grand-canonical insertion method where the average energy was found to be generally lower and the rescaling was always successful. At $\sigma_F = 0.8$, the grand-canonically inserted system was eventually used.

Dynamics The differences in the dynamics caused by the two insertion mechanisms were again tested with the van-Hove function. In fig. A.4 *(top)*, it is shown for two systems with one created with the naïve particle insertion (lines) and the other created with the grand-canonical particle insertion (bullets), which are otherwise the same. The systems contain interacting fluid particles of diameter $\sigma_F = 0.8$ at the number density $n_F = 0.0625$. The only difference in the dynamics is found on short distances, where the naïvely created system shows enhanced localization compared to the grand-canonically inserted system. This shows that the former is more likely to create particles which are trapped in small pockets of the matrix, also leading to the increase in potential energy discussed above. The dynamics on lengthscales $r > 0.2$ are completely the same, regardless of the insertion method. Also note that the enhanced localization on very small lengthscales has no measurable influence on the average MSD, for instance, where the contribution of strongly localized particles on the system average is marginal compared to the contribution of delocalized particles or even particles localized on large lengthscales. Qualitatively the same situation occurs in fig. A.4 *(bottom)*, where the number density has been increased to $n_F = 0.625$. But there, the effect is less pronounced. At lower σ_F, the differences between the insertion methods become less apparent in the dynamics.

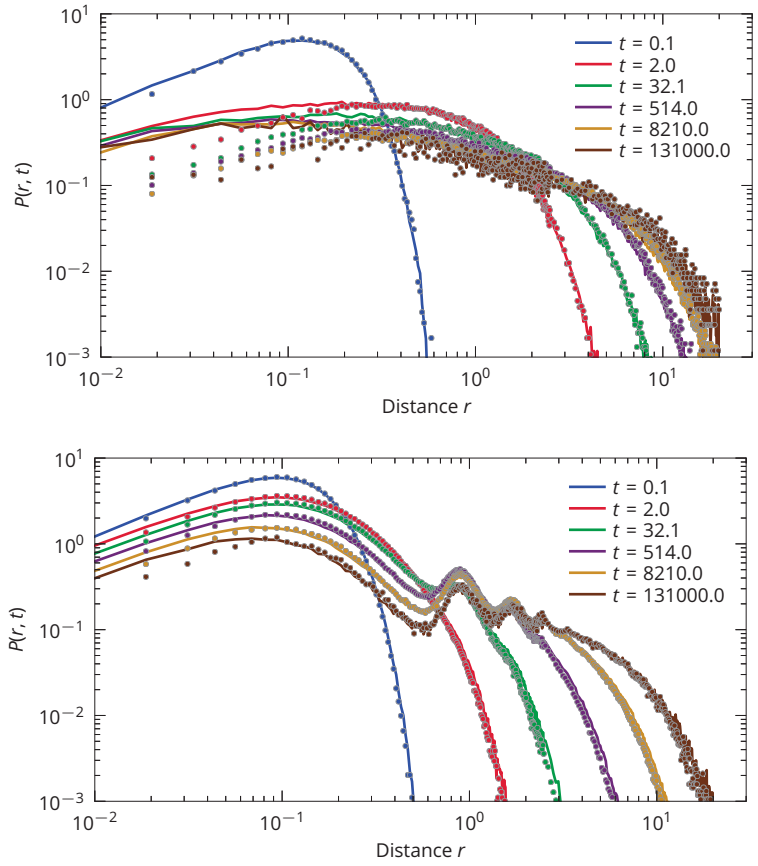

Figure A.4: *Top:* The self part of the van-Hove function as a function of distance r for a range of times as indicated in the legend. Comparison of the naïve (lines) and the grand-canonical particle insertion methods (bullets) for a system of interacting particles with diameter $\sigma_F = 0.8$ and $n_F = 0.0625$. *Bottom:* The same plot for $\sigma_F = 0.8$ and $n_F = 0.625$.

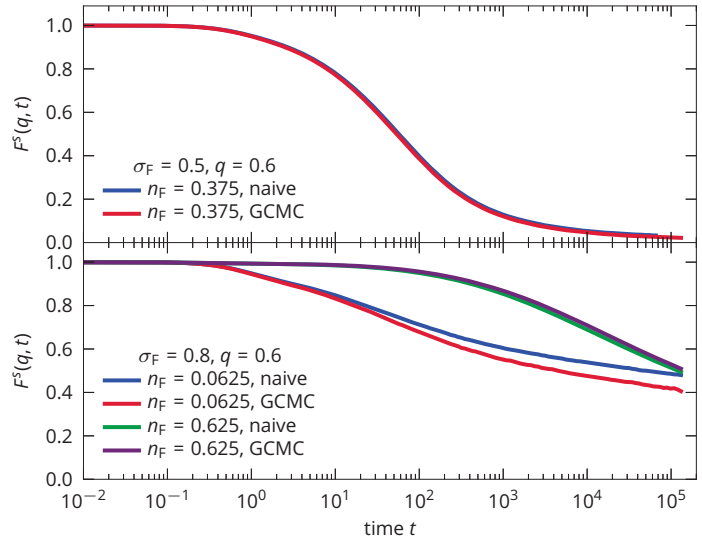

Figure A.5: *Top:* Plot of the intermediate scattering function at $\sigma_F = 0.5$ as a function of time t at wave number $q = 0.6$ for the naive and the grand-canonical (GCMC) insertion methods. *Bottom:* The same plot at $\sigma_F = 0.8$.

The intermediate scattering function is equally very much unchanged by the different insertion methods. On the delocalized side, there is no change at all, which is exemplarily shown for the particle diameter $\sigma_F = 0.5$, the wavenumber $q = 0.6$ and $n_F = 0.375$ in fig. A.5 *(top)*. On the localized side, there is a slight difference between the ISF obtained from the two insertion methods. This is shown exemplarily in fig. A.5 *(bottom)* for $\sigma_F = 0.8$, $q = 0.6$ and for two number densities, $n_F = 0.0625$ and $n_F = 0.625$. There, the relaxation time seems to vary between the two insertion methods: more so in the $n_F = 0.0625$ case and less so in the $n_F = 0.625$ case. This difference is almost certainly due to the increased difficulty of obtaining the ensemble average at large diameters. The difference in the dynamics between the insertion mechanisms becomes the greater, the larger the particle diameter is and the state at $\sigma_F = 0.8$ was the only one to show significant differences in the ISF (or other quantities) between the insertion mechanisms, and there the GCMC-inserted systems were used.

For the interpretation of the data, the insertion method is thus not relevant at all. Both the van-Hove function and the intermediate scattering function, which both give a full description of the dynamics, are effectively unaffected by the choice of the insertion method.

Bibliography

(Andersen, 1980) Andersen, H. C. (1980). Molecular dynamics simulations at constant pressure and/or temperature. *J. Chem. Phys.*, 72(4):2384.

(Barker and Henderson, 1967) Barker, J. A. and Henderson, D. (1967). Perturbation theory and equation of state for fluids .2. A successful theory of liquids. *J. Chem. Phys.*, 47(11):4714–4721.

(Bauer et al., 2010) Bauer, T., Höfling, F., Munk, T., Frey, E., and Franosch, T. (2010). The localization transition of the two-dimensional Lorentz model. *Eur. Phys. J.-Spec. Top.*, 189(1):103–118.

(Bayer, 2007) Bayer, M. (2007). *Microscopic models for viscoelasticity in two dimensional colloidal suspensions Diploma Thesis*. PhD thesis.

(Beijeren, 1982) Beijeren, H. V. (1982). Transport properties of stochastic Lorentz models. *Rev. Mod. Phys.*, 54(1):195–234.

(Ben-Avraham and Havlin, 2000) Ben-Avraham, D. and Havlin, S. (2000). *Diffusion and Reactions in Fractals and Disordered Systems*. Cambridge University Press, Cambridge, first edition.

(Binder et al., 2004) Binder, K., Horbach, J., Kob, W., Paul, W., Varnik, F., and Fathollah, V. (2004). Molecular dynamics simulations. *J. Phys. Condens. Matter*, 16(5):429.

(Chang et al., 2004) Chang, R., Jagannathan, K., and Yethiraj, A. (2004). Diffusion of hard sphere fluids in disordered media: A molecular dynamics simulation study. *Phys. Rev. E*, 69(5):1–9.

(Das et al., 2006) Das, S., Fisher, M., Sengers, J., Horbach, J., and Binder, K. (2006). Critical Dynamics in a Binary Fluid: Simulations and Finite-Size Scaling. *Phys. Rev. Lett.*, 97(2):025702.

(de Gennes, 1976) de Gennes, P. G. (1976). La percolation: un concept unificateur. *Recherche*, 7(72):919–927.

(Einstein, 1905) Einstein, A. (1905). Über die von der molekularkinetischen Theorie der Wärme geforderte Bewegung von in ruhenden Flüssigkeiten suspendierten Teilchen. *Ann. Phys.*, 322(8):549–560.

(Elam et al., 1984) Elam, W., Kerstein, A., and Rehr, J. (1984). Critical properties of the void percolation problem for spheres. *Phys. Rev. Lett.*, 52(17):1516–1519.

(Ernst and Weyland, 1971) Ernst, M. and Weyland, A. (1971). Long time behaviour of the velocity auto-correlation function in a Lorentz gas. *Phys. Lett. A*, 34A(1):39–40.

(Franosch et al., 2011) Franosch, T., Spanner, M., Bauer, T., Schröder-Turk, G. E., and Höfling, F. (2011). Space-resolved dynamics of a tracer in a disordered solid. *J. Non. Cryst. Solids*, 357(2):472–478.

(Franosch and Voigtmann, 2002) Franosch, T. and Voigtmann, T. (2002). Completely monotone solutions of the mode-coupling theory for mixtures. *J. Stat. Phys.*, 109(1):237–259.

(Goldenfeld, 1992) Goldenfeld, N. (1992). *Lectures on Phase Transitions and the Renormalization Group*, volume 85 of *Frontiers in Physics*. Perseus Books.

(Götze, 2009) Götze, W. (2009). *Complex Dynamics of Glass-Forming Liquids: A Mode-Coupling Theory (International Series of Monographs on Physics)*, volume 143. Oxford University Press.

(Götze et al., 1981a) Götze, W., Leutheusser, E., and Yip, S. (1981a). Correlation functions of the hard-sphere Lorentz model. *Phys. Rev. A*, 24(2):1008–1015.

(Götze et al., 1981b) Götze, W., Leutheusser, E., and Yip, S. (1981b). Dynamical theory of diffusion and localization in a random, static field. *Phys. Rev. A*, 23(5):2634–2643.

(Götze et al., 1982) Götze, W., Leutheusser, E., and Yip, S. (1982). Diffusion and localization in the two-dimensional Lorentz model. *Phys. Rev. A*, 25(1):533–539.

(Grassberger, 1999) Grassberger, P. (1999). Conductivity exponent and backbone dimension in 2-d percolation. *Phys. A Stat. Mech. its Appl.*, 262(3-4):251–263.

(Hairer et al., 2002) Hairer, E., Lubich, C., and Wanner, G. (2002). *Geometric Numerical Integration: Structure-Preserving Algorithms for Ordinary Differential Equations*. Springer-Verlag, Berlin Heidelberg New York, 1st edition.

(Hansen and McDonald, 2006) Hansen, J. and McDonald, I. (2006). *Theory of simple liquids*. Academic Press, London, 3rd edition.

(Höfling et al., 2011) Höfling, F., Bamberg, K.-U., and Franosch, T. (2011). Anomalous transport resolved in space and time by fluorescence correlation spectroscopy. *Soft Matter*, 7(4):1358.

(Höfling and Franosch, 2013) Höfling, F. and Franosch, T. (2013). Anomalous transport in the crowded world of biological cells. *Rep. Prog. Phys.*, 76(4):046602.

(Höfling et al., 2006) Höfling, F., Franosch, T., and Frey, E. (2006). Localization transition of the three-dimensional lorentz model and continuum percolation. *Phys. Rev. Lett.*, 96(16):165901.

(Höfling et al., 2008) Höfling, F., Munk, T., Frey, E., and Franosch, T. (2008). Critical dynamics of ballistic and Brownian particles in a heterogeneous environment. *J. Chem. Phys.*, 128(16):164517.

(Hohenberg and Halperin, 1977) Hohenberg, P. and Halperin, B. (1977). Theory of dynamic critical phenomena. *Rev. Mod. Phys.*, (3).

(Horbach et al., 2001) Horbach, J., Kob, W., and Binder, K. (2001). Structural and dynamical properties of sodium silicate melts: an investigation by molecular dynamics computer simulation. *Chem. Geol.*, 174(1-3):87–101.

(Horbach et al., 2010) Horbach, J., Voigtmann, T., Hofling, F., Franosch, T., and Höfling, F. (2010). Localization phenomena in models of ion-conducting glass formers. *Eur. Phys. J. Spec. Top.*, 189(1):141–145.

(Kammerer et al., 2008) Kammerer, A., Höfling, F., and Franosch, T. (2008). Cluster-resolved dynamic scaling theory and universal corrections for transport on percolating systems. *Europhys. Lett.*, 84(6):66002.

(Kertesz and Metzger, 1983) Kertesz, J. and Metzger, J. (1983). Properties of the density relaxation function in classical diffusion models with percolation transition. *J. Phys. A. Math. Gen.*, 735.

(Kim et al., 2009) Kim, K., Miyazaki, K., and Saito, S. (2009). Slow dynamics in random media: Crossover from glass to localization transition. *Europhys. Lett.*, 88(3):36002.

(Kim et al., 2010) Kim, K., Miyazaki, K., and Saito, S. (2010). Molecular dynamics studies of slow dynamics in random media: Type {A}-{B} and reentrant transitions. *Eur. Phys. J.-Spec. Top.*, 189(1):135–139.

(Kim et al., 2011) Kim, K., Miyazaki, K., and Saito, S. (2011). Slow dynamics, dynamic heterogeneities, and fragility of supercooled liquids confined in random media. *J. Phys. Condens. Matter*, 23(23):234123.

(Krakoviack, 2005) Krakoviack, V. (2005). Liquid-Glass Transition of a Fluid Confined in a Disordered Porous Matrix: A Mode-Coupling Theory. *Phys. Rev. Lett.*, 94:65703.

(Krakoviack, 2007) Krakoviack, V. (2007). Mode-coupling theory for the slow collective dynamics of fluids adsorbed in disordered porous media. *Phys. Rev. E*, 75(3):031503.

(Krakoviack, 2009) Krakoviack, V. (2009). Tagged-particle dynamics in a fluid adsorbed in a disordered porous solid: Interplay between the diffusion-localization and liquid-glass transitions. *Phys. Rev. E*, 79(6):1–16.

(Krakoviack, 2010) Krakoviack, V. (2010). Statistical mechanics of homogeneous partly pinned fluid systems. *Phys. Rev. E*, 82(6):61501.

(Krakoviack, 2011) Krakoviack, V. (2011). Mode-coupling theory predictions for the dynamical transitions of partly pinned fluid systems. *Phys. Rev. E*, 84(5).

(Kurzidim et al., 2009) Kurzidim, J., Coslovich, D., and Kahl, G. (2009). Single-particle and collective slow dynamics of colloids in porous confinement. *Phys. Rev. Lett.*, 103(13):138303.

(Kurzidim et al., 2010) Kurzidim, J., Coslovich, D., and Kahl, G. (2010). Impact of random obstacles on the dynamics of a dense colloidal fluid. *Phys. Rev. E*, 82(4):1–15.

(Kurzidim et al., 2011) Kurzidim, J., Coslovich, D., and Kahl, G. (2011). Dynamic arrest of colloids in porous environments: disentangling crowding and confinement. *J. Phys. Condens. Matter*, 23(23):234122.

(Lorentz, 1905) Lorentz, H. (1905). The motion of electrons in metallic bodies. *Proc. R. Acad. Sci. Amsterdam*, 7:438–453.

(Lowe et al., 1997) Lowe, C., Frenkel, D., and van der Hoef, M. (1997). Deviations from Fick's Law in Lorentz Gases. *J. Stat. Phys.*, 87:1229–1244.

(Machta and Moore, 1985) Machta, J. and Moore, S. S. M. (1985). Diffusion and long-time tails in the overlapping Lorentz gas. *Phys. Rev. A*, 32(5):3164–3167.

(Meroni et al., 1996) Meroni, A., Levesque, D., and Weis, J. J. (1996). Correlation functions of hard sphere fluids adsorbed in porous media. *J. Chem. Phys.*, 105(3):1101.

(Mittal et al., 2006) Mittal, J., Errington, J., and Truskett, T. (2006). Using available volume to predict fluid diffusivity in random media. *Phys. Rev. E*, 74(4):040102.

(Moreno and Colmenero, 2006) Moreno, A. J. and Colmenero, J. (2006). Anomalous dynamic arrest in a mixture of large and small particles. *Phys. Rev. E*, 74(2).

(Moreno and Colmenero, 2008) Moreno, A. J. and Colmenero, J. (2008). Entangledlike Chain Dynamics in Nonentangled Polymer Blends with Large Dynamic Asymmetry. *Phys. Rev. Lett.*, 100(12):126001.

(Pandey, 1984) Pandey, R. (1984). Classical diffusion, drift, and trapping in random percolating systems. *Phys. Rev. B*, 30(1):489–491.

(Rice, 1988) Rice, J. A. (1988). *Mathematical Statistics and Data Analysis*, volume 72. Duxbury, 3rd edition.

(Rintoul, 2000) Rintoul, M. (2000). Precise determination of the void percolation threshold for two distributions of overlapping spheres. *Phys. Rev. E*, 62(1 Pt A):68–72.

(Schnyder, 2010) Schnyder, S. K. (2010). *Analysis of transport processes in glass-forming fluids in mode-coupling theory*. Diploma thesis, Universität Konstanz.

(Schnyder et al., 2011) Schnyder, S. K., Höfling, F., Franosch, T., and Voigtmann, T. (2011). Long-wavelength anomalies in the asymptotic behavior of mode-coupling theory. *J. Phys. Condens. Matter*, 23(23):234121.

(Skinner et al., 2013) Skinner, T. O. E., Schnyder, S. K., Aarts, D. G. A. L., Horbach, J., and Dullens, R. P. A. (2013). Localization Dynamics of Fluids in Random Confinement. *Phys. Rev. Lett.*, 111(12):128301.

(Spanner, 2010) Spanner, M. (2010). *Anomalous Transport in Porous Media near the Percolation Transition*. Diploma thesis, Universität Erlangen.

(Spanner et al., 2013) Spanner, M., Schnyder, S. K., Höfling, F., Voigtmann, T., and Franosch, T. (2013). Dynamic arrest in model porous media—intermediate scattering functions. *Soft Matter*, 9:1604.

(Stauffer and Aharony, 2003) Stauffer, D. and Aharony, A. (2003). *Introduction to Percolation Theory*. Taylor & Francis, London, rev. 2nd edition.

(Sung and Yethiraj, 2008a) Sung, B. J. and Yethiraj, A. (2008a). Lateral diffusion of proteins in the plasma membrane: spatial tessellation and percolation theory. *J. Phys. Chem. B*, 112(1):143–9.

(Sung and Yethiraj, 2008b) Sung, B. J. and Yethiraj, A. (2008b). The effect of matrix structure on the diffusion of fluids in porous media. *J. Chem. Phys.*, 128(5):054702.

(Torquato, 2002) Torquato, S. (2002). *Random Heterogeneous Materials*. Springer-Verlag.

(van Hove, 1954) van Hove, L. (1954). Correlations in Space and Time and Born Approximation Scattering in Systems of Interacting Particles. *Phys. Rev.*, 95(1).

(Verlet, 1967) Verlet, L. (1967). Computer "Experiments" on Classical Fluids. I. Thermodynamical Properties of Lennard-Jones Molecules. *Phys. Rev.*, 159(1):98–103.

(Virnau and Müller, 2004) Virnau, P. and Müller, M. (2004). Calculation of free energy through successive umbrella sampling. *J. Chem. Phys.*, 120(23):10925–30.

(Voigtmann and Horbach, 2009) Voigtmann, T. and Horbach, J. (2009). Double Transition Scenario for Anomalous Diffusion in Glass-Forming Mixtures. *Phys. Rev. Lett.*, 103(20):205901.

(Weeks et al., 1971) Weeks, J., Chandler, D., and Andersen, H. C. (1971). Role of repulsive forces in determining the equilibrium structure of simple liquids. *J. Chem. Phys.*, 54(12):5237.

(Widder, 1972) Widder, D. V. (1972). *The Laplace Transform*. Princeton University Press, 8th edition.